
Studies on the G. sulfurreducens
PCA Porin Cytochrome Complex
ExtABCD

Joshua A. J. Burton

PhD Thesis

2024

University of East Anglia
School of Biological Sciences
Norwich
UK

This copy of the thesis has been supplied on condition that anyone who consults it is understood to recognise that its copyright rests with the author and that use of any information derived therefrom must be in accordance with current UK Copyright Law. In addition, any quotation or extract must include full attribution.

Abstract

Electroactive Gram-negative bacteria can respire on solid metals and minerals within anoxic environments by transferring electrons generated from intracellular metabolism to the bacterial cell surface. Many Gram-negative bacteria utilise porin cytochrome complexes (PCC) to traverse electrons across the bacterial outer membrane. The model electroactive bacterium *Geobacter sulfurreducens* PCA contains a total of five known PCC with the *extABCD* gene cluster being shown to enhance electron transfer. Strains of *Geobacter* expressing solely the *extABCD* cluster outperform WT strains with 1.4x higher current generated. Whilst *Geobacter* strains only expressing one of the other four PCC saw approximately 4x diminished electroactivity.

Work presented in this thesis has endeavoured to generate methods for the recombinant expression of the *extA*, *extC* and *extD* genes encoding a periplasmic dodecaheme and two outer membrane cytochromes respectively. UV-vis spectroscopy of ExtD and ExtA atypical cytochrome characteristics with a reduced split-Soret were uncovered, suggesting substantial differences in the heme environment to other multiheme cytochromes. Whilst ExtC displayed typical cytochrome spectral features. Through analytical sedimentation and gel filtration it was shown that ExtA forms a trimer with conjugation of the monomers predicted at the N-terminus. Generating a unique 'heme junction' which has not previously been shown in nature.

Interactions of the cytochromes from ExtABCD were additionally investigated with evidence suggesting that only ExtC and ExtD form a stable interaction. With the use of AlphaFold 2 and 3 potential PCC models of ExtABCD were analysed and compared to experimental evidence gathered in this thesis. Through this a new model for ExtABCD is proposed with ExtA acting as a trimeric periplasmic shuttle, ExtBC forming the porin-cytochrome interface and ExtD as the sole extracellular multiheme cytochrome.

Access Condition and Agreement

Each deposit in UEA Digital Repository is protected by copyright and other intellectual property rights, and duplication or sale of all or part of any of the Data Collections is not permitted, except that material may be duplicated by you for your research use or for educational purposes in electronic or print form. You must obtain permission from the copyright holder, usually the author, for any other use. Exceptions only apply where a deposit may be explicitly provided under a stated licence, such as a Creative Commons licence or Open Government licence.

Electronic or print copies may not be offered, whether for sale or otherwise to anyone, unless explicitly stated under a Creative Commons or Open Government license. Unauthorised reproduction, editing or reformatting for resale purposes is explicitly prohibited (except where approved by the copyright holder themselves) and UEA reserves the right to take immediate 'take down' action on behalf of the copyright and/or rights holder if this Access condition of the UEA Digital Repository is breached. Any material in this database has been supplied on the understanding that it is copyright material and that no quotation from the material may be published without proper acknowledgement.



Acknowledgments

First thanks must be given to my amazing supervisory team without whom I would not have made it through this PhD; Professors Tom Clarke, David Richardson and Julea Butt. All of you have helped me immensely throughout this process and shaped me into a better scientist than I was before I started.

To Dr Marcus Edwards, it is because of you that this thesis became what it was by allowing me the opportunity to work with ExtD and ExtC. Who knows what direction I would have gone if you hadn't come to the rescue.

To all the members of 'BIO 2.30' past and present who I have met through this experience. You have all helped me in some way or another, be it offering sage scientific guidance or making me laugh.

Finally, to my family, particularly my mum and dad. You have always loved and supported me throughout all my endeavours. My lotions and potions have finally brewed.

Table of Contents

1.	General Introduction	1
1.1.	Electroactive Bacteria.....	2
1.1.1.	<i>Environmental Impact of Electroactive Bacteria</i>	2
1.1.2.	<i>Biotechnological Uses of Electroactive Bacteria</i>	3
1.2.	Iron-Oxidising Bacteria	6
1.2.1.	<i>Rhodopseudomonas palustris</i> TIE-1	6
1.2.2.	<i>Acidithiobacillus ferrooxidans</i>	9
1.2.3.	<i>Sideroxydans lithotrophicus</i> ES-1.....	11
1.3.	Iron-Reducing Bacteria	14
1.3.1.	<i>Thermincola potens</i> JR	14
1.3.2.	<i>Shewanella oneidensis</i> MR-1.....	16
1.3.3.	<i>Geobacter sulfurreducens</i> PCA	18
1.4.	Spectral Properties of Cytochromes	24
1.5.	Aims of this thesis	28
1.6.	References.....	28
2.	Experimental Methods.....	37
2.1.	General Methods	38
2.1.1.	<i>Media Preparation</i>	38
2.1.2.	<i>Plasmid Maps</i>	38
2.1.3.	<i>Agarose Gel Electrophoresis for DNA Visualization</i>	39
2.1.4.	<i>SDS-PAGE for Protein Visualization</i>	40
2.1.5.	<i>Transformation of plasmids into Escherichia coli</i>	41
2.1.6.	<i>Electroporation of plasmids into Shewanella oneidensis</i> LS527.....	42
2.1.7.	<i>Long Term Storage of Bacterial Strains</i>	43
2.2.	Polymerase Chain Reaction	43
2.2.1.	<i>Affinity Tag Switch of ExtC and ExtD</i>	45
2.2.2.	<i>Construction of pMEGGAx_extA</i>	46
2.2.3.	<i>Generation of N-truncated ExtA</i>	46
2.2.4.	<i>Sequencing of Plasmids</i>	47
2.3.	Protein Purification	47
2.3.1.	<i>HIS-Tag Purification</i>	47
2.3.2.	<i>STREP-II Tag Purification</i>	48
2.3.3.	<i>Size Exclusion Chromatography</i>	48
2.4.	Physical Characterization of Proteins	48

2.4.1.	<i>Liquid Chromatography Mass Spectroscopy</i>	48
2.4.2.	<i>Analytical Ultracentrifugation</i>	49
2.5.	Spectroelectrochemical Characterisation of Proteins	51
2.5.1.	<i>UV-Visible Spectroscopy</i>	51
2.5.2.	<i>Pyridine Hemochrome Assay</i>	51
2.5.3.	<i>Methyl Viologen Assay</i>	52
2.5.4.	<i>Electron Paramagnetic Resonance</i>	52
2.6.	Electrochemistry	53
2.6.1.	<i>Construction of ITO electrodes</i>	55
2.6.2.	<i>Protein Film Electrochemistry</i>	55
2.6.3.	<i>Spectroelectrochemistry</i>	56
2.7.	AlphaFold	57
2.8.	References	61
3.	Expression, Purification and Characterisation of Outer Membrane Lipo-Cytochrome ExtD from <i>Geobacter sulfurreducens</i> PCA	63
3.1.	Introduction	64
3.2.	Methods	65
3.2.1.	<i>Optimisation of ExtD Expression and Purification</i>	65
3.3.	Results	67
3.3.1.	<i>Optimization of Expression and Purification of ExtD</i>	67
3.3.1.1.	<i>Expression of ExtD-His in Escherichia coli BL21</i>	67
3.3.1.2.	<i>Expression of ExtD_His in Shewanella oneidensis LS527</i>	70
3.3.1.3.	<i>Expression of ExtD_STREP in Shewanella oneidensis LS527</i>	73
3.3.2.	<i>Bioinformatical analysis of ExtD</i>	78
3.3.3.	<i>Physical Characterization of ExtD</i>	79
3.3.4.	<i>Computational Characterisation of ExtD</i>	81
3.3.5.	<i>Electronic Paramagnetic Resonance</i>	87
3.3.6.	<i>UV-Visible spectroscopy</i>	88
3.3.7.	<i>Protein Film Voltammetry</i>	92
3.3.8.	<i>Methyl Viologen Studies</i>	97
3.4.	Discussion	98
3.5.	References	102
4.	Protein Characterisation of dodecaheme cytochrome ExtA from <i>Geobacter sulfurreducens</i> PCA	106
4.1.	Introduction	107
4.2.	Results	108

4.2.1.	<i>Heterologous expression of ExtA in S. oneidensis LS527</i>	108
4.2.2.	<i>UV-Visible Spectroscopy</i>	113
4.2.3.	<i>Protein Film Voltammetry</i>	116
4.2.4.	<i>Spectroelectrochemistry</i>	121
4.2.5.	<i>Exploration of Oligomeric State of ExtA</i>	125
4.2.6.	<i>In-silico modelling of ExtA</i>	130
4.2.7.	<i>N-terminus truncation of ExtA</i>	135
4.3.	Discussion	140
4.4.	References	144
5.	Initial Characterisation of lipo-cytochrome ExtC and exploration ExtABCD interactions from <i>Geobacter sulfurreducens</i> PCA	147
5.1.	Introduction	148
5.2.	Results	149
5.2.1.	<i>Expression and Initial Physical Characterisation of ExtC</i>	149
5.2.2.	<i>Sedimentation Velocity Studies of ExtACD Interactions</i>	159
5.2.3.	<i>in-silico Characterisation of Porin ExtB</i>	167
5.3.	Discussion	176
5.4.	References	179
6.	General Discussion	183
6.1.	Thesis Summary	184
6.2.	Models of <i>Geobacter</i> Porin Cytochrome Complexes	187
6.2.1.	<i>AlphaFold modelling of predicted PCCs Gcp1 and Gcp2</i>	188
6.2.2.	<i>AlphaFold modelling of predicted PCC ExtEFG</i>	189
6.2.3.	<i>AlphaFold modelling of predicted PCC ExtHIJKL</i>	193
6.3.	Future Perspectives	197
6.4.	References	198
7.	Appendix	201

Table of Figures

		Page
Figure 1.1	Schematic of a Microbial Fuel Cell	4
Figure 1.2	Schematic of the proposed electron transport pathway in <i>Rhodopseudomonas palustris</i> TIE-1	9
Figure 1.3	Schematic of the proposed electron transport pathway in <i>Acidithiobacillus ferrooxidans</i>	11
Figure 1.4	Schematic of the proposed electron transport pathway in <i>Sideroxydans lithotrophicus</i> ES-1	13
Figure 1.5	Schematic of the proposed electron transport pathway in <i>Thermincola potens</i> JR	15
Figure 1.6	Schematic of the proposed electron transport pathway in <i>Shewanella oneidensis</i>	17
Figure 1.7	Schematic of the proposed electron transport pathway in <i>Geobacter sulfurreducens</i>	19
Figure 1.8	Structure of c-type heme	25
Figure 1.9	Typical spectra of a c-type cytochrome	27
Figure 2.1	Plasmid Maps	39
Figure 2.2	Schematic of three-electrode cell	56
Figure 3.1	SDS-PAGE of ExtD_HIS expressed from <i>E. coli</i> BL21 with varied arabinose concentration	68
Figure 3.2	SDS-PAGE of ExtD_HIS expressed from <i>E. coli</i> BL21 with varied harvest time	69
Figure 3.3	SDS-PAGE of AKTA product following HisTrap with step elution	70
Figure 3.4	SDS-PAGE of ExtD_HIS expressed from <i>S. oneidensis</i> LS527 with varied arabinose concentration	71
Figure 3.5	SDS-PAGE of ExtD_HIS expressed from <i>S. oneidensis</i> LS527 in varied media	72
Figure 3.6	SDS-PAGE of ExtD_HIS expressed from <i>S. oneidensis</i> LS527 with varied growth temperature	73
Figure 3.7	Gel electrophoresis of PCR products from affinity tag switch of <i>extD</i>	74
Figure 3.8	Gel Electrophoresis of pMEGGAx_extD_STREP plasmid re-circularisation	75

Figure 3.9	SDS-PAGE of purified ExtD_STREP from <i>S. oneidensis</i> LS527	76
Figure 3.10	AKTA elution profiles at 410 nm of ExtD_HIS and ExtD_STREP	77
Figure 3.11	Sequence alignment of ExtD from <i>G. sulfurreducens</i> PCA	79
Figure 3.12	Sedimentation Velocity analysis of ExtD	81
Figure 3.13	AlphaFold 2 modelling of ExtD	83
Figure 3.14	AlphaFold 3 modelling of ExtD	84
Figure 3.15	EPR spectrum of ExtD	87
Figure 3.16	UV-Visible spectra of ExtD	90
Figure 3.17	UV-Visible difference spectra of ExtD	92
Figure 3.18	Voltammograms of bare ITO electrode and ITO with ExtD adsorbed	93
Figure 3.19	Faradaic currents of ExtD at varying pH	95
Figure 3.20	Comparison of heme packing between known split Soret cytochromes and STC	102
Figure 4.1	Gel Electrophoresis of Golden Gate product from <i>pMEGGAx_extA</i> plasmid construction	109
Figure 4.2	Amino Acid sequence of ExtA	110
Figure 4.3	Whole cell SDS-PAGE of <i>S. oneidensis</i> LS527 expressing ExtA with varied arabinose concentration	111
Figure 4.4	SDS-PAGE of purified ExtA from <i>S. oneidensis</i> LS527	112
Figure 4.5	UV-Visible spectra of ExtA	115
Figure 4.6	Voltammograms of bare ITO electrode and ITO with ExtA adsorbed	117
Figure 4.7	Faradaic currents of ExtA	118
Figure 4.8	Faradaic currents of ExtA with simulated n=1 redox centres	120
Figure 4.9	Spectroelectrochemistry of ExtA adsorbed to ITO electrode	122
Figure 4.10	Difference spectra of ExtA adsorbed to ITO electrode	125
Figure 4.11	Sedimentation Velocity analysis of ExtA	127
Figure 4.12	Sedimentation Equilibrium analysis of ExtA	128
Figure 4.13	Analytical Gel Filtration assessment of ExtA	130
Figure 4.14	AlphaFold 2 model of monomeric ExtA	132
Figure 4.15	AlphaFold 2 model of trimeric ExtA	133
Figure 4.16	AlphaFold 2 models of dimeric and tetrameric ExtA	134
Figure 4.17	Gel Electrophoresis of Golden Gate reaction to construct <i>pMEGGAx_extA.1</i>	136

Figure 4.18	SDS-PAGE of purified ExtA.1	137
Figure 4.19	UV-Visible spectra of ExtA.1	138
Figure 4.20	Sedimentation Velocity analysis of ExtA.1	140
Figure 5.1	Gel electrophoresis of PCR products from affinity tag switch of <i>extC</i>	150
Figure 5.2	Amino Acid Sequence of Optimized ExtC	151
Figure 5.3	SDS-PAGE of purified ExtC	152
Figure 5.4	UV-Visible spectra of ExtC	153
Figure 5.5	Sedimentation Velocity analysis of ExtC	155
Figure 5.6	AlphaFold 2 model of ExtC	157
Figure 5.7	Sedimentation Velocity analysis of interactions between ExtA and ExtD	161
Figure 5.8	Sedimentation Velocity analysis of interactions between ExtA and ExtC	163
Figure 5.9	Sedimentation Velocity analysis of interactions between ExtC and ExtD	166
Figure 5.10	PRED-TMBB analysis of ExtB	168
Figure 5.11	AlphaFold 2 modelling of ExtB and ExtBC complex	170
Figure 5.12	AlphaFold 3 modelling of ExtAB and ExtBD	173
Figure 5.13	AlphaFold 3 modelling of ExtABCD complex	175
Figure 5.14	Comparison of lipobox amino acid sequences from known lipoproteins	178
Figure 6.1	Cartoon schematics of ExtABCD complex	186
Figure 6.2	Comparison of Outer Membrane Cytochromes	187
Figure 6.3	AlphaFold Models of proposed porin cytochrome complex Gcp1 and Gcp2 from <i>Geobacter sulfurreducens</i> PCA	189
Figure 6.4	AlphaFold Models of proposed porin cytochrome complex ExtEFG from <i>Geobacter sulfurreducens</i> PCA	192
Figure 6.5	AlphaFold Models of proposed porin cytochrome complex ExtHIJKL from <i>Geobacter sulfurreducens</i> PCA	196

Table of Tables

		Page
Table 2.1	Reagents used to produce Resolving and Stacking gels for SDS-PAGE	41
Table 2.2	Primers used in PCR reactions	44
Table 3.1	Solvent Accessible Surface Area of hemes from Alphafold models of ExtD	86
Table 3.2	Midpoint potentials of n=1 simulations from PFV of ExtD	96
Table 3.3	Methyl Viologen assay of ExtD	98
Table 4.1	Midpoint potentials of n=1 simulations from PFV and Spectroelectrochemistry of ExtA	124
Table 4.2	Molecular Masses of Proteins Used in Analytical Gel Filtration	129
Table 4.3	Comparison of Physical Characterisation Results of ExtA	135
Table 4.4	Midpoint potentials of known inner membrane and periplasmic cytochromes involved in extracellular electron transfer from <i>G. sulfurreducens</i> PCA	143
Table 5.1	Solvent Accessible Surface Area of hemes from Alphafold 2 model of ExtC	158
Table 5.2	Comparison of Physical Characterisation Results of ExtC	159
Table 5.3	Solvent Accessible Surface Area of hemes from Alphafold 2 model of ExtBC complex	171

List of Abbreviations

% (v/v)	Percentage by Volume Per Volume
% (wt/vol)	Percentage by Weight by Volume
APS	Ammonium Persulfate
ATP	Adenosine Triphosphate
AUC	Analytical Ultracentrifuge
BLAST	Basic Local Alignment Search Tool
CE	Control Electrode
CNW	Cytochrome Nanowire
CV	Column Volume
EAB	Electroactive Bacteria
EDTA	Ethylenediaminetetraacetic Acid
EET	Extracellular Electron Transport
FTO	Fluorine-Doped Tin Oxide
HEPES	(4-(2-Hydroxyethyl)-1-Piperazineethanesulfonic Acid)
IM	Inner Membrane
ITO	Indium Tin Oxide
LB	Luria Broth
LC-MS	Liquid Chromatography Mass Spectroscopy
LH-RC	Light Harvesting Reaction Centre
MDC	Microbial Desalination Cell
MFC	Microbial Fuel Cell
MHC	Multi Heme Cytochrome
MSE	Mean Square Error
NMR	Nuclear Magnetic Resonance
OM	Outer Membrane
OMC	Outer Membrane Cytochrome
PCC	Porin Cytochrome Complex
PFV	Protein Film Voltammetry

pLDDT	Predicted Local Distance Difference Test
RE	Reference Electrode
RO	Reverse Osmosis
SASA	Solvent Accessible Surface Area
SDS	Sodium Dodecyl Sulphate
SDS-PAGE	Sodium Dodecyl Sulphate–Polyacrylamide Gel Electrophoresis
SE	Sedimentation Equilibrium
SEC	Size Exclusion Chromatography
SHE	Standard Hydrogen Electrode
SOC	Super Optimal Broth
SV	Sedimentation Velocity
TAE	Triethylamine
TEA	Terminal Electron Acceptor
TEMED	Tetramethylethylenediamine
TMBD	3,3',5,5'-Tetramethylbenzidine Dihydrochloride Hydrate
TRIS	Tris(Hydroxymethyl)Aminomethane Hydrochloride
UV-VIS	Ultraviolet-Visible
WE	Working Electrode

Chapter 1: General Introduction

1.1. Electroactive Bacteria

Electroactive Bacteria (EAB), alternatively known as electrogens or electrogenic bacteria, constitute a distinctive group of microorganisms characterized by the '*electrifying*' ability to transfer electrons across exterior biological membranes¹. Unlike typical bacteria, whose metabolism remains confined within the bacterial cell, EAB perform extracellular respiration where electrons generated through metabolism are used to reduce extracellular terminal electron acceptors (TEAs), generally metal oxides. The first prediction that bacteria could pair the oxidation of organic compounds to the reduction of extracellular metal oxides was noted in 1894². This was followed in the early 1900s with the fermentation process of *Saccharomyces cerevisiae* being shown to generate an electrical output, however at the time this was not attributed to the bacteria being electroactive and instead believed to be caused by the catalytic breakdown of organic compounds³. It has only been since the 1980s with the discovery of EAB, such as *Shewanella* and *Geobacter sp.*, that the study of EAB has emerged as an interdisciplinary field which intersects microbiology, biochemistry and electrochemistry coined 'Electromicrobiology'^{1,4}. The number of bacteria that have been shown to transfer electrons across their exterior membrane is constantly increasing, as are their potential uses in biotechnology.

1.1.1. *Environmental Impact of Electroactive Bacteria*

EAB perform a critical role in many biogeochemical cycles of the world, allowing for the turnover of different metal oxidation states, such as iron, manganese, and vanadium, along with other elements such as sulfur^{1,5}. Of particular significance is the role EAB have in the iron cycle. Iron is indispensable for the majority of life, being incorporated into many proteins in the forms of heme and iron-sulfur cofactors. These proteins can perform numerous tasks including the use of iron-sulfur clusters to regulate gene expression, the transport of oxygen and found in multiple electron transport chains^{6,7}. Whilst the majority of iron found in proteins is in the form of heme or iron-sulfur clusters some proteins bind iron directly, such as transferrin and ferritin which allows for transport and

storage of metal iron in living organisms whilst minimising the possibility of oxidative damage ⁸.

Therefore, the uptake of iron into an organism is essential to life. Despite iron being the fourth most abundant element in the earth's crust it has limited bioavailability due to being predominantly in the Fe(III) state. Only Fe(II) state being soluble at neutral pH is bioavailable to bacterial lifeforms. However, the uptake of Fe(II) has to be tightly relegated, as free Fe(II) poses the risk of toxicity to the cell as it is capable of forming hydroxyl radicals under the Haber-Weiss reaction ⁹. Therefore, the ability of EAB to reduce Fe(III) to a bioavailable Fe(II) state is extremely important, as there is now a greater amount of Fe(II) that bacteria are able to utilise.

In addition to many geographical habits, EAB have also been found in the gut microbiome of mammals, an ideal place for their growth, being both temperature-controlled and having low oxygen concentrations. EAB have been shown to be part of the microbiome of multiple animals: including humans, mice and termites among others: predominately located in the intestines, lungs and oral cavities ¹⁰. Characterization of EAB within the microbiome of animals is limited however research has shown EAB found in the gut microbiome of mice can increase the recruitment of lymphocytes to the intestinal tract when rates of extracellular electron transport (EET) are amplified ¹¹.

1.1.2. Biotechnological Uses of Electroactive Bacteria

EAB have garnered significant attention in the field of biotechnology owing to their potential use in sustainable energy production. Among the various diverse applications, microbial fuel cells (MFCs) have emerged as a predominant area of interest. MFCs exploit the innate metabolic ability of EAB to generate sustainable energy ¹². The potential for MFCs has been acknowledged since the early 1900s ³, but it was only been since the early 2000s that they gained research interest and became the subject of investigation ¹³.

The basic design of a MFC consists of two chambers, the anodic and cathodic compartments, separated by a permeable membrane, as shown in *Figure 1.1*. In the majority of MFCs EAB capable of reducing extracellular substrates are placed in the anodic compartment and when grown using a compatible carbon source can use their natural metabolism to expel electrons extracellularly but instead of using a natural TEA, such as Fe(III), electrons are used to reduce an electrode. Protons generated through bacterial metabolism are able to diffuse through the permeable membrane providing a source of protons in the cathodic chamber where typically oxygen acts as the TEA being reduced to water.

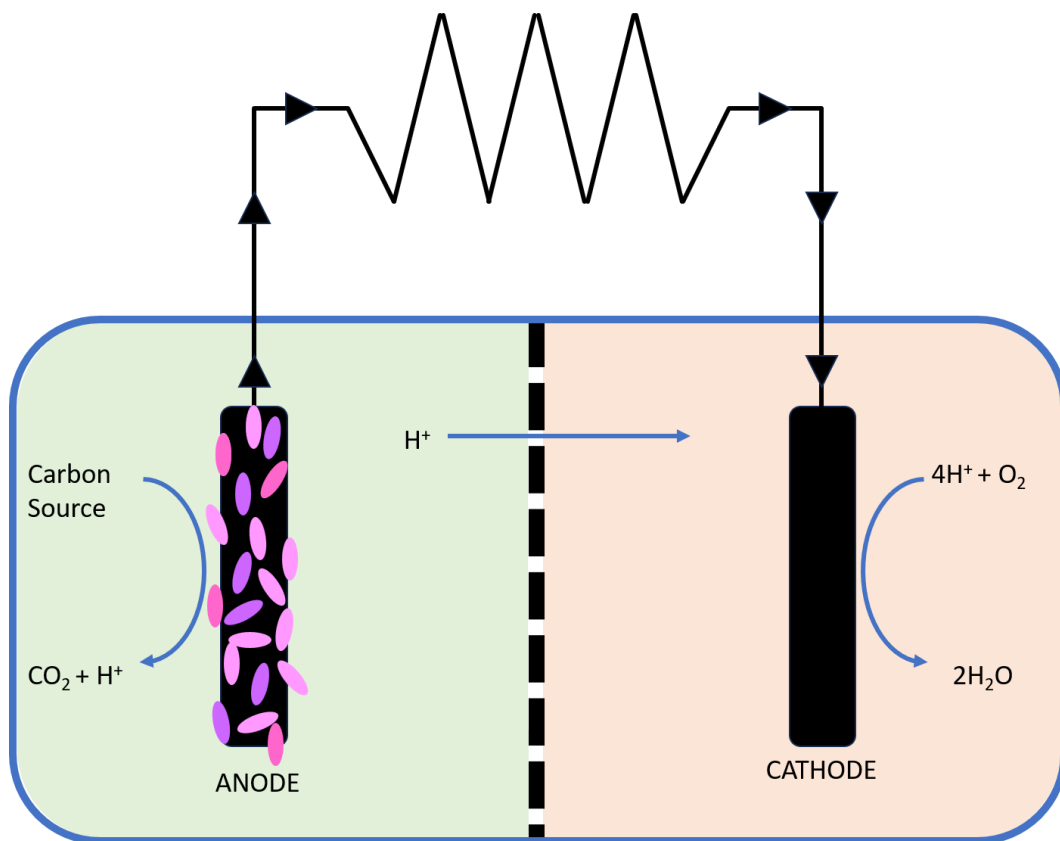


Figure 1.1- Schematic of a basic microbial fuel cell design. The anodic and cathodic chambers are separated by a proton exchange membrane. Bacteria (pink ovals) in the anodic chamber metabolise the carbon source to produce electrons, CO_2 and H^+ . Protons are able to migrate to the cathodic chamber for reduction of O_2 .

Power outputs from MFCs currently range from tens to thousands of mW/m^2 , with higher power outputs shown in MFCs that contain a consortium of bacteria,

with pure culture MFCs significantly underperforming comparatively ¹⁴⁻¹⁶. To date, MFCs have not been successfully scaled up to industrial levels, primarily due to their limited life spans and associated costs for electrode and proton exchange membrane replacements ^{12,17}. Improvements can be made to MFCs to increase their power-out, for example developing different anodes that can interact more efficiently with the EAB ¹⁷. The choice of anodes for MFCs is an extremely important factor when designing MFCs, as this is the site of interaction with the EAB and therefore anodes need to be non-toxic to the bacteria whilst also possessing good conductivity and preferably low cost for the manufacturer ¹⁷. These have seen a rise in power output but come with an added cost that makes them economically unsustainable ¹⁸. Although they are not currently a viable substitute for fossil fuels, their appeal is bolstered when integrated with other applications, such as wastewater remediation and metal recovery ^{19,20}.

With minor modifications, MFCs can be adapted for the sole purpose of wastewater redemption and/or desalination. Desalination is an important process that removes salts from water therefore making it consumable, this is a highly important process as 97.5 % of the total water on earth contains salts ²¹ and currently, it is estimated that 1.9 billion people do not have access to clean drinking water ²². Currently, the industrial desalination processes are costly requiring extensive energy to power ²³, this makes the prospect of utilising bacteria for this process highly favourable as it will result in significant cost benefits and the generation of electricity through renewable resources ²⁴.

The biotechnology that utilizes EAB for desalination is called a microbial desalination cell (MDC) and is structured similarly to an MFC a key difference is the use of an extra chamber between the anode and cathode chambers named the desalination chamber ²⁴. This chamber is separated from the other two chambers by an anion exchange membrane (AEM) and a cathode exchange membrane (CEM) ²⁴. The premise of an MDC is the same as in a MFC with EAB in the anode chamber reducing the anode and generating an electrical circuit with electrons then externally passed into the cathode chamber ²⁴. In the desalination

chamber Na^+ ions in the seawater move across the CEM to the cathode chamber whilst Cl^- ions move across the AEM to the anode ²⁴, the same process applies to any other ions that are seen in the seawater.

The practical applications of MDCs have shown to be promising with reports generally showing above 90 % desalination efficiency ^{24–26}. The process has also been shown to be more energy efficient than other commonly used desalination processes, due to the fact that MDCs produce bio-energy whilst running and can therefore be made to run self-sufficiently ²⁷. MDCs have also been paired to water softening, production of hydrogen gas and acid/base synthesis proving the technology to be multidisciplinary technology. Currently, the major drawbacks of MDCs are very similar to MFC drawbacks including expense and low current output ^{27,28}.

1.2. Iron-Oxidising Bacteria

Bacteria that are capable of respiring using Fe(II) as an electron donor are an important group of EAB. Iron-oxidising bacteria are capable of coupling the oxidation of Fe(II) to the reduction of a range of TEAs for growth ^{29,30}. Iron oxidising bacteria have been noticed as early as the 1830s, however due to difficulty with growing these bacteria the characterisation of these bacteria did not fully develop until the 1990s ³⁰. Here the predicted metabolism of some key iron-oxidising bacteria is presented to show the diversity of EAB.

1.2.1. Rhodospseudomonas palustris TIE-1

Rhodospseudomonas (R.) palustris TIE-1 is a versatile Gram-negative bacterium and has been shown to process all four modes of metabolism: photoautotrophy, photoheterotrophy, chemoheterotrophy, and chemoautotrophy ^{31,32}. This adaptability has led *R. palustris* TIE-1 to be found in a diverse array of environmental niches, such as alkaline waters, earthworm faeces and sludge ^{32,33}. The *pio* cluster is predicted to allow the bacteria to perform photoferrotrophy, believed to be the oldest form of photoautotrophy and a precursor to photosynthesis, as a means for metabolism ³⁴. The *pio* operon is

comprised of three components *pioA*, a gene predicted to encode a decaheme c-type cytochrome; *pioB*, encoding a predicted porin-like protein; and *pioC*, a small high potential iron-sulfur protein (HiPIP). The oxidation of iron by *R. palustris* TIE-1 happens in the absence of oxygen with the driving force of iron oxidation coming from light ($h\nu$) and culminating in the fixation of CO₂ ³⁵.

PioAB is predicted to form a porin cytochrome complex (PCC) localised to the outer membrane of *R. palustris* enabling the transfer of electrons from Fe(II) to PioC ³⁶. PioB is predicted to be a porin-like protein insulating the multiheme cytochrome (MHC) PioA. The PioAB complex is predicted to be localised in the outer membrane and is hypothesised to be the site of iron oxidation in *R. palustris* TIE-1. Transcribed as a protein of 540 amino acids PioA undergoes post-secretory proteolysis at the N-terminus to a ~300 amino acid protein ³⁷. The reason for this truncation is currently unknown, but in addition to acting as a signal peptide translocating PioA to the periplasm it may play an undiscovered role in the stabilisation and formation of the PioAB complex. PioA contains ten c-type hemes with at least seven hemes being His/His axially ligated with research suggesting the presence of His/Met and His/H₂O (pentaheme) heme axial ligation ³⁶. The significance of these axial ligands in PioA is currently unknown, but it has been suggested that an increase in reduction potential these ligands generate could be used as a way to store electrons before delivery to periplasmic electron donors, namely PioC ³⁶. Research on various cytochromes has shown that the axial ligands of heme cofactors can have a large effect on the redox potential of the protein and are therefore an important factor on the functionality of the cytochrome ^{38,39}. Hemes with a His/Met or pentaheme coordination are generally seen to have more positive potentials than a bis-His ligated heme ^{40,41}. The reason for the shift in potential is largely due to the donor capacity of the amino acid with more negatively charged axial ligands capable of stabilising the oxidised form of heme centres ³⁸.

PioC is the third component of the *pio* operon and is predicted to be a small high potential iron-sulphur protein (HiPIP), comprised of 54 amino acids making it the

smallest known HiPIP to date ³¹. Localized to the periplasm PioC is speculated to bridge the periplasmic gap and deliver electrons from PioA to the reaction centre positioned at the inner membrane ³¹. As the [4Fe-4S] cluster located in PioC is paramagnetic at both oxidation states ([4Fe-4S]^{2+/3+}), researchers were able to solve the structure using paramagnetic relaxation enhancement driven NMR ⁴². PioC has been predicted to form a complex with the light-harvesting reaction centre (LH-RC) located in the inner membrane and has been shown capable of reducing the LH-RC ^{31,35,43}.

R. palustris TIE-1 also encodes two additional genes predicted to also reduce the LH-RC, a cytochrome *c2* (CycA) and a secondary HiPIP. However, it was discovered that whilst CycA was able to reduce the LH-RC it does so at a lower rate than PioC and CycA is believed to be involved with cyclic electron transfer between the LH-RC and cytochrome *bc₁*, whilst PioC is predicted to solely reduce the LH-RC ⁴³. Cyclic electron transfer allows for the generation of a proton gradient across the IM allowing for ATP synthesis. The electron transport chain of *R. palustris* TIE-1 is visually summarised in *Figure 1.2*.

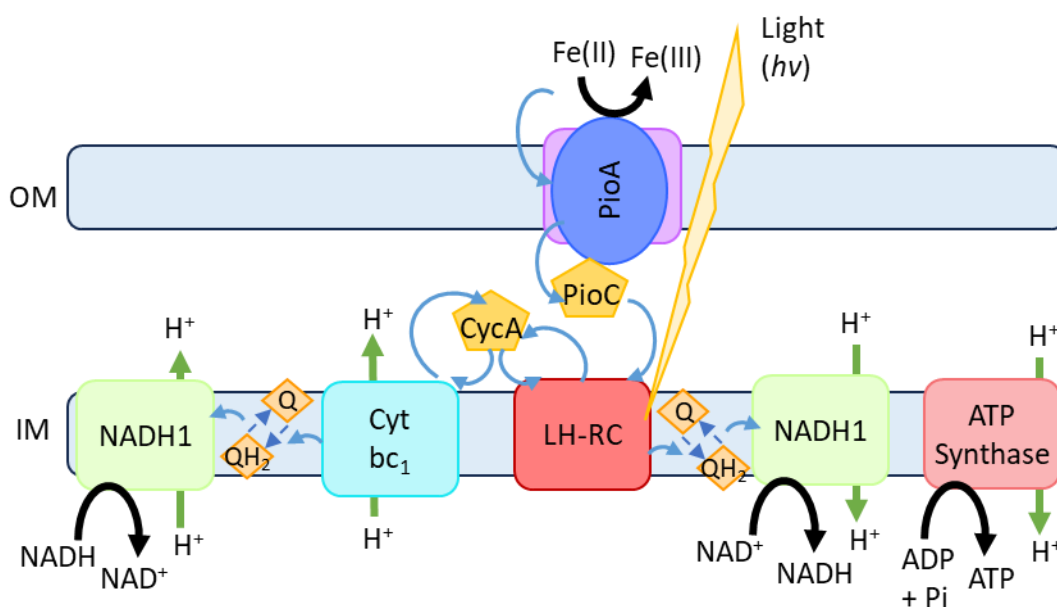


Figure 1.2- Schematic of the proposed electron transport pathway in *Rhodospseudomonas palustris* TIE-1. Transfer of electrons (blue arrows) is shown from the outer membrane (OM) to the inner membrane (IM) with Fe(II) used as the initial electron donor. Transfer of protons across a membrane is shown by green arrows. Redox state change of quinols (Q and QH₂) is shown by blue dashed lines. Black arrows show chemical reactions.

1.2.2. *Acidithiobacillus ferrooxidans*

Acidithiobacillus (A.) ferrooxidans is a chemolithoautotrophic Gram-negative bacterium that couples the oxidation of iron or sulphur containing minerals with the fixation of carbon and cell growth^{44,45}. *A. ferrooxidans* are part of a family of acidophiles, with optimal growth at pH 2⁴⁶, previously isolated from a variety of natural environments, including salt and fresh water, volcanic ash and sulfur springs amongst other environments⁴⁷. As the bacteria thrive in acidic environments the predominant form of iron will be Fe(II), due to the high level of protons able to reduce Fe(III)^{29,48}.

A. ferrooxidans has been shown to catalyse the oxidation of Fe(II) and is predicted to occur at the bacterial outer membrane primarily involving the cytochrome Cyc2, a monoheme porin:cytochrome fusion protein⁴⁹. Cyc2 is predicted to fold into a β -barrel structure and be positioned in the outer membrane of *A. ferrooxidans* forming a channel between the periplasm and the extracellular space⁴⁹. The protein sequence for Cyc2 contains a single c-type

heme binding domain, CxxCH, and it is this heme group that is predicted to allow for the oxidation of Fe(II) and transfer of electrons into the bacteria. Cyc2 is predicted to be the protein responsible for the oxidation of Fe(II). Research using electron paramagnetic resonance (EPR) was able to observe the loss of signals corresponding to oxidised heme when Fe(II) was added ⁵⁰, supporting the prevalent theory that Cyc2 acts as the outer membrane component linking electron transfer to periplasmic shuttles and further to the cytoplasmic membrane.

Cyc2 is predicted to be unique in its structure as it is predicted to only bind one heme group. This is unusual as similar cytochromes predicted to have the same function contain multiple sites for covalent attachment of c-type hemes, most often predicted to contain 10 heme cofactors. Due to this the functionality of Cyc2 has been questioned in how a single heme cofactor is capable of allowing for a transfer of electrons across the outer membrane. Additionally, computational modelling utilising Rosetta, a biomolecular modeling and design software, suggests that the heme cofactor would be positioned at the inner leaflet of the outer membrane and therefore any Fe(II) that would be oxidised would have to pass through the porin channel. Therefore, it is currently hypothesised that Cyc2 could contain additional metal binding sites to facilitate the transfer of electrons across the membrane ⁵¹.

Cyc2 is predicted to be the site of Fe(II) oxidation with electrons transferred ultimately to the inner membrane allowing for the generation of a proton gradient enabling ATP synthesis. The pathway linking iron oxidation to ATP synthase is still unresolved with the predominant pathway hypothesized by researchers beginning with the oxidation of Fe(II) by Cyc2. From there known periplasmic shuttle, rusticyanin, a copper protein ⁵², is expected to be reduced leading to a division in the electron transfer pathway resulting in a 'downhill' and an 'uphill' pathway. Electrons transferred along the 'downhill' electron pathway are next passed to the periplasmic cytochrome Cyc1 which then reduces inner membrane *aa3* cytochrome oxidase (Cox) for the final reduction of O₂ to H₂O in

the periplasm. The 'downhill' electron pathway is coupled with the translocation of H^+ from the cytoplasm to the periplasm generating a proton gradient facilitating ATP synthases. Electrons transferred through the 'uphill' pathway transfer from rusticyanin to CycA1, also called Cyc42, to the bc_1 complex from the reduction of the quinol pool and finally synthesis of NADH^{46,47,53}. All proteins involved in the 'uphill' and 'downhill' pathways are shown in *Figure 1.3*. The 'downhill' pathway is the more favourable of the two as electrons passed to the Cox complex are predicted to lead to a transfer of protons into the periplasm generating a proton gradient which in turn leads to the synthesis of ATP⁵⁴.

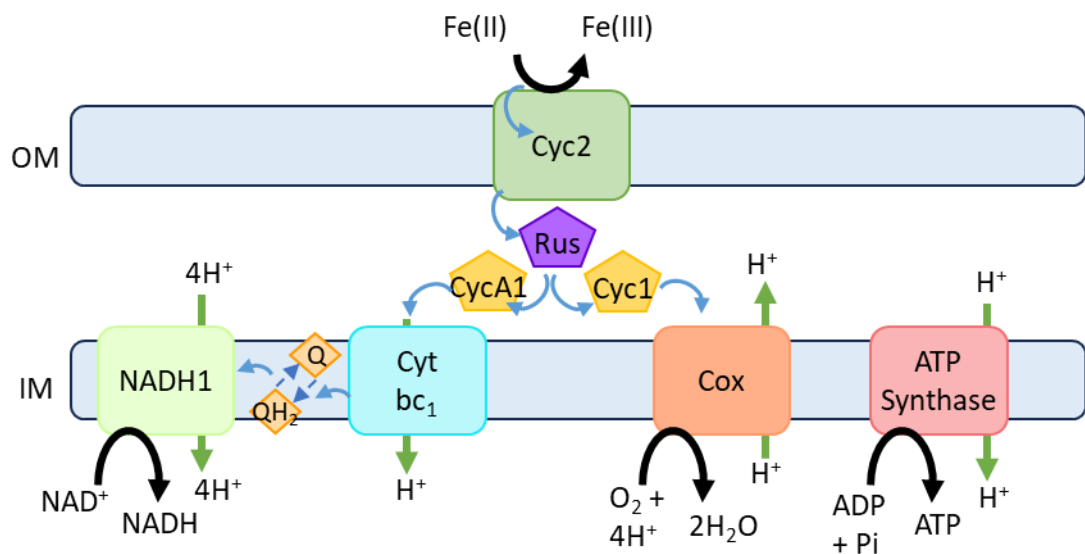


Figure 1.3- Schematic of the proposed electron transport pathway in Acidithiobacillus ferrooxydans. Transfer of electrons (blue arrows) is shown from the outer membrane (OM) to the inner membrane (IM) with Fe(II) used as the initial electron donor. Transfer of protons across a membrane is shown by green arrows. Redox state change of quinols (Q and QH₂) is shown by blue dashed lines. Black arrows show chemical reactions.

1.2.3. Sideroxydans lithotrophicus ES-1

Sideroxydans (Si.) lithotrophicus ES-1 is a Gram-negative bacterium first isolated in Michigan from groundwater containing Fe(II) at a neutral pH⁵⁵. *Si. lithotrophicus* ES-1 was noted as an iron-oxidising bacteria capable of coupling the oxidation of $FeCO_3$ or FeS to the production of ATP⁵⁵. Through the sequencing of the genome, researchers were able to identify multiple candidates

of genes which would encode proteins enabling the oxidation of Fe(II) by *Si. lithotrophicus* ⁵⁶. The MtoAB complex is another porin cytochrome complex, close in homology to PioAB from *R. palustris* TIE-1 ³⁶, predicted to be comprised of MtoA, a decaheme cytochrome C, and MtoB, a porin-like structure that insulates MtoA in the outer membrane ⁵⁶. The *mto* operon contains two additional genes encoding for MtoD, a monoheme cytochrome C that acts as a periplasmic shuttle, and ImoA, a tetraheme quinol reductase also referred to as CymA_{ES-1} ^{57,58}. The MtoD cytochrome contains a single heme that is His/His axially bound with a molecular weight of 11 kDa and is believed to be present in the periplasm acting as the primary electron shuttle between the MtoAB complex and the quinol pool ^{56,57}.

A recent genomic analysis of Fe(II) oxidising bacteria looking for potential genes involved in EET identified novel gene clusters that diverge from the known PCC, eg PioAB/MtoAB, these new clusters have been designated PCC3 ⁵⁹. Two PCC3 gene clusters were identified in *Si. lithotrophicus* ES-1, *slit_0867-80* and *slit_1446-49* ⁵⁹. This is an unusual PCC system that has not been seen before and raises questions as to why *Si. lithotrophicus* ES-1 would need a direct conduit from the inner membrane to the outer membrane. PCC3 complexes are formed from four hypothetical proteins; an inner membrane b-type cytochrome, a periplasmic c-type MHC (predicted heme number ranges from 18 to 24), a porin (with up to 42 predicted transmembrane regions) and an extracellular MHC (with predicted heme number ranging from 18 to 85) ⁵⁹. The extracellular components of these clusters are expected to be covalently bound to the outer membrane of *Si. Lithotrophicus* ES-1 through a Cys residue present at the end of the signal peptide, marking them as a lipo-protein. The potential of new PCC systems shows the diversity in these complexes and suggests that whilst EAB have evolved to transfer electrons across the outer membrane the mechanisms in place to do this may be larger than previously hypothesised.

Alongside MtoAB and the two PCC3 *Si. lithotrophicus* ES-1 also contains genes encoding for three homologs of the *A. ferrooxydans* Cyc2, so called Cyc2_1,

Cyc2_2 and Cyc2_3⁵⁹. However, whilst the *cyc2* gene from *A. ferrooxydans* was located in a gene cluster predicted to encode complementary periplasmic shuttles to Cyc2 so far these have not been identified in *Si. lithotrophicus* ES-1. The diversity of outer membrane components in *Si. lithotrophicus* allows for the potential of overlapping electron pathways, however it has been shown through transcriptomics that not all proteins are expressed equally in *Si. lithotrophicus*. It was revealed that both the PCC3 complexes are both downregulated with Fe(II)-citrate as an electron source, suggesting they do not perform a crucial role in Fe(II) oxidation under these conditions⁶⁰. Whilst expression of MtoA was seen under the same conditions it was under much lower levels and the three Cyc2 homologs had the highest expression out of the potential pathways, with Cyc2_1 being significantly expressed. With Cyc2_1 also being highly expressed in the absence of Fe(II) Cyc2_1 is probably the predominant pathway for Fe(II) oxidation in *Si. lithotrophicus*⁶⁰. All these proteins are shown with the predicted location and interactions *Figure 1.4*.

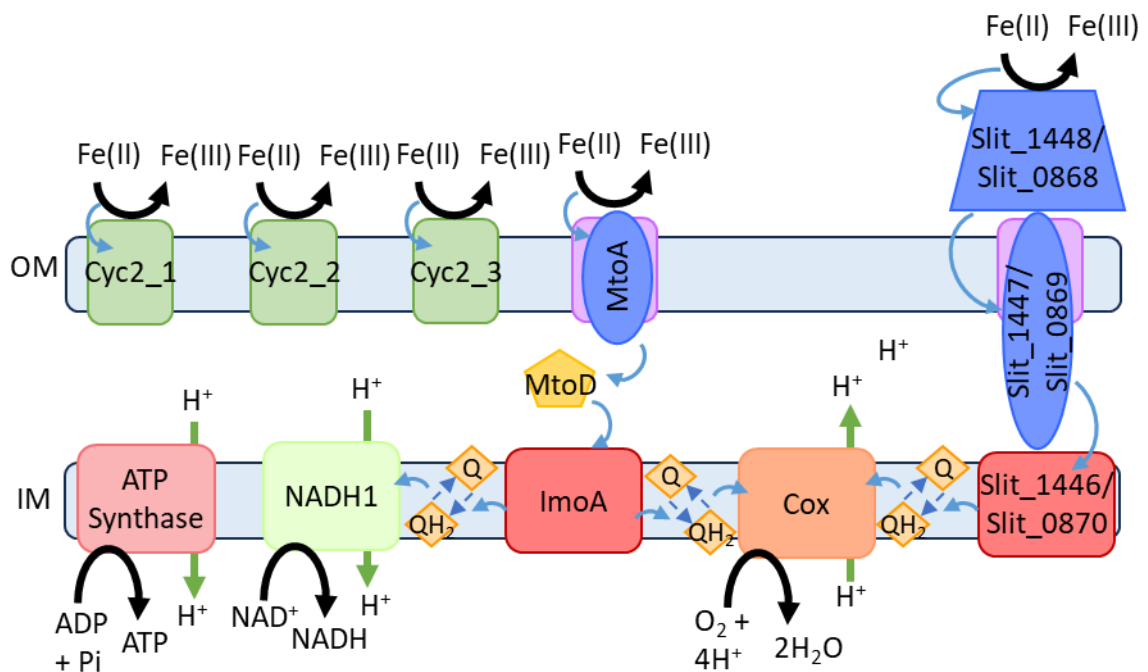


Figure 1.4- Schematic of the proposed electron transport pathway in Sideroxydans lithotrophicus ES-1. Transfer of electrons (blue arrows) is shown from the outer membrane (OM) to the inner membrane (IM) with Fe(II) used as the initial electron donor. Transfer of protons across a membrane is shown by green arrows. Redox state change of quinols (Q and QH₂) is shown by blue dashed lines. Black arrows show chemical reactions.

1.3. Iron-Reducing Bacteria

A wide variety of bacteria have been shown capable of coupling the oxidation of organic matter to the reduction of extracellular Fe(III) to Fe(II). Similar to iron-oxidising bacteria, a high diversity of iron-reducing bacteria have been reported from many genera of prokaryotes, including both Gram-negative and Gram-positive bacteria⁶¹⁻⁶³. Many bacteria that are capable of respiring using Fe(III) as a TEA have also been shown capable of reducing a wide range of metals, including manganese and uranium amongst other transition metals⁶³. Here the predicted metabolic pathways of a few well-characterised iron-reducing bacteria are shown.

1.3.1. *Thermincola potens* JR

Whilst a range of Gram-negative bacteria have long been shown to be electroactive it is only very recently that Gram-positive bacteria have been additionally shown to also be electroactive^{63,64}. Previously, it was believed the thick peptidoglycan cell wall, S-layer, would prevent Gram-positive bacteria from being redox-active with extracellular substrates⁶⁵. The *Thermincola* (*T.*) species was first noted as being an EAB from constructed MFCs produced to work at higher temperatures⁶⁶. *T. potens* JR was isolated from these MFCs and shown capable of producing currents at higher levels than most Gram-negative bacteria, 0.42 mA⁶⁷. has been of key interest to researchers but the debate surrounding whether Gram-positive bacteria are electroactive remained dynamic for many years⁶⁸.

To date the most studied Gram-positive EAB is *T. potens* JR, with the electron transfer pathway predicted to be formed predominately from four multiheme cytochromes MHC⁶⁷. Predicted to be situated at the cytoplasmic membrane and interacting with the quinol pool ImdcA is a decaheme cytochrome⁶⁷. ImdcA is predicted to act with the hypothetical periplasmic decaheme PdcA to shuttle electrons across the periplasm to the cell wall. At the cell wall, CwcA is predicted to shuttle electrons to the extracellular environment. CwcA is a hexaheme

cytochrome predicted to form a homo-polymer with one heme cofactor in each monomer being bound to a histidine residue of an adjacent monomer as a heme axial ligand, allowing for direct electron transfer through the cell wall of *T. potens* JR to surface-exposed MHCs⁶⁷. There is currently no porin associated with this transfer of electrons across the cell wall, or knowledge if one is required or CwcA functions independently. On the cell surface is predicted a predicted nonheme cytochrome OcwA. The crystal structure of OcwA was recently resolved, at 2.2 Å resolution. The crystal structure revealed that out of nine hemes eight hemes a His/His coordinated and the final heme is His/Met coordinated⁶⁴. These four cytochromes functioning together are predicted to be capable of forming a nanowire that crosses the cell wall and allows for the transfer of electrons out of the bacteria⁶⁷, as shown in Figure 1.5.

Currently knowledge of Gram-positive EAB is limited, primarily due to only being recently discovered. Today approximately 20 Gram-positive bacteria have been shown to be electroactive⁶³.

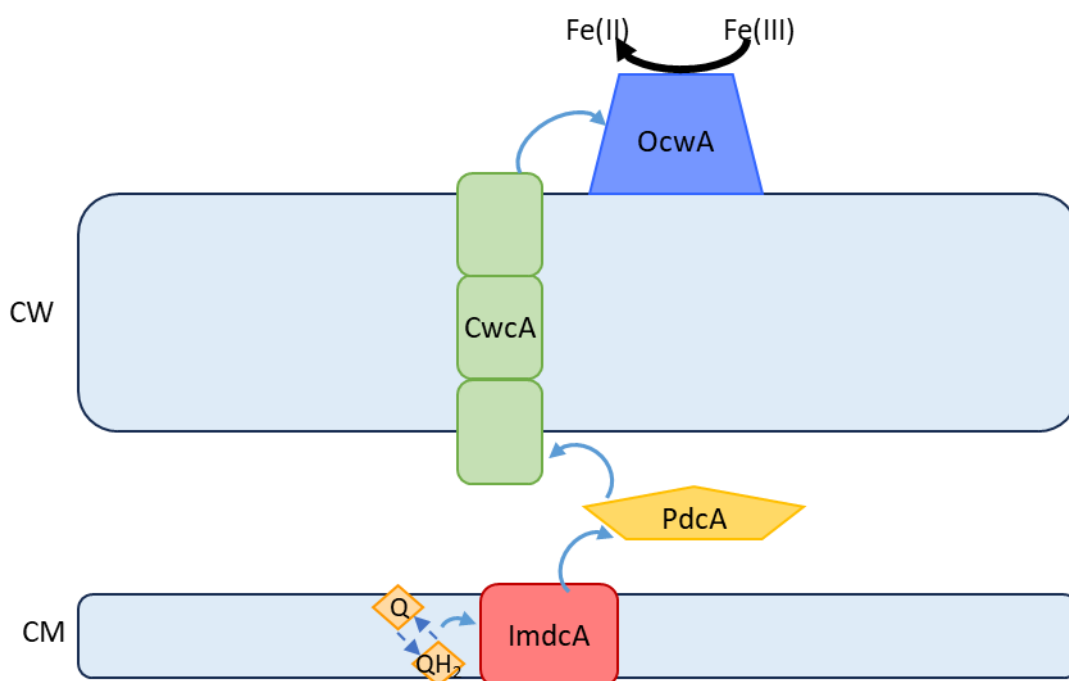


Figure 1.5- Schematic of the proposed electron transport pathway in *Thermophilum potens* JR. Transfer of electrons (blue arrows) is shown from the cytoplasmic membrane (CM) to the cell wall (CW) with Fe(III) used as the terminal electron acceptor. Redox state change of quinols (Q and QH₂) is shown by blue dashed lines. Black lines show chemical reactions.

1.3.2. *Shewanella oneidensis* MR-1

The most characterized EAB is *Shewanella (S.) oneidensis* MR-1, a Gram-negative facultative anaerobe, and acts as a model organism in the field of electromicrobiology due to its quick growing time and simplistic EET pathway. *S. oneidensis*' primary method for ATP production is anaerobic substrate-level phosphorylation originating in the oxidation of organic acids, such as lactate, in the cytoplasm⁶⁹. Oxidation of organic acids is coupled with the reduction of quinones, specifically menaquinone, which go on to reduce CymA, a quinol dehydrogenase^{70,71}. CymA is a tetraheme c-type cytochrome of the NapC/NirT superfamily, anchored to the periplasmic side of the inner membrane^{70,72}. Unlike other quinol dehydrogenases, CymA is capable of reducing multiple electron acceptors allowing for a diverse array of electron pathways with a singular starting point^{62,71}. The periplasmic shuttles STC and FccA, both tetraheme cytochromes found at high levels in the periplasm⁶² and have been shown to transiently interact with CymA for electron transfer but are not predicted to form a stable complex⁷³. STC and FccA transport electrons across the periplasm to the PCC MtrABC, *Figure 1.6*.

The MtrCAB complex is the most important PCC found in the *Shewanella* genus, positioned in the outer membrane and consisting of two decaheme cytochromes, MtrA and MtrC, forming a nanowire across the outer membrane into the extracellular environment for the reduction of TEAs⁷⁴. MtrA stretches across the outer membrane and is insulated by a porin-like β -barrel, MtrB, which is composed of 26 antiparallel beta strands^{74,75}. The cytochrome MtrC resides extracellularly and is responsible for contacting TEAs. Reduction of iron by *S. oneidensis* only happens under anaerobic conditions, under aerobic conditions there is an increased risk of the bacteria generating harmful reactive oxygen species and therefore EET needs to be inhibited. The site of inhibition is believed to be a di-sulphide bridge present in MtrC which under aerobic conditions is broken and prevents the MHC from functioning⁷⁶.

The structure of MtrCAB from *Shewanella baltica* was the first and to date only PCC structure that has been solved ⁷⁴ and is used as a model for how other PCC complexes predicted in other EAB would form. The *Shewanella* genus also contains a homologous gene cluster encoding the PCC MtrDEF, however gene knockouts of *mtrDEF* do not result in a significant loss of Fe(III) reduction. Whilst Δmtr strains of *Shewanella* only have a partially resorted Fe(III) reduction phenotype when supplemented with MtrDEF ⁷⁷.

Whilst in nature the electron transfer pathway has been characterised as solely metal reducing, researchers hypothesised it was possible to reverse the flow of electrons in *S. oneidensis*. Cultures of *S. oneidensis* were grown under standard conditions before being coated onto an electrode and a current applied ⁷⁸. The current was monitored and it was seen that *S. oneidensis* participated in electron uptake from the electrode. Cultures of *S. oneidensis* that were able to survive prolonged periods of electron uptake were sequenced to identify genes that had been upregulated during this period. From this, it is predicted that MtrCAB whilst naturally utilized for the reduction of extracellular substrates can also function for electron uptake.

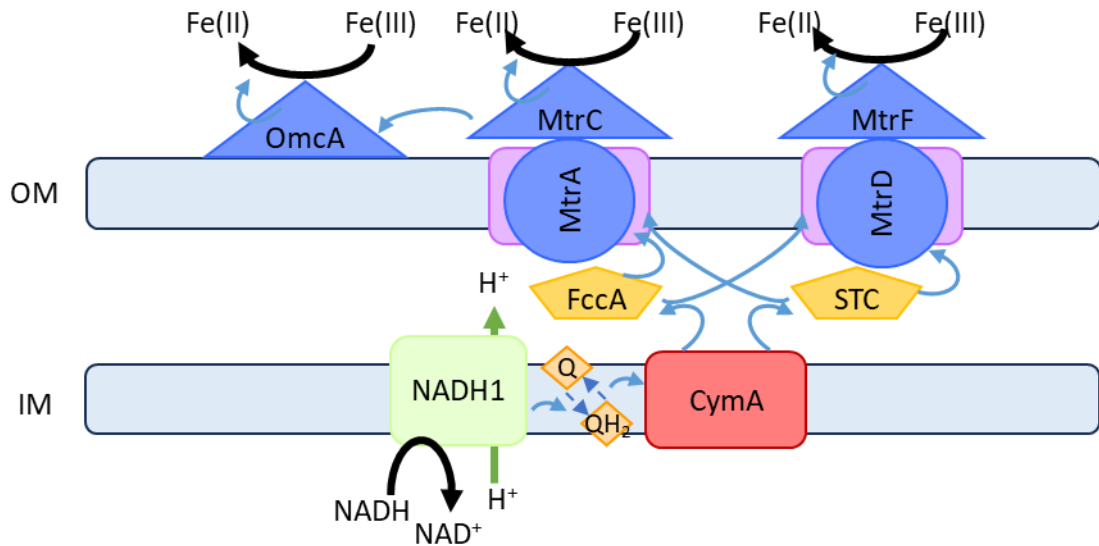


Figure 1.6- Schematic of the proposed electron transport pathway in *Shewanella oneidensis* MR-1. Transfer of electrons (blue arrows) is shown from the inner membrane (IM) to the outer membrane (OM) with the reduction of Fe(III) used as an example of a terminal electron acceptor. Transfer of protons across a membrane is shown by green arrows. Redox state change of quinols (Q and QH₂) is shown by blue dashed lines. Black arrows show chemical reactions.

1.3.3. *Geobacter sulfurreducens* PCA

The *Geobacter* (*G.*) genus relates to a group of Gram-negative bacteria and was first proposed in 1993 with the discovery of *Geobacter metallireducens*⁷⁹. The species *Geobacter sulfurreducens* PCA was discovered the following year in 1994⁸⁰, from surface sediments of a hydrocarbon-contaminated ditch in Norman, Oklahoma. Analysis of the 16S rRNA found *G. sulfurreducens* PCA to be of the delta proteobacteria family and a close relative of *Geobacter metallireducens*⁸⁰. *G. sulfurreducens* however, was noted for its unique ability to utilize hydrogen or acetate as the sole electron donor in its metabolism⁸⁰. The *Geobacter* genus has been shown to be diverse in the mechanisms used for respiration, being shown to respire using the reduction of Fe, Mn, V, As and U metals as well as organohalides, nitrate and selenite as terminal electron acceptors^{81–90}. *Geobacter* also has one of the most diverse and interweaving electron transport chains, especially in comparison to previously discussed EAB. A visual representation is shown in Figure 1.7 and highlights the vast number of cytochromes that are predicted to be involved in the transport of electrons through the periplasm to extracellular electron acceptors.

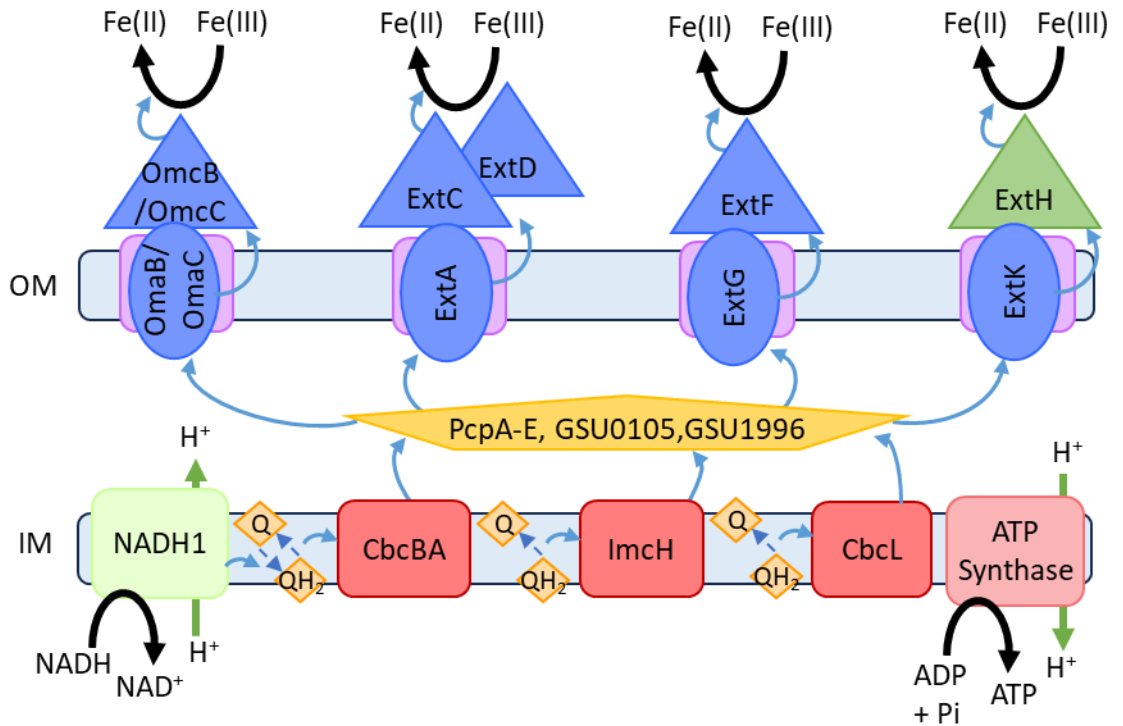


Figure 1.7- Schematic of the electron transport pathway in *Geobacter sulfurreducens* PCA. Transfer of electrons (blue arrows) is shown from the inner membrane (IM) to the outer membrane (OM) with the reduction of Fe(III) used as an example of a terminal electron acceptor. Transfer of protons across a membrane is shown by green arrows. Redox state change of quinols (Q and QH₂) is shown by blue dashed lines. Black arrows show chemical reactions.

The generation of ATP within *G. sulfurreducens* is entirely dependent on the EET pathway, with acetate being the primary energy source used for metabolized through the citric acid cycle. Through this process, quinols are reduced and electrons are then transferred to one of three inner membrane quinol dehydrogenases: ImcH, CbcL or CbcBA^{62,91,92}. The differing inner membrane quinol dehydrogenases have been identified to function at different potentials suggesting a mechanism for switching pathways.

The inner membrane quinol dehydrogenase ImcH is a multiheme c-type cytochrome and a member of the NapC/NirT/NrfH family⁹³, a family known for its redox interaction with the quinol pool. ImcH is predicted to covalently bind a total of 7 hemes, with all hemes predicted to be bis-His coordinated except for

Heme 1 which is suggested to have His/Gln coordination ⁹⁴. The second known quinol dehydrogenase is CbcL which is predicted to be a multiheme bc-cytochrome containing a total of 11 heme cofactors, nine of the heme cofactors being c-type and the remaining two b-type hemes. The b-type hemes are predicted to be located in the transmembrane regions of the cytochrome and the c-type heme cofactors are located in the periplasmic exposed domain ⁹⁵. Interestingly, researchers have shown that in *G. sulfurreducens* cells where only CbcL is available as a quinol dehydrogenase cells are able to respire to a max potential of -0.1 V vs SHE. However, mutation of residue Val205 suppress the inactivation of the cytochrome and allows the cells to respire to a max potential of 0.2 V vs SHE ⁹⁶. The final quinol dehydrogenase of *G. sulfurreducens* is CbcBA, which was only categorized as a quinol dehydrogenase in 2021 ⁹⁷. CbcBA is formed from two cytochromes the b-type diheme cytochrome CbcB and the c-type heptaheme cytochrome CbcA ^{97,98}.

All three of the quinol dehydrogenases are functional in *G. sulfurreducens* however the expression levels of the quinol dehydrogenase are variable depending on the potential of the terminal electron acceptor. ImcH has been shown to be expressed when *G. sulfurreducens* is grown at higher potentials, > -0.1 V vs SHE. CbcL was shown to be active between -0.21 - -0.1 V vs SHE and CbcBA was shown to be functional at potentials -0.21 V vs SHE to the limit of respiration at -0.3 V vs SHE ^{96,97,99}. The mechanism for production has not been defined but interestingly it appears that ImcH is abundant across a plethora of different redox potentials ^{100,101}. This could be explained by ImcH predicted to be the most beneficial pathway due to theoretical energy that can be coupled to a proton motive force and ATP synthesis ⁹⁷. In contrast CbcBA is predicted to not be viable as the sole mechanism of growth, as seen in *G. sulfurreducens* PCA mutant strains lacking ImcH and CbcL ⁹⁷.

The ability of *G. sulfurreducens* PCA to switch between different quinol dehydrogenases has not been elucidated yet but recent work has discovered a transcription factor, BccR, located upstream of the *cbcBA* cluster that is seen in

93 of 96 known *Geobacteraceae*⁹⁷. Deletion of this gene sees *G. sulfurreducens* PCA mutants unable to reduce substrates below a redox potential of -0.21 V vs SHE, suggesting that ImcH and CbcL are still expressed but CbcBA are not being expressed⁹⁷. ImcH and CbcL have no known transcriptional factors but recent research has shown that CbcL contains an amino acid switch that activates the quinol dehydrogenase at potentials lower than -0.1 V vs SHE⁹⁶.

Geobacter sulfurreducens contains a multitude of proteins located in the periplasm that are predicted to act as electron shuttles between the quinol dehydrogenases of the inner membrane and the PCCs of the outer membrane. These shuttles include; five tri-heme cytochromes PpcA-E as well as dodecaheme cytochrome GSU1996 and trimeric cytochrome GSU0105 amongst others^{102–105}. This is a large abundance of periplasmic shuttles and all are predicted to perform the same role leading to a redundant functionality. However, it has been shown that whilst all periplasmic shuttles are capable of being reduced by the inner membrane quinol dehydrogenases there is a slight bias towards some interactions, particularly dependent on the redox potential of the final terminal electron acceptor¹⁰³.

To date the most widely studied PCCs in *G. sulfurreducens* are from the tandem gene clusters *orfR-ombB-omaB-omcB* and *orfS-ombC-omaC-omcC*. For ease of discussion, these clusters will be referred to Gcp1 and Gcp2 respectively. These genes encode predicted porin-like proteins OmbB/C, predicted periplasmic octaheme c-type cytochromes OmaB/C and predicted extracellular lipo-dodecaheme c-type cytochromes OmcB/C. The two complexes share a high homology, 100 % for the porin and periplasmic components and 71 % for the extracellular lipo-cytochromes, and are believed to be both present in *Geobacter* due to a gene duplication^{106,107}. Interestingly, whilst the two complexes share a high homology there has been debate over whether the complexes can compensate for one another in gene knockouts. One study has shown gene deletion of *omcB* in *G. sulfurreducens* DL1 led to the bacteria's impaired ability to reduce extracellular Fe(III)¹⁰⁸, whereas a similar study conducted with *G.*

sulfurreducens PCA showed that OmcC was capable of compensating for lack of OmcB ¹⁰⁹.

The predicted remaining PCCs of *Geobacter* include ExtEFG, ExtHIJKL and ExtABCD. These clusters are modelled to form a homologous structure with *S. oneidensis* MtrCAB, but to date the formation of these complexes has not been proven and could differentiate from the MtrCAB dogma.

Full characterisation on the role of ExtEFG has yet to be determined but has been shown to play a role specifically in the reduction Fe(III) oxide, but not other Fe(III) substrates ^{98,101}. The cluster consists of a predicted porin-like protein, ExtE, and two lipo-cytochromes predicted to contain five and 20 hemes, ExtF and ExtG respectively. The complex is proposed to be expressed at the highest level when *G. sulfurreducens* is using a high potential terminal electron acceptor, such as fumarate ¹¹⁰. Gene knockouts of the *extEFG* cluster have shown to have the biggest impact on the bacteria's growth using Fe(III) citrate as a terminal electron acceptor, but other PCCs in *G. sulfurreducens* were capable of compensating ⁸⁸.

The ExtHIJKL is a predicted PCC that has been shown to have a role in selenite reduction ^{87,111}. It is predicted to be comprised of a rhodanese-like lipo-protein ExtH, a porin-like protein ExtI, a small periplasmic protein of unknown function ExtJ, a pentaheme periplasmic cytochrome ExtK and a secondary small periplasmic protein of unknown function ExtL. Interestingly, ExtKL has been speculated to be one protein with the stop codon that separates the predicted genes encoding a selenocysteine residue ^{87,112}. The ExtHIJKL PCC is unique to previously identified clusters as it is only predicted to contain one cytochrome component, with the rhodanese-like protein ExtH predicted to function as the extracellular component of the cluster ⁸⁸.

The *extABCD* cluster contains four genes that are predicted to encode: a predicted periplasmic dodecaheme cytochrome C, ExtA; a porin, ExtB; an extracellular pentaheme cytochrome C, ExtC; and an extracellular hexaheme

cytochrome C, ExtD. Mutant strains of *G. sulfurreducens* in which the genome was lacking all known PCC bar the *extABCD* cluster, coined the *extABCD*⁺ strain, were shown to increase the current generation of bacteria grown on electrodes by 1.4x compared to wildtype strains⁸⁸. This was in contrast to other mutant strains in which only one of the other four PCC gene clusters was encoded and the current output was 4x lower than wildtype strains. Interestingly, mRNA levels of the *extABCD* genes between wildtype and *extABCD*⁺ remain comparable showing that the increased current generation is not due to an increase of the ExtABCD complex in the outer membrane. It has been suggested that this phenomenon could be due to the streamlining theory¹¹³ wherein it is beneficial to the bacterium to only produce one electron transfer pathway rather than five to conserve resources. However, as the *Geobacter* family has retained five PCCs across different species the cost of producing this many complexes must have a beneficial impact on the species survival.

On the cell surface of *G. sulfurreducens* are additional extracellular cytochromes, OmcZ, OmcS and OmcE amongst others. In recent years these cytochromes have been structurally characterised as polymers that form cytochrome nanowires expanding into the extracellular space. OmcS was the first wire to be structurally resolved in 2019¹¹⁴. This cytochrome was first identified as being important for Fe(III) oxide reduction, later the use of immunogold labelling showed that OmcS was present in the conductive fibres that were produced by *Geobacter*¹¹⁵. Cryo-electron microscopy revealed the structure of hexaheme OmcS, with each unit ~4.8 nm in length. The six hemes present in OmcS have been shown to have low solvent accessible solvent areas, with the highest solvent exposed hemes being Heme 2 and Heme 6 suggestive of where the electrons enter/exit the heme chain.

Since the structure of OmcS has been resolved several more cytochrome nanowires have now been characterised. OmcE was structurally characterized whilst researchers were mutating the axial ligands of OmcS which led to the unforeseen phenotype of an upregulation in OmcE¹¹⁶. Structurally OmcS and

OmcE were shown to have different morphology, with only the arrangement of hemes in the structures having high homology. OmcZ is the most recent of *G. sulfurreducens* cytochrome nanowires to have its structure resolved and has the largest heme subunit of eight hemes, compared to OmcS with six and OmcE with four. Interestingly, whilst OmcS/OmcE have an almost identical heme arrangement the heme arrangement in OmcZ does not follow the same pattern. OmcZ shows the possibility for branched cytochrome nanowires with Heme 6 being highly surface exposed allowing for contact with terminal electron acceptors.

The polymerization of OmcS and OmcE subunits is attributed to the terminal heme of each subunit being coordinated by a histidine residue of the next subunit. However, with OmcZ heme coordination between subunits is not present with polymerization between subunits happening due to electrostatic and hydrophobic interactions. OmcZ further differs from OmcS/OmcE in that it undergoes posttranslational modifications before polymerization can occur. Natively expressed as a 50 kDa protein a proteolytic maturation occurs in which a subtilisin-like serine protease, OzpA, digests OmcZ into a 30 kDa form that is able to form cytochrome nanowires^{117,118}.

G. sulfurreducens PCA has shown to be one of the most diverse EAB in terms of outer membrane cytochromes predicted to facilitate electrons from the periplasm to extracellular terminal electron acceptors. These proteins and their predicted interactions are shown in *Figure 1.8*.

1.4. Spectral Properties of Cytochromes

Cytochromes are any protein that contains at least one heme cofactor. Hemes are formed from a protoporphyrin IX that contains an iron centre¹¹⁹. The two most common forms of heme are referred to as b-type and c-type and are primarily differentiated based on whether they are noncovalent, b-type, or covalently, c-type, bound to proteins¹¹⁹. To synthesise a c-type heme first a b-

type heme needs to be produced by the bacteria, meaning that whilst all organisms that produce heme proteins are capable of producing b-type hemes not all also produce c-type hemes^{119,120}. C-type hemes are formed when the two vinyl groups of a b-type heme form a thioether bond with a Cys residue. The structure of a b-type compared to a c-type heme is shown in *Figure 1.8*. Less common variants of hemes also exist including a-type, d₁-type and o-type which are all similar in structure to a b-type heme but contain at least one different functional group, generally instead of a vinyl or methyl group as seen in a b-type heme. A-type hemes contain hydroxyfarnesyl and formyl groups and are found in cytochrome c oxidases¹²¹. D₁-type hemes contain carbonyl and acetate groups and are commonly found in nitrate reductases¹²². O-type hemes contain a hydroxyfarnesyl group and are found in some bacteria oxidases¹¹⁹.

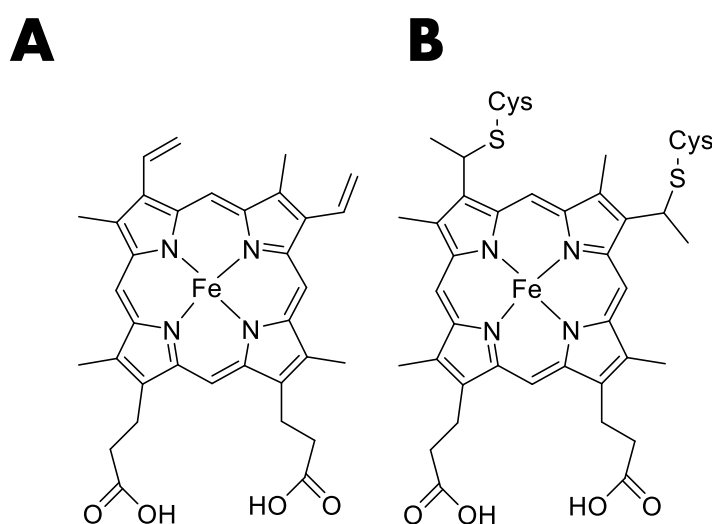


Figure 1.8- Structure of hemes. A) b-type heme. B) c-type heme.

Due to the presence of the heme cofactors cytochrome proteins exhibit a unique spectrum, which encompasses not only the standard 280 nm, due to the absorbance of aromatic amino acids in the peptide backbone, but additionally a

strong absorbance in the 370 to 450 nm region, denoted as the Soret band, and a weaker absorbance in the 500 to 650 nm region, denoted as the Q bands (or separated as the α and β bands)¹²³. The presence of the Soret band results from π to π^* transitions in the porphyrin ring of the heme¹²⁴. Electrons can be excited from one of five π orbitals and raised in energy to one of the five π^* orbitals. As a result, the differences in the origin of electrons to the orbitals they are excited to give rise to the α and β bands, collectively referred to as the Q-bands¹²⁴.

The oxidised and reduced spectra of cytochromes are also different. With the Soret maxima undergoing a red-shift to higher wavelength and the splitting of the Q bands into distinct α/β bands. The difference between the oxidized and reduced spectra of cytochromes is illustrated in *Figure 1.9*.

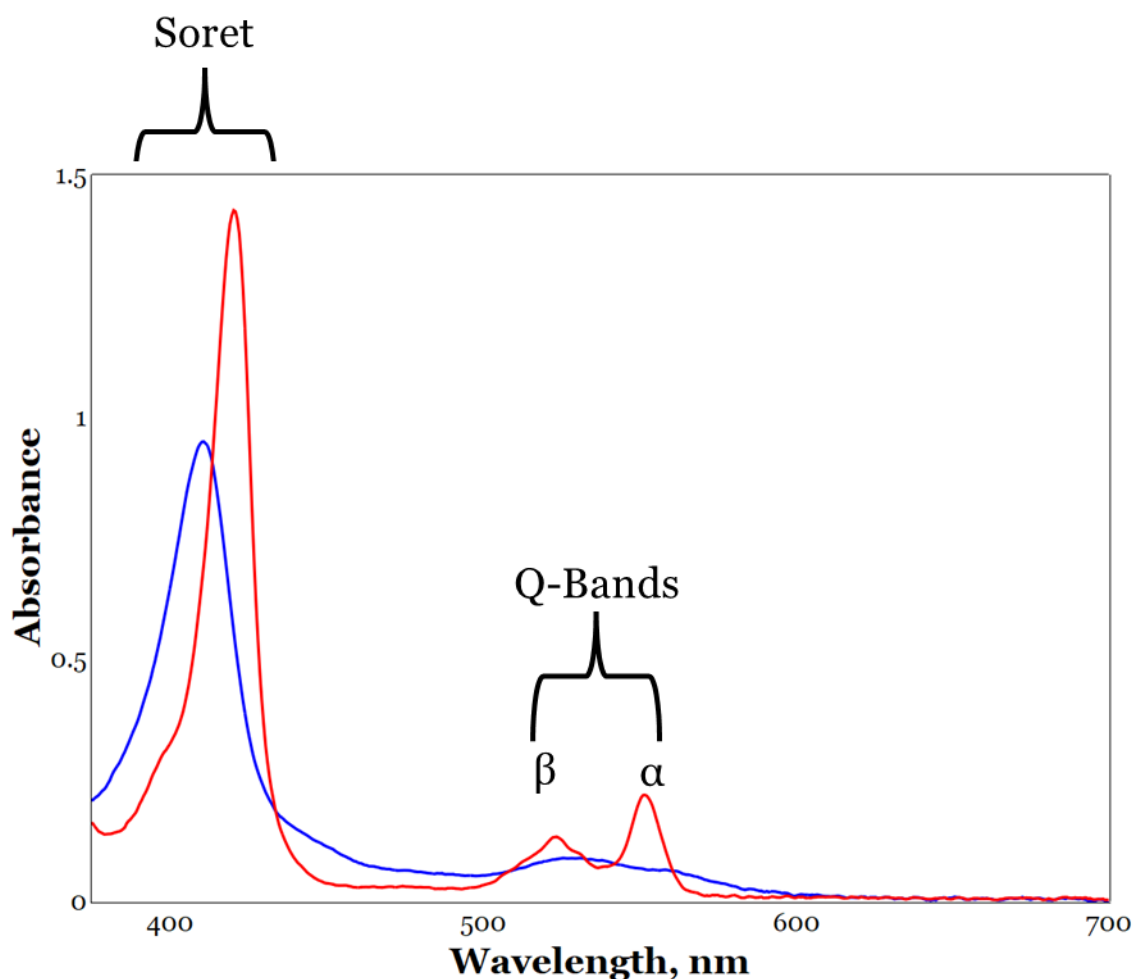


Figure 1.9- Typical spectra of a c-type cytochrome. Oxidised spectrum shown in blue, and reduced spectrum shown in red. Labelled on spectra are positions of Soret and Q-bands. Spectra from MtrC from *Shewanella oneidensis*

The coordination and spin state of the heme cofactor has been shown to impact the spectral properties of the cytochrome due to a change in the energy levels of the π orbitals. Investigations into the change of axial ligands has shown that five-coordinate high-spin hemes are associated with a blue shift in the Soret band

In multiheme cytochromes, all hemes display the same the presence of a single Soret is generally observed, even though each heme group would be expected to produce a distinct π to π^* transition. Therefore, the presence of a single Soret band in multiheme cytochrome spectra has been attributed to the delocalisation of orbitals generating an electron tunnel synchronising all the π and π^* orbital to

the same energy level therefore resulting in the presence of a single Soret band

125.

1.5. Aims of this thesis

This thesis aims to optimize the heterologous expression of genes encoding the cytochrome components of the ExtABCD cluster from *Geobacter sulfurreducens* PCA. This will allow for these cytochromes' spectroscopic, redox and biophysical characteristics to be resolved. As ExtABCD has previously only been characterised by studying the effects of gene knockouts in *G. sulfurreducens* characterisation of these proteins on an individual level is essential to fully understand their functionality. The expression of *extA*, *extC* and *extD* will be optimised in heterologous hosts *E. coli* BL21 and *S. oneidensis* LS527 using either a HIS-tag or STREP-II tag to purify the cytochrome. Purified proteins will then be characterised to probe their biophysical, redox and spectral properties in an attempt to increase the understanding of the ExtABCD complex.

Additionally, using *in-silico* techniques the potential structure of ExtABCD alongside the other four predicted PCCs from *G. sulfurreducens* can be conducted. This will allow for an increase in knowledge of how PCCs are constructed. Currently, the only resolved structure of a PCC is MtrCAB from *S. baltica* and this work will test to see if PCCs from *G. sulfurreducens* share a high structural homology or if the structures of PCCs are more diverse than previously hypothesised.

1.6. References

1. Lovley, D. R. & Holmes, D. E. Electromicrobiology: the ecophysiology of phylogenetically diverse electroactive microorganisms. *Nat Rev Microbiol* **20**, 5–19 (2022).
2. Adeney, W. On the reduction of manganese peroxide in sewage. *Sci. Proc. R. Dublin Soc* **8**, 247–251 (1894).
3. Potter, M. , C. Electrical effects accompanying the decomposition of organic compounds. *Proceedings of the Royal Society of London. Series B, Containing Papers of a Biological Character* **84**, 260–276 (1911).

4. Neelson, K. H. & Rowe, A. R. Electromicrobiology: realities, grand challenges, goals and predictions. *Microb Biotechnol* **9**, 595–600 (2016).
5. Rao, A. M. F., Malkin, S. Y., Hidalgo-Martinez, S. & Meysman, F. J. R. The impact of electrogenic sulfide oxidation on elemental cycling and solute fluxes in coastal sediment. *Geochim Cosmochim Acta* **172**, 265–286 (2016).
6. Shi, R., Hou, W., Wang, Z.-Q. & Xu, X. Biogenesis of Iron–Sulfur Clusters and Their Role in DNA Metabolism. *Front Cell Dev Biol* **9**, (2021).
7. Sánchez, M., Sabio, L., Gálvez, N., Capdevila, M. & Dominguez-Vera, J. M. Iron chemistry at the service of life. *IUBMB Life* **69**, 382–388 (2017).
8. Dutt, S., Hamza, I. & Bartnikas, T. B. Molecular Mechanisms of Iron and Heme Metabolism. *Annu Rev Nutr* **42**, 311–335 (2022).
9. Frawley, E. R. & Fang, F. C. The ins and outs of bacterial iron metabolism. *Mol Microbiol* **93**, 609–616 (2014).
10. Stevens, E. & Marco, M. L. Bacterial extracellular electron transfer in plant and animal ecosystems. *FEMS Microbiol Rev* **47**, (2023).
11. Ericsson, A. C., Davis, D. J., Franklin, C. L. & Hagan, C. E. Exoelectrogenic capacity of host microbiota predicts lymphocyte recruitment to the gut. *Physiol Genomics* **47**, 243–252 (2015).
12. Slate, A. J., Whitehead, K. A., Brownson, D. A. C. & Banks, C. E. Microbial fuel cells: An overview of current technology. *Renewable and Sustainable Energy Reviews* **101**, 60–81 (2019).
13. Schröder, U. Discover the possibilities: microbial bioelectrochemical systems and the revival of a 100-year-old discovery. *Journal of Solid State Electrochemistry* **15**, 1481–1486 (2011).
14. Choudhury, P. *et al.* Performance improvement of microbial fuel cells for waste water treatment along with value addition: A review on past achievements and recent perspectives. *Renewable and Sustainable Energy Reviews* **79**, 372–389 (2017).
15. Kouam Ida, T. & Mandal, B. Microbial fuel cell design, application and performance: A review. *Mater Today Proc* **76**, 88–94 (2023).
16. Yaqoob, A. A., Ibrahim, M. N. M. & Guerrero-Barajas, C. Modern trend of anodes in microbial fuel cells (MFCs): An overview. *Environ Technol Innov* **23**, 101579 (2021).
17. Cai, T. *et al.* Application of advanced anodes in microbial fuel cells for power generation: A review. *Chemosphere* **248**, (2020).
18. Boas, J. V., Oliveira, V. B., Simões, M. & Pinto, A. M. F. R. Review on microbial fuel cells applications, developments and costs. *J Environ Manage* **307**, 114525 (2022).
19. Abourached, C., Catal, T. & Liu, H. Efficacy of single-chamber microbial fuel cells for removal of cadmium and zinc with simultaneous electricity production. *Water Res* **51**, 228–233 (2014).

20. Ali, J. *et al.* Bioelectrochemical recovery of silver from wastewater with sustainable power generation and its reuse for biofouling mitigation. *J Clean Prod* **235**, 1425–1437 (2019).
21. Elsaid, K. *et al.* Environmental impact of desalination technologies: A review. *Science of The Total Environment* **748**, (2020).
22. Dupas, P., Nhlema, B., Wagner, Z., Wolf, A. & Wroe, E. Expanding Access to Clean Water for the Rural Poor: Experimental Evidence from Malawi. *American Economic Journal: Economic Policy*, (2020).
23. Al-Mamun, A., Ahmad, W., Baawain, M. S., Khadem, M. & Dhar, B. R. A review of microbial desalination cell technology: Configurations, optimization and applications. *J Clean Prod* **183**, (2018).
24. Saeed, H. M. *et al.* Microbial desalination cell technology: A review and a case study. *Desalination* **359**, (2015).
25. Salman, H. H. & Ismail, Z. Z. Desalination of actual wetland saline water associated with biotreatment of real sewage and bioenergy production in microbial desalination cell. *Sep Purif Technol* **250**, (2020).
26. Rahman, S. *et al.* Towards upscaling microbial desalination cell technology: A comprehensive review on current challenges and future prospects. *J Clean Prod* **288**, (2021).
27. Tawalbeh, M. *et al.* Microbial desalination cells for water purification and power generation: A critical review. *Energy* **209**, (2020).
28. Odunlami, O. A., Vershima, D. A., Tagbo, C. V., Ogunlade, S. & Nkongho, S. Microbial desalination cell technique - A review. *S Afr J Chem Eng* **46**, 312–329 (2023).
29. Hedrich, S., Schlömann, M. & Johnson, D. B. The iron-oxidizing proteobacteria. *Microbiology (N Y)* **157**, 1551–1564 (2011).
30. Emerson, D., Fleming, E. J. & McBeth, J. M. Iron-Oxidizing Bacteria: An Environmental and Genomic Perspective. *Annu Rev Microbiol* **64**, 561–583 (2010).
31. Jiao, Y. & Newman, D. K. The *pio* Operon Is Essential for Phototrophic Fe(II) Oxidation in *Rhodospseudomonas palustris* TIE-1. *J Bacteriol* **189**, (2007).
32. Larimer, F. W. *et al.* Complete genome sequence of the metabolically versatile photosynthetic bacterium *Rhodospseudomonas palustris*. *Nat Biotechnol* **22**, (2004).
33. Rayyan, A., Meyer, T. & Kyndt, J. Draft Whole-Genome Sequence of the Purple Photosynthetic Bacterium *Rhodospseudomonas palustris* XCP. *Microbiol Resour Announc* **7**, (2018).
34. Camacho, A., Walter, X. A., Picazo, A. & Zopfi, J. Photoferrotrophy: Remains of an Ancient Photosynthesis in Modern Environments. *Front Microbiol* **08**, (2017).
35. Bird, L. J., Bonnefoy, V. & Newman, D. K. Bioenergetic challenges of microbial iron metabolisms. *Trends Microbiol* **19**, 330–340 (2011).
36. Li, D.-B. *et al.* His/Met heme ligation in the PioA outer membrane cytochrome enabling light-driven extracellular electron transfer by *Rhodospseudomonas palustris* TIE-1. *Nanotechnology* **31**, 354002 (2020).

37. Gupta, D. *et al.* Photoferrotrophs Produce a PioAB Electron Conduit for Extracellular Electron Uptake. *mBio* **10**, (2019).
38. Rydberg, P., Sigfridsson, E. & Ryde, U. On the role of the axial ligand in heme proteins: a theoretical study. *JBIC Journal of Biological Inorganic Chemistry* **9**, 203–223 (2004).
39. Poulos, T. L. The role of the proximal ligand in heme enzymes. *JBIC Journal of Biological Inorganic Chemistry* **1**, 356–359 (1996).
40. Miller, G. T., Zhang, B., Hardman, J. K. & Timkovich, R. Converting a c-type to a b-type Cytochrome: Met61 to His61 Mutant of Pseudomonas Cytochrome c -551. *Biochemistry* **39**, 9010–9017 (2000).
41. Mao, J., Hauser, K. & Gunner, M. R. How Cytochromes with Different Folds Control Heme Redox Potentials. *Biochemistry* **42**, 9829–9840 (2003).
42. Trindade, I. B., Invernici, M., Cantini, F., Louro, R. O. & Piccioli, M. PRE-driven protein NMR structures: an alternative approach in highly paramagnetic systems. *FEBS J* (2020).
43. Bird, L. J. *et al.* Nonredundant Roles for Cytochrome c 2 and Two High-Potential Iron-Sulfur Proteins in the Photoferrotroph Rhodospseudomonas palustris TIE-1. *J Bacteriol* **196**, 850–858 (2014).
44. Ingledew, W. J. Thiobacillus Ferrooxidans the bioenergetics of an acidophilic chemolithotroph. *Biochimica et Biophysica Acta (BBA) - Reviews on Bioenergetics* **683**, 89–117 (1982).
45. Temple, K. L. & Colmer, A. R. The Autotrophic Oxidation of Iron by a New Bacterium: *Thiobacillus Ferrooxidans*. *J Bacteriol* **62**, 605–611 (1951).
46. Valdés, J. *et al.* Acidithiobacillus ferrooxidans metabolism: from genome sequence to industrial applications. *BMC Genomics* **9**, 597 (2008).
47. Zhang, S. *et al.* *Acidithiobacillus ferrooxidans* and its potential application. *Extremophiles* **22**, 563–579 (2018).
48. Stumm, W. & Morgan, J. J. Aquatic chemistry: chemical equilibria and rates in natural waters. *Choice Reviews Online* **33**, 33-6312-33–6312 (1996).
49. Yarzabal, A. *et al.* The High-Molecular-Weight Cytochrome c Cyc2 of *Acidithiobacillus ferrooxidans* Is an Outer Membrane Protein. *J Bacteriol* **184**, 313–317 (2002).
50. Castelle, C. *et al.* A New Iron-oxidizing/O₂-reducing Supercomplex Spanning Both Inner and Outer Membranes, Isolated from the Extreme Acidophile *Acidithiobacillus ferrooxidans*. *Journal of Biological Chemistry* **283**, 25803–25811 (2008).
51. Jiang, V., Khare, S. D. & Banta, S. Computational structure prediction provides a plausible mechanism for electron transfer by the outer membrane protein Cyc2 from *Acidithiobacillus ferrooxidans*. *Protein Science* (2021).
52. Liu, W. *et al.* Overexpression of Rusticyanin in *Acidithiobacillus ferrooxidans* ATCC19859 Increased Fe(II) Oxidation Activity. *Curr Microbiol* **62**, 320–324 (2011).
53. Barrie Johnson, D. & Hallberg, K. B. Carbon, Iron and Sulfur Metabolism in Acidophilic Micro-Organisms. in 201–255 (2008).

54. Quatrini, R. *et al.* Extending the models for iron and sulfur oxidation in the extreme Acidophile *Acidithiobacillus ferrooxidans*. *BMC Genomics* **10**, 394 (2009).
55. Emerson, D. & Moyer, C. Isolation and characterization of novel iron-oxidizing bacteria that grow at circumneutral pH. *Appl Environ Microbiol* **63**, 4784–4792 (1997).
56. Liu, J. *et al.* Identification and Characterization of MtoA: A Decaheme c-Type Cytochrome of the Neutrophilic Fe(II)-Oxidizing Bacterium *Sideroxydans lithotrophicus* ES-1. *Front Microbiol* **3**, (2012).
57. Beckwith, C. R. *et al.* Characterization of MtoD from *Sideroxydans lithotrophicus*: a cytochrome c electron shuttle used in lithoautotrophic growth. *Front Microbiol* **6**, (2015).
58. Jain, A., Coelho, A., Madjarov, J., Paquete, C. M. & Gralnick, J. A. Evidence for Quinol Oxidation Activity of ImoA, a Novel NapC/NirT Family Protein from the Neutrophilic Fe(II)-Oxidizing Bacterium *Sideroxydans lithotrophicus* ES-1. *mBio* **13**, (2022).
59. He, S., Barco, R. A., Emerson, D. & Roden, E. E. Comparative Genomic Analysis of Neutrophilic Iron(II) Oxidizer Genomes for Candidate Genes in Extracellular Electron Transfer. *Front Microbiol* **8**, (2017).
60. Zhou, N., Keffer, J. L., Polson, S. W. & Chan, C. S. Unraveling Fe(II)-Oxidizing Mechanisms in a Facultative Fe(II) Oxidizer, *Sideroxydans lithotrophicus* Strain ES-1, via Culturing, Transcriptomics, and Reverse Transcription-Quantitative PCR. *Appl Environ Microbiol* **88**, (2022).
61. Lovley, D. R. DISSIMILATORY METAL REDUCTION. *Annu Rev Microbiol* **47**, 263–290 (1993).
62. Clarke, T. A. Plugging into bacterial nanowires: a comparison of model electrogenic organisms. *Curr Opin Microbiol* **66**, 56–62 (2022).
63. Paquete, C. M. Electroactivity across the cell wall of Gram-positive bacteria. *Comput Struct Biotechnol J* **18**, (2020).
64. Costa, N. L. *et al.* How Thermophilic Gram-Positive Organisms Perform Extracellular Electron Transfer: Characterization of the Cell Surface Terminal Reductase OcwA. *mBio* **10**, (2019).
65. Ehrlich, H. L. Are gram-positive bacteria capable of electron transfer across their cell wall without an externally available electron shuttle? *Geobiology* **6**, (2008).
66. Wrighton, K. C. *et al.* A novel ecological role of the Firmicutes identified in thermophilic microbial fuel cells. *ISME J* **2**, 1146–1156 (2008).
67. Faustino, M. M. *et al.* Crossing the Wall: Characterization of the Multiheme Cytochromes Involved in the Extracellular Electron Transfer Pathway of *Thermincola ferriacetica*. *Microorganisms* **9**, (2021).
68. Cournet, A., Délia, M.-L., Bergel, A., Roques, C. & Bergé, M. Electrochemical reduction of oxygen catalyzed by a wide range of bacteria including Gram-positive. *Electrochem commun* **12**, (2010).

69. Hunt, K. A., Flynn, J. M., Naranjo, B., Shikhare, I. D. & Gralnick, J. A. Substrate-Level Phosphorylation Is the Primary Source of Energy Conservation during Anaerobic Respiration of *Shewanella oneidensis* Strain MR-1. *J Bacteriol* **192**, 3345–3351 (2010).
70. Marritt, S. J. *et al.* A functional description of CymA, an electron-transfer hub supporting anaerobic respiratory flexibility in *Shewanella*. *Biochemical Journal* **444**, 465–474 (2012).
71. McMillan, D. G. G., Marritt, S. J., Butt, J. N. & Jeuken, L. J. C. Menaquinone-7 Is Specific Cofactor in Tetraheme Quinol Dehydrogenase CymA. *Journal of Biological Chemistry* **287**, 14215–14225 (2012).
72. Myers, J. M. & Myers, C. R. Role of the Tetraheme Cytochrome CymA in Anaerobic Electron Transport in Cells of *Shewanella putrefaciens* MR-1 with Normal Levels of Menaquinone. *J Bacteriol* **182**, 67–75 (2000).
73. Fonseca, B. M. *et al.* Mind the gap: cytochrome interactions reveal electron pathways across the periplasm of *Shewanella oneidensis* MR-1. *Biochemical Journal* **449**, 101–108 (2013).
74. Edwards, M. J., White, G. F., Butt, J. N., Richardson, D. J. & Clarke, T. A. The Crystal Structure of a Biological Insulated Transmembrane Molecular Wire. *Cell* **181**, 665-673.e10 (2020).
75. Edwards, M. J. *et al.* Structural modeling of an outer membrane electron conduit from a metal-reducing bacterium suggests electron transfer via periplasmic redox partners. *Journal of Biological Chemistry* **293**, 8103–8112 (2018).
76. Norman, M. P. *et al.* A Cysteine Pair Controls Flavin Reduction by Extracellular Cytochromes during Anoxic/Oxic Environmental Transitions. *mBio* **14**, (2023).
77. Coursolle, D. & Gralnick, J. A. Reconstruction of Extracellular Respiratory Pathways for Iron(III) Reduction in *Shewanella Oneidensis* Strain MR-1. *Front Microbiol* **3**, (2012).
78. Rowe, A. R. *et al.* Identification of a pathway for electron uptake in *Shewanella oneidensis*. *Commun Biol* **4**, 957 (2021).
79. Lovley, D. R. *et al.* *Geobacter metallireducens* gen. nov. sp. nov., a microorganism capable of coupling the complete oxidation of organic compounds to the reduction of iron and other metals. *Arch Microbiol* **159**, 336–344 (1993).
80. Caccavo, F. *et al.* *Geobacter sulfurreducens* sp. nov., a hydrogen- and acetate-oxidizing dissimilatory metal-reducing microorganism. *Appl Environ Microbiol* **60**, 3752–3759 (1994).
81. Mahadevan, R. *et al.* Characterization of Metabolism in the Fe(III)-Reducing Organism *Geobacter sulfurreducens* by Constraint-Based Modeling. *Appl Environ Microbiol* **72**, 1558–1568 (2006).
82. Ortiz-Bernad, I., Anderson, R. T., Vrionis, H. A. & Lovley, D. R. Vanadium Respiration by *Geobacter metallireducens* : Novel Strategy for In Situ Removal of Vanadium from Groundwater. *Appl Environ Microbiol* **70**, 3091–3095 (2004).
83. Lovley, D. R., Phillips, E. J. P., Gorby, Y. A. & Landa, E. R. Microbial reduction of uranium. *Nature* **350**, 413–416 (1991).

84. Wagner, D. D. *et al.* Genomic determinants of organohalide-respiration in *Geobacter lovleyi*, an unusual member of the Geobacteraceae. *BMC Genomics* **13**, 200 (2012).
85. Tsuchiya, T., Ehara, A., Kasahara, Y., Hamamura, N. & Amachi, S. Expression of Genes and Proteins Involved in Arsenic Respiration and Resistance in Dissimilatory Arsenate-Reducing *Geobacter* sp. Strain OR-1. *Appl Environ Microbiol* **85**, (2019).
86. Lovley, D. R. & Phillips, E. J. P. Novel Mode of Microbial Energy Metabolism: Organic Carbon Oxidation Coupled to Dissimilatory Reduction of Iron or Manganese. *Appl Environ Microbiol* **54**, 1472–1480 (1988).
87. Jahan, Mst. I., Tobe, R. & Mihara, H. Characterization of a Novel Porin-Like Protein, Extl, from *Geobacter sulfurreducens* and Its Implication in the Reduction of Selenite and Tellurite. *Int J Mol Sci* **19**, 809 (2018).
88. Jiménez Otero, F., Chan, C. H. & Bond, D. R. Identification of Different Putative Outer Membrane Electron Conduits Necessary for Fe(III) Citrate, Fe(III) Oxide, Mn(IV) Oxide, or Electrode Reduction by *Geobacter sulfurreducens*. *J Bacteriol* **200**, (2018).
89. Campeciño, J. *et al.* Cytochrome c nitrite reductase from the bacterium *Geobacter lovleyi* represents a new NrfA subclass. *Journal of Biological Chemistry* **295**, 11455–11465 (2020).
90. Pearce, C. I. *et al.* Investigating different mechanisms for biogenic selenite transformations: *Geobacter sulfurreducens*, *Shewanella oneidensis* and *Veillonella atypica*. *Environ Technol* **30**, 1313–1326 (2009).
91. Paquete, C. M., Morgado, L., Salgueiro, C. A. & Louro, R. O. Molecular Mechanisms of Microbial Extracellular Electron Transfer: The Importance of Multiheme Cytochromes. *Frontiers in Bioscience - Landmark* vol. 27 Preprint at <https://doi.org/10.31083/j.fbl2706174> (2022).
92. Ueki, T. Cytochromes in Extracellular Electron Transfer in *Geobacter*. *Appl Environ Microbiol* **87**, (2021).
93. Levar, C. E., Chan, C. H., Mehta-Kolte, M. G. & Bond, D. R. An Inner Membrane Cytochrome Required Only for Reduction of High Redox Potential Extracellular Electron Acceptors. *mBio* **5**, (2014).
94. Pimenta, A. I. *et al.* Characterization of the inner membrane cytochrome ImcH from *Geobacter* reveals its importance for extracellular electron transfer and energy conservation. *Protein Science* **32**, (2023).
95. Antunes, J. M. A., Silva, M. A., Salgueiro, C. A. & Morgado, L. Electron Flow From the Inner Membrane Towards the Cell Exterior in *Geobacter sulfurreducens*: Biochemical Characterization of Cytochrome CbcL. *Front Microbiol* **13**, (2022).
96. Joshi, K., Chan, C. H., Levar, C. E. & Bond, D. R. Single Amino Acid Residues Control Potential-Dependent Inactivation of an Inner Membrane bc-Cytochrome. *ChemElectroChem* (2022).
97. Joshi, K., Chan, C. H. & Bond, D. R. *Geobacter sulfurreducens* inner membrane cytochrome CbcBA controls electron transfer and growth yield near the energetic limit of respiration. *Mol Microbiol* **116**, 1124–1139 (2021).

98. Aklujkar, M. *et al.* Proteins involved in electron transfer to Fe(III) and Mn(IV) oxides by *Geobacter sulfurreducens* and *Geobacter uraniireducens*. *Microbiology (N Y)* **159**, 515–535 (2013).
99. Zacharoff, L., Chan, C. H. & Bond, D. R. Reduction of low potential electron acceptors requires the CbcL inner membrane cytochrome of *Geobacter sulfurreducens*. *Bioelectrochemistry* **107**, 7–13 (2016).
100. Ding, Y.-H. R. *et al.* The proteome of dissimilatory metal-reducing microorganism *Geobacter sulfurreducens* under various growth conditions. *Biochimica et Biophysica Acta (BBA) - Proteins and Proteomics* **1764**, 1198–1206 (2006).
101. Ding, Y.-H. R. *et al.* Proteome of *Geobacter sulfurreducens* grown with Fe(III) oxide or Fe(III) citrate as the electron acceptor. *Biochimica et Biophysica Acta (BBA) - Proteins and Proteomics* **1784**, 1935–1941 (2008).
102. Choi, S., Chan, C. H. & Bond, D. R. Lack of Specificity in *Geobacter* Periplasmic Electron Transfer. *J Bacteriol* **204**, (2022).
103. Morgado, L., Bruix, M., Pessanha, M., Londer, Y. Y. & Salgueiro, C. A. Thermodynamic Characterization of a Triheme Cytochrome Family from *Geobacter sulfurreducens* Reveals Mechanistic and Functional Diversity. *Biophys J* **99**, 293–301 (2010).
104. Fernandes, T. M., Folgosa, F., Teixeira, M., Salgueiro, C. A. & Morgado, L. Structural and functional insights of GSU0105, a unique multiheme cytochrome from *G. sulfurreducens*. *Biophys J* **120**, 5395–5407 (2021).
105. Alves, M. N., Fernandes, A. P., Salgueiro, C. A. & Paquete, C. M. Unraveling the electron transfer processes of a nanowire protein from *Geobacter sulfurreducens*. *Biochimica et Biophysica Acta (BBA) - Bioenergetics* **1857**, 7–13 (2016).
106. Liu, Y., Fredrickson, J. K., Zachara, J. M. & Shi, L. Direct involvement of ombB, omaB, and omcB genes in extracellular reduction of Fe(III) by *Geobacter sulfurreducens* PCA. *Front Microbiol* **6**, (2015).
107. Liu, Y. *et al.* A trans-outer membrane porin-cytochrome protein complex for extracellular electron transfer by *Geobacter sulfurreducens* PCA. *Environ Microbiol Rep* **6**, 776–785 (2014).
108. Leang, C., Coppi, M. V. & Lovley, D. R. OmcB, a c-Type Polyheme Cytochrome, Involved in Fe(III) Reduction in *Geobacter sulfurreducens*. *J Bacteriol* **185**, 2096–2103 (2003).
109. Liu, Y., Fredrickson, J. K., Zachara, J. M. & Shi, L. Direct involvement of ombB, omaB, and omcB genes in extracellular reduction of Fe(III) by *Geobacter sulfurreducens* PCA. *Front Microbiol* **6**, (2015).
110. Howley, E., Krajmalnik-Brown, R. & Torres, C. I. Cytochrome gene expression shifts in *Geobacter sulfurreducens* to maximize energy conservation in response to changes in redox conditions. *Biosens Bioelectron* **237**, 115524 (2023).
111. Jahan, Mst. I. *et al.* Selenite uptake by outer membrane porin ExtI and its involvement in the subcellular localization of rhodanese-like lipoprotein ExtH in *Geobacter sulfurreducens*. *Biochem Biophys Res Commun* **516**, 474–479 (2019).

112. Fujita, M., Mihara, H., Goto, S., Esaki, N. & Kanehisa, M. Mining prokaryotic genomes for unknown amino acids: a stop-codon-based approach. *BMC Bioinformatics* **8**, 225 (2007).
113. Giovannoni, S. J., Cameron Thrash, J. & Temperton, B. Implications of streamlining theory for microbial ecology. *ISME J* **8**, 1553–1565 (2014).
114. Wang, F. *et al.* Structure of Microbial Nanowires Reveals Stacked Hemes that Transport Electrons over Micrometers. *Cell* **177**, 361-369.e10 (2019).
115. Leang, C., Qian, X., Mester, T. & Lovley, D. R. Alignment of the c-Type Cytochrome OmcS along Pili of *Geobacter sulfurreducens*. *Appl Environ Microbiol* **76**, 4080–4084 (2010).
116. Wang, F. *et al.* Cryo-EM structure of an extracellular *Geobacter* OmcE cytochrome filament reveals tetrahaem packing. *Nat Microbiol* **7**, 1291–1300 (2022).
117. Gu, Y. *et al.* Structure of *Geobacter* cytochrome OmcZ identifies mechanism of nanowire assembly and conductivity. *Nat Microbiol* **8**, 284–298 (2023).
118. Kai, A. *et al.* Proteolytic Maturation of the Outer Membrane c-Type Cytochrome OmcZ by a Subtilisin-Like Serine Protease Is Essential for Optimal Current Production by *Geobacter sulfurreducens*. *Appl Environ Microbiol* **87**, (2021).
119. Bowman, S. E. J. & Bren, K. L. The chemistry and biochemistry of heme c: functional bases for covalent attachment. *Nat Prod Rep* **25**, 1118 (2008).
120. Stevens, J. M., Daltrop, O., Allen, J. W. A. & Ferguson, S. J. C -type Cytochrome Formation: Chemical and Biological Enigmas. *Acc Chem Res* **37**, 999–1007 (2004).
121. Hederstedt, L. Heme A biosynthesis. *Biochimica et Biophysica Acta (BBA) - Bioenergetics* **1817**, 920–927 (2012).
122. Bali, S., Palmer, D. J., Schroeder, S., Ferguson, S. J. & Warren, M. J. Recent advances in the biosynthesis of modified tetrapyrroles: the discovery of an alternative pathway for the formation of heme and heme d 1. *Cellular and Molecular Life Sciences* **71**, 2837–2863 (2014).
123. Simpson, M. C. & Novikova, N. I. Porphyrins: Electronic Structure and Ultraviolet/Visible Absorption Spectroscopy. in *Fundamentals of Porphyrin Chemistry* 505–586 (Wiley, 2022).
124. Moore, G. R. & Pettigrew, G. W. *Cytochromes c: Evolutionary, Structural and Physicochemical Aspects*. (Springer Berlin Heidelberg, Berlin, Heidelberg, 1990).
125. van Wonderen, J. H. *et al.* Do multiheme cytochromes containing close-packed heme groups have a band structure formed from the heme π and π^* orbitals? *Curr Opin Electrochem* **47**, 101556 (2024).

Chapter 2: Experimental Methods

2.1. General Methods

2.1.1. Media Preparation

Luria Broth (LB) media was prepared by the addition of 25 g/L of premixed LB to RO water. M72 media was prepared by adding Casein digest peptone 15 g/L, peptone digest of soybean 5 g/L and NaCl 5 g/L to RO water. All media was autoclaved before use for bacteria growth with the addition of supplements 20 mM sodium lactate, 30 mM sodium fumarate and 20 mM HEPES to M72 media.

In this work the use of three antibiotics was employed: kanamycin, chloramphenicol and carbenicillin. Kanamycin resistance was provided by the pMEGGAx vector, chloramphenicol resistance was provided by the pEC86 vector and carbenicillin/ampicillin resistance was provided by plasmids bought from Eurofins, pEX-128A.

All stocks of antibiotics were prepared at 30 mg/mL with kanamycin and carbenicillin dissolved in RO water and chloramphenicol dissolved in 70 % ethanol. All antibiotic stock solutions were filtered through a 0.22 µm syringe filter. Stock solutions were stored at -20 °C until required.

2.1.2. Plasmid Maps

This thesis primarily utilised two plasmids, *pEC86* and *pMEGGAx*. The *pEC86* vector is a commonly used vector that encodes the *ccmABCDEFGH* operon from *E. coli* and also provided resistance to chloramphenicol ¹. The *pMEGGAx* vector was provided by Dr Marcus Edwards (Essex University, UK) and is based on the *pBAD202* vector ². The *pMEGGAx* vector provides kanamycin resistance and contains an arabinose inducible promoter, the *araBAD* operon. Additionally, the *pMEGGAx* vector also contains a pink coral reef gene with restriction sites for Esp3I at the 5' and 3' ends of the gene. This allowed for Golden Gate cloning to remove the pink coral reef gene and insert a gene of interest whilst also providing a pink/white screening test. Plasmid maps of *pEC86* and *pMEGGAx* are shown in *Figure 2.1*.

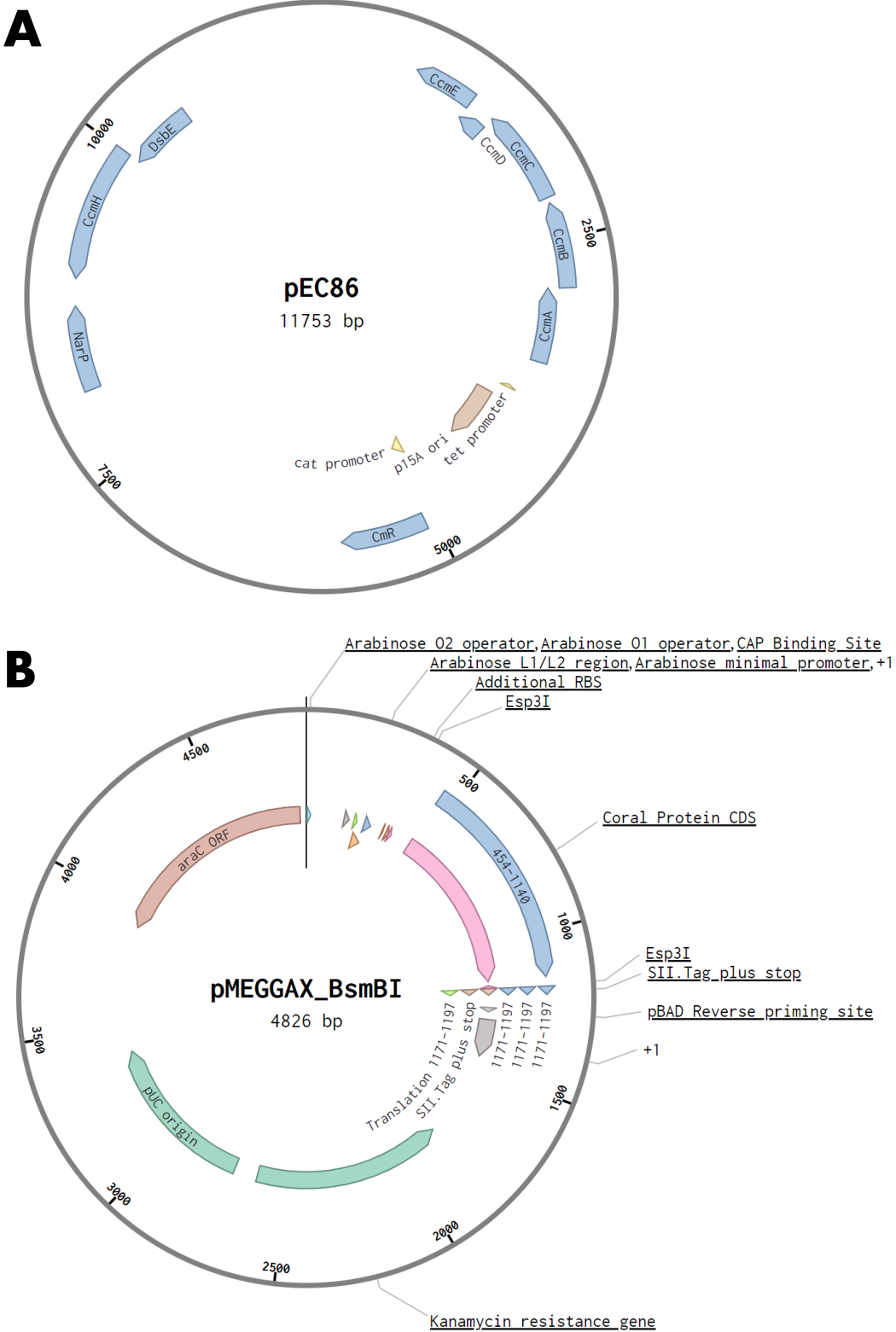


Figure 2.1- Plasmid maps of A) pEC86 and B) pMEGGAX

2.1.3. Agarose Gel Electrophoresis for DNA Visualization

Agarose gels were prepared with 1 % (wt/v) agarose of 40 mM Tris, 20 mM acetic acid, and 1 mM EDTA pH 7.6 (TAE buffer). Agarose was dissolved in TAE buffer by microwaving contents for two minutes. The agarose solution was cooled to approximately 50 °C and 5 µL of 10 mg/mL ethidium bromide solution was added before being poured into a casting tray to set. A comb was added to the top of the casting tray to produce wells for DNA insertion.

Preparation of DNA samples to be visualised through electrophoresis was performed by combining 2 µL of 6x orange loading dye with 5 µL of DNA sample. A 1 Kb Plus DNA ladder (Invitrogen) was loaded into the first well of each agarose gel run, in order to estimate the size of DNA samples. DNA samples were loaded onto an agarose gel and the gel aligned so that the top of the gel was positioned closest to the cathode. A potential of 120 mV was applied to the agarose gel for up to two hours.

2.1.4. SDS-PAGE for Protein Visualization

Proteins were visualized using SDS-PAGE gels made with 15 % acrylamide. SDS-PAGE gels were prepared in-house by preparing a 'Resolving Gel' and a 'Stacking Gel', see *Table 2.1* for the composition of reagents³. Both 'Resolving Gel' and 'Stacking Gel' were prepared to make a total of four gels. Once prepared 4.5 mL of 'Resolving Gel' was added to the cassette and left to set for 15 mins, before setting 200 µL of saturated butanol was added to the top of the gel to create a flat top. Once 'Resolving Gel' had set saturated butanol was removed and 'Stacking Gel' was added to the casket until full and left to set for a further 15 minutes. Once set SDS-PAGE gels were stored at 4 °C in wrapped in a wet paper towel for up to two weeks.

Table 2.1 – Reagents used to produce Resolving and Stacking gels for SDS-PAGE

Reagent	Volume of Reagent used in Resolving Gel, mL	Volume of Reagent used in Stacking Gel, mL
30 % Acrylamide	10	1.66
1.5 M Tris, pH 8.8	5	0
0.5 M Tris, pH 6.8	0	1.26
10 % SDS	0.2	0.05
H ₂ O	12	6.8
10 % APS	0.2	0.05
TEMED	0.02	0.01

Protein samples to be analysed through SDS-PAGE were prepared by addition of 3 μ L of 'Loading Buffer', composed of 0.5 M Tris pH 6.8, 5 % (wt/vol) SDS, 20 % (vol/vol) glycerol, 6 M urea and 0.005 % (wt/vol) bromophenol blue, to 7 μ L of protein sample. The analyte was heated at 90 °C for 20 minutes before being loaded onto the gel. SDS-PAGE running buffer used in the tank was composed of 25 mM Tris, 200 mM glycine and 3.5 mM SDS at pH 8.5. A Precision Plus Protein Dual Colour Standards from Bio-Rad was used as a protein molecular weight marker. SDS-PAGE gels were run for 90 minutes at 30 mA, 50 V.

Protein migration on SDS-PAGE gels was visualized through heme-linked peroxidase staining. Gels were first removed from the gel tank and washed with 20 mL of RO water for 5 minutes in a clean gel tray with slight agitation. Water was removed from the tray and addition of 20 mL of 0.25 mM sodium acetate pH 5.0 for 5 minutes. A 20 mL solution of 1 mg/mL TMBD prepared in methanol was added to the gel tray followed by 200 μ L of 30 % hydrogen peroxidase.

2.1.5. Transformation of plasmids into *Escherichia coli*

Competent *E. coli* (strain TOP10 or BL21) cells were prepared by streaking the desired strain from a glycerol stock onto LB Agar plates and allowed to grow overnight at 37 °C. Single colonies were selected for growth in 10 ml LB and grown overnight at 30 °C with 180 rpm. The following day overnight cultures were collected, 1 mL was used to inoculate a 100 mL of LB and allowed to grow at 30 °C until an $OD_{600} = 0.4-0.6$ was achieved. *E. coli* cells were harvested by centrifugation at 3,500 x g for 20 minutes. The pelleted cells were resuspended in 20 mL of 100 mM calcium chloride, prepared at 4 °C, and incubated on ice for 20 minutes. Resuspended *E. coli* cells were centrifuged for 20 minutes at 3,500 x g and the pellets were resuspended in 2.4 mL 100 mM calcium chloride + 20 % glycerol. Resuspended *E. coli* cells were aliquoted into 50 μ L fractions and frozen with liquid nitrogen and stored at -80 °C.

To 50 μ L aliquots of *E. coli* (strain TOP10 or BL21) competent cells, 3 μ L of desired plasmid was added and incubated on ice for 1 hour. Competent cells were heat shocked at 42 °C for 40 seconds before being placed immediately back on ice for a minimum of five minutes. During this incubation period, 200 μ L of LB was added to recover cells. After incubation on ice competent cells now containing the desired plasmid were incubated at 37 °C with shaking, 550 rpm, for 1h 30min. The transformed solution was plated on LB agar plates containing 30 μ g/mL of the desired antibiotic (dependent on plasmid kanamycin, chloramphenicol or carbenicillin used.) Plates were incubated overnight at 30 °C. White colonies that had grown in the plate were picked and transferred to 10 mL LB containing the desired antibiotic and incubated overnight at 37 °C whilst shaking at 180 rpm. Successfully grown cultures were screened for plasmid incorporation through plasmid prep and sequencing. Cell cultures determined to have been successfully transformed were stored in glycerol at -80 °C.

2.1.6. Electroporation of plasmids into *Shewanella oneidensis* LS527

A 10 mL overnight of LB with 30 μ g/mL of antibiotic containing *S. oneidensis* LS527 was incubated overnight at 30 °C 180 rpm. The next morning 2 mL of the bacteria culture was pelleted at 7000 rpm and washed three times with 1 mL of

10 % glycerol, pelleting the cells at 7000 rpm and discarding the supernatant after each wash. Washed pellet was resuspended in 70 μL of 10 % glycerol and 2 μL of desired plasmid (approximate concentration of 50 -150 ng/ μL) was added. Samples were electroporated by shocking at 120 mV followed by the addition of 1 mL of SOC medium (ThermoFisher). Electroporated cells were recovered at 30 $^{\circ}\text{C}$, 100 rpm for at least 1 hour before being plated on LB agar containing 30 $\mu\text{g}/\text{mL}$ of the desired antibiotic. Plates were grown at 30 $^{\circ}\text{C}$ overnight with single colonies selected for growth in liquid LB containing 30 $\mu\text{g}/\text{mL}$ of the desired antibiotic.

2.1.7. Long Term Storage of Bacterial Strains

Bacteria strains selected for long term storage were stored as a 25 % glycerol stock. To prepare glycerol stock 1 mL of LB bacterial overnight was combined with 1 mL of 50 % glycerol before use autoclaved. Glycerol stock was flash frozen in liquid nitrogen and stored at -80 $^{\circ}\text{C}$ for short term and stored in liquid nitrogen long term.

2.2. Polymerase Chain Reaction

Primers used for polymerase chain reactions are listed in *Table 2.2*, alongside their intended use and melting temperatures.

Table 2.2- Primers used in PCR reaction

Primer Name	Use	DNA Sequence, 5' to 3'	Melting Point, °C
<i>HIS_STREP_For</i>	Affinity Tag switch from His-Tag to STREP-tag for both ExtC and ExtD	AGTGCCTGGAGCC ATCCACAATTC	64.4
<i>HIS_STREP_extD_Rev</i>	Affinity Tag switch from His-Tag to STREP-tag for ExtD	ACGTACAATGGTA GGATGGCACAACA	65.0
<i>HIS_STREP_extC_Rev</i>	Affinity Tag switch from His-Tag to STREP-tag for ExtD	GCCATGACAAGGA CGACACGTG	64.0
<i>extA_SignalPep_For</i>	Amplification of DNA encoding MtrB signal peptide for N-terminus truncation of ExtA	AACGTCTCAATCC ATGAAGTTCAAAC TGAACCTCATTAC GCTTG	66.2
<i>extA_SignalPep_Rev</i>	Amplification of DNA encoding MtrB signal peptide for N-terminus truncation of ExtA	AACGTCTCATGAC GCCATCAGCCGCA ACTGCCAGACCA	72.9
<i>extA_Heme_For</i>	Amplification of DNA encoding heme containing region of ExtA for N-terminus truncation of ExtA	AACGTCTCAGTCA CTCAGTGTGGCCA ATGTCACCCGTC	70.1
<i>extA_Heme_Rev</i>	Amplification of DNA encoding heme containing region of ExtA for N-terminus truncation of ExtA	TTCGTCTCTCACT CCGTTGACGAACC GGTGGATTATGC	68.8
<i>pMEGGAx_For</i>	Primer for sequencing the <i>pMEGGAx</i> vector	ATGCCATAGCATT TTTATCC	51.1
<i>pMEGGAx_Rev</i>	Primer for sequencing the <i>pMEGGAx</i> vector	GATTTAATCTGTA TCAGG	46.9

2.2.1. Affinity Tag Switch of *ExtC* and *ExtD*

Both the *extC* and *extD* genes were kindly provided by Dr Marcus Edwards (Essex University, UK) in the *pMEGGAx* vector. The 5' ends of both genes contained the corresponding sequence for a HIS affinity tag. In this work, an affinity tag switch was performed to encode a STREP-II affinity tag instead of the already present HIS affinity tag. The *pMEGGAx* vector was previously encoded to include the corresponding sequence for a STREP-II tag positioned at the 5' end of the gene, downstream of the HIS tag and STOP codon. Therefore, plasmids were designed to amplify the plasmid and corresponding gene, without amplification of the HIS tag or STOP codon separating the gene and the STREP-II tag. In both cases, the forward primer *HIS_STREP_For* was used as this primer anneals to the DNA encoding the STREP-II Tag. Reverse primers, *HIS_STREP_extC_Rev* and *HIS_STREP_extD_Rev*, were designed to bind the 5' end of the corresponding gene and specific to each PCR.

Amplification of DNA fragments was performed following the protocol: 25 μL PCR Master Mix (ThermoFisher), 1 μL of *HIS_STREP_For* primer, 1 μL complementary reverse primer, 0.5 μL of *pMEGGAx* vector encoding either *extC* or *extD*, 22.5 μL of dH_2O . The stock of primers was 100 pmol/ μL and plasmid concentration varied between 70 to 150 ng/ μL . Amplification was repeated in quintuplicate to allow for variation of annealing temperatures. PCR was cycled 35 times using protocol: 98 °C for 15 seconds, 64 to 54 °C for 30 seconds, and 72 °C for 5 minutes.

Amplification of DNA was analysed through DNA electrophoresis with successful fragments extracted from gel using a Gel Extraction Kit from Merck. Amplified DNA was circularised by phosphorylating the blunt ends and ligating them together. Phosphorylation protocol: 2 μL of 10x reaction buffer A for T4 polynucleotide kinase, 2 μL of 10 mM stock ATP, 1 μL T4 polynucleotide kinase, 2.5 μL dH_2O , 12.5 μL of PCR product. The reaction was incubated at 37 °C for 20 minutes to allow for the reaction to occur. The reaction was heat shocked at 75 °C for 10 minutes to denature T4 polynucleotide kinase. Phosphorylated DNA

was extracted following PCR Purification Kit by Merck. Ligation of phosphorylated DNA ends was performed following the protocol: 2 μ L of 10x reaction buffer for T4 ligase, 1 μ L of T4 ligase, 7 μ L dH₂O, and 10 μ L of phosphorylated DNA product. Reaction was incubated at room temperature overnight with the completed reaction transformed into *E. coli* cells.

2.2.2. Construction of *pMEGGAx_extA*

The *extA* gene was synthesised by Eurofins and provided in the *pEX-A128* vector. The gene contained complementary Golden Gate restriction sites at the 5' and 3' end of the gene for insertion into the *pMEGGAx* vector.

Golden Gate reaction was performed by combining 4 μ L of 920 μ g/mL of *pEX-A128_extA*, 2 μ L of 60 μ g/mL *pMEGGAx*, 1.5 μ L of restriction enzyme Esp3I, 1.5 μ L of T4 DNA ligase, 2 μ L of T4 DNA ligase buffer and 4 μ L of dH₂O. Reaction was cycled 45 times at 37 °C for five minutes, 16 °C for five minutes before denaturing of the Esp3I restriction enzyme at 65 °C for five minutes and 80 °C for five minutes. Products of Golden Gate reaction were analysed using gel electrophoresis and sequenced by Eurofins.

2.2.3. Generation of N-truncated *ExtA*

Golden Gate cloning was utilized in order to generate an N-truncated *ExtA* variant. Primers were designed to amplify selected regions of *pMEGGAx_extA* so that the first 42 amino acid residues after the signal peptide would be absent from the final structure and the protein would start three residues downstream from the first CxxCH motif at Val67. Primers were generated with restriction sites complementary for Esp3I in order for reassembly back into the *pMEGGAx* expression vector.

Amplification of DNA fragments was performed through PCR amplification, in two individual reactions. For the first reaction primers *ExtA_SignalPep_For* and *ExtA_SignalPep_Rev* were used whilst the second reaction utilised primers *ExtA_Heme_For* and *ExtA_Heme_Rev*, all other conditions were identical for

each reaction. PCR reaction mixes contained 2.5 μL of 52 $\mu\text{g}/\text{mL}$ of *pMEGGAx_extA*, 1 μL of forward and reverse primers, 25 μL of Phusion Flash High-Fidelity PCR Master Mix (Thermo Scientific) and 20.5 μL of molecular water. PCR was cycled 45 through steps of denaturing at 98 $^{\circ}\text{C}$ for 15 seconds, annealing of primers at a gradient of 54 to 64 $^{\circ}\text{C}$ for 30 seconds and amplification of DNA fragments at 72 $^{\circ}\text{C}$ for 2 minutes. Generating DNA fragments here named *ExtA_SignalPep* and *ExtA_Heme*. Amplified DNA was analysed by gel electrophoresis to ensure amplification of correct size and extracted with the use of the DNA extract kit from Merck. DNA fragments were ligated into the *pMEGGAx* vector in a one-step Golden Gate PCR reaction consisting of 2 μL of *pMEGGAx*, 2 μL of DNA fragment *ExtA_SignalPep*, 2 μL of DNA fragment *ExtA_Heme*, 1.5 μL of restriction enzyme *Esp3I*, 1.5 μL of T4 DNA ligase, 2 μL of T4 DNA ligase buffer and 4 μL of dH_2O . Golden Gate reaction samples were analysed using gel electrophoresis and bands at the correct size were extracted and sent for sequencing (Eurofins). Conformation of the synthesis of this new plasmid through sequencing was confirmed, from here on this plasmid will be referred to as *pMEGGAx_extA.1*.

2.2.4. Sequencing of Plasmids

Plasmids were sequenced by Eurofins using primers *pMEGGAx_For* and *pMEGGAx_Rev*. Aliquots of 15 μL of plasmid were combined with 2 μL of primer, from a stock primer concentration of 10 pmol/ μL .

2.3. Protein Purification

2.3.1. HIS-Tag Purification

His tag column (HisTrap HP, Cytiva) was equilibrated with 5 column volumes (CVs) of 20 mM NaPO_4 , 500 mM NaCl , and 30 mM Imidazole pH 7.4 (Buffer 1). Sample was added to the column and washed with 5 CVs of Buffer 1. Elution took place over 20 CVs starting with 100 % of Buffer 1 and 0 % of Buffer 2, 20 mM NaPO_4 , 500 mM NaCl , 500 mM Imidazole and ending with 0 % Buffer 1 and 100 % Buffer 2. The column was stripped with 20 mM NaPO_4 , 500 mM NaCl 50 mM EDTA.

2.3.2. STREP-II Tag Purification

The supernatant containing lysed bacteria cells expressing STREP-II tagged proteins was passed through a 5 mL Strep-tactin XT Superflow Column (IBA Solutions for Lifesciences) which was equilibrated with 50 mM Tris, 100 mM NaCl (Buffer A) for 5 CV. The sample was loaded onto the column and washed with 5 CV of Buffer A. Sample was eluted with 50 mM Biotin in Buffer A, and 0.9 CVs was passed through the column before AKTA was paused for 30 mins to allow for protein to be unbound from the matrix before a further 5 CV to elute the protein.

2.3.3. Size Exclusion Chromatography

Size exclusion chromatography (SEC) was performed in order to further purify protein samples after affinity chromatography. SEC also allowed for ease of buffer exchange, in particular removal of imidazole from ExtD fractions. Protein samples from affinity chromatography were collected and concentrated to approximately 1 mL and loaded onto a HiLoad 16/600 Superdex 75 column equilibrated with 2 CV of 100 mM Tris, 50 mM NaCl, 1 mM EDTA pH 8. Protein was passed through a column at 0.5 mL/min and collected in 2 mL fractions. Purified protein was analysed using SDS-PAGE.

To estimate molecular mass SEC was utilised using a Superose 6 10/300 GL column equilibrated with 100 mM Tris, 50 mM NaCl at pH 8. A molecular ladder was constructed using proteins of varying masses: MtrC from *Shewanella oneidensis*; L-glutamic dehydrogenase; ExtD from *Geobacter sulfurreducens*; L-Lactic Dehydrogenase; and Bovine serum albumin.

2.4. Physical Characterization of Proteins

2.4.1. Liquid Chromatography Mass Spectroscopy

LC-MS was kindly carried out by Dr Jessica Van Wonderen. Protein samples were concentrated to an excess of 30 μ M with a 20 μ L sample of protein added to 180 μ L 1 % acetonitrile, 0.3 % formic acid. The sample was loaded onto a ProSwift

RP-1S column, 4.6 × 50 mm, Thermo Scientific, on an Ultimate 3000 uHPLC system. Sample was eluted over a gradient from 2-100 % acetonitrile, and 0.1 % formic acid. Positive mode electrospray ionisation mass spectrometry was carried out on the eluate in a Bruker microQTOF-QIII mass spectrometer.

2.4.2. Analytical Ultracentrifugation

Analytical Ultracentrifuge (AUC) is a biophysical technique shown to have great potential for characterizing proteins in terms of their relative shape, size, and quaternary structure, while requiring relatively low concentrations⁴. During AUC, an analyte is observed at a specific wavelength while a centrifugal force is applied, and the sedimentation is documented. As cytochromes have a rich absorption spectrum, it allows for sedimentation to be monitored at different wavelengths, not just at 280 nm as is usual for proteins. There are two main experiments utilized when performing AUC, Sedimentation Velocity (SV) and Sedimentation Equilibrium (SE)^{4,5}. Both methods involve the application of a centrifugal force to the analyte being observed with a high force being applied for SV and a lower force for SE. While both methods share many attributes the use of SV more easily allows for a determination of size, shape and molecular interactions of the analyte whilst SE more easily allows for the determination of association constants and stoichiometry. In this thesis, SV is the method primarily used.

The use of SV relies on an understating of the forces acting on an analyte in a solution that has a centrifugal force applied to it. There are many forces to consider. The first is the gravitational force acting upon the analyte, F_s , and the counterforce of the buoyancy of the analyte, F_b . For both these forces they can be defined as using the speed of rotation in radians per second, ω , and the radius of rotation, r , and either the mass of the particle, M_p , or the mass of the solvent displaced by the analyte, M_s . Equations are shown in *Equation 2.1* and *2.2*.

$$F_s = M_p \omega^2 r$$

Equation 2.1

$$F_b = M_s \omega^2 r$$

Equation 2.2

The frictional force of the analyte moving through the solution also needs to be defined. This can be defined using *Equation 2.3*. Where F_r is the frictional force, f is the frictional ratio and u is the velocity.

$$F_r = fu$$

Equation 2.3

By balancing Equations 2.1-3 the Svedberg equation is revealed which defines the sedimentation coefficient (S), *Equation 2.4*. Where M_b is the buoyant molar mass⁶.

$$S \equiv \frac{v}{\omega^2 r} = \frac{M_p(1 - vp)}{f} = \frac{M_b}{f}$$

Equation 2.4

Importantly *Equation 2.4* shows that that S is proportional to M_b and inversely proportional to the frictional ratio.

Two methods using AUC were used in this thesis, sedimentation velocity (SV) and sedimentation equilibrium (SE). For both SV experiments protein samples were concentrated so that absorbance in a 1 cm cuvette gave an $A_{410} \approx 0.7$, for each cytochrome studied approximately 0.6 μM for ExtA, 1.17 μM for ExtD and 1.12 μM for ExtC. Once concentrated to the desired level 410 μL of individual cytochrome to be studied were added to one side of a quartz double sector cell with 410 μL of corresponding cytochrome buffer added to the opposing sector.

In SV experiments cytochrome interactions were analysed equimolar concentrations of cytochrome were used with 205 μL of each cytochrome added to the sector cell. Cells were placed in Ti50 rotor in a Beckman Optima XL-A Analytical Ultracentrifuge and centrifuged at 10,000 rpm. Absorbance was monitored at 410 nm and over the course of 20 hours 300 spectra were taken. Throughout the experiment a constant temperature of 20 $^{\circ}\text{C}$ was maintained.

For SE experiments only one cytochrome was studied, ExtA, at concentrations of 0.24, 0.78 and 2.13 μM . For the two lower concentrations absorbance was monitored at 410 nm and for the highest concentration sedimentation was monitored at 552 nm.

Data from both SV and SE experiments were analysed using Sedfit ⁷ to generate the $c(s)$ distribution, with buffer density calculated using SEDNTERP 3 ⁸.

2.5. Spectroelectrochemical Characterisation of Proteins

2.5.1. UV-Visible Spectroscopy

Spectra of cytochromes were taken between 350 - 800 nm under oxidised and reduced conditions. Cytochromes were sealed in a cuvette using a Suba-seal and sparged for 5 minutes with nitrogen gas. The spectrum of cytochrome was recorded at this point to obtain the oxidised spectrum. Cytochromes were reduced using a stock solution of 10 mg/mL of sparged sodium dithionate. If a reduction titration was to be carried out sodium dithionite would be serially diluted to 10 $\mu\text{g}/\text{mL}$ and 2 μL of solution added to cuvette and spectrum recorded. This was repeated until cytochrome was fully reduced. If reduction titration was not being performed an excess of 20 μL of 10 mg/mL sodium dithionite was added to cytochrome containing cuvette. Data was analysed by subtracting the corresponding buffer blank and the dilution factor was accounted for.

2.5.2. Pyridine Hemochrome Assay

The pyridine hemochrome assay⁹ is a method for the determination of a cytochrome's extinction coefficient. From an unknown concentration of cytochrome, a 100 μL aliquot was taken and added to a solution of 100 mM Tris, 150 mM NaCl, and 1 mM EDTA pH 8 to a total volume of 200 μL . The spectra of the cytochrome solution were recorded under air oxidised and reduced with sodium dithionite between 350 to 800 nm. The method is repeated this time denaturing a new 100 μL aliquot of the cytochrome in 100 μL of 0.1 M NaOH 20 % (v/v) pyridine and recording the oxidised and reduced spectra. Pyridine will displace the native axial ligands of the heme cofactors generating hemes with a bis pyridine ligation. The extinction coefficient for one heme is $\epsilon_{550-535} = 23.97 \text{ mM}^{-1}\text{cm}^{-1}$ from the pyridine 'reduced minus oxidised' spectrum.

2.5.3. Methyl Viologen Assay

Assays were conducted to investigate possible terminal electron acceptors (TEA) for ExtD. An assay was conducted in 2 mL of 50 mM HEPES at pH 7 investigating possible TEA by the addition of stock solutions: 100 mM sodium nitrite; 100 mM sodium sulfate; 100 mM sodium sulfite; 100 μM flavin mononucleotide; or 100 mM hydroxylamine. To 2 mL of 50 mM HEPES addition of methyl viologen, ExtD and sodium dithionite to final concentrations of 0.8 μM , 3 nM and 0.25 mM respectively. All reagents were sealed with rubber Suba sealed and sparged with nitrogen gas for 10 minutes before assay. Absorbance was monitored at 600 nm, with reduced methyl viologen having an $\epsilon_{600} = 13,700 \text{ M}^{-1}\text{cm}^{-1}$, before and after the addition of TEA for approximately 30 seconds to establish a baseline. After the baseline was defined 10 μL of potential TEA was added to the cuvette and the rate of decrease in A_{600} was determined. A decrease in absorbance would be caused by the oxidation of methyl viologen by ExtD, which correlated to the reduction of TEA by ExtD. As a control NfrA from *E. coli* was used in place of ExtD to reduce TEA NaNO_2 as shown previously in research¹⁰.

2.5.4. Electron Paramagnetic Resonance

Electron paramagnetic resonance (EPR) was kindly carried out by Dr Dimitri Svistunenکو (Essex University, UK). EPR spectra were recorded at 10 K using a

Bruker E500 (X-band) EPR spectrometer and Oxford Instruments liquid helium systems. Instrument parameters were as follows: microwave frequency $\nu_{\text{MW}} = 9.467$ GHz, modulation frequency $\nu_{\text{M}} = 100$ kHz, time constant $\tau = 82$ ms, microwave power = 3.19 mW, modulation amplitude AM = 5 G, scan rate $\nu = 22.6$ Gs⁻¹. Wilmad SQ EPR tubes (Wilmad Glass, Buena, NJ) with OD = 4.05 ± 0.07 mm and ID = 3.12 ± 0.04 mm (mean \pm range) were used for freezing EPR samples in methanol cooled with solid CO₂. After freezing, the EPR tubes with samples were kept in liquid nitrogen until required for measurements.

2.6. Electrochemistry

Protein Film Voltammetry (PFV) is a form of cyclic voltammetry in which the redox active protein being analysed is adsorbed onto a working electrode (WE), common working electrodes include Indium Tin Oxide (ITO) and modified gold amongst others^{11–13}. For experiments carried out in this thesis, an ITO working electrode was used. The WE was suspended in a buffer solution also containing the counter electrode (CE) and a reference electrode (RE). PFV differs from other types of cyclic voltammetry as the protein is adsorbed onto a working electrode allowing for easy transfer of electrode between pH and other variables. Further, as the protein is not in solution there is no diffusion effect seen in the voltammograms.

During PFV the voltage of the WE is varied producing sweeps in either a decreasing voltage direction (reductive sweep) or an increasing voltage direction (oxidative sweep). In each voltammogram produced there will be visualisation of the non-Faradaic current, generated from the electrode and buffer, and the Faradaic current, produced by the adsorbed protein. To assess the redox properties of the adsorbed protein only the Faradaic current needs to be considered. The Faradaic current can be described using *Equation 2.6*, where E is the potential of the WE, E^0 the reduction potential, n the number of electrons transferred in the corresponding half-reaction, F is the Faraday's constant, R is the gas constant, T is the absolute temperature, ν is voltammetric scan rate (V/s),

A is the surface area of the WE (cm²), and Γ is electroactive redox protein coverage (moles/cm²).

$$|i| = \frac{\exp\left(\frac{nF}{RT}(E - E^0)\right)}{\left(1 + \exp\left(\frac{nF}{RT}(E - E^0)\right)\right)^2} \cdot \frac{n^2 F^2 v A \Gamma}{RT}$$

Equation 2.6

The shape of the Faradaic current, as described by *Equation 2.6*, would therefore be Gaussian in nature and have both a negative and positive curve, when performing a full sweep. Both the negative and positive curves should be identical in shape if the protein being studied is fully reduced and oxidised with each scan and there is no catalytic activity of the enzyme.

From *Equation 2.6* it is possible to map the Faradaic peaks which would have an equal magnitude in both the reductive and oxidative reversible half-reactions. These peaks would therefore have equal stoichiometry of electrons transferred, a shorthand for determining this stoichiometry can be defined from *Equation 2.7*.

$$W_{1/2} = \frac{2RT}{nF} \ln(3 + 2\sqrt{2})$$

Equation 2.7

Under standard temperatures, 25 °C, the half-height width of a n=1 reversible redox half-reaction would result in $W_{1/2} = 90$ mV. Therefore, *Equation 2.8* can be used to estimate the number of half-reactions that were involved in the Faradaic current. To determine the moles of electroactive redox cofactors, $A \cdot \Gamma$, involved in a half-reaction a relationship between the area of the Faradaic peak, Π , can be defined, in *Equation 2.8*. As this thesis utilizes ITO electrodes the definitive area of the working electrode cannot be defined as it is hierarchical, so moles of electroactive redox cofactors are given per cm².

$$A. \Gamma = \frac{\Pi}{nFv}$$

Equation 2.8

2.6.1. Construction of ITO electrodes

ITO dispersion was prepared by sonicating 35 mg of ITO nanoparticles in 300 μL of water:methanol 1:6 (v/v) for 3 hours. Dispersion was added to a polystyrene pellet that had been washed in methanol. Polystyrene:ITO solution was vortexed for 2 minutes before sonicated in ice-cold water for 5 minutes. Fluorine-doped tin oxide (FTO) glass with a resistance of 8 Ω was cut to a size of 25 mm by 7.5 cm. FTO was cleaned by sonicating in isopropanol alcohol followed by ethanol for 3 minutes each. Excess ethanol was removed and a template for drop casting of ITO was added to the conductive side of FTO glass, either a circle of 0.25 cm^2 or a rectangle of 0.65 cm^2 . An aliquot of ITO dispersion was drop cast onto FTO glass and dried in excess of 4 hours. FTO with dried ITO dispersions were transferred to the furnace and heated to 500 $^{\circ}\text{C}$, in increments of 1 $^{\circ}\text{C}/\text{min}$, with peak temperature maintained for 20 mins. Once cooled FTO:ITO electrodes were cleaned by washing in 30 % Hydrogen peroxide:H₂O:ammonium 1:5:1 (v/v) at 70 $^{\circ}\text{C}$ for 15 minutes. Electrodes were rinsed with water and transferred to the furnace for heating to 180 $^{\circ}\text{C}$ for 1 hour. Cooled electrodes were then ready for protein adsorption.

2.6.2. Protein Film Electrochemistry

Protein film voltammetry¹¹ was performed with a three-electrode set up, *Figure 2.2*. Platinum was utilised as the counter electrode, and ITO deposited on FTO glass acted as the working electrode. Both electrodes were positioned in the main chamber of the apparatus. A reference electrode of Ag/AgCl (saturated in KCl), was positioned in a side arm. A 10 μL aliquot of ExtD at 30 μM in 50 mM Tris pH 8 was drop cast onto an ITO electrode and incubated on ice for ten minutes allowing for adsorption. Protein that was not adsorbed to the electrode was removed by washing with molecular water. ITO electrode was connected to a

platinum wire and positioned into the desired buffer. The current was recorded across varying voltages of -0.9 to 0 V vs reference with scan rates of 0.01, 0.02, 0.05, 0.1 and 0.2 V/s.

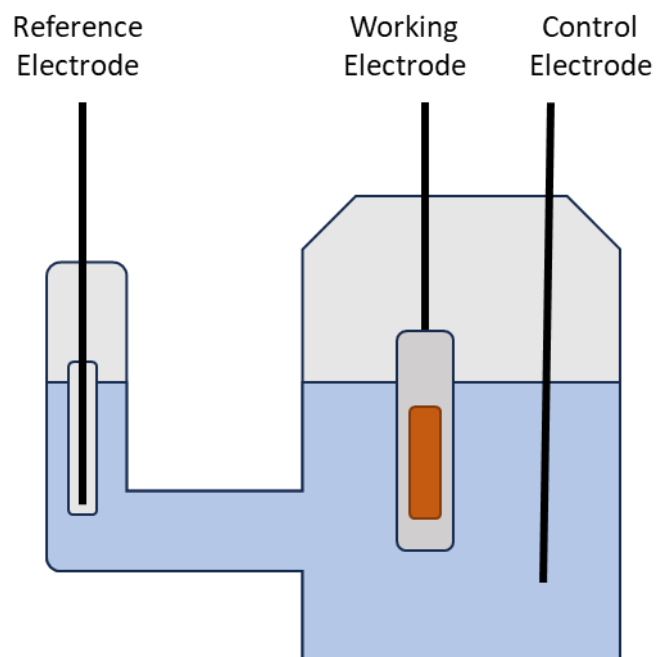


Figure 2.2- Schematic of three-electrode cell. The working and control electrode are positioned in the main chamber with the reference electrode positioned in a connected side arm.

2.6.3. Spectroelectrochemistry

As ITO electrodes are optically transparent spectra can be recorded of cytochromes adsorbed on their surface. Preparation of cytochrome adsorbed onto ITO surface was performed as previously performed for PFV. Spectroelectrochemistry was performed outside of the glove box due to the use of a Jasco 600 spectrometer. Therefore, the ITO electrode was positioned in a sealed cuvette sparged with nitrogen gas. A reference electrode of silver wire coated in AgCl was constructed through electrolysis. This was done by submerging the Ag wire in 10 % HCl with a platinum wire. Both wires were connected to a battery with the Ag wire acting as the anode and the Pt wire as the cathode. Wires were left submerged for an excess of 15 minutes, and a AgCl deposition was seen on the Ag wire.

Construction of an electrochemical cell was performed in the absence of oxygen. The cell was made using a plastic cuvette with the working electrode of ITO with adsorbed cytochrome, a reference electrode of AgCl coated Ag wire and a control electrode of Pt. All electrodes were positioned in the cuvette and submerged in 50 mM Tris, 100 mM NaCl pH 8, care was taken to ensure wires did not touch. The cuvette was anaerobically sealed with SCUBA seal, electrode wires previously threaded through the seal, and wrapped in parafilm.

The electrochemical cell was positioned in a Jasco 600 spectrometer and also connected to a potentiostat. Spectra were recorded in 50 mV intervals, poisoning the ITO electrode at a specified potential for 1 minute before recording spectra. Spectra were gathered by decreasing potential until fully reduced cytochrome spectra were recorded followed by increasing potential until the spectrum showed fully oxidised cytochrome.

Before and after each run the AgCl-coated Ag wire was calibrated with potassium hexa-cyanoferrate(III). Cyclic voltammetry was performed using 30 mM potassium hexa-cyanoferrate(III) in 50 mM tris, 100 mM NaCl at pH 8. The midpoint potential of potassium hexa-cyanoferrate(III) against the AgCl-coated Ag wire was noted and converted to +420 mV vs SHE. Each spectroelectrochemical run could then be converted to vs SHE.

2.7. AlphaFold *in-silico* protein modelling

The recent advent of artificial intelligence assisted modelling of proteins based on their amino acid sequences through programs such as AlphaFold¹⁴ has revolutionised the understanding of previously uncharacterised proteins, allowing for structural predictions of unique proteins. Previously homology modelling was the main method utilized for protein structure modelling. Allowing for the prediction of protein structures without experimentally determining the structure, however required a homologous protein to have been previously structurally characterised. AlphaFold has revolutionized

computational structural biology with the ability to predict protein structure based solely on the amino acid sequence, partly solving the 'protein folding problem' ¹⁴⁻¹⁶.

The original version of AlphaFold was capable of modelling monomeric protein structures ¹⁴. Protein models were generated through two complementary processes focusing on the evolutionary history of the protein and the potential interactions between the amino acid sequence ¹⁴. AlphaFold utilizes a multiple sequence alignment (MSA) to track evolutionary biology in order to generate a list of key residues that may interact. Evoformer, a building block network, aligns residues in a 3D model based on the pairwise output from the MSA taking into account physical interactions of attraction and repulsion of the amino acid residues ¹⁴. The main drawback of AlphaFold was the inability to model protein complexes, however with the use of linkers, usually generated from 20 glycine residues linking two protein sequences, it was possible to generate pseudo-complex interactions ^{17,18}.

The researchers behind AlphaFold later released AlphaFold-Multimer ¹⁵ which allowed for the modelling of protein complexes without the need of encoding a linker. AlphaFold and AlphaFold-Multimer were both based on the same code, with small changes made to the AlphaFold-Multimer code to allow for complex modelling ^{14,15}. The use of AlphaFold-Multimer was essential in this thesis for allowing protein interactions to be hypothesised, both in the form of identifying potential homopolymers and with identifying how a porin cytochrome complex could be constructed.

However, neither of these earlier versions of AlphaFold allowed for inclusion of various cofactors when predicting a proteins structure. Resources that allow for cofactor modelling only doing so after the protein structure has been finalised and not including cofactors in the generation of protein models. Additional artificial intelligence methods were generated to solve this problem, such as AlphaFill where AlphaFold models were inputted into the algorithm and

compared to experimentally determined structures in the PDB, if a high homology was found any cofactors from the PDB structure were transplanted onto the AlphaFold model¹⁹. Additionally, this could be performed manually, without the use of algorithms such as AlphaFill, if the cofactors were known or there was no homology between the AlphaFold model and structures in the PDB.

However, whilst cofactors could be inserted after protein modelling the algorithms did not take into account how a protein structure could be affected by the presence of a cofactor. In response to this AlphaFold 3 was developed allowing for the modelling of protein complexes with common cofactors, such as c- and b-type hemes, chlorophyll A and B, nucleic acids and various metal ions¹⁶. Whilst AlphaFold and AlphaFold-Multimer utilise an evolutionary history approach for building a protein model, AlphaFold 3 greatly reduced the use of MSA. Instead, the Evoformer module was improved to allow for a diffusion-based approach for generating a 3D protein structure^{16,20}. In diffusion models all the placement of amino acids in a three-dimensional plane is originally randomised, generating a model that is considered 'noisy'. The model is refined through multiple diffusions until an acceptable model is generated. Whilst diffusion-based models have the potential to revolutionise structural modeling there are drawbacks to the approach, the largest being the diffusion model's proclivity to hallucinate structures^{16,20}.

All amino acid residues modelled using any version of AlphaFold are assessed on a predicted local distance difference test (pLDDT), with AlphaFold 3 additionally providing pLDDT scores for individual elements of amino acids as well as cofactors present in the model. This allows for local confidence to be allocated to each amino acid residue, based on the C α local difference test²¹. The pLDDT score is a good indication of a residue correct placement in the structural model with a maximum score of 100 and a low score of 0. The overall average pLDDT score of the structural model can also be calculated to give an estimate of AlphaFold's confidence for the whole model. The pLDDT score has also been used by some researchers to suggest areas of flexibility, where areas absent of

defined secondary structure in AlphaFold models have on average a lower pLDDT score ²².

2.7.1. Generation of Protein Models

In this thesis, AlphaFold-Multimer ¹⁵ was utilised in order to generate structural models of individual proteins as well as protein complexes. AlphaFold-multimer was run using the 'ADA' cluster of UEA's high-power computer. The protein sequence was analysed prior to structural modelling with signal peptides identified using SignalP 5.0 ²³ and not included in the modelling. AlphaFold models were simulated through GPU-P5000-2 using available PDB models published up to January 2022. The maximum memory and time allocated for each simulation was 300 G and 48 hours. Additionally, in some cases AlphaFold 3 was utilised when protein models from AlphaFold-Multimer yield poor results, based on average pLDDT. Protein sequences were processed the same as with AlphaFold-Multimer, however structural models were created through the Google Deepmind's AlphaFold server. AlphaFold 3 was not used to generate all models due to its recent release.

For every sequence input AlphaFold generates five potential models ranked 0 to 4, rank 0 being the highest quality ¹⁴. Models in this thesis showed only very minor differences in the ranked models, and therefore the ranked 0 model was used. In cases where there were considerable differences in predicted structure between the ranked models, the model with the highest average pLDDT is shown. All five ranked models are included in the *Appendix* for each ExtABCD simulation.

Simulated AlphaFold models were visualised using Pymol. Heme cofactors were added manually to AlphaFold-multimer models predicted to be cytochromes using a c-type heme from STC (PDB ID: 6HR0) ²⁴ and allying to CxxCH motifs present in the structural model.

AlphaFold models were validated using multiple techniques. The solvent-accessible surface area of residues/cofactors was determined using Areaimol through the CCP4 suite ²⁵. The electrostatic potential of AlphaFold models was visualised using APBS ²⁶. Structural homology of AlphaFold model to experimental structures in the PDB was performed using PDBeFold ²⁷.

2.8. References

1. Arslan, E., Schulz, H., Zufferey, R., Künzler, P. & Thöny-Meyer, L. Overproduction of the *Bradyrhizobium japonicum* c-Type Cytochrome Subunits of the cbb3 Oxidase in *Escherichia coli*. *Biochem Biophys Res Commun* **251**, 744–747 (1998).
2. Guzman, L. M., Belin, D., Carson, M. J. & Beckwith, J. Tight regulation, modulation, and high-level expression by vectors containing the arabinose PBAD promoter. *J Bacteriol* **177**, 4121–4130 (1995).
3. Laemmli, U. K. Cleavage of Structural Proteins during the Assembly of the Head of Bacteriophage T4. *Nature* **227**, 680–685 (1970).
4. Cole, J. L., Lary, J. W., P. Moody, T. & Laue, T. M. Analytical Ultracentrifugation: Sedimentation Velocity and Sedimentation Equilibrium. in 143–179 (2008).
5. Edwards, G. B., Muthurajan, U. M., Bowerman, S. & Luger, K. Analytical Ultracentrifugation (AUC): An Overview of the Application of Fluorescence and Absorbance AUC to the Study of Biological Macromolecules. *Curr Protoc Mol Biol* **133**, (2020).
6. Lebowitz, J., Lewis, M. S. & Schuck, P. Modern analytical ultracentrifugation in protein science: A tutorial review. *Protein Science* **11**, 2067–2079 (2002).
7. Schuck, P. Size-Distribution Analysis of Macromolecules by Sedimentation Velocity Ultracentrifugation and Lamm Equation Modeling. *Biophys J* **78**, 1606–1619 (2000).
8. Philo, J. S. SEDNTERP: a calculation and database utility to aid interpretation of analytical ultracentrifugation and light scattering data. *European Biophysics Journal* (2023)
9. Barr, I. & Guo, F. Pyridine Hemochromagen Assay for Determining the Concentration of Heme in Purified Protein Solutions. *Bio Protoc* **5**, (2015).
10. Clarke, T. A. *et al.* *Escherichia coli* Cytochrome c Nitrite Reductase NrfA. in 63–77 (2008).
11. Butt, J. N., Jeuken, L. J. C., Zhang, H., Burton, J. A. J. & Sutton-Cook, A. L. Protein film electrochemistry. *Nature Reviews Methods Primers* **3**, 77 (2023).
12. Hirst, J. Elucidating the mechanisms of coupled electron transfer and catalytic reactions by protein film voltammetry. *Biochimica et Biophysica Acta (BBA) - Bioenergetics* **1757**, 225–239 (2006).

13. Léger, C. & Bertrand, P. Direct Electrochemistry of Redox Enzymes as a Tool for Mechanistic Studies. *Chem Rev* **108**, 2379–2438 (2008).
14. Jumper, J. *et al.* Highly accurate protein structure prediction with AlphaFold. *Nature* **596**, 583–589 (2021).
15. Evans, R. *et al.* Protein complex prediction with AlphaFold-Multimer. Preprint at <https://doi.org/10.1101/2021.10.04.463034> (2021).
16. Abramson, J. *et al.* Accurate structure prediction of biomolecular interactions with AlphaFold 3. *Nature* (2024)
17. Mirdita, M. *et al.* ColabFold: making protein folding accessible to all. *Nat Methods* **19**, 679–682 (2022).
18. Ko, J. & Lee, J. Can AlphaFold2 predict protein-peptide complex structures accurately? Preprint at <https://doi.org/10.1101/2021.07.27.453972> (2021).
19. Hekkelman, M. L., de Vries, I., Joosten, R. P. & Perrakis, A. AlphaFill: enriching AlphaFold models with ligands and cofactors. *Nat Methods* **20**, 205–213 (2023).
20. Desai, D. *et al.* Review of AlphaFold 3: Transformative Advances in Drug Design and Therapeutics. *Cureus* (2024)
21. Mariani, V., Biasini, M., Barbato, A. & Schwede, T. IDDT: a local superposition-free score for comparing protein structures and models using distance difference tests. *Bioinformatics* **29**, 2722–2728 (2013).
22. Ma, P., Li, D. & Brüschweiler, R. Predicting protein flexibility with AlphaFold. *Proteins: Structure, Function, and Bioinformatics* **91**, 847–855 (2023).
23. Almagro Armenteros, J. J. *et al.* SignalP 5.0 improves signal peptide predictions using deep neural networks. *Nat Biotechnol* **37**, 420–423 (2019).
24. Fonseca, B. M. *et al.* Optimizing Electroactive Organisms: The Effect of Orthologous Proteins. *Front Energy Res* **7**, (2019).
25. Agirre, J. *et al.* The CCP4 suite: integrative software for macromolecular crystallography. *Acta Crystallogr D Struct Biol* **79**, 449–461 (2023).
26. Jurrus, E. *et al.* Improvements to the APBS biomolecular solvation software suite. *Protein Science* **27**, 112–128 (2018).
27. Krissinel, E. & Henrick, K. Secondary-structure matching (SSM), a new tool for fast protein structure alignment in three dimensions. *Acta Crystallogr D Biol Crystallogr* **60**, 2256–2268 (2004).

*Chapter 3: Expression, Purification and
Characterisation of Outer Membrane
Lipo-Cytochrome ExtD from Geobacter
sulfurreducens PCA*

3.1. Introduction

Terminal or outer membrane multiheme cytochromes (MHCs) are an under explored aspect of electromicrobiology, with many being known but few characterised in depth. *Geobacter sulfurreducens* PCA is predicted to contain multiple outer membrane MHCs however their functionality has been underexplored with many characterisations only looking at the effect of gene deletions^{1,2}. The ExtABCD porin cytochrome cluster (PCC) is one of five predicted PCCs to be present in *Geobacter sulfurreducens* PCA and is predicted to contain two outer membrane cytochromes (OMCs), ExtC and ExtD. The predicted hexaheme cytochrome ExtD (gene: GSU2642) contains a putative lipo-box presumed to allow for covalent binding of ExtD to the outer membrane of *G. sulfurreducens* PCA.

Single gene deletions of *extD* have previously been shown to decrease total current density produced from *G. sulfurreducens* cells by approximately 80 %, from cells grown on graphite electrodes poised at +240 mV^{1,2}. ExtD has also been linked with the reduction of Fe(III) oxide with the *extD* gene shown to be significantly upregulated when *G. sulfurreducens* is grown on Fe(III)³. However, whole gene knockout of the *extABCD* cluster was shown to have minimal effect on Fe(III) reduction compared to wildtype *G. sulfurreducens*¹.

ExtD is predicted to be a unique outer membrane cytochrome, conserved primarily in the *Geobacter* genus with only 14 homologs identified outside of the *Geobacteraceae* family. Here initial characterisation of the outer membrane cytochrome ExtD from *G. sulfurreducens* PCA, encoded in the *extABCD* gene cluster (GSU2642 to GSU2645), by heterologous expression in *Escherichia coli* BL21 and *Shewanella oneidensis* LS527. This chapter aims to optimise the expression of *extD* using heterologous hosts *E.coli* BL21 and *S. oneidensis* LS527, in order to begin protein characterisation propping into the size, redox behaviour and functionality of ExtD.

3.2. Methods

3.2.1. *Optimisation of ExtD Expression and Purification*

The pMEGGAx vector containing the *extD* gene (GSU2642) from *Geobacter sulfurreducens* PCA was codon optimized for protein expression in *E. coli* K12 and kindly provided by Dr Marcus Edwards (Essex University, UK), plasmid referred to here as pMEGGAx_ExtD_HIS. The *extD* gene had previously been modified to substitute the DNA sequence predicted to encode the native signal peptide to instead encode the sequence of the signal peptide of MtrB from *Shewanella oneidensis* MR-1. At the 3' end of the *extD* gene, the DNA sequence corresponding to a His-tag was encoded allowing for ease of purification. The pMEGGAx vector also provided kanamycin resistance to host bacteria, allowing for selective growth.

The pMEGGAx_ExtD_HIS vector was transferred to *E. coli* BL21 component cells, see method section, for protein expression. The *E. coli* BL21 cells also contained a secondary plasmid, pEC86, encoding for genes related to the cytochrome c maturation pathways which are otherwise absent in the *E. coli* BL21 strain⁴. Additionally, the pEC86 vector provided chloramphenicol resistance allowing for bacteria selection. Overnight cultures of 10 mL LB with 30 µg/mL of kanamycin and chloramphenicol were inoculated with *E. coli* BL21 containing pMEGGAx_ExtD_HIS and pEC86 were grown overnight at 30 °C, shaking at 180 rpm. After an incubation period of over 18 hours, cultures were used in expression trials of ExtD. Expression trials consisted of 50 mL of LB media containing 30 µg/mL of kanamycin and chloramphenicol were inoculated with 1 % (v/v) of the overnight culture and grown at 30 °C with 180 rpm. Cultures were grown until an OD₆₀₀ of 0.4 was reached at which point the pMEGGAx_ExtD_HIS vector was induced with arabinose to begin expression of extD. For the first expression trial, each 50 mL culture was induced with a different concentration of arabinose ranging from 0 to 20 mM. Cells were then returned to 30 °C with 180 rpm and harvested between 1 and 18 hours after initial induction to determine the most effective procedure.

Protein expression was varied, each trial changing one of the conditions (arabinose concentration, harvesting time after induction, temperature). Ultimately, it was discovered that the highest protein expression was seen when cells were grown at 30 °C with 180 rpm to an OD₆₀₀ of 0.4 and induced with 10 mM of arabinose with harvesting occurring 4 hours after induction. The *pMEGGAx_extD_HIS* vector was also electroporated into *Shewanella oneidensis* LS527 competent cells and the optimization was repeated to determine if expression of ExtD could be increased. As *S. oneidensis* LS527 cells already contain genes encoding a cytochrome c maturation pathway the *pEC86* vector was not electroporated in *S. oneidensis* LS527 cells, and therefore chloramphenicol was not added to growth cultures.

Bacterial cultures expressing ExtD_His, either *E. coli* BL21 or *S. oneidensis* LS527, were harvested by centrifugation using the Beckman Avanti J-20 High-Capacity centrifuge with 8.1000 rotor centrifuging for 20 minutes at 3,000 xg, 4 °C. Pelleted cells were resuspended in 100 mM Tris 150 mM NaCl 1 mM EDTA pH 8 with DNase and cComplete EDTA-free Protease Inhibitor tablet (Merck). Resuspended cells were lysed by passing through the French Press at 1,000 psi twice. Soluble protein was then extracted from cell lysate by ultracentrifugation at 200,000 xg for 1 hour 30 mins at 4 °C using the Beckman Optima XL-100K Ultracentrifuge with the 45 Ti rotor. Soluble cell fraction was collected and ExtD_His loaded onto a 5 mL Cytiva HisTrap HP column equilibrated with 20 mM NaPO₄ 500 mM NaCl 30 mM Imidazole pH 7.4 with 5 column volumes (CV) of buffer run through to remove unbound proteins. ExtD_His bound to the column was eluted across a gradient by increasing imidazole concentration up to 500 mM across 20 CV. Eluted protein was then concentrated to 1 mL in a 3 kDa Amicon Ultra Centrifuge filter from Merck. Concentrated ExtD was injected onto a Superdex 75 16/60 gel filtration column pre-equilibrated with 100 mM Tris 150 mM NaCl 1 mM EDTA pH 8, to increase the purity of ExtD_His as well as remove imidazole that may act as an axial ligand to heme cofactors.

Finally, the C-terminus HIS affinity tag was switched to a STREP-II affinity tag in an attempt to increase the yield of ExtD as usage of STREP-II tag has been shown to increase produce higher purity of target protein. Additionally, as the histidine residue in the HIS-tag has the potential to also act as an axial ligand to one of the heme cofactors the use of the STREP-tag would remove this possibility. The *pMEGGAx_extD_STREP* vector was electroporated into *S. oneidensis* LS527 with protein expression and cell lysis following the same protocol as the optimised protocol described above. Protein purification was carried out on AKTA-prime with soluble cell lysate loaded into a 5 mL IBA Strep-Tactin XT Superflow Column equilibrated with 100 mM Tris 150 mM NaCl 1 mM EDTA pH 8. The column was washed with the same buffer to remove unbound protein. Protein bound to the column was then eluted with the addition of 40 mM biotin to the running buffer. Eluted protein showing absorbance at 410 nm was consolidated and concentrated in a 3 kDa Amicon Ultra Centrifuge filter from Merck to a volume of 1 mL before being injected Superdex 75 16/60 gel filtration column pre-equilibrated with 100 mM Tris 150 mM NaCl 1 mM EDTA pH 8.

3.3. Results

3.3.1. Optimization of Expression and Purification of ExtD

3.3.1.1. Expression of ExtD-His in Escherichia coli BL21

LB media containing 30 µg/mL kanamycin and chloramphenicol were inoculated with 1 % (v/v) *E. coli* BL21 containing *pMEGGAx_extD_HIS* and *pEC86* vectors were grown at 30 °C with 180 rpm shaking. When an OD₆₀₀ of 0.4 was reached samples were induced at 0 mM, 1 mM, 10 mM and 20 mM and harvested after 18 hours through centrifugation. Cells were lysed and analysed using SDS-PAGE and visualized through heme-linked peroxidase staining. The predicted size of full length ExtD_His with six heme cofactors incorporated is 27.7 kDa however no protein band was seen on the SDS-PAGE and expression of ExtD was inferred to not have occurred.

By shortening the induction time before harvesting from 18 hours down to 4 hours it was hoped that the presence of ExtD would be detected. Harvested cells

containing the *pMEGGAx_extD_HIS* were lysed and protein expression was determined using SDS-PAGE staining with peroxidase, *Figure 3.1*. A protein band when cells were induced with 10 mM arabinose was visualized around the 25 kDa molecular marker approximately the size that ExtD is expected to express. From this, it was confirmed that the *E. coli* cells were expressing *extD* but the cytochrome is potentially recognized as non native and the breakdown of ExtD begins at some point between 4 hours and 18 hours after initial induction of plasmid in the bacteria.

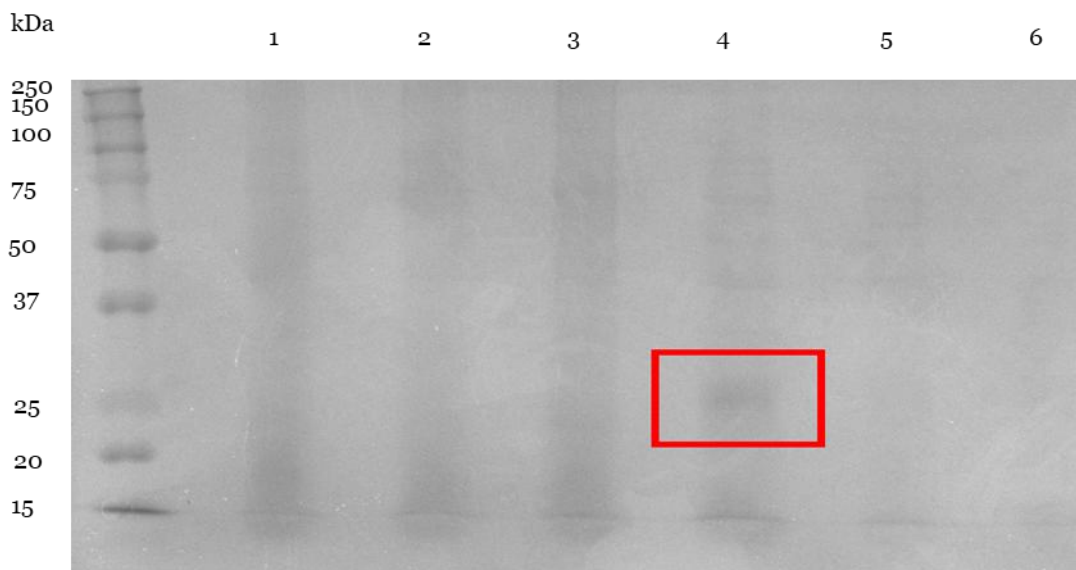


Figure 3.1- SDS-PAGE of whole cell E. coli BL21 containing vectors pEC86 and pMEGGAx_extD_HIS. Cells were harvested 4 hours post induction. 1) Control of E. coli BL21 pEC86 lacking pMEGGAx_extD_HIS. 2-6) E. coli BL21 transformed with pEC86 and pMEGGAx_extD_HIS induced with 2) 0 mM 3) 1 mM 4) 10 mM 5) 15 mM and 6) 20 mM. Visualisation of cytochromes performed by peroxidase-linked heme staining.

In order to determine the optimal induction time a new trial was set up growing *E. coli* BL21 cells at 30 °C with 180 rpm shaking to an OD₆₀₀ of 0.4 inducing with 10 mM arabinose. Bacteria cultures were then left to produce ExtD and harvested in intervals of 1 hour after initial induction. Harvested cells lysed and expression of ExtD analysed using SDS-PAGE visualising expressed cytochrome using peroxidase-like staining, *Figure 3.2*. The strongest cytochrome band observed was in lane 4 and corresponded to harvesting or induced bacteria after

4 hours. It was noted that band intensity in lanes 5 and 6 was decreasing, likely due to breakdown of ExtD and no band corresponding to ExtD expression was seen in the lane correlating to bacteria harvested 18 hours after initial induction time.

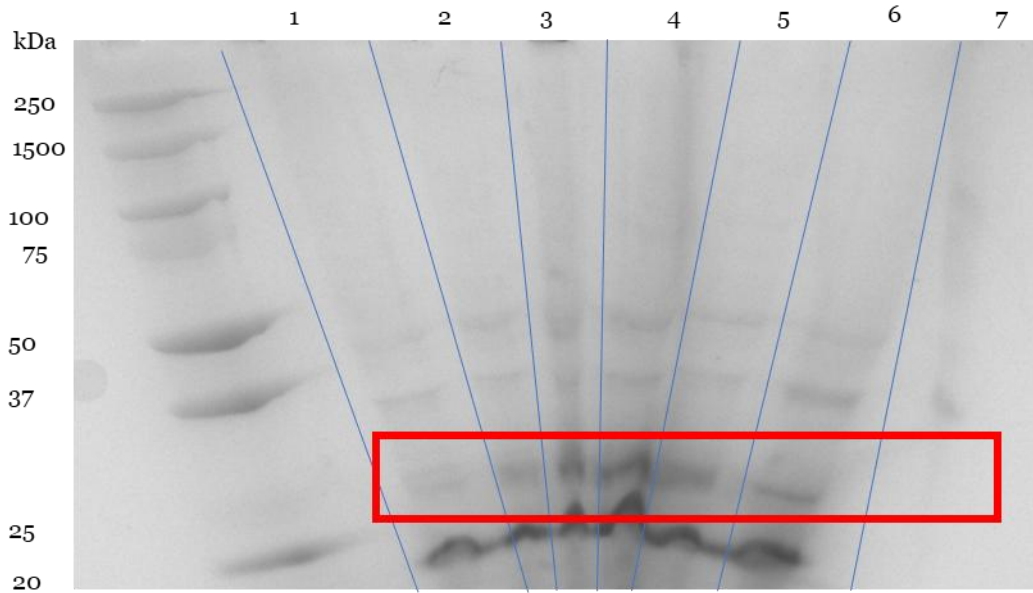


Figure 3.2- SDS-PAGE of whole cell *E. coli* BL21 cells expressing *extD*, visualised with peroxidase-linked heme staining. All cells induced with 10 mM of arabinose with cell harvesting staggered. Cells harvested after 1) 1 hour, 2) 2 hours, 3) 3 hours, 4) 4 hours, 5) 5 hours, 6) 6 hours and 7) 18 hours.

Expression of *E. coli* BL21 cells containing the *pMEGGAx_extD_HIS* vector was scaled up to 12 L in LB, 30 µg/mL kanamycin, with the aim of purifying ExtD from lysed cells. *E. coli* BL21 cells were grown at 30 °C with 180 rpm shaking, after being inoculated with 1 % (v/v) of *E. coli* BL21 containing *pMEGGAx_extD_HIS* grown overnight, until an OD₆₀₀ of 0.4 was reached at which point cells were induced with 10 mM of arabinose. Harvesting of cultures was performed 4 hours after induction by centrifugation at 3,000 xg. Harvested cells were resuspended in 100 mM Tris 150 mM NaCl pH 8 and DNase and cComplete EDTA-free Protease Inhibitor tablet from Merck. Resuspended cells were then lysed by use of the French press and soluble protein was extracted by ultracentrifugation at 200,000 xg. The supernatant from the ultracentrifugation run was collected and passed

through a HisTrap HP prepacked column from Cytiva. ExtD was eluted from the column using 300 mM of imidazole, monitored at 410 nm.

Fractions eluted from the HisTrap HP column (Cytiva) that showed absorbance at 410 nm were analysed using SDS-PAGE, *Figure 3.3*. SDS-gels were stained with a peroxidase-linked heme stain in order to visualise cytochromes present. A band corresponding to a cytochrome of an approximate weight of 25 kDa was visualised and believed to be ExtD. However, the concentration of ExtD was extremely low with some ExtD predicted to be lost during the purification process.

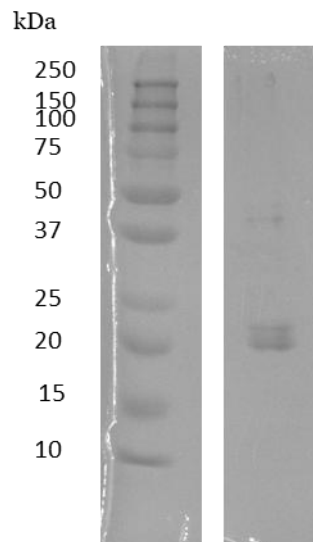


Figure 3.3- SDS-PAGE of heme containing fraction eluted from AKTA using a step elution profile. Hemes visualised through peroxidase-linked heme staining.

3.3.1.2. Expression of ExtD_His in *Shewanella oneidensis* LS527

The *pMEGGAx_extD_HIS* vector was electroporated into *S. oneidensis* LS527 and expression of ExtD was tested by growing at 30 °C in LB containing 30 ug/mL kanamycin. Cells were induced with arabinose, between 0 and 10 mM, when an OD₆₀₀ of 0.4 was achieved. Cells were harvested four hours after induction and lysed. Lysed cells were run on SDS gel, *Figure 3.4*, with expression of ExtD_His observed in lanes correlating to *S. oneidensis* LS527 containing *pMEGGAx_extD_HIS* induced with 2.5 mM and 5 mM of arabinose. This differs from the concentration seen to express the highest amounts

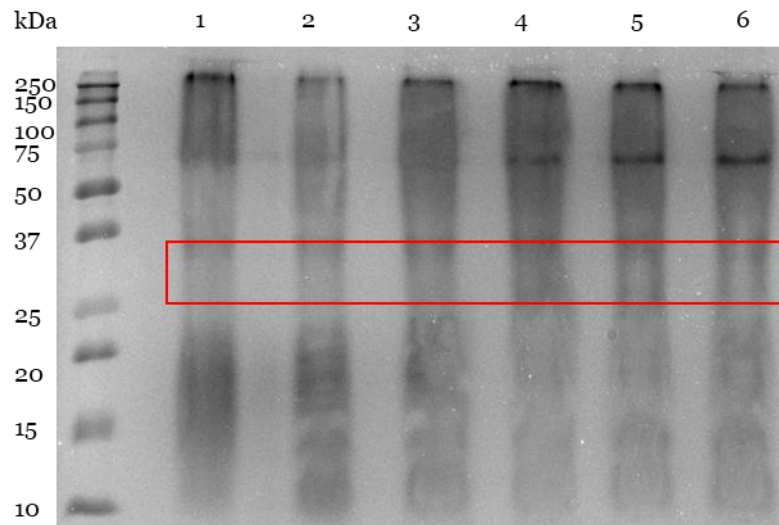


Figure 3.4- Whole cell expression of 1) *S. oneidensis* LS527 2-6) *S. oneidensis* LS527 containing *pMEGGAx_extD_His* trialling different concentrations of arabinose induction. 1-2) 0 mM arabinose 3) 1 mM arabinose 4) 2.5 mM arabinose 5) 5 mM arabinose 6) 10 mM arabinose. Visualised with peroxidase-linked heme staining.

It was determined that the induction of cells with 2.5 mM of arabinose was sufficient for protein expression and used in future expression trials. To find the optimal media for expression of ExtD_His *S. oneidensis* LS527 containing *pMEGGAx_extD_HIS* were grown in 100 mL aliquots of varied media; LB without supplements, LB containing 100 μ M Fe(III) citrate, M72 (Casein digest peptone 15 g/L, peptone digest of soybean 5 g/L and NaCl 5 g/L supplemented with 20 mM sodium lactate, 30 mM sodium fumarate and 20 mM HEPES) and Terrific Broth (yeast extract 24 g/L, tryptone 12 g/L and glycerol 4 g/L supplemented with 0.17 mM KH_2PO_4 and 0.72 K_2HPO_4). Bacteria were grown in the desired media following the optimised method as described above with whole cell lysate run on SDS-PAGE to determine which media yielded the highest quantity of ExtD_His, Figure 3.5.

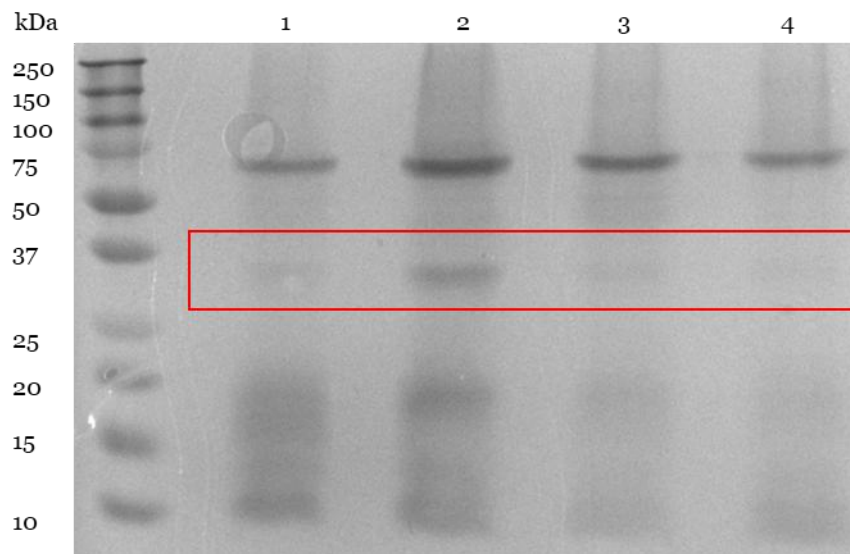


Figure 3.5- Whole cell expression of *S. oneidensis* LS527 containing *pMEGGAx_extD_His*, visualised with peroxidase-linked heme staining. Cells grown in 1) LB media 2) M72 media 3) Terrific Broth 4) LB media supplemented with 100 μ M Fe(III) Citrate. Highlighted in the red box is where *ExtD_His* is expected to be expressed.

A temperature trial was performed to determine the ideal temperature used to grow *S. oneidensis* LS527 containing *pMEGGAx_extD_HIS* for optimal expression of *extD*. *S. oneidensis* LS527 containing *pMEGGAx_extD_HIS* was grown in M72 media at 16, 25, 30, 37 and 40 °C until an OD_{600} of 0.4 was reached. Cells were induced with 2.5 mM of arabinose and harvested by centrifugation 4 hours later. Whole-cell SDS-PAGE was used to analysis cytochrome content of the cells, Figure 3.6, expression of *extD* proved to be minimal with the greatest amount of ExtD visualised from cells grown at 30 °C.

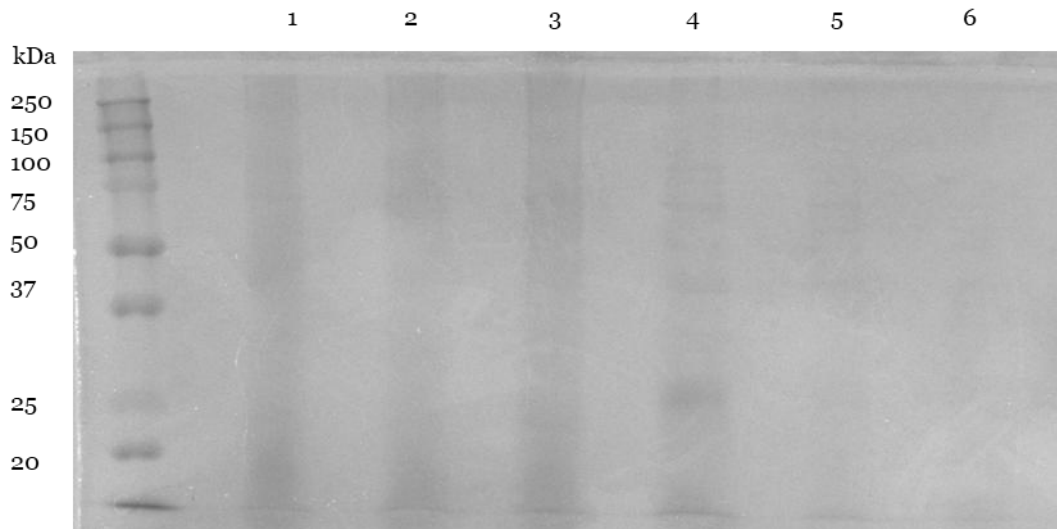


Figure 3.6- Whole cell expression of 1) *S. oneidensis* LS527 2-6) containing *pMEGGAx_extD_His*, visualised with peroxidase-linked heme staining. Cells grown in M72 media at 2) 16 °C, 3) 25 °C, 4) 30 °C, 5) 37 °C and 6) 40 °C.

Expression of *S. oneidensis* LS527 cells containing the *pMEGGAx_extD_HIS* vector was scaled up to 12 L of M72 media, 30 µg/mL kanamycin, with the aim of purifying ExtD from lysed cells. *E. coli* BL21 cells were grown at 30 °C with 180 rpm shaking, after being inoculated with 1 % (v/v) of *E. coli* BL21 containing *pMEGGAx_extD_HIS* grown overnight, until an OD₆₀₀ of 0.4 was reached at which point cells were induced with 2.5 mM of arabinose. Harvesting of cultures was performed 4 hours after induction by centrifugation at 3,000 xg using the Beckman J20 with the 8.1000 rotor.

3.3.1.3. Expression of ExtD_STREP in *Shewanella oneidensis* LS527

A different purification method for ExtD was trialed in an attempt to increase production of ExtD switching the His-Tag for a STREP-II tag. The *pMEGGAx* vector already includes the gene sequence encoding for a STREP-II tag, located at the 3' end of the *extD_HIS* gene separated by a STOP codon, therefore a simple PCR would achieve the removal of the encoded HIS tag. Primers were designed to be attached to the 3' end of *extD_HIS* and the 5' end of the sequence encoding the STREP-II tag so that amplification would generate linear DNA that was absent of

HIS-tag and the stop codon separating the extD and the STREP-II tag sequence. Amplification was analysed using gel electrophoresis, *Figure 3.7*. The expected size of the PCR product was 4,747 bp and bands corresponding to that size were visualized on the DNA agarose gel.

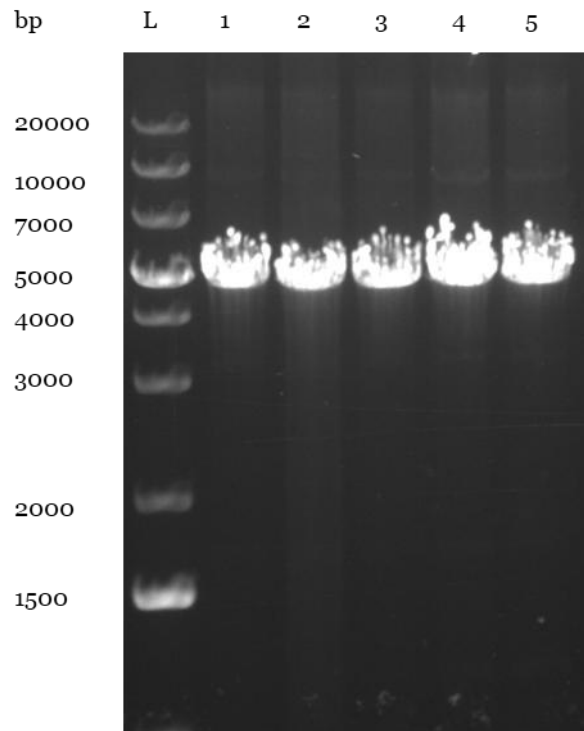


Figure 3.7- Agarose gel electrophoresis visualising PCR amplification for affinity tag switch of ExtD. Lanes 1-5 all show PCR reaction products. DNA visualised with ethidium bromide.

The linear DNA encoding *pMEGGAx_extD_STREP* was phosphorylated to allow for ligation of the blunt ends to generate circularised DNA. The product was then transformed into *E. coli* TOP10 cells. To confirm successful transformation *E. coli* TOP10 cells containing *pMEGGAx_extD_STREP* were grown in liquid LB, containing 30 µg/mL of kanamycin, overnight at 30 °C shaking at 180 rpm. The cultured cells were then miniprepmed to isolate the plasmid and products analysed by DNA gel electrophoresis, *Figure 3.8*. As previously stated, the expected size of *pMEGGAx_extD_STREP* was 4,747 bp. The agarose gel revealed DNA bands corresponding to a plasmid size between 3000 and 4000 bp. As the plasmids were now in a supercoiled state it is expected to run 'fast' on an agarose gel and therefore appear at a lower size. Between the four lanes, there was a

difference in size between the plasmids suggesting a difference in the backbone of the plasmid. Therefore, the only way to determine if any of the plasmids encoded the desired *pMEGGAx_extD_STREP* vector was to sequence each of them. Sequencing was performed through Eurofins using a primer complementary to the *pMEGGAx* vector, *pMEGGAx_seq_Rev*. Sequencing revealed that the plasmid visualized in Lane 4 of *Figure 3.8* had been successfully formed with the gene encoding *extD_STREP* successfully encoded within the vector.

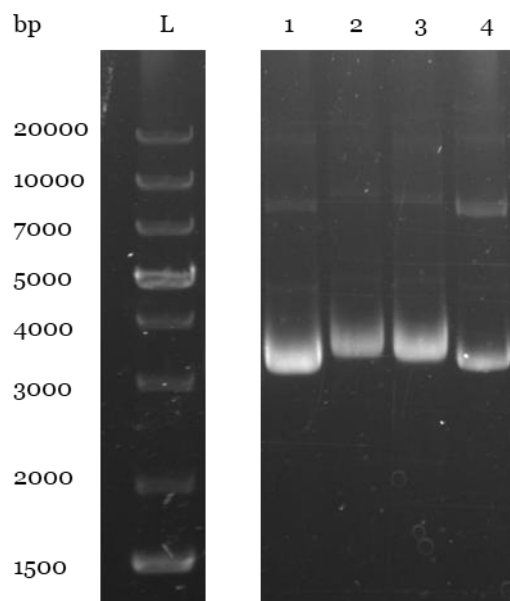


Figure 3.8- Agarose gel electrophoresis of re-circularised pMEGGAx_extD_STREP. DNA visualised with ethidium bromide

Following successful sequencing of the *pMEGGAx_extD_STREP* vector, the plasmid was electroporated into *S. oneidensis* LS527. Expression and purification of ExtD_STREP was performed following the optimised method for expressing ExtD_HIS. The protocol only differed in the use of affinity chromatography utilising a STREP-II tag affinity as opposed to HIS-tag affinity. The purity of ExtD_STREP was analysed through SDS-PAGE with visualisation of cytochrome from AKTA fractions performed using peroxidase-linked heme staining, *Figure 3.9*. As seen in the SDS-PAGE gel a cytochrome band correlating to the established molecular weight seen previously of ExtD_His, in line with the

molecular marker for 25 kDa. However, this band was extremely faint even after staining for >1 hour. This was suggestive of a low yield of ExtD_STREP.

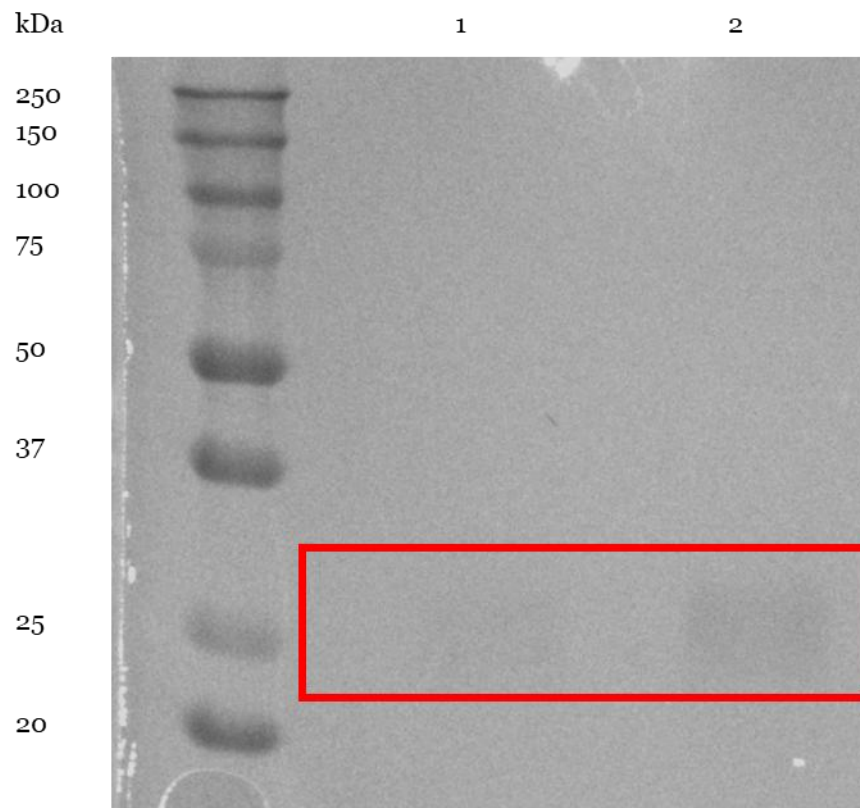


Figure 3.9- SDS-PAGE analysis of purified ExtD_STREP, visualized using peroxidase- linked heme staining. Both lane 1 and 2 contain ExtD_STREP in 1) dilute and 2) concentrated aliquots.

The quantity of cytochrome production between purification methods of ExtD_STREP and ExtD_HIS was compared to determine which method produced a higher concentration of cytochrome. This was assessed by purifying each form of ExtD from a 6 L culture of *S. oneidensis* LS527 containing relevant plasmid, *pMEGGAx_extD_STREP* or *pMEGGAx_extD_HIS*, were grown at 30 °C and induced with 2.5 mM of arabinose when an OD₆₀₀ of 0.4 was reached. Both cells were then lysed and ExtD purified from cell lysate utilising either STREP-II tag affinity or HIS-Tag affinity chromatography. The elution profile from each affinity chromatography run was recorded at 410 nm and compared to determine which method produced the highest yield of ExtD, Figure 3.10.

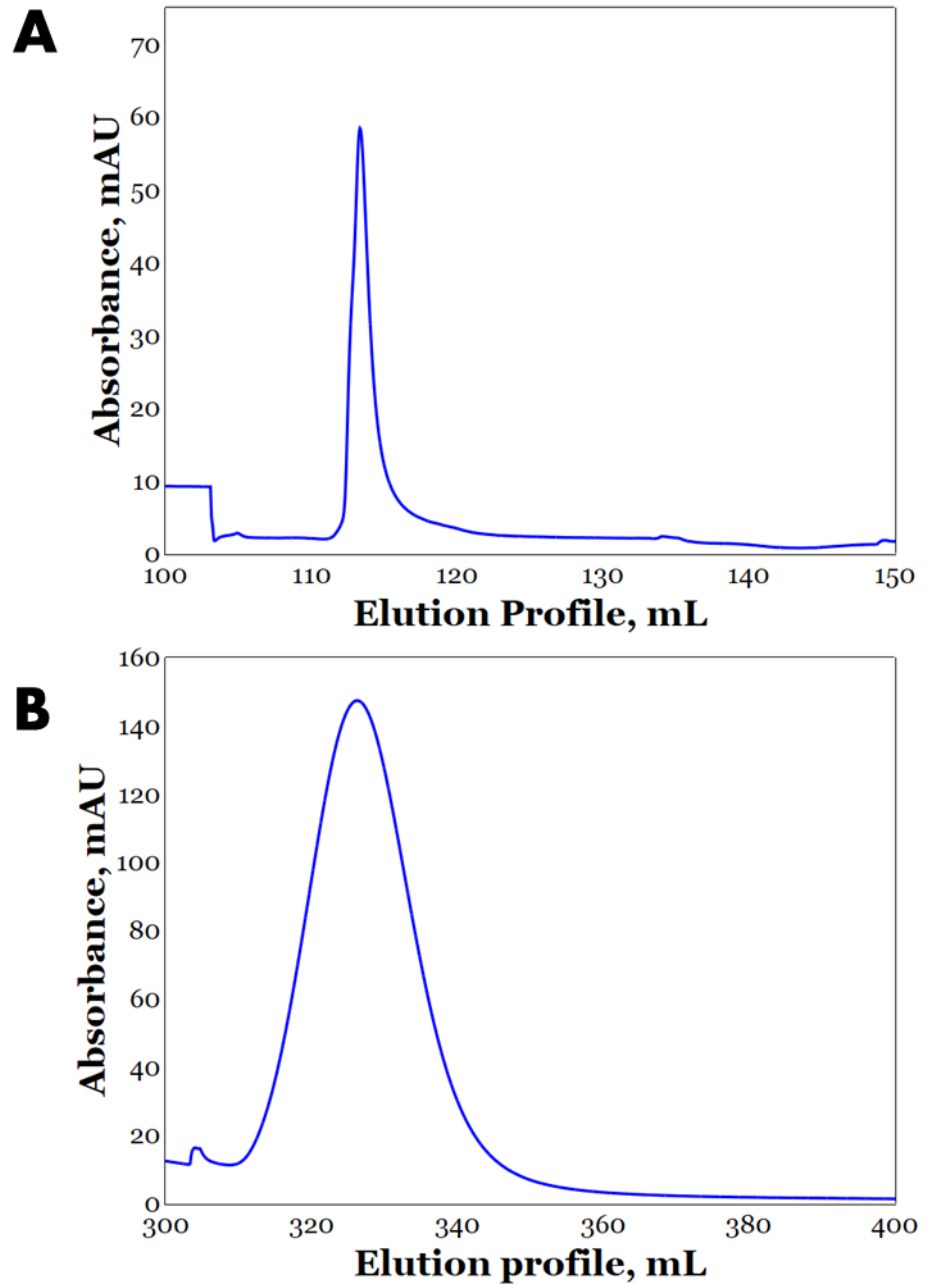


Figure 3.10- Elution profile from AKTA prime purifying A) ExtD_STREP and B) ExtD_His. Elution monitored in both cases using absorbance at 410 nm.

Elution of ExtD_STREP, Figure 3.10A, was observed over a small window of 3 mL with a peak maximum at an absorbance of 57. Comparatively, the elution profile for ExtD_His, Figure 3.10B, showed ExtD eluted across a larger window of 35 mL with a maximum peak absorbance at 146. Overall, the approximate area for each

elution peak was calculated and the purification of ExtD_His was shown to be approximately 30x greater than the purification of ExtD_STREP. Further optimisation of ExtD_STREP purification wasn't possible at this time and it was determined that the yield of ExtD_HIS was sufficient to move forward and begin protein characterisation. Any characterisation of ExtD discussed following is therefore of ExtD_HIS unless otherwise specified. The quantity of ExtD produced per 1 L of culture grown was calculated to be 2.8 ng.

3.3.2. Bioinformatical analysis of ExtD

The amino acid sequence of ExtD is shown in Figure 3.11 with predicted signal peptide and canonical heme binding motifs highlighted. The signal peptide, highlighted yellow in Figure 3.9, for ExtD was predicted using SignalP 5.0⁵ with cleavage of the signal peptide after Gly17. Therefore, the mature protein would have an N-terminus Cys residue which is expected to form a lipid anchor, covalently binding ExtD to the outer membrane of *G. sulfurreducens* PCA. Predictions of the heme axial ligands can be drawn knowing that the most abundant distal axial ligand for a heme cofactor is His⁶. ExtD contains an additional six histidine residues, highlighted pink in Figure 3.11, that are not a part of the CxxCH motif, signifying the possibility that all six hemes would have bis-His ligation. Sequence alignment using BLAST⁷ yielded 34 homologs of ExtD predominately from the *Geobacter* genus, with no similarity found to proteins from the *Shewanella* genus. Figure 3.11 additionally shows a sequence alignment of ExtD alongside homologs from five different bacteria, alignment generated using Clustal Omega⁸. The CxxCH motif, blue in Figure 3.11, is shown to be highly retained throughout all sequences and it is only the fifth CxxCH motif present in the homologues sequences that do not align with ExtD from *G. sulfurreducens*. Also highly conserved were the six histidine residues expected to act as heme distal ligands. Interestingly, tandem repeated histidine residues at position 177 and 178 in the *G. sulfurreducens* sequence were highly conserved in all homologs yet the probability that both behave as heme axial ligands is low due to the proximity the heme cofactors would have to be in to maintain the coordination.

Da⁹). Through LC-MS the mass of ExtD was experimentally determined to be 27,680.98 Da. The experimental mass matches the predicted mass very closely, differing by 5.71 Da, with the variance in mass predicted to be caused by variation in the protonation state of ExtD.

The biophysical properties of ExtD in solution sedimentation velocity (SV) was performed on a sample of ExtD at 1.17 μ M in 50 mM Tris, 100 mM NaCl, and 1 mM EDTA at pH 8. Sedimentation was monitored at 410 nm, using the Beckman Optima XLA-I analytical ultracentrifuge. The viscosity and density of the buffer were calculated to be 1.0274 cp and 1.00405 g/mL at 20 °C using SEDNTERP¹⁰ and the partial specific volume used for ExtD was estimated from the AlphaFold model using US-SUMO¹¹ at 0.745 mL/g.

A $c(s)$ distribution was generated by fitting data to the Lamm equation using SEDFIT¹², *Figure 3.12*. Revealing a single homogeneous species with a single sedimentation coefficient normalised to a S_{w20} of 2.49 S. The molecular weight corresponding to this sedimentation peak was estimated by SEDFIT using the Svedberg equation. The molecular mass attributed to this sedimentation peak was 30.3 kDa. This mass was larger than expected, however SV only provides an estimate for the molecular mass of an analyte and whilst theoretically should provide an accurate definition of molecular mass small inconsistencies in buffer density and temperature can cause an increased error¹³. The $c(s)$ analysis of ExtD in solution additionally confirmed a monomeric protein with a frictional coefficient (f/f_0) of 1.19. The f/f_0 is used to compare the shape of a protein (f) to that of a perfect sphere (f_0) and therefore a f/f_0 of 1 would indicate a protein that is a perfect sphere with increasing f/f_0 ratios describing a protein that is more elongated at the poles. An f/f_0 ratio of 1.19 would indicate that ExtD is globular in appearance.

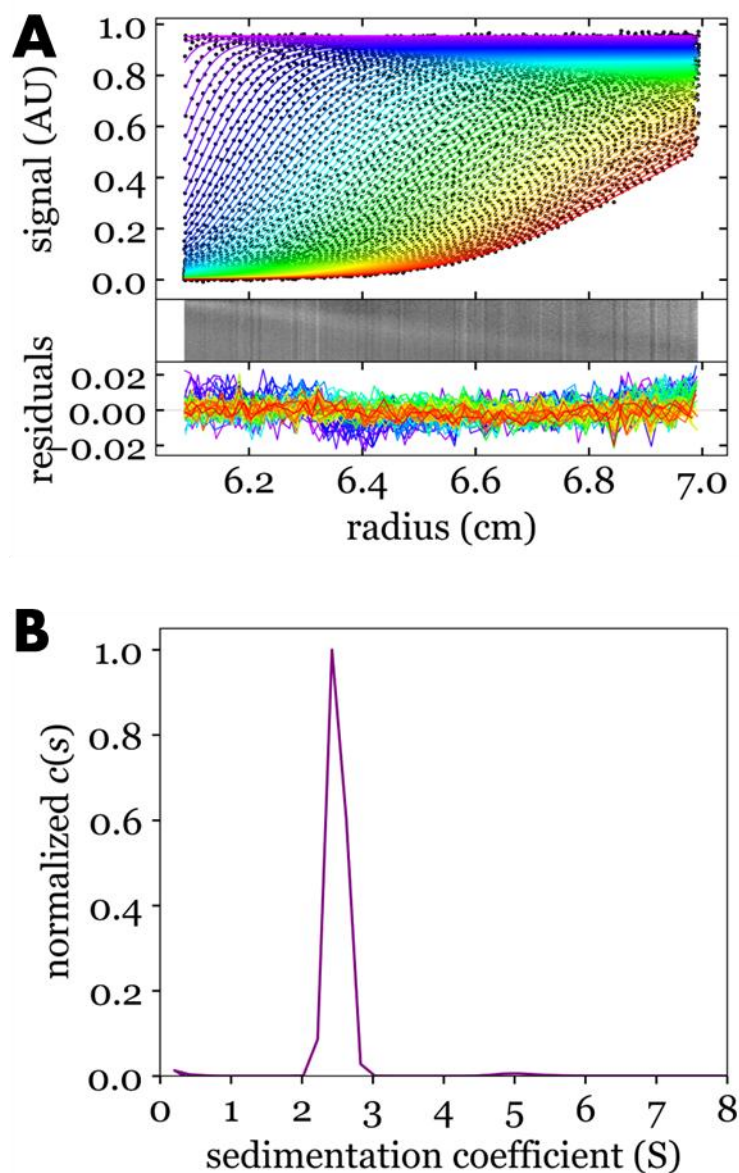


Figure 3.12- Sedimentation velocity analysis of ExtD.

3.3.4. Computational Characterisation of ExtD

AlphaFold 2¹⁴ was used to produce a structural model for ExtD, Figure 3.13, as AlphaFold 2 is not able to model cofactors, hemes were manually inserted by aligning a c-type heme from the *Shewanella algae* periplasmic cytochrome STC (PDB ID: 6HR0)¹⁵ to the CxxCH motifs of the ExtD model. For every model generated using AlphaFold each residue in the protein sequence is ascribed a predicted local distance difference test (pLDDT), between 0 and 100 %, describing the relative confidence of each amino acid residue modelled. The

pLDDT score is based on the local distance difference test $C\alpha$ (IDDT- $C\alpha$) comparing how accurately a model would conform with an experimentally determined structure^{14,16}. Using the pLDDT the AlphaFold model can be coloured to show areas of the model that have the highest and lowest pLDDT score. This is shown on the ExtD model by using a colour range of yellow, pLDDT score of 0, to magenta, pLDDT score of 100. The average pLDDT for an AlphaFold model can be calculated to gain insight into the overall probability of an accurate model. The model of ExtD had an average pLDDT of 54.0 %, which is an extremely low score for an AlphaFold model. Validation of AlphaFold models has been shown by comparing experimentally solved structures to AlphaFold simulations, in which the experimental structure was not a part of the dataset for protein simulation. In these cases, it was shown that simulations had pLDDT scores of individual residues higher than 95 % correlating to being within 0.85 – 1.16 Å of the experimentally determined structure¹⁴. Therefore, the ExtD simulation having an average pLDDT score of 54.0 % is suggestive of an incorrect structure that does not accurately depict the real structure.

The model is further shown to be inaccurate with the manual insertion of the six heme cofactors. Whilst AlphaFold has successfully positioned the CxxCH motives so that the cysteines would form a thioether bond with the vinyl groups of the hemes and the histidine is correctly positioned to act as the proximal distal ligand, the spatial coordinates were incorrect. This is seen when manual insertion of the hemes caused overlap in Hemes 1 and 2 as well as Hemes 4 and 5. Whilst the AlphaFold 2 is an inaccurate model for ExtD possibilities of the distal heme axial were shown. Interestingly, whilst the amino acid sequence contains enough histidine residues for all hemes to be bis-His ligated only hemes 1,2,4 and 5 show bis-His coordination. Heme 3 shows the possibility of His/Tyr coordination, an atypical heme coordination only seen in 1.1 % of heme coordination existing in the PDB⁶, which would be associated with a lower redox potential than a His/His ligated due to Lewis's acid theory¹⁷. The possibility of the His/Tyr coordination is also shown through the sequence alignment of ExtD homologues, *Figure 3.9rver*, were Tyr93 is highly conserved between all

sequences. Heme 6 is modelled as a His/- coordinated heme, with no obvious axial ligand in the surrounding environment.

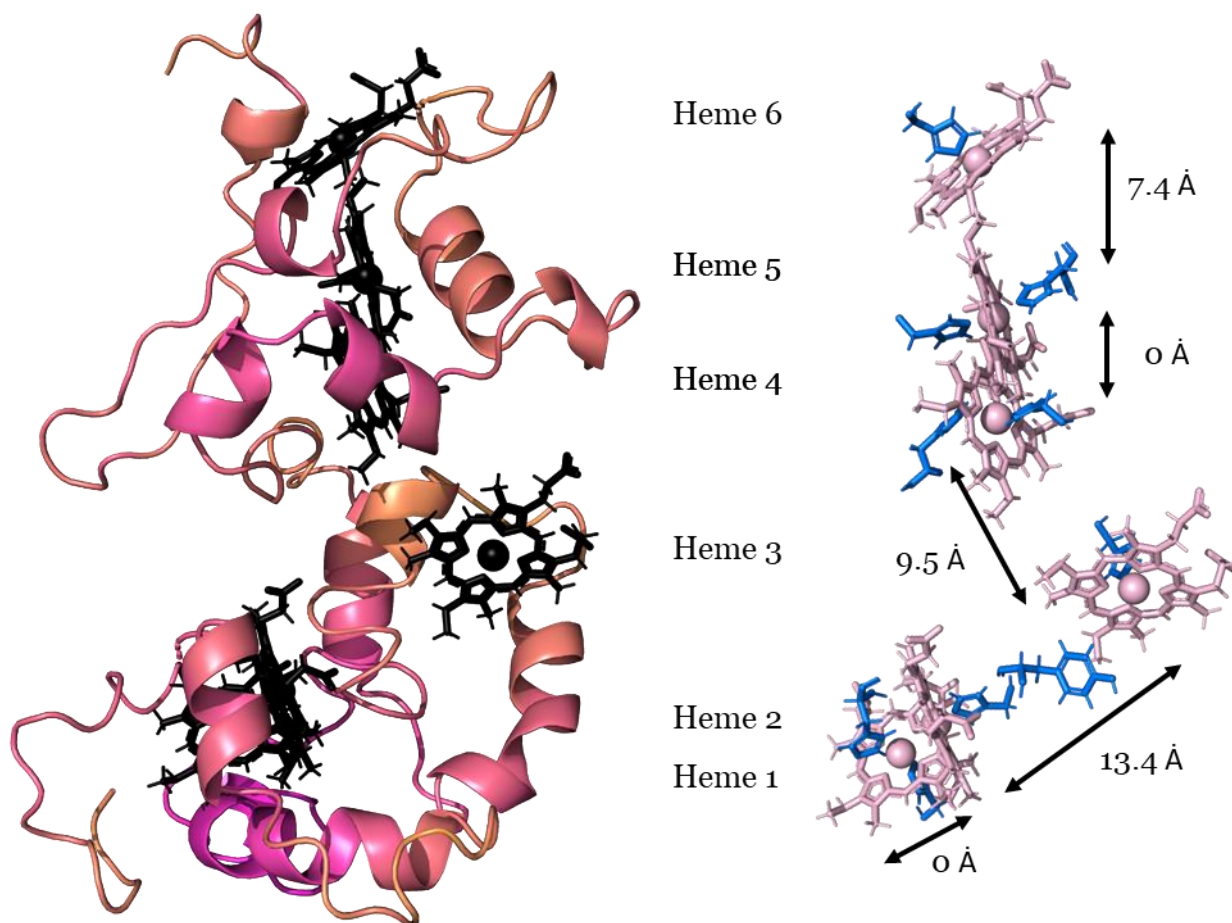


Figure 3.13- AlphaFold 2 model of ExtD. A) Cartoon representation of ExtD coloured by pLDDT score from 0 % (yellow) to 100 % (magenta). Hemes coloured black as have not been assigned a pLDDT score B) Predicted heme arrangement of ExtD from the AlphaFold 2 simulation.

In contrast, the newly available AlphaFold 3¹⁸ was also used to generate a structural model for ExtD. Whereas AlphaFold was not able to also simulate cofactors, AlphaFold 3 is now capable of modelling numerous cofactors, including c-type hemes, removing the need for manual insertion of cofactors. The AlphaFold 3 model is shown in *Figure 3.14* and has an average pLDDT of 72.5 %, a drastic increase in confidence from the AlphaFold 2 simulation. Whilst the AlphaFold 2 model generated a more linear protein the AlphaFold 3 model is more globular in shape, which aligns with results from sedimentation velocity analysis. All hemes, bar Heme 2, were predicted to be bis-His coordinated, with

Heme 2 showing His/- coordination. Interestingly, Heme 5 and 6 would be distally coordinated by adjacent His residues, His177-178, which brings the heme cofactors into close proximity to each other. Unsurprisingly the pLDDT scores associated with Hemes 5 and 6 are the lowest of the cytochrome.

The predicted arrangement of the heme cofactors in the AlphaFold 3 model does not conform to the canonical t-shaped and stacked heme packing seen in the majority of MHCs ¹⁹. Hemes 1-3 all show typical heme packing, specifically stacked hemes, between Heme 3 and Heme 4 the packing is predicted to be T-shaped. However, between Heme 4 and Hemes 5 there is a potential break in the heme chain with a heme edge to edge distance of 9.3 Å, close to the proposed limit of 10 Å. Heme cofactors of other well characterised MHCs are typically closely packed, < 5 Å in edge-to-edge distances, allowing for rapid electron transfer ^{20,21}. Therefore, the spatial separation of hemes predicted in ExtD through AlphaFold 3 may suggest a slower electron transfer rate.

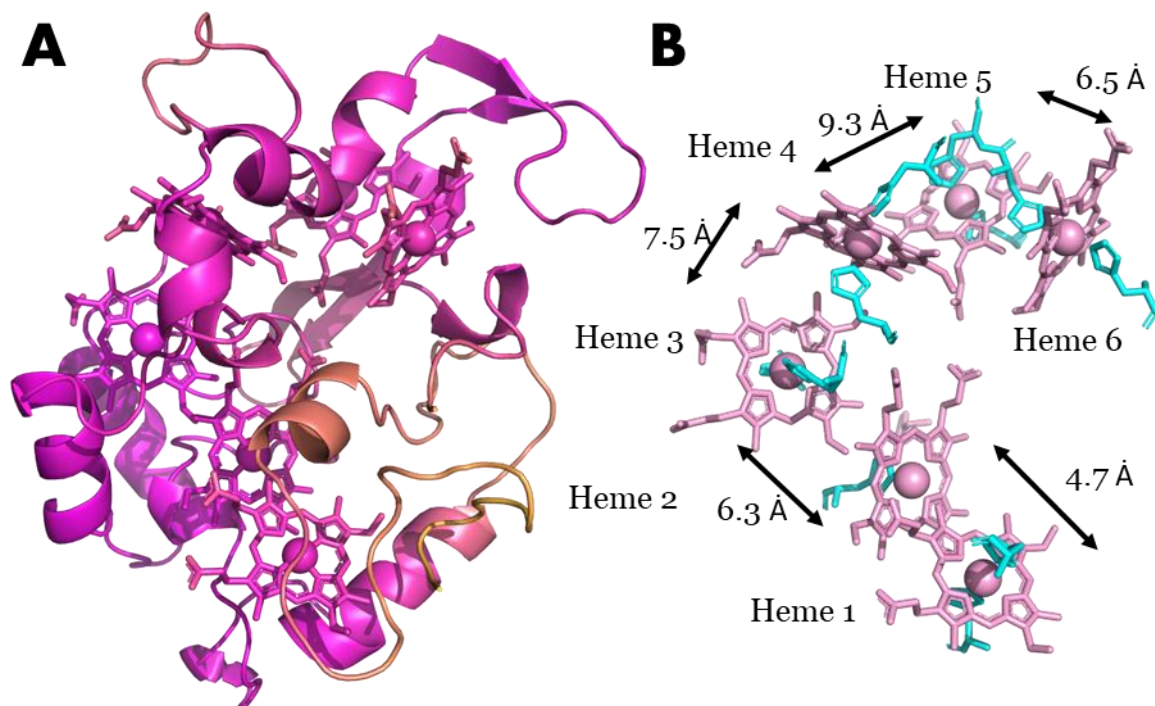


Figure 3.14- AlphaFold 3 model of ExtD. A) Cartoon representation of ExtD coloured by pLDDT score from 0 % (yellow) to 100 % (magenta). B) Predicted heme arrangement of ExtD from the AlphaFold 3 simulation.

Comparison of each heme cofactors total solvent accessible surface area differs considerably between the AlphaFold 2 and 3 models. From the AlphaFold 2 model Heme 6 is predicted to have a high solvent accessible surface area (SASA), determined using Areaimol^{22,23} of 422.6 Å². This corresponds to 51.2 % of the heme being solvent accessible. This is likely an artefact of an inaccurate model produced by AlphaFold 2 as the SASA for heme cofactors described as 'exposed' is generally seen as 37 % and above²⁴. Increasing SASA above this is potentially detrimental to the attachment of heme cofactors which are hydrophobic. The remaining hemes have comparatively low SASA, *Table 3.1*, with only Heme 3 showing an increased SASA, suggesting a possible site for oxidation/reduction of ExtD. Hemes 1 and 2 have the lowest SASA, in the AlphaFold 2 model. They therefore would be buried deep in the protein and likely unable to interact with compatible redox partners outside of the ExtD protein. In contrast, heme SASA predicted from AlphaFold 3 model of ExtD have, on average, a decreased SASA. Heme 1 is now predicted to have a surface area were 16.9 % is solvent accessible, making it a likely site for redox interaction with the ExtABC complex and/or terminal electron acceptors. Heme 6 is still shown to have a high SASA, however it is decreased from the AlphaFold 2 prediction and now is within accepted levels of heme exposure.

Table 3.1- ExtD solvent accessible surface area of heme cofactors from AlphaFold models

Heme Number	AlphaFold 2		AlphaFold 3	
	Solvent Accessible Surface Area, Å ²	Percentage of Heme Solvent Accessible, %	Solvent Accessible Surface Area, Å ²	Percentage of Heme Solvent Accessible, %
1	38.3	4.6	139.4	16.9
2	38.2	4.6	30.8	3.7
3	384.4	42.2	153.4	18.6
4	114.0	13.8	234.4	28.4
5	110.7	13.4	118.8	14.4
6	442.6	51.2	192.1	23.3

Using US-SOMO ¹¹ the AlphaFold models can be compared to experimentally determined biophysical data. US-SOMO predicts that the AlphaFold 2 model for ExtD would have a f/f_0 ratio of 1.27 and a sedimentation coefficient of 2.38 S, whilst the AlphaFold 3 model is predicted to have a f/f_0 ratio of 1.17 and a sedimentation coefficient of 2.78 S. close to the parameters determined by SV of 1.19 and 2.49 S. The predicted sedimentation coefficients of both the AlphaFold models diverge from the experimentally determined value. The predicted frictional coefficient of the AlphaFold 3 model is close to the experimentally determined value whilst the AlphaFold 2 model f/f_0 prediction is much higher. This likely suggests that whilst both models have been unable to fully represent the native structure of ExtD the AlphaFold 3 model is likely a more accurate representation in terms of globular shape.

The AlphaFold models were compared to the previously published structures using PDBeFold, to assess if there were any structurally similar proteins that had

a divergent amino acid sequence. However, PDBeFold did not find any structural homologues in the PDB with a significant structural similarity.

3.3.5. Electronic Paramagnetic Resonance

Protein samples of ExtD were sent to collaborators at Essex University, UK, where electronic paramagnetic resonance (EPR) was kindly carried out by Dr Dimitri Svistunenko. Shown in *Figure 3.15* is the EPR spectrum for ExtD, analysed to show the g-factor signals. The EPR signal at $g = 4.30$ suggests that the Fe centres of the heme were in a low spin conformation, $S = 1/2$, with no evidence suggesting the presence of a high spin heme. The signal at $g = 3.0$ is also consistent with cytochromes that were bis-His coordinated. There was no suggestion of a high spin ($S = 5/2$) heme centre. The EPR data suggests that all hemes were of the same conformation with no evidence of distinct groups of hemes.

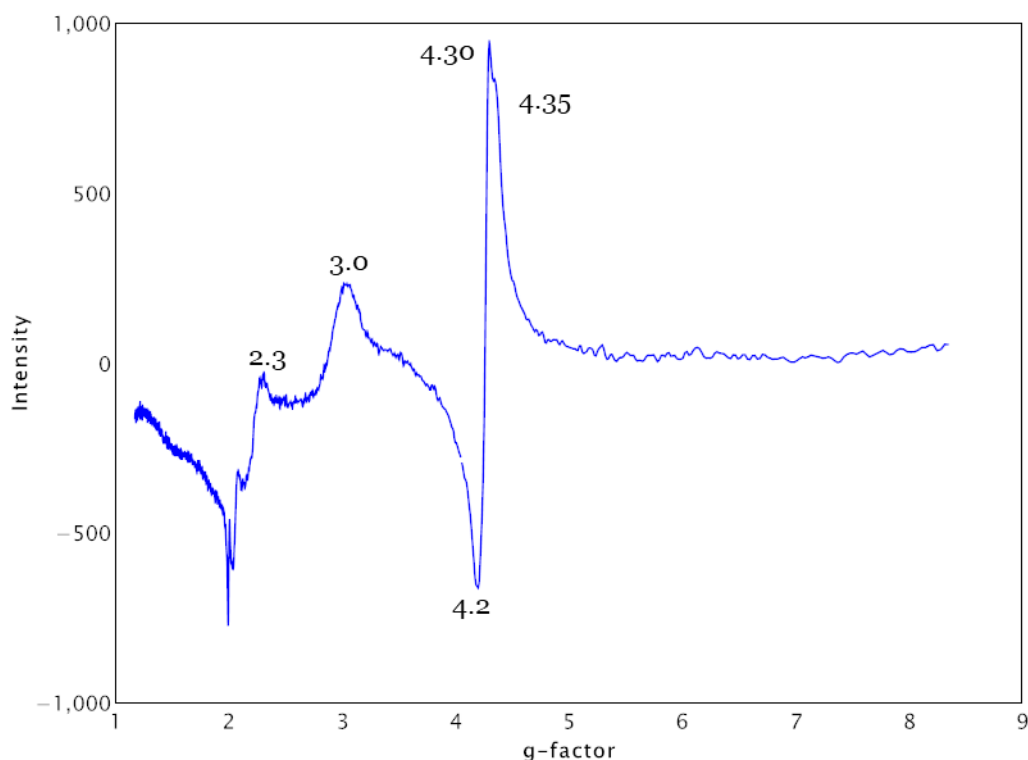


Figure 3.15- Low temperature, 10 K, EPR spectrum of ExtD.

3.3.6. UV-Visible spectroscopy

Purified ExtD was investigated using UV-Vis between the wavelengths 350-800 nm. ExtD was characterized in air oxidised conditions and reduced with 10 mM sodium dithionite (-660 mV vs SHE)²⁷, *Figure 3.16A*. The spectra of ExtD displays a broad oxidised Soret with peak maxima at 410 nm and a reduced split Soret with peak maxima at 417 nm and 423 nm. Splitting of a reduced Soret band is not a typical feature found in literature, with known multiheme cytochromes showing a single reduced Soret peak. The presence of a reduced split Soret has been observed in nature only a handful of times, with no definitive explanation given to explain this feature²⁸⁻³⁰.

To further investigate this unique feature sodium dithionite was titrated into an oxidised sample of ExtD under anaerobic conditions *Figure 3.16B*. With the addition of dithionite, a shift in the Soret is first originally seen from 410 nm to a reduced Soret at 423 nm, and an increasing concentration of dithionite reveals the peak at 417 nm. This staggered reduction of the hemes suggests a significant difference in the reduction potential of the hemes. Using the AlphaFold models as a prediction for the heme axial ligands four of the hemes are predicted to have bis-His coordination with Heme 3 being His/- or His/Tyr and Heme 6 being His/- the presence of a higher potential hemes would be attributed to the bis-His coordinated hemes and the lower potentials a result of Heme 3 and 6.

The extinction coefficient of ExtD was determined using the pyridine hemochromagen assay, a common method for determining the extinction coefficient based on the known extinction coefficient of bis-pyridine ligated heme²⁵. Spectra of ExtD in native; 100 mM Tris, 150 mM NaCl, 1 mM EDTA pH 8; and denatured; 50 mM Tris, 75 mM NaCl, 0.5 mM EDTA, 0.1 M NaOH, 20 % (v/v) pyridine pH 8; forms were recorded between 350-800 nm. For both samples recorded spectra were recorded under air oxidised and reduced with 10 μ M sodium dithionite. The difference spectrum of the reduced minus oxidised spectra was calculated from denatured ExtA and using the literature value for a

bis-pyridine ligated c-type heme of $\epsilon_{550-535} = 23.97 \text{ mM}^{-1}\text{cm}^{-1}$ ²⁶, the extinction coefficient was calculated for a cytochrome containing 6 hemes, $\epsilon_{550-535}$ therefore being $143.82 \text{ mM}^{-1}\text{cm}^{-1}$. For spectra recorded in this analysis concentration of ExtD was calculated to be $1.4 \text{ }\mu\text{M}$. As the denatured and native concentrations are the same the extinction coefficients of native oxidised ExtD can be calculated. Of key note and used for all concentration calculations hereafter in the ϵ_{410} which was determined to be $688.94 \text{ mM}^{-1}\text{cm}^{-1}$. The spectra of ExtD denatured by pyridine is shown in *Figure 3.16C*. Interestingly, the spectra of denatured ExtD treated with sodium dithionite no longer displays a split-Soret. Under these conditions all heme distal axial ligands are predicted to be pyridine, suggesting that the axial ligands of the heme cofactors are the potential cause of the split Soret in ExtD.

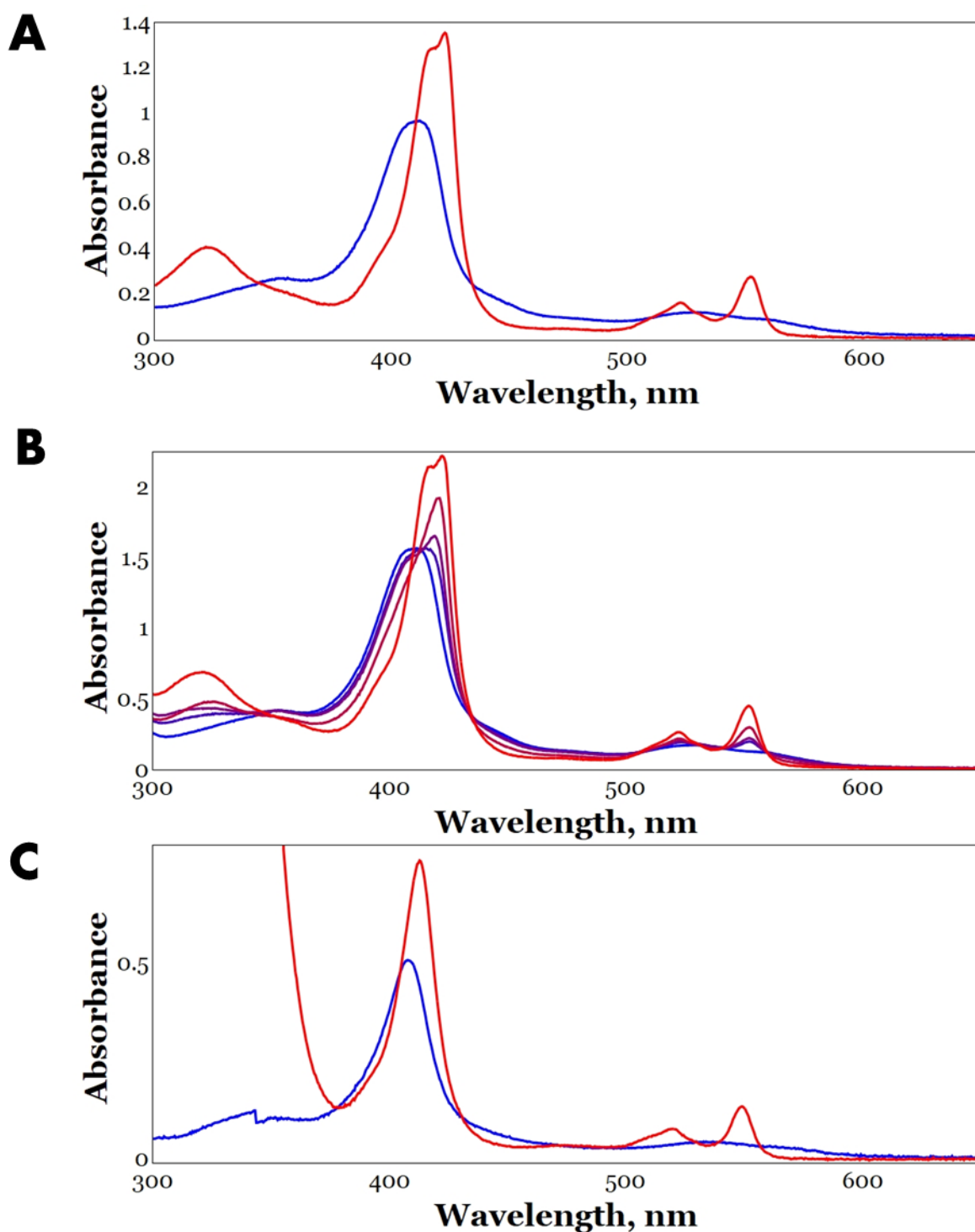


Figure 3.16- A) UV-Visible spectra of ExtD under air oxidised and reduced by 10 mM sodium dithionite conditions. Spectra were taken between 350 and 800 nm. B) UV-Visible spectra of ExtD with increasing concentrations of sodium dithionite. C) UV-Visible of spectra denatured ExtD in 50 mM Tris, 75 mM NaCl, 0.5 mM EDTA, 0.1 M NaOH, 20 % (v/v) pyridine pH 8, under oxidised and reduced conditions. For all spectra A-C) colour spectrum blue to red, oxidised to reduced protein.

By analysing spectra gathered through the dithionite titration experiment the rise of the split Soret feature can be mapped. By ranking the spectra from oxidised to reduced, the most oxidised spectrum was subtracted from the 2nd most oxidised. This pattern was followed throughout with the final difference spectra formed from the 2nd most reduced spectrum being subtracted from the fully reduced spectrum, *Figure 3.17*. Features are revealed through the difference spectra showing the impact the increase of the reducing agent sodium dithionite has on the cytochrome ExtD. With a minimal reducing agent it is seen that the formation of the reduced Soret peak at 423 nm is the first to form, and by increasing the concentration of reductant further formation of the 423 nm Soret peak is observed. It is only with the highest amount of reducing agent present that the Soret peak at 417 nm is observed and the split Soret formed. Further addition of reducing agent after this point showed no changes.

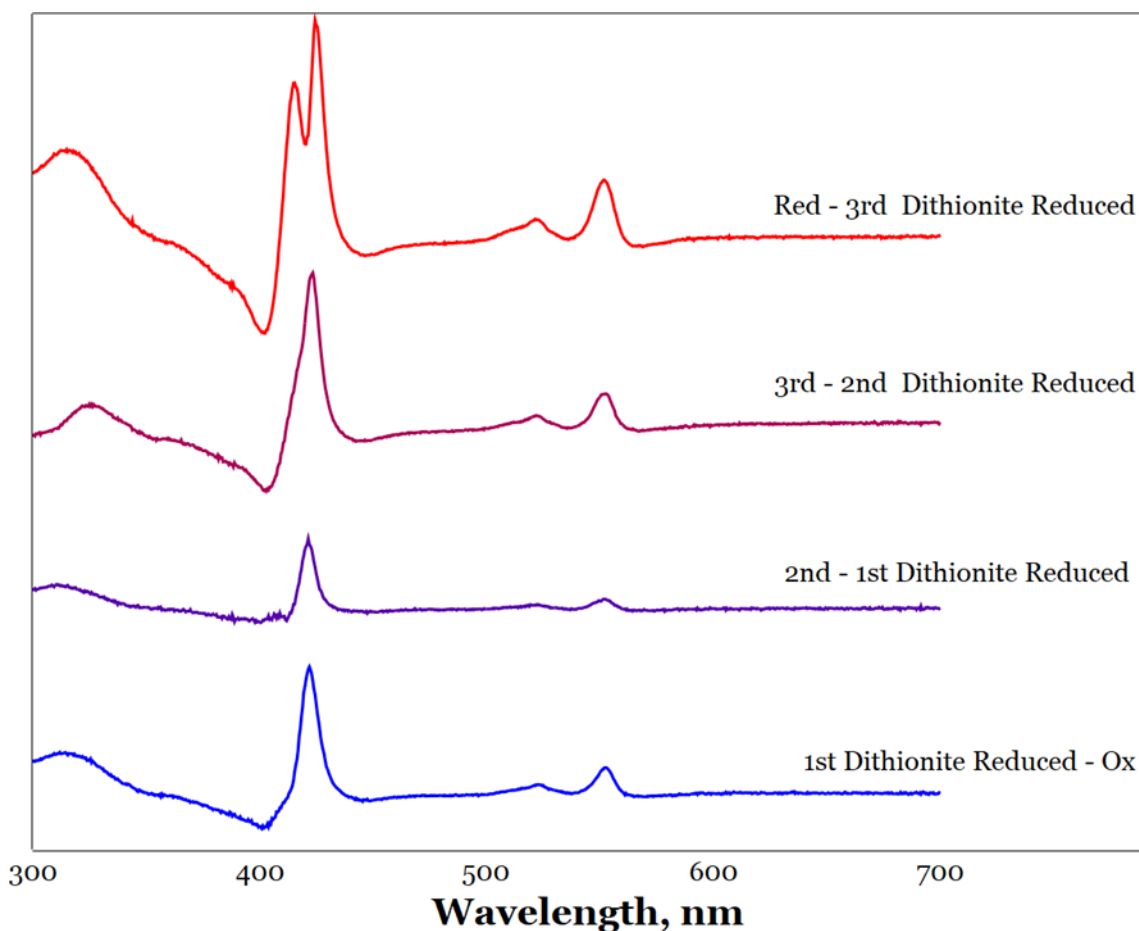


Figure 3.17- Difference spectra of ExtD. Spectra derived from sodium dithionite titration.

3.3.7. Protein Film Voltammetry

Determination of the reduction potential of ExtD was conducted through protein film voltammetry (PFV) using optically transparent indium tin oxide (ITO) electrodes. ExtD was absorbed onto the ITO electrode by drop casting 30 μM of ExtD in 50 mM Tris pH 8. ExtD was left to absorb onto the ITO electrode for >15 minutes, incubating on ice. ITO electrode with absorbed ExtD was connected to a three electrode system in a nitrogen filled chamber. A control electrode of a platinum wire and a reference electrode of a Ag/AgCl wire (saturated in KCl) were also connected to a potentiostat. Data was collected by performing potential sweeps from 0 V to -0.8 V vs Ag/AgCl reference electrode across a pH range of 6-9. For each pH data was collected at a scan rate of 2, 1, 0.5, 0.2 and 0.1 V/s. In order to convert voltage from vs Ag/AgCl to vs SHE data was shifted

by +195 mV. Before absorption of ExtD to ITO electrodes a PFV was run using a blank electrode in order to define the non-Faradaic current. Shown in *Figure 3.18*, is the bare electrode overlaid with ExtD adsorbed electrode at pH 8.

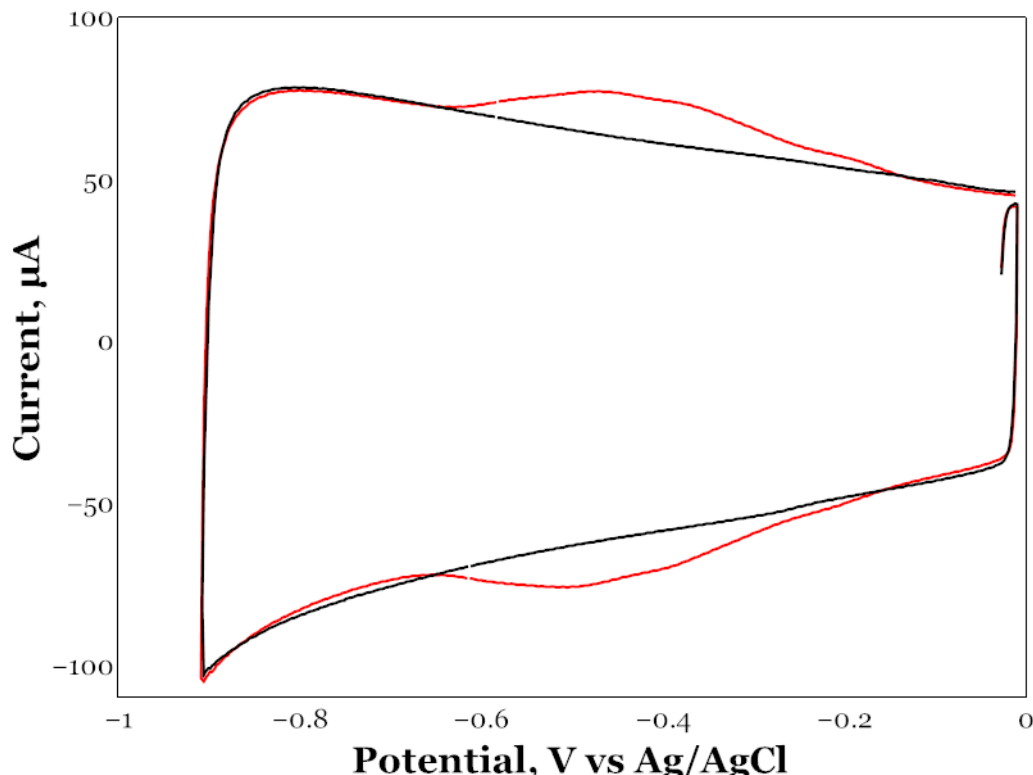


Figure 3.18- PFV performed of bare ITO electrode (black) overlaid with ExtD adsorbed ITO electrode (red). PFV performed in 50 mM Tris, 150 mM NaCl pH8, scan rate 0.1 V/s

Data was analysed using QSoas³¹ with the non-Faradaic current calculated from the bare electrode and manually removed from ITO with ExtD adsorbed electrodes. This gave rise to voltammograms that showed only the Faradaic current attributed to the potential of ExtD, *Figure 3.19*. The potential window for ExtD was seen to be between 0 V and -0.5 V vs SHE, over all four pH's tested. At lower pH's ExtD was shown to have a more positive potential, at pH 6 the redox window is seen between 0 V and -0.4 V, whilst with increasing pH the redox window shifts towards more negative potentials, at the highest pH the redox window is between -0.1 V and -0.5 V. This trend towards negative potentials with increasing pH is to be expected due to the deprotonation of proteins at higher pH leading to an overall net negative charge. As the method used to generate ITO electrodes does not result in a uniform layering of ITO nanoparticles the

electroactive coverage cannot be determined. However, the moles of redox active cofactor can be determined from the area of the individual oxidative or reductive voltammograms. Using this equation, it was determined that 45.6 ± 2.2 pmol ($n= 32$) of redox active cofactor had been adsorbed onto the ITO electrode.

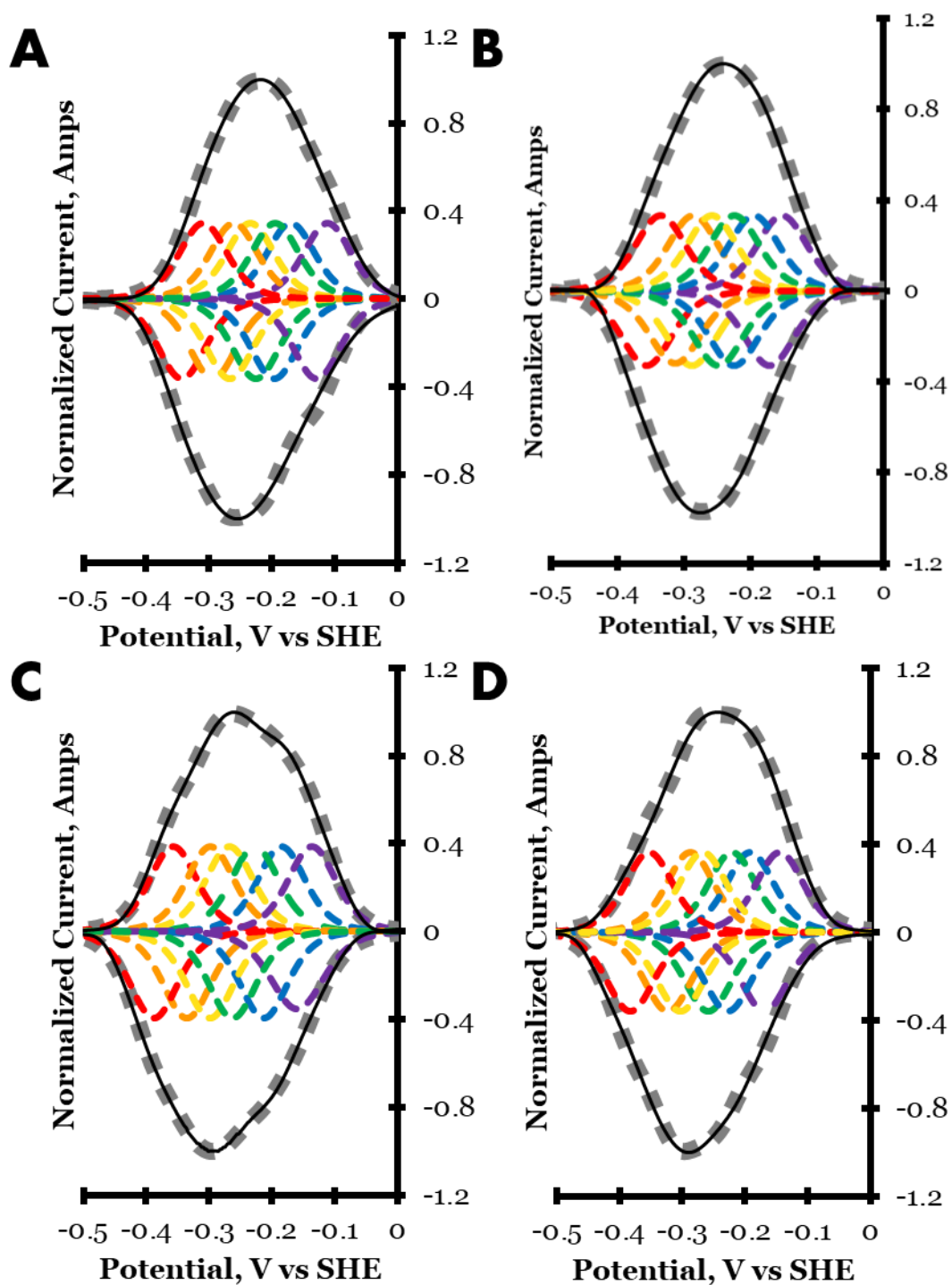


Figure 3.19- Cyclic Voltammograms of ExtD absorbed onto fluorine-doped tin oxide glass coated with indium tin oxide at pH 6, 7, 8 and 9. Scan rate of 0.1 V/s used for all shown voltammograms. Solid black line shows recorded current whilst varying voltage alongside the fit, grey squares, formed from the combination of six equal 1 electron centres, coloured dashed lines.

The peak potential recorded through PFV are noted in *Table 3.2*. Between each modelled $n=1$ redox centre there was an average of 20 mV shift in negative potential moving from pH 6 to pH 8. Between pH 8 and pH 9 there are minor differences noted in the potentials of the modelled $n=1$ centres with the majority of midpoints simulated to be identical. This is likely a factor of the redox-Bohr effect with little to no differences in the protonation of heme cofactors and surrounding residues therefore not allowing for an increased stabilisation of charge³².

Table 3.2- Midpoint potentials of simulated $n=1$ redox centres mapped to PFV of ExtD at varied pH

pH	6	7	8	9
Centre 1 Midpoint Potential, V	-0.326	-0.346	-0.373	-0.368
Centre 2 Midpoint Potential, V	-0.28	-0.3	-0.32	-0.31
Centre 3 Midpoint Potential, V	-0.251	-0.273	-0.284	-0.285
Centre 4 Midpoint Potential, V	-0.21	-0.236	-0.246	-0.24
Centre 5 Midpoint Potential, V	-0.183	-0.21	-0.199	-0.21
Centre 6 Midpoint Potential, V	-0.12	-0.162	-0.149	-0.158

3.3.8. Methyl Viologen Studies

To investigate the potential specificity of ExtD towards various terminal electron acceptors (TEAs) was investigated using the small redox active molecule methyl viologen. The utilization of methyl viologen is a widely used method for determining the reduction of a TEA by coupling it to the oxidation of methyl viologen which can be monitored using UV-VIS spectroscopy³³. The rate of oxidation for methyl viologen is observable due to the high absorbance of reduced methyl viologen at 600 nm, ϵ_{600} of $13,700 \text{ M}^{-1}\text{cm}^{-1}$ ³⁴, with absorbance decreasing when methyl viologen is oxidised. ExtD was assessed for the capability to reduce five different TEAs namely; NaNO_2 , NaSO_4 , NaSO_3 , flavin mononucleotide (FMN) and hydroxylamine. A positive control of NrfA from *E. coli* was used with activity tested against NaNO_2 as it has been previously shown to have a strong activity, $K_m = 38 \mu\text{M}$ ³³.

The control of NrfA showed a high change in absorbance at 600 nm with the addition of NaNO_2 , showing that the method for determining TEA was effective. However, methyl viologen assays assessing ExtD's ability to reduce common TEAs showed no redox activity. Absorbance at 600 nm remained constant over the observation period, suggesting ExtD could not reduce any of the TEA tested in the assay. The change in absorbance with addition of each TEA is shown in *Table 3.3*.

Table 3.3- Methyl Viologen Assay of ExtD

<i>Protein</i>	Terminal Electron Acceptor	Change in Absorbance
<i>NrfA</i>	NaNO ₂	0.003
<i>ExtD</i>	NaNO ₂	0.00006
	NaSO ₄	0.00002
	NaSO ₃	0.00001
	Flavin Mononucleotide	0.00005
	Hydroxylamine	0.00001

3.4. Discussion

Heterologous expression of *extD* in *E. coli* BL21 proved to yield insufficient yields of ExtD, with optimisation of ExtD production not observed to increase the yield of cytochrome. Alternative heterologous host *Shewanella oneidensis* LS527 for expression of *extD* initially showed higher yields of cytochrome production. By optimising ExtD production in *S. oneidensis* sufficient ExtD was purified allowing for initial characterisation of the outer membrane cytochrome. The total yield of ExtD_HIS from *S. oneidensis* cultures remained low, approximately producing 2.8 ng per litre of culture grown. This yield was sufficient to begin the characterisation of this cytochrome but insufficient for many techniques such as X-ray crystallography.

The molecular weight of ExtD was determined through LC-MS to be 27680.98 Da differing only by 6 Da from the predicted mass of 27686.69 Da. Therefore, it is believed that ExtD has correctly formed with all six hemes covalently attached. This was additionally confirmed with sedimentation velocity which estimated the

mass of ExtD at 30 kDa and furthermore revealed ExtD to be monomeric in solution.

Modelling of ExtD using AlphaFold 2 and 3 yielded structural models with average pLDDT scores of 54.0 and 72.5 %, respectively. The accuracy of AlphaFold models can be recognised by their associated pLDDT scores. Models with an average pLDDT score of >90 % are considered highly accurate with simulations of the protein backbone and sidechain alignments deemed to be reflective of the native protein structure, pLDDT scores of >70 % are considered to show corrected modelling of the protein backbone and pLDDT scores less than 50 % considered widely inaccurate¹⁴. This suggests that both models are inaccurate in depicting the native structure of ExtD, with the AlphaFold 2 model being improbable and the AlphaFold 3 model potentially modelling portions of the protein backbone correctly. The AlphaFold 2 model is additionally highlighted to be incorrect with the overlap of manually inserted heme cofactors that would be impossible. With AlphaFold 3 the hemes were simulated with the protein and do not show the same overlap. The inability of both AlphaFold 2 and 3 to generate a successful model for ExtD suggests that ExtD has a unique structure dissimilar to previously published structures in the PDB. This is not highly unexpected as BLAST searches for homologues of ExtD have shown that the *extD* gene is predominantly conserved to the *Geobacteraceae* class with few homologues found in separate classes.

Methyl viologen assays investigating possible terminal electron acceptors for ExtD did not suggest the potential for ExtD to reduce a wide variety of TAEs. In previously published studies investigating TEA in whole cell *Geobacter sulfurreducens*, knockouts of the ExtABCD complex revealed the cluster had the highest affinity for reducing Fe(III) citrate and man-made electrodes, but were not essential for the reduction of Fe(III)/Mn(IV) oxides¹. Suggesting that the ExtABCD PCC is extremely selective and is not capable of acting as a universal donor to TEA.

Perhaps the most intriguing characterisation of ExtD is the presence of the split Soret when investigated through UV-Vis spectrometry. Whilst the cause of these features has not yet been determined but could suggest non-canonical heme stacking present within ExtD. Comparison to cytochromes also displaying split Soret previously reported and characterised can be used to try and identify the cause of the split Soret. Reviewing literature, a split Soret cytochrome has been reported on at least three occasions: cytochrome bc complex from *Rhodothermus marinus*²⁸; Cytochrome c554 from *Nitrosomonas europaea*²⁹; and split Soret cytochrome c (Ssc) from *Desulfovibrio desulfuricans* ATCC 27774^{30,35}, however for all previous split Soret cytochromes the cause of the split Soret has not been deduced. Also of note, researchers found that mutating heme axial ligands of mitochondrial cytochrome C to introduce a bis-Met heme axial ligation generated a cytochrome that when characterised displayed a split Soret³⁶. However, the canonical protein sequence for ExtD contains only CxxCH motifs and it is therefore improbable that a bis-Met axially ligated heme would be present as the His residue from each motif is expected to act as the proximal axial ligand.

A potential first assumption for a split Soret observed in MHCs would be the presence of hemes with differing distal ligands. However, many MHCs have been reported in the literature that possess hemes with varying axial ligands that do not show a split Soret. For example, PioA from *Rhodopseudomonas palustris* TIE-1 was purified heterologous in *S. oneidensis* with ten CxxCH binding motifs seven of these are predicted to be bis-His coordinated with the remaining three hemes predicted to be either His/Met or His/- axially ligated³⁷. Unlike ExtD the spectrum for PioA is typical for a MHC with a single Soret peak at 419 nm when reduced. Further evidence of MHCs containing diverse heme axial ligands yet a single reduced Soret peak can be seen throughout the literature³⁸⁻⁴⁰. Therefore, the reason for the split Soret seen in ExtD is not expected to be the axial coordination of the hemes.

Alternatively, the presence of a split Soret may indicate the presence of two distinct heme groups within the cytochrome⁴¹. Stacking of the heme cofactors causes overlap of π -orbitals to facilitate electron tunnelling through MHCs. Therefore, the Soret can be seen as a culmination of all the hemes when they are stacked together with ExtD containing two distinct pathways which cause the split Soret. As each heme is associated with a $\pi \rightarrow \pi^*$ transition having hemes at different potentials could potentially result in a split Soret. However, as observed previously in nature MHC with varying heme cofactors only have a single reduced Soret peak. In monoheme cytochromes mutation of the axial ligands results in a shift in the reduced Soret maxima^{36,42,43} demonstrating the important relationship between axial ligands and $\pi \rightarrow \pi^*$. Therefore, it is hypothesised that ExtD contains two distinct heme chains that are non-overlapping and will likely vary in axial ligand coordination therefore producing the split Soret.

Structures are available for the split Soret cytochromes from *Nitrosomonas europaea* and *Desulfovibrio desulfuricans* and comparing the spatial arrangement of the heme cofactors to STC from *Shewanella algae*¹⁵, a periplasmic tetraheme cytochrome that is not characterised to have a split Soret. Heme arrangements of the three tetraheme cytochromes are shown in *Figure 3.20*. By comparing the spatial arrangements of the hemes it can be seen that for cyt c554 and Ssc the heme packing can be split into two pair of stacked hemes with hemes 2 and 3 in both cases being adjacent to each other with a distance between the heme Fe centres of 12 and 14 Å respectively. Comparatively, STC does not contain any hemes which are adjacent to each other instead showing both canonical stacked and perpendicular heme packing. It is plausible that the arrangement of the hemes in an adjacent packing would lead to non-overlapping pi orbitals between the cofactors consequently generating two distinct heme chains. Therefore, the split Soret seen in ExtD could originate from this atypical heme stacking with two or more of the six hemes present in ExtD being stacked adjacently rather than the typically observed stacked and perpendicular. Attempts to find similar structures in the PDB to cyt c554 and Ssc based on

sequence similarity yielded no results and it was therefore not possible to expand this hypothesis to further cytochromes.

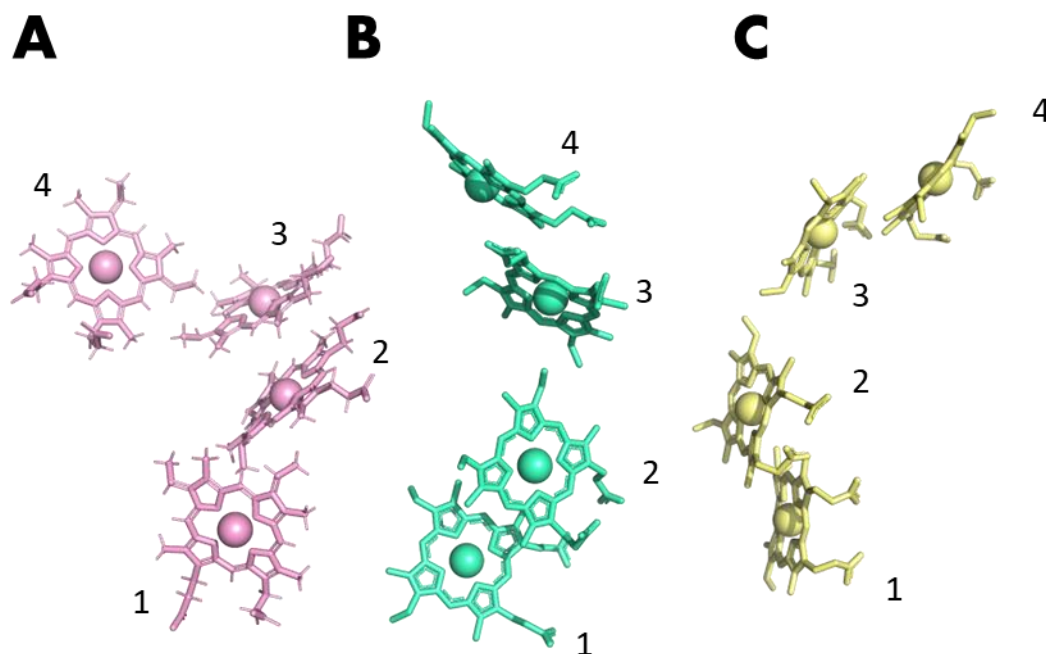


Figure 3.20- Comparison of heme arrangements of tetraheme cytochromes. A) STC from *Shewanella algae* (PDB: 6HR0). B) Cytochrome c554 from *Nitrosomonas europaea* (PDB:1FT5). C) split Soret cytochrome C from *Desulfovibrio desulfuricans* ATCC 27774 (PDB: 1H21).

3.5. References

1. Jiménez Otero, F., Chan, C. H. & Bond, D. R. Identification of Different Putative Outer Membrane Electron Conduits Necessary for Fe(III) Citrate, Fe(III) Oxide, Mn(IV) Oxide, or Electrode Reduction by *Geobacter sulfurreducens*. *J Bacteriol* **200**, (2018).
2. Jiménez Otero, F. *et al.* Evidence of a Streamlined Extracellular Electron Transfer Pathway from Biofilm Structure, Metabolic Stratification, and Long-Range Electron Transfer Parameters. *Appl Environ Microbiol* **87**, (2021).
3. Aklujkar, M. *et al.* Proteins involved in electron transfer to Fe(III) and Mn(IV) oxides by *Geobacter sulfurreducens* and *Geobacter uraniireducens*. *Microbiology (N Y)* **159**, 515–535 (2013).
4. Arslan, E., Schulz, H., Zufferey, R., Künzler, P. & Thöny-Meyer, L. Overproduction of the *Bradyrhizobium japonicum* c-Type Cytochrome Subunits of the cbb3 Oxidase in *Escherichia coli*. *Biochem Biophys Res Commun* **251**, 744–747 (1998).
5. Almagro Armenteros, J. J. *et al.* SignalP 5.0 improves signal peptide predictions using deep neural networks. *Nat Biotechnol* **37**, 420–423 (2019).

6. Imada, Y., Nakamura, H. & Takano, Y. Density functional study of porphyrin distortion effects on redox potential of heme. *J Comput Chem* **39**, 143–150 (2018).
7. Altschul, S. F., Gish, W., Miller, W., Myers, E. W. & Lipman, D. J. Basic local alignment search tool. *J Mol Biol* **215**, 403–410 (1990).
8. Madeira, F. *et al.* Search and sequence analysis tools services from EMBL-EBI in 2022. *Nucleic Acids Res* **50**, W276–W279 (2022).
9. Yang, F. *et al.* Characterization of Purified c-Type Heme-Containing Peptides and Identification of c-Type Heme-Attachment Sites in *Shewanella oneidensis* Cytochromes Using Mass Spectrometry. *J Proteome Res* **4**, 846–854 (2005).
10. Philo, J. S. SEDNTERP: a calculation and database utility to aid interpretation of analytical ultracentrifugation and light scattering data. *European Biophysics Journal* (2023)
11. Brookes, E. & Rocco, M. Recent advances in the UltraScan SOLUTION MOdeller (US-SOMO) hydrodynamic and small-angle scattering data analysis and simulation suite. *European Biophysics Journal* **47**, 855–864 (2018).
12. Schuck, P. Size-Distribution Analysis of Macromolecules by Sedimentation Velocity Ultracentrifugation and Lamm Equation Modeling. *Biophys J* **78**, 1606–1619 (2000).
13. Cole, J. L., Lary, J. W., P. Moody, T. & Laue, T. M. Analytical Ultracentrifugation: Sedimentation Velocity and Sedimentation Equilibrium. in 143–179 (2008).
14. Jumper, J. *et al.* Highly accurate protein structure prediction with AlphaFold. *Nature* **596**, 583–589 (2021).
15. Fonseca, B. M. *et al.* Optimizing Electroactive Organisms: The Effect of Orthologous Proteins. *Front Energy Res* **7**, (2019).
16. Mariani, V., Biasini, M., Barbato, A. & Schwede, T. IDDT: a local superposition-free score for comparing protein structures and models using distance difference tests. *Bioinformatics* **29**, 2722–2728 (2013).
17. Rydberg, P., Sigfridsson, E. & Ryde, U. On the role of the axial ligand in heme proteins: a theoretical study. *JBIC Journal of Biological Inorganic Chemistry* **9**, 203–223 (2004).
18. Abramson, J. *et al.* Accurate structure prediction of biomolecular interactions with AlphaFold 3. *Nature* (2024)
19. Moore, G. R. & Pettigrew, G. W. *Cytochromes c: Evolutionary, Structural and Physicochemical Aspects*. (Springer Berlin Heidelberg, Berlin, Heidelberg, 1990).
20. Moser, C. C., Keske, J. M., Warncke, K., Farid, R. S. & Dutton, P. L. Nature of biological electron transfer. *Nature* **355**, 796–802 (1992).
21. van Wonderen, J. H. *et al.* Nanosecond heme-to-heme electron transfer rates in a multiheme cytochrome nanowire reported by a spectrally unique His/Met-ligated heme. *Proceedings of the National Academy of Sciences* **118**, (2021).
22. Lee, B. & Richards, F. M. The interpretation of protein structures: Estimation of static accessibility. *J Mol Biol* **55**, 379-IN4 (1971).

23. Saff, E. B. & Kuijlaars, A. B. J. Distributing many points on a sphere. *The Mathematical Intelligencer* **19**, 5–11 (1997).
24. Li, T., Bonkovsky, H. L. & Guo, J. Structural analysis of heme proteins: implications for design and prediction. *BMC Struct Biol* **11**, 13 (2011).
25. Barr, I. & Guo, F. Pyridine Hemochromagen Assay for Determining the Concentration of Heme in Purified Protein Solutions. *Bio Protoc* **5**, (2015).
26. Berry, E. A. & Trumpower, B. L. Simultaneous determination of hemes a, b, and c from pyridine hemochrome spectra. *Anal Biochem* **161**, 1–15 (1987).
27. Mayhew, S. G. The Redox Potential of Dithionite and SO₂ from Equilibrium Reactions with Flavodoxins, Methyl Viologen and Hydrogen plus Hydrogenase. *Eur J Biochem* **85**, 535–547 (1978).
28. Pereira, M. M., Carita, J. N. & Teixeira, M. Membrane-Bound Electron Transfer Chain of the *Thermohalophilic* Bacterium *Rhodothermus marinus*: A Novel Multihemic Cytochrome bc, a New Complex III. *Biochemistry* **38**, 1268–1275 (1999).
29. Arciero, D. M., Balny, C. & Hooper, A. B. Spectroscopic and rapid kinetic studies of reduction of cytochrome c554 by hydroxylamine oxidoreductase from *Nitrosomonas europaea*. *Biochemistry* **30**, 11466–11472 (1991).
30. Abreu, I. A. *et al.* A novel iron centre in the split-Soret cytochrome c from *Desulfovibrio desulfuricans* ATCC 27774. *JBIC Journal of Biological Inorganic Chemistry* **8**, 360–370 (2003).
31. Fourmond, V. QSoas: A Versatile Software for Data Analysis. *Anal Chem* **88**, 5050–5052 (2016).
32. Papa, S., Guerrieri, F. & Izzo, G. Redox bohr-effects in the cytochrome system of mitochondria. *FEBS Lett* **105**, 213–216 (1979).
33. Clarke, T. A. *et al.* *Escherichia coli* Cytochrome c Nitrite Reductase NrfA. In *Methods in Enzymology, Chapter 4, pages 63–77* (2008).
34. Mayhew, S. G. The Redox Potential of Dithionite and SO₂ from Equilibrium Reactions with Flavodoxins, Methyl Viologen and Hydrogen plus Hydrogenase. *Eur J Biochem* **85**, 535–547 (1978).
35. Liu, M. C. *et al.* Cytochrome components of nitrate- and sulfate-respiring *Desulfovibrio desulfuricans* ATCC 27774. *J Bacteriol* **170**, 5545–5551 (1988).
36. Mendez, D. L. *et al.* Engineered holocytochrome c synthases that biosynthesize new cytochromes c. *Proceedings of the National Academy of Sciences* **114**, 2235–2240 (2017).
37. Li, D.-B. *et al.* His/Met heme ligation in the PioA outer membrane cytochrome enabling light-driven extracellular electron transfer by *Rhodopseudomonas palustris* TIE-1. *Nanotechnology* **31**, 354002 (2020).
38. Doyle, R.-M. A. S. *et al.* Contrasting catalytic profiles of multiheme nitrite reductases containing CxxCK heme-binding motifs. *JBIC Journal of Biological Inorganic Chemistry* **18**, 655–667 (2013).

39. Pires, R. H. *et al.* Characterization of the *Desulfovibrio desulfuricans* ATCC 27774 DsrMKJOP Complex A Membrane-Bound Redox Complex Involved in the Sulfate Respiratory Pathway. *Biochemistry* **45**, 249–262 (2006).
40. Fernandes, T. M., Folgosa, F., Teixeira, M., Salgueiro, C. A. & Morgado, L. Structural and functional insights of GSU0105, a unique multiheme cytochrome from *G. sulfurreducens*. *Biophys J* **120**, 5395–5407 (2021).
41. van Wonderen, J. H. *et al.* Do multiheme cytochromes containing close-packed heme groups have a band structure formed from the heme π and π^* orbitals? *Curr Opin Electrochem* **47**, 101556 (2024).
42. Girvan, H. M. *et al.* Structural and Spectroscopic Characterization of P450 BM3 Mutants with Unprecedented P450 Heme Iron Ligand Sets. *Journal of Biological Chemistry* **282**, 564–572 (2007).
43. Ojha, S., Wu, J., LoBrutto, R. & Banerjee, R. Effects of Heme Ligand Mutations Including a Pathogenic Variant, H65R, on the Properties of Human Cystathionine β -Synthase. *Biochemistry* **41**, 4649–4654 (2002).

*Chapter 4: Protein
Characterisation of dodecaheme
cytochrome ExtA from Geobacter
sulfurreducens PCA*

4.1. Introduction

ExtA is predicted to be a dodecaheme c-type cytochrome, encoded in the *extABCD* cluster suggested to encode a porin cytochrome complex (PCC). ExtA is hypothesised to be the periplasmic component of the ExtABCD complex and therefore would be insulated in the outer membrane by the porin-like protein ExtB^{1,2}. Interestingly whilst previously speculated to be insulated by the porin ExtB, to form the PCC, genomic evaluation of multiple *Geobacter* species has shown that genes encoding homologous of the ExtA cytochrome were not always located in the same gene cluster as *extBCD* and can in some cases be absent from the genome entirely¹.

Single gene knockouts of the *extABCD* cluster, in *G. sulfurreducens* PCA cells, showed that the absence of ExtB, ExtC and ExtD have the most dire defects for cell growth when *G. sulfurreducens* cells were grown on graphite electrodes at +240 mV vs SHE². With gene knockouts of *extA* still showing the current output of *G. sulfurreducens* PCA cells grown on an electrode to be near comparable to wildtype levels². As current output from *G. sulfurreducens* PCA can be correlated to the performance of the ExtABCD PCC this would suggest that ExtA is not an integral part of the ExtABCD complex. Previous studies looking at the effect of knocking out MtrA from *Shewanella oneidensis* MR-1, comparable to ExtA's expected role in *Geobacter*, showed that MR-1 became incapable of reducing a range of terminal electron acceptors³. As ExtA and MtrA were both proposed to have identical roles in PCCs deletion of ExtA would be expected to show similar results. However, as gene deletion of *extA* from *Geobacter* does not have the same effect it is possible that ExtA plays a different role in the ExtABCD PCC.

This chapter begins work on expressing the *extA* gene from *G. sulfurreducens* PCA in the heterologous host *Shewanella oneidensis* LS527. The ExtA cytochrome expressed from the heterologous host can then be purified allowing for characterisation of spectral features, oligomeric state and redox proteins of the cytochrome.

4.2. Results

4.2.1. Heterologous expression of ExtA in *S. oneidensis* LS527

The gene corresponding to predicted dodecaheme cytochrome ExtA from *G. sulfurreducens* PCA (gene: GSU2645) was synthesised by Eurofins. The *extA* gene was optimised to allow for ease of expression in heterologous host *Shewanella oneidensis* LS527. The signal peptide of the native ExtA cytochrome was predicted using SignalP 5.0 ⁴ and the DNA bases corresponding were removed from the synthesised gene and substituted with the DNA sequence corresponding to the signal peptide associated with MtrB from *S. oneidensis* MR-1. For ease of purification, the nucleotides encoding a C-terminus STREP-II affinity tag (amino acid sequence: SAWSHPQFEK) were added to the 5' end of the *extA* gene, therefore allowing for purification of cytochrome through STREP affinity chromatography. Synthesised *extA* was additionally codon optimised for *Escherichia coli* K12 and provided by Eurofins in the *pEX-A128* vector which additionally provides ampicillin resistance when transformed into bacterial host cells.

The *extA* gene was transferred from the *pEX-A128* vector to the expression plasmid *pMEGGAx*, generating *pMEGGAx_extA*. The *pMEGGAx* vector additionally provides kanamycin resistance to host cells. This was done through Golden Gate cloning as the optimised *extA* gene in *pEX-A128* contained 5' and 3' flanking regions that contained type II restriction cut sites for Esp3I. Golden Gate reaction was carried out by combining *pMEGGAx* with *pEX-A128_extA*, in the presence of restriction enzyme Esp3I. Golden Gate products were transformed in *E. coli* TOP10 cells and grown overnight in LB containing 30 µg/mL of kanamycin. Overnight cultures that were successfully grown were screened based on a pink-white test. Between the Golden Gate sites used to clone in *extA* in *pMEGGAx* is the presence of a pink coral reef gene. If successful Golden Gate has been performed insertion of the desired gene will replace the pink coral reef gene. Therefore, if bacteria were pink, it can be inferred that the pink coral reef gene is still present within *pMEGGAx* and therefore unsuccessful insertion of the *extA* gene.

Conformation of *extA* gene insertion into *pMEGGAx* was performed by visualisation of the *pMEGGAx_extA* by extraction of plasmid from *E. coli* TOP10 cells through plasmid miniprep. Isolated plasmids were analysed through gel electrophoresis, *Figure 4.1*. The predicted size for *pMEGGAx_extA* is 4,933 bp and *pMEGGAx* is 4,826 bp. The main DNA band seen in *Figure 4.1* is slightly larger than 3000 bp, this is a lower mass than the predicted size and is likely due to the plasmid being supercoiled. Analysis showed that *pMEGGAx_extA* ran at a larger mass than the control of *pMEGGAx*. The difference between the two plasmids is minimal, differing by 107 bp. Additionally, the *pMEGGAx_extA* vector was sequenced by Eurofins. Sequencing confirmed the successful insertion of the *extA* gene into *pMEGGAx*, with no identification of mutated bases. *E. coli* TOP10 cells containing confirmed *pMEGGAx_extA* were stored in 25 % glycerol at -80 °C.

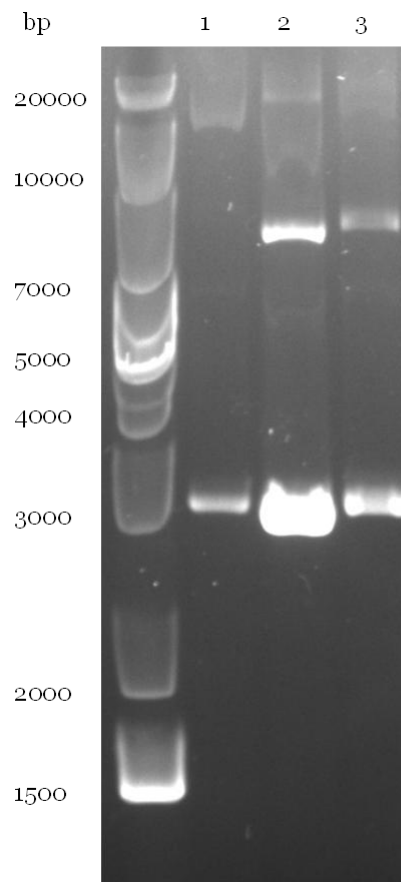


Figure 4.1- Gel electrophoresis analysis of Golden Gate product pMEGGAx_extA. Lane 1) Diluted pMEGGAx 2) Concentrated pMEGGAx 3) Golden Gate product pMEGGAx_extA

The amino acid sequence predicted from the synthesised *extA* gene is displayed in *Figure 4.2*. The predicted molecular weight for the expressed ExtA construct was predicted at 34,028.71 Da. This value included the MtrB encoded signal peptide which would be removed after translocation of the cytochrome to the periplasm. Cleavage of the signal peptide was predicted through SignalP 5.0⁴ with the new N-terminus predicted to be Ala22. Therefore, the predicted molecular mass of ExtA once translocated to the periplasm is 31,831.11 Da. ExtA is additionally predicted to covalently bind 12 heme through the CxxCH motifs present in the secondary structure, each heme addition has a mass of 615.2 Da totalling 7,397.76 Da for all 12 hemes covalently bound. Therefore, the total predicted mass for ExtA incorporating 12 hemes is 39,229 Da.

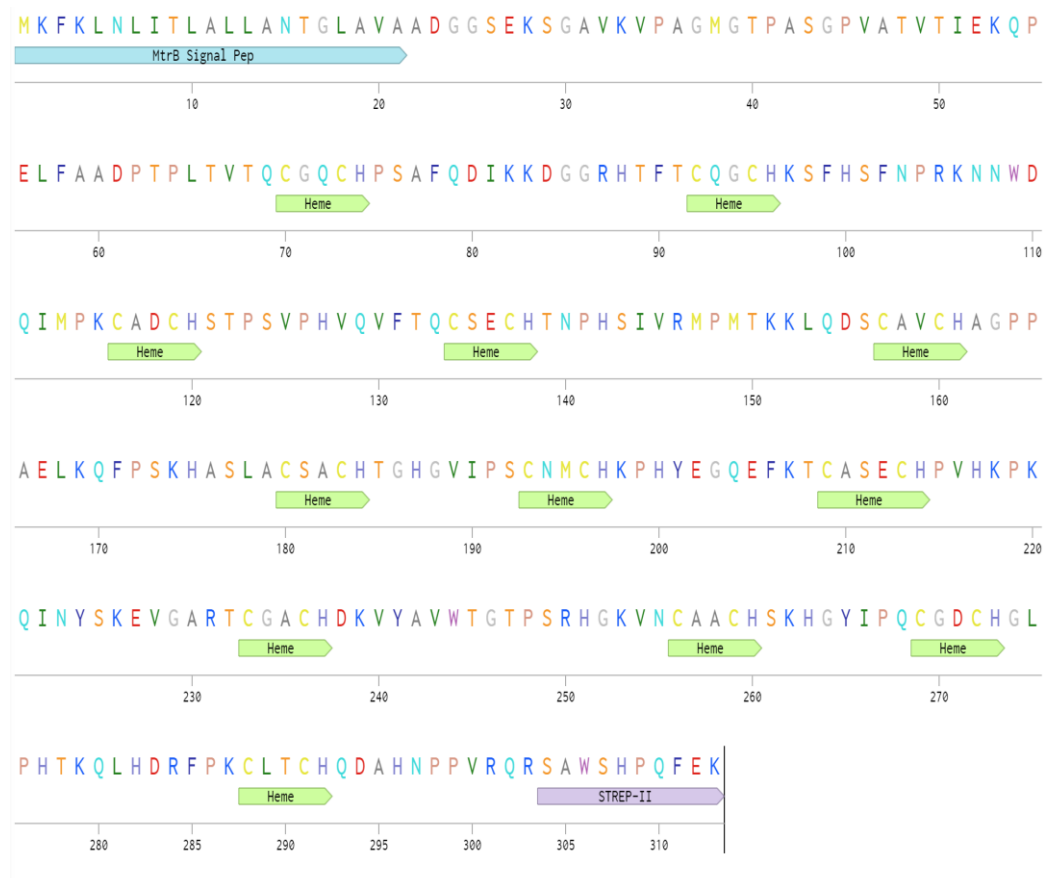


Figure 4.2- Amino acid sequence of ExtA from synthesised extA gene.

The *pMEGGAx_extA* vector was electroporated into *S. oneidensis* LS527 for synthesis, isolation and initial characterisation of ExtA. ExtA was purified by inoculating *S. oneidensis* LS527 cells containing the *pMEGGAx_extA* vector in 1 L of M72 media and incubating at 30 °C with 180 rpm shaking. An expression trial for *extA* was performed varying the concentration of arabinose from 0 mM to 10 mM, *Figure 4.3*. Arabinose was added to cells when an OD₆₀₀ of 0.4 was reached and cultures were left overnight at 30 °C with shaking at 180 rpm. The following day cultures were harvested by centrifugation and a whole-cell SDS-PAGE was performed to assess levels of ExtA, *Figure 4.3*. The SDS-PAGE was visualised with a peroxidase linked heme stain and showed that the largest concentration of ExtA was observed when cells were induced with 2.5 mM of arabinose. Unlike ExtD which required a shorter induction time it was also seen that cultures expression ExtA were suitable for overnight induction, approximately 16 hours.

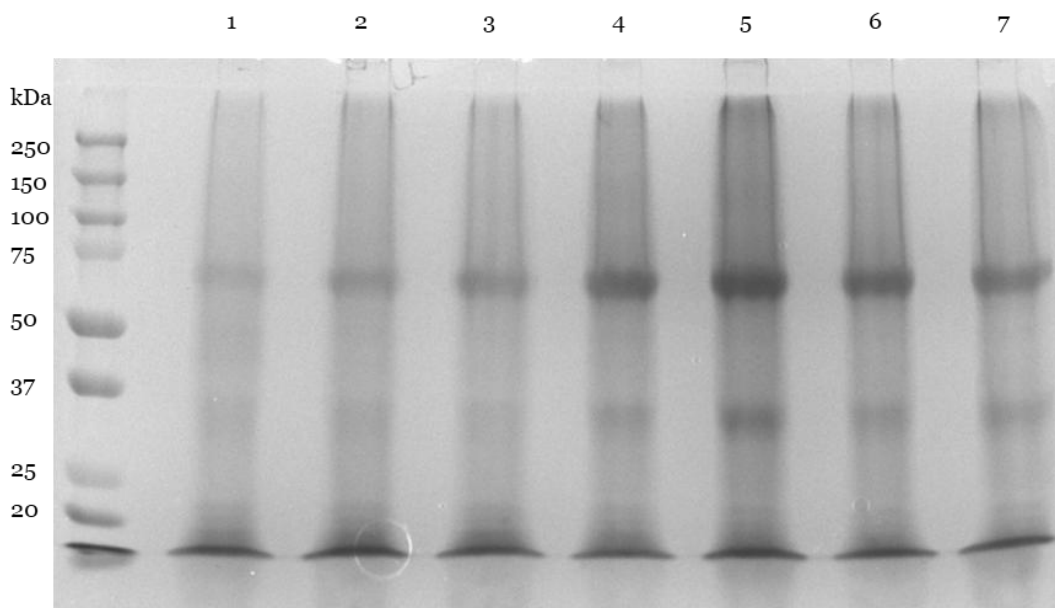


Figure 4.3- Whole Cell SDS-PAGE of 1) LS527 and 2-7) LS527 containing pMEGGAx_extA. Cultures were induced with 1-2) 0 mM 3) 0.5 mM 4) 1 mM 5) 2.5 mM 6) 5 mM or 7) 10 mM of arabinose. Cytochromes were visualised through peroxidase linked heme staining.

Cultures of LS527 containing *pMEGGAx_extA* were grown at 30 °C with 180 rpm. Induction of cells with 2.5 mM arabinose occurred when cultures had reached an OD₆₀₀ of 0.4. Cells were harvested after 16 hours by centrifugation and lysed by passing through the French Press. The cell lysate was then passed through a

STREP column and a size exclusion column to purify ExtA. Product from AKTA purification was analysed using SDS-PAGE with visualization of the protein bands performed using peroxidase-linked heme staining, *Figure 4.4*. From the SDS-gel it was evident that a cytochrome was isolated between the masses of 25 and 37 kDa. Although this is lower than the predicted mass of ExtA, it is not unusual for cytochromes of this nature to be visualised at a lower molecular mass than expected. The quantity of ExtA expressed from 1 L of M72 media was calculated to be 2.4 ng.

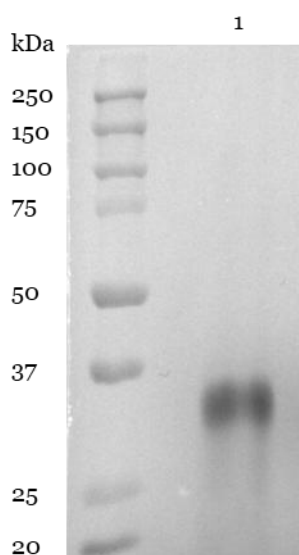


Figure 4.4- SDS-PAGE visualisation of purified ExtA after extraction from cell lysate through STREP-II tag affinity chromatography and SEC. Cytochrome visualised through heme linked peroxidase staining.

To confirm that ExtA had been successfully purified from *S. oneidensis* LS527 cells liquid chromatography mass spectrometry (LC-MS) was performed on the isolated ExtA sample. Results confirmed a protein mass of 39,218 Da. This differs from the expected protein mass of ExtA of 39,229 Da by 11 Da. This difference was minimal and was potentially due to the protonation state of ExtA. The LC-MS therefore suggested that ExtA had been successfully purified from *S. oneidensis* LS527 cells. With the correctly predicted post-translation modifications of ExtA to covalently bind all 12 hemes, and removal of the signal peptide.

4.2.2. UV-Visible Spectroscopy

Purified ExtA was investigated using UV-visible spectroscopy between the wavelengths 350-600 nm. The cytochromes were characterised in air oxidised conditions and reduced with 10 mM sodium dithionite (-660 mV vs SHE⁵). The oxidised spectrum showed a Soret peak present at 410 nm which is much broader than a typical cytochrome Soret, with a plateaued peak from 404 to 415 nm. With the addition of sodium dithionite, the reduced spectrum is revealed and the Soret transitions to a split Soret when reduced with maxima at 415 and 424 nm. Reduced spectrum also exhibited canonical Q-bands at 554 nm for the α -band and 525 nm for the β -band, *Figure 4.5A*.

A dithionite titration, *Figure 4.5B*, was carried out to observe the formation of the split Soret present in the reduced ExtA spectrum. Sodium dithionite was titrated against a solution of 0.41 μ M ExtA. Incremental additions of sodium dithionite began to reduce ExtA, as evidenced by the formation of α - and β -peaks and the blue-shift of the Soret peak. The reduced Soret peak split into two peaks with maxima at 415 and 424 nm at an equal concentration of sodium dithionite with the peak at 424 nm finishing at a higher absorption than the peak at 415 nm. Interestingly, with the cytochrome being sequentially reduced the oxidised Soret does not transition linearly to the reduced peak. Initially, the plateau of the oxidised peak at 404 nm disappeared from the spectra leaving only the absorbance at 415 nm, as seen in the oxidised spectrum. Sequential reduction then shifts the 415 nm peak to 424 nm generating a split Soret.

The extinction coefficient of ExtA was determined using the pyridine hemochromagen assay⁶ and thus allows for determination of cytochrome concentration. Spectra of ExtA in native, 100 mM Tris 150 mM NaCl and 1 mM EDTA at pH 8, and denatured with 10 % (v/v) pyridine, forms were recorded between 350-800 nm. For both samples recorded spectra were recorded under air oxidised and reduced with sodium dithionite. The difference spectrum of the reduced minus oxidised spectra was calculated from denatured ExtA and using

the literature value for the extinction coefficient of a bis-pyridine ligated c-type heme ⁷ of $\epsilon_{550-535} = 23.97 \text{ mM}^{-1}\text{cm}^{-1}$ the concentration was calculated for a cytochrome containing 12 hemes, $\epsilon_{550-535}$ therefore being $287.64 \text{ mM}^{-1}\text{cm}^{-1}$. For spectra recorded concentration was calculated to be 427.68 nM. As the denatured and native concentrations were the same the extinction coefficients of native oxidised ExtA can be calculated. Therefore, it was determined that the extinction coefficient of ExtA at 410 nm was $1185.64 \text{ mM}^{-1}\text{cm}^{-1}$. The spectra of denatured ExtA under oxidised and reduced conditions is shown in *Figure 4.5C*. As seen with ExtD in Chapter 3, the presence of pyridine removed the presence of the split-Soret in the reduced form of ExtA and also considerably narrows the oxidised Soret. This potentially suggests the axial ligands of ExtA under native conditions were a key factor in the presence of the reduced split Soret.

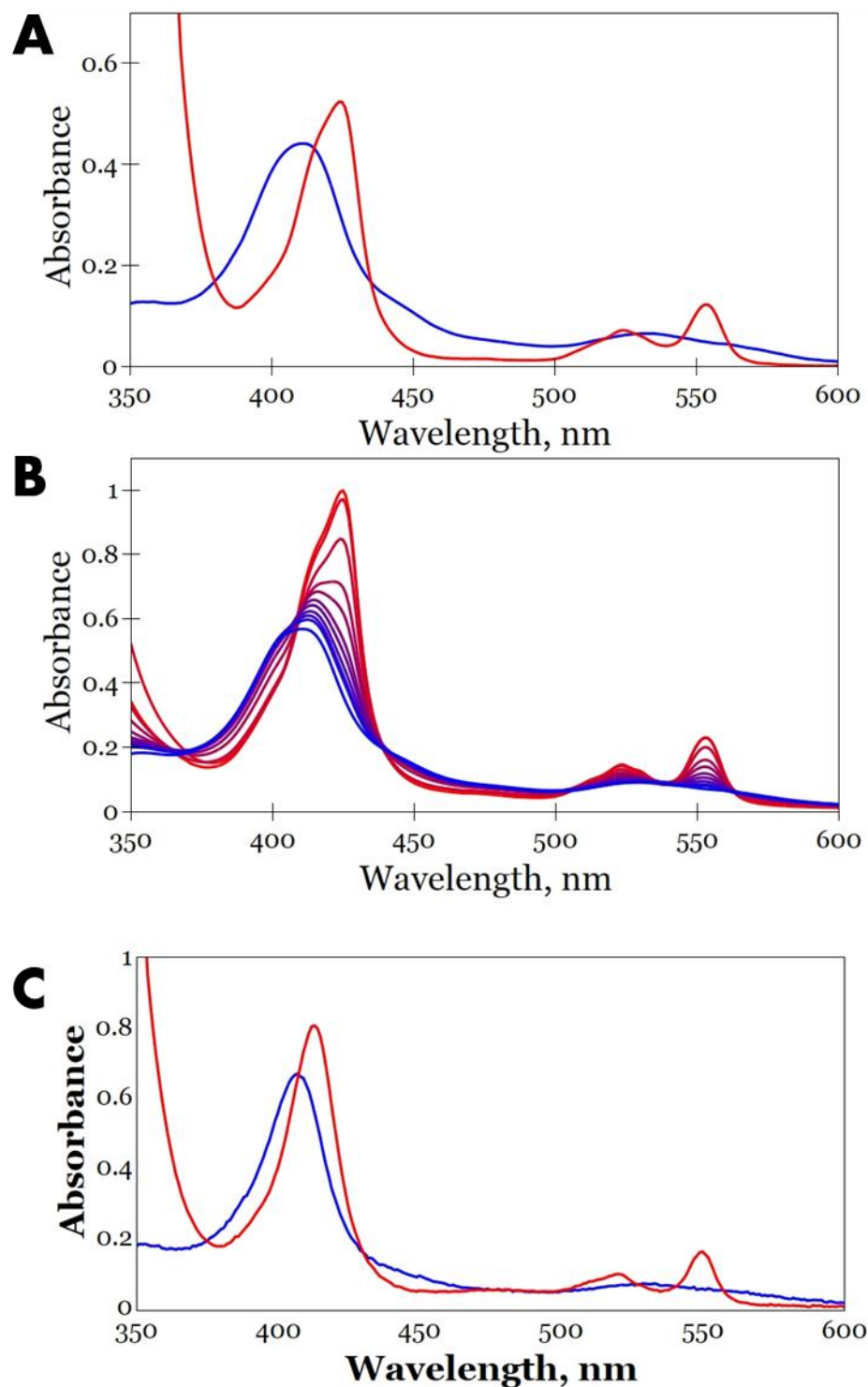


Figure 4.5- A) UV-Visible spectra of ExtA under air oxidised and reduced by 10 mM sodium dithionite conditions. Spectra were taken between 350 and 800 nm. B) UV-Visible spectra of ExtA with increasing concentrations of sodium dithionite. C) UV-Visible of spectra denatured ExtA in 50 mM Tris, 75 mM NaCl, 0.5 mM EDTA, 0.1 M NaOH, 20 % (v/v) pyridine pH 8, under oxidised and reduced conditions. For all spectra A-C) colour spectrum blue to red, oxidised to reduced protein.

4.2.3. Protein Film Voltammetry

The redox properties of ExtA were probed utilising protein film voltammetry (PFV). Purified ExtA was adsorbed onto ITO electrode by incubating ITO electrodes suspending in 2 μ M ExtA, 100 mM Tris 150 mM NaCl pH 8, overnight at 4 °C. Data was collected by performing potential sweeps from 0.5 V to -0.8 V vs Ag/AgCl reference electrode in 100 mM Tris 150 mM NaCl pH 8 at a scan rate of 0.02 V/s. To convert voltage from Ag/AgCl to SHE data was shifted by +195 mV. Before the adsorption of ExtA to ITO electrodes, a PFV was performed using a blank electrode in 100 mM Tris 150 mM NaCl pH 8, allowing for the definition of the non-Faradaic current. *Figure 4.6* shows voltammograms relating to the bare electrode overlaid with ExtA adsorbed electrode both at a scan rate of 0.02 V/s. The voltammogram correlating to the blank electrode was not able to be directly subtracted from the ITO electrode with adsorbed ExtA due to a poor alignment of the voltammograms below -600 mV. This is not uncommon as this is close to the limit of the available redox window for an ITO electrode and therefore variations in the potential window can be expected. However, the presence of Faradic current linked to the redox activity of ExtA can be seen between -600 and -200 vs Ag/AgCl as the voltammograms of the blank ITO electrode and ExtA adsorbed ITO electrode separate.

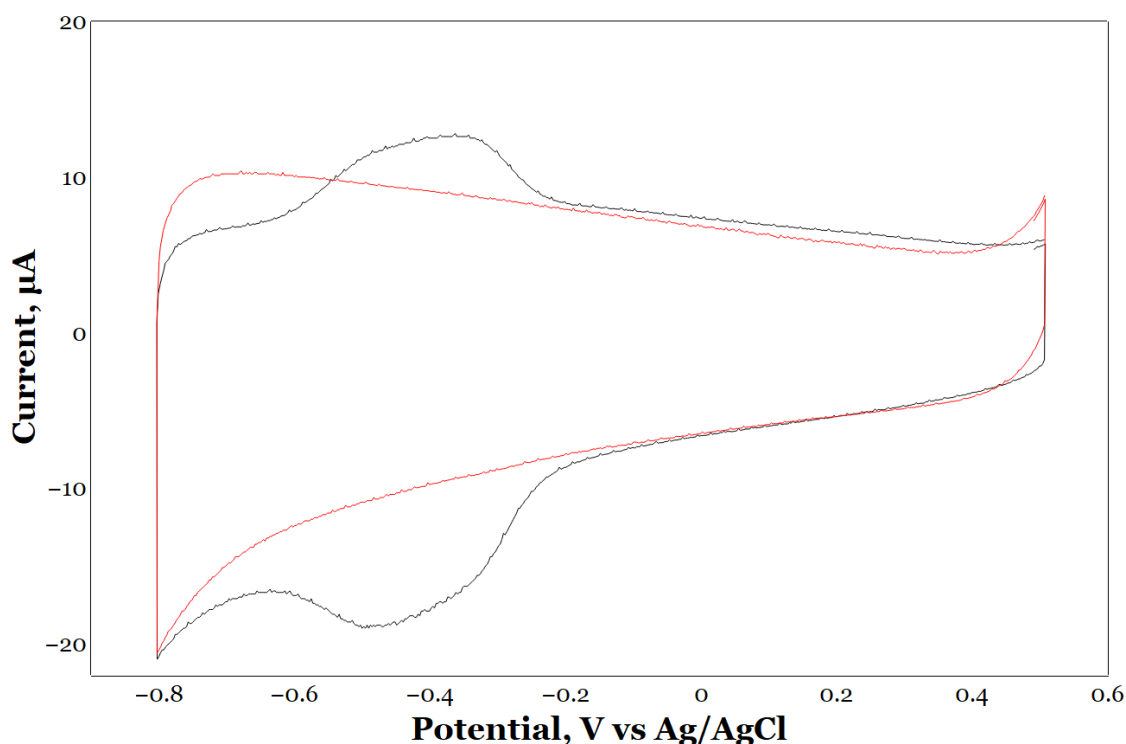


Figure 4.6- Raw PFV of bare ITO electrode (red) and ITO electrode adsorbed with ExtA (black). Voltammograms were recorded at pH 8 in 100 mM Tris, 150 mM NaCl pH 8 at a scan rate of 0.002 V/s.

Voltammograms collected from the PFV of ExtA were analysed using QSoas⁸ removing the non-Faradaic current by manually generating a baseline. By isolating the Faradic current associated with ExtA, Figure 4.7, a single peak with a midpoint potential of -215 mV vs SHE with a potential window observed between 0 and -450 mV vs SHE at pH 8. Whilst the reductive peak is seen to plateau between -150 to -270 mV vs SHE the oxidative peak does not follow the same symmetry with a higher current observed at -150 mV compared to -270 mV. This suggests the heme potentials are dynamic with the average potential required to reduce all the heme cofactors being lower than the potential required to oxidise the heme cofactors. This slight difference in redox potential is likely linked to the Redox-Bohr effect.

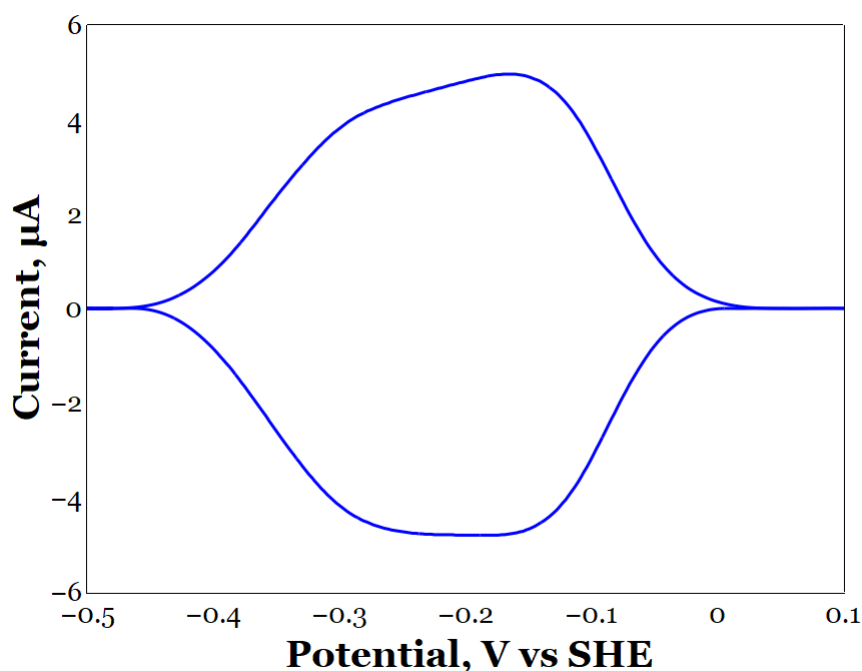


Figure 4.7- Faradaic current of ExtA adsorbed to ITO electrode. Voltammogram recorded in 100 mM Tris, 150 mM NaCl pH 8 at a scan rate of 0.02 V/s. No-Faradaic current was removed from voltammogram by manually generating a baseline through QSoas.

The total moles of redox active cofactor ($\text{A}\Gamma$) present in the Faradaic current were determined. In total ten voltammograms were analysed using different scan rates; 0.2, 0.1, 0.05, 0.02 and 0.01 V/s to remove bias. $\text{A}\Gamma$ was determined to be 57.8 ± 0.88 pmol.

A single distinct one electron reaction ($n=1$) would produce a Faradaic curve with a half-height width of 90 mV⁹, the half-height width of the Faradaic current observed in ExtA was calculated to be 271 mV. Therefore, the minimum amount of distinct single electron redox reactions present in ExtA is three, originating from four groups of three hemes with identical redox potentials. To investigate the amount of $n=1$ reactions probable to occur in ExtA a simulated fit was generated using QSoas starting with 3 distinct $n=1$ reactions and increasing the amount of $n=1$ centres until the simulated fit matched the observed Faradaic current. However, care was taken to not increase the amount of distinct $n=1$ centres too much as to generate a fitting bias by increased parameters.

The modelling of three distinct $n=1$ redox reactions is depicted in *Figure 4.8A* and yielded a poor simulated voltammogram in comparison to the experimentally determined Faradaic current. Although three distinct $n=1$ redox reactions were sufficient to bridge the redox window observed through PFV, the simulated fit, which was derived from combining the individual $n=1$ redox reactions, was unable to match the shape of the experimental voltammogram.

Consequently, an additional $n=1$ redox reaction was added to the simulation to produce a simulated fit formed from four clusters of $n=1$, as shown in *Figure 4.8B*. This simulated fit demonstrated a higher degree of accuracy in aligning with the experimental data compared to the three $n=1$ distinct redox reactions. The main disparity between the experimental data and the simulated fit was observed at the most negative simulated $n=1$ reaction.

The simulation was increased to include six distinct $n=1$ redox reactions, with five $n=1$ redox reactions not being modelled as it is not a factor of 12, which generated a simulated fit that was identical to the recorded voltammogram, *Figure 4.8C*. This would suggest the total number of distinct $n=1$ redox reactions present ExtA's voltammogram to be six, originating from pairs of hemes with similar redox potentials. However as stated above by increasing the number of parameters, $n=1$ redox reactions, used to generate the simulated fit an unintended bias is also generated. Further modelling of increasing $n=1$ centres beyond this point was not conducted for the same reason.

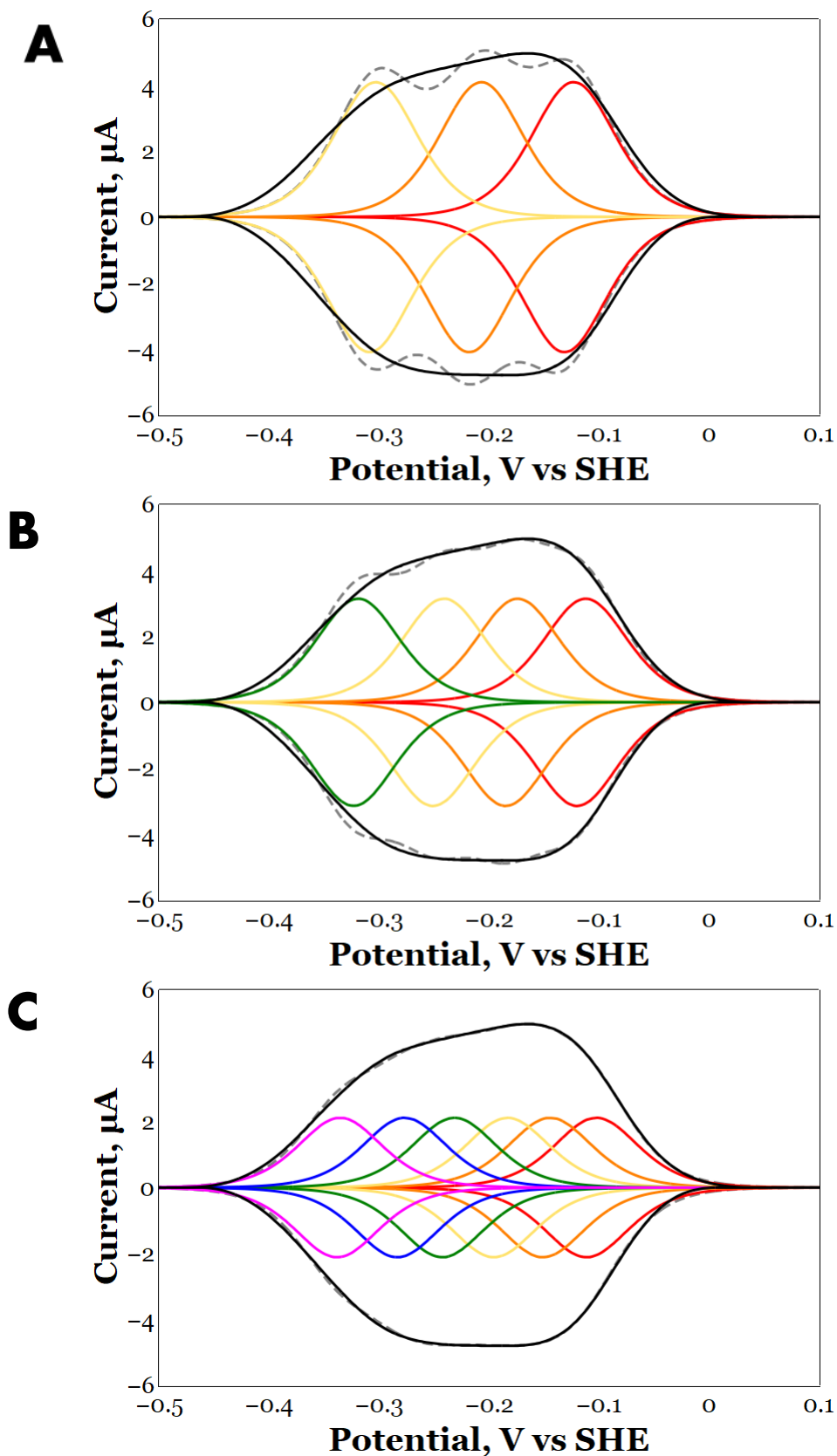


Figure 4.8- Simulation of increasing $n=1$ centres onto Faradaic current of ExtA adsorbed onto ITO electrode. Voltammogram collected at a scan rate of 0.02 V/s in 100 mM Tris , 150 mM NaCl at $\text{pH } 8$. Non-Faradaic current was removed through manual baseline using Qsoas. The simulated $n=1$ centres were modelled with A) $n=3$, B) $n=4$ and C) $n=6$ distinct redox centres through Qsoas. The black line shows observed Faradaic current, grey dashed the fit from simulated $n=1$ centres (coloured lines)

4.2.4. Spectroelectrochemistry

To further investigate the electrochemical nature of ExtA a potentiometric titration was performed, utilising ITO electrodes as they are optically transparent allowing spectra of ExtA to be captured at defined potentials. Adsorption of ExtA was done following the same procedure for PFV. The ITO electrode containing adsorbed ExtA was then anaerobically sealed in a three-electrode chemical cell, containing an Ag/AgCl reference electrode and a platinum counter electrode. The electrode cell was positioned in a Jasco 6000 UV/visible spectrometer with a bare ITO electrode, in a buffer solution of 50 mM Tris and 100 mM NaCl pH 8, positioned in the reference beam. Spectra were taken at 50 mV intervals between the range of 0 to -800 mV vs Ag/AgCl at room temperature. The Ag/AgCl electrode was calibrated after each run by performing cyclic voltammetry with potassium ferricyanide, using the AgCl-coated wire as a reference electrode. The midpoint potential was measured and equated to +420 mV vs SHE. Measurements were taken in both reductive and oxidative directions to ensure the reduction of ExtA was reversible.

The spectra of ExtA adsorbed to ITO electrode poised at varying potentials are shown in *Figure 4.9A*. By decreasing the potential ExtA is poised at spectral features characteristic of reduced ExtA begin to be formed after the potential is lower than 70 mV vs SHE with full reduction of ExtA seen at -530 mV vs SHE. The formation of the split-Soret can be seen across the potential window as well as the appearance of the α and β peaks at 552 and 524 nm respectively, identical to features seen of ExtA in solution reduced with sodium dithionite.

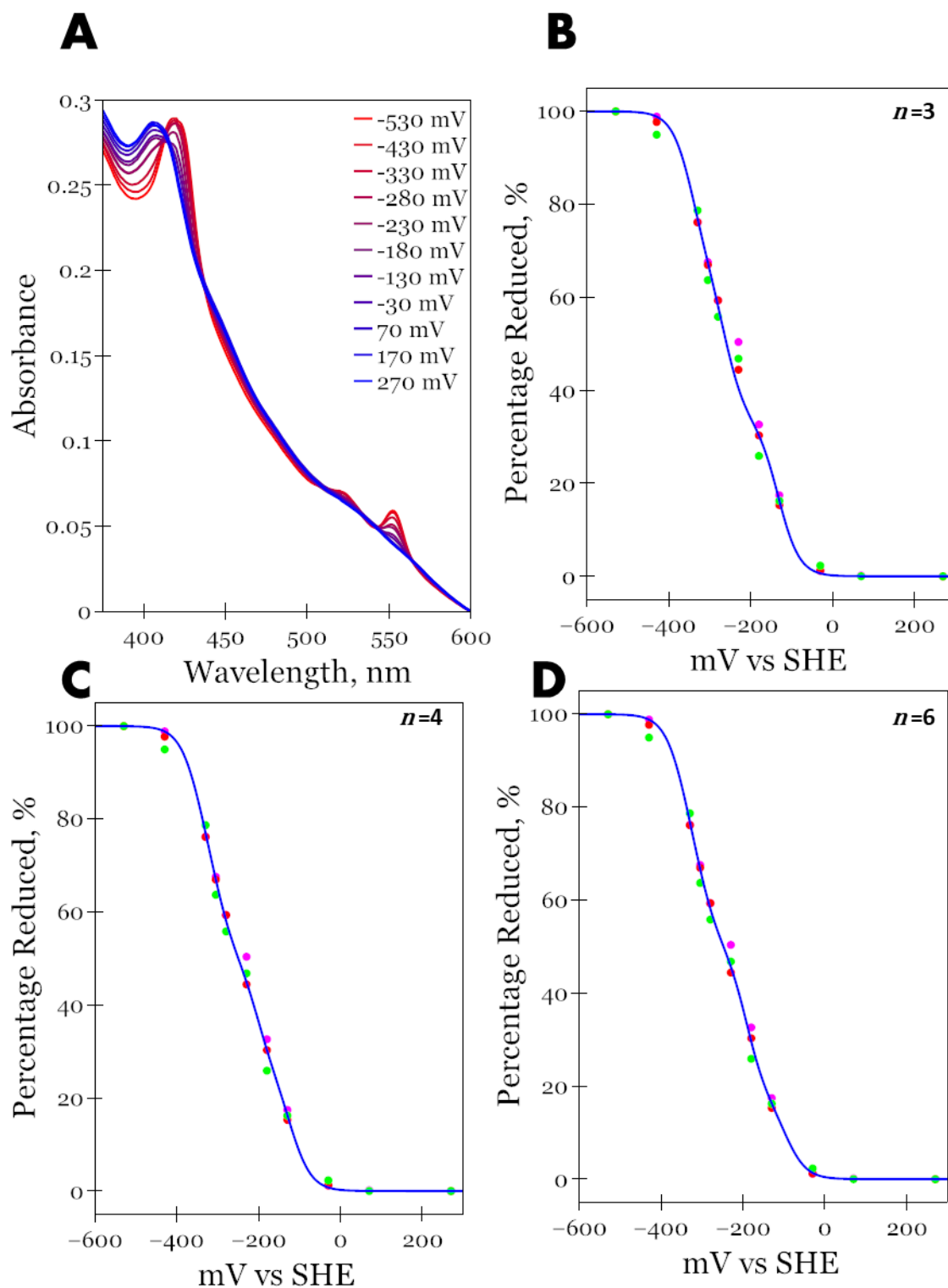


Figure 4.9-Analysis of spectroelectrochemical assessment of ExtA adsorbed onto ITO electrode
 A) Spectrum of ExtA adsorbed on ITO electrode poised at varying potentials, 270 to -530 mV vs SHE. B-D) Using the absorption change at 552 nm the percentage reduced of ExtA was calculated by using the spectrum at 270 mV at 0% reduced and the spectrum at -530 mV as 100% reduced. The Nernst Equation (blue line) was then fitted to experimental data (coloured dots) using B) $n=3$ C) $n=4$ D) $n=6$

From the spectra recorded the absorbance at 552 nm was noted, the α -band, and was plotted as a function against the potential at which the spectrum was recorded. The highest absorbance at 552 nm was correlated with ExtA being 100 % reduced, and *vice a versa* with the lowest absorbance correlating to 0 % reduction. This generated a plot showing the percentage reduction of ExtA across the active redox window. The data was then fitted to the Nernst equation using three, four and six $n=1$ redox reactions, *Figure 4.9B-D*, as was previously done with PFV. Fitting of the Nernst equation using three $n=1$ reactions generated a fit which overlaid closely to the experimental data with few deviations. Fitting the Nernst equation to the data using four and six $n=1$ redox reactions yielded a very close match to the experimental data. For each simulated Nernst equation, the mean squared error (MSE) was calculated to determine the effectiveness of the simulation fitted to experimental data. The Nernst equation fitting three $n=1$ redox reactions the MSE was calculated to be 4.710, for the fitting of four $n=1$ redox reactions the MSE was calculated to be 0.889 and for the fitting of six $n=1$ redox reactions the MSE was 0.496. Showing that the fitting of three $n=1$ redox reactions is poor and fitting of the data increases drastically with the addition of an extra $n=1$ redox reaction. However, between the fitting of four and six $n=1$ redox reactions, there is only a small change observed in the MSE, with the fitting of six $n=1$ redox reactions being closer to the experimentally calculated. It can therefore be suggested that the use of four $n=1$ redox reactions is sufficient to correctly fit the data, aligning with what was previously also seen with PFV.

Midpoint potentials for the redox centres modelled using the Nernst equation are shown in *Table 4.1* alongside those simulated for PFV. A comparison of the two shows that the midpoint potential for each centre is extremely close, with differences seen between midpoint redox centres ranging from a minimum of 3 mV to a maximum of 58 mV, with the average difference in potential being ± 30 mV. Midpoint potentials simulated from PFV were on average more positive than those derived from the spectroelectrochemical characterisation of ExtA, possibly arising from the use of homemade Ag/AgCl wire in the spectroelectrochemical

analysis of ExtA. A paired t-test was performed to assess the differences between the midpoint potentials between each simulation. For the simulations modelling three $n=1$ redox reactions, the t-test returned a score of 0.072, for four $n=1$ redox reactions a score of 0.036, and for six $n=1$ redox reactions a score of 0.037. As simulations modelling four and six $n=1$ redox reactions had a p-value of less than 0.05 it can be stated that there was no statistical difference between the midpoint potentials simulated between the two methods used. With the simulations modelling $n=4$ redox centres having the closest midpoint potentials, it is probable that these are the most accurate results and that in nature the midpoint potentials of hemes from ExtA are clustered into four groups of three hemes with similar potentials between each cluster.

Table 4.1- Midpoint potentials of redox centres predicted by fitting the Nernst equation to the percentage reduced of cytochrome across a potential window. Data from spectroelectrochemical titration and protein film voltammetry.

Redox Centres	Method	Centre 1, mV	Centre 2, mV	Centre 3, mV	Centre 4, mV	Centre 5, mV	Centre 6, mV
<i>n=3</i>	Titration	-0.132	-0.262	-0.343	-	-	-
	PFV	-0.127	-0.212	-0.305	-	-	-
<i>n=4</i>	Titration	-0.120	-0.203	-0.300	-0.348	-	-
	PFV	-0.115	-0.179	-0.245	-0.320	-	-
<i>n=6</i>	Titration	-0.093	-0.190	-0.192	-0.295	-0.327	-0.352
	PFV	-0.107	-0.147	-0.189	-0.237	-0.280	-0.336

Spectra gathered from the potential controlled UV-Vis absorbance of ExtA were analysed subtracting the positive potential spectrum from the adjacent negative potential spectrum, *Figure 4.10*, therefore showing the differences between the two spectra and allowing for spectral features to be observed as they arise with decreasing potential. Observing the difference spectra, it was seen that the first signs of reduction in ExtA is between -30 and -130 mV vs SHE and then steadily becomes reduced until a fully reduced spectrum is reached a -530 mV vs SHE.

Formation of the split-Soret is seen not to happen in the early stages of cytochrome reduction appearing when ExtA is 77% reduced at -330 mV vs SHE. During the reduction of ExtA it is possible to identify three separate Soret peaks, between 0 and 47 % (-230 mV vs SHE) of ExtA being reduced a Soret peak at 421 nm is identified shifting to 424 nm at 58 % reduced (-280 mV vs SHE) followed by the presence of the split-Soret at 415 and 424 nm from 77 % reduced (-330 mV vs SHE) onwards. This is suggestive of a mixed population of hemes within ExtA that have two distinct reduction potentials probably also causing the signature split Soret as seen in the UV-Vis absorbance.

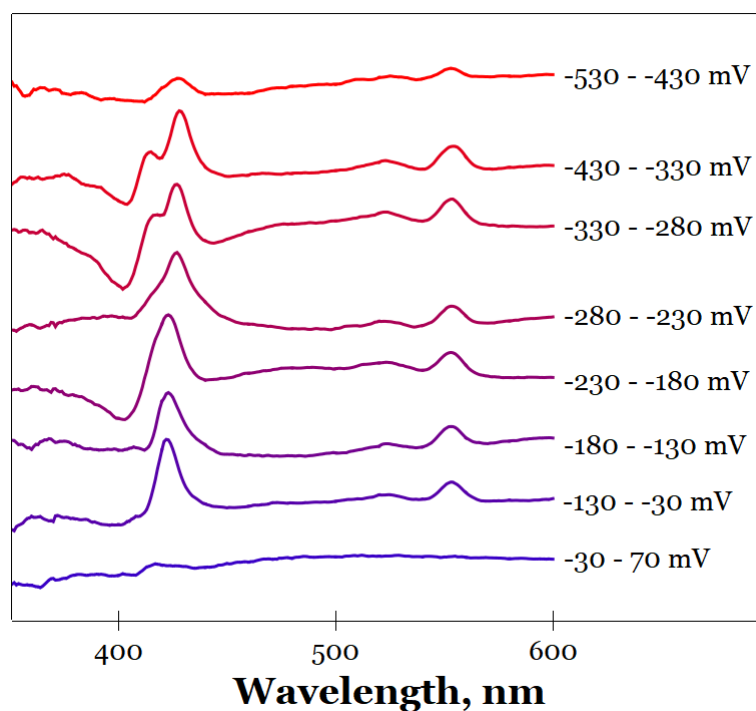


Figure 4.10- Difference spectra taken from ExtA adsorbed to ITO electrodes, potentials reported vs SHE.

4.2.5. Exploration of Oligomeric State of ExtA

Biophysical characterisation of ExtA was performed using sedimentation velocity (SV) in a Beckman Ultra Centrifuge. ExtA was concentrated to 0.6 μM in 100 mM Tris, 150 mM NaCl, 1 mM EDTA and 1 % Glycerol at pH 8 with sedimentation of

analyte monitored using the strong absorbance of the Soret band at 410 nm. Absorbance at 410 nm was recorded periodically throughout the entirety of the SV experiment and correlated to the position of cytochrome in the chamber. Data collected was processed through SEDFIT to obtain the $c(s)$ distribution by fitting the absorbance data to the Lamm equation, *Figure 4.11*. The partial specific volume of ExtA was predicted using SOMO¹⁰ and the buffer properties using SEDNTERP 3¹¹.

Analysis revealed a $c(s)$ distribution with a predominant peak correlating to a sedimentation coefficient, converted to S_{w20} , of 4.96 S with a frictional coefficient (f/f_0) of 1.55. The molecular mass was estimated from this peak at 129.5 kDa differing greatly from the molecular mass of ExtA seen through LC-MS of 39.2 kDa. However, this molecular mass approximately correlates to ExtA having a trimeric stoichiometry. Using the observed mass from LC-MS a trimeric version of ExtA would be expected to have a molecular mass of 117.6 kDa which is only 12 kDa lower than that predicted through SV. This sedimentation peak contributes the majority of the absorbance data collected and therefore it is predicted that whilst in solution ExtA is predominately present in a trimeric conformation. Under the assumption that ExtA is trimeric, the frictional ratio was calculated to be 1.78 suggesting that ExtA is elongated at the poles at diverges from the geometry of a perfect sphere.

The $c(s)$ distribution also shows smaller peaks at 2.43 S and 7.18 S which correlate to 2.50 and 1.87% of the total absorption spectra respectively. The peak at 2.43 S correlates to a molecular weight of 46.1 kDa whilst the peak at 7.10 S correlates to a molecular weight of 234 kDa possibly representing a monomeric and hexameric form of ExtA. This suggests that whilst the most dominant form of ExtA is trimeric, in solution ExtA is dynamic and shifts between monomeric, trimeric and hexameric conformations.

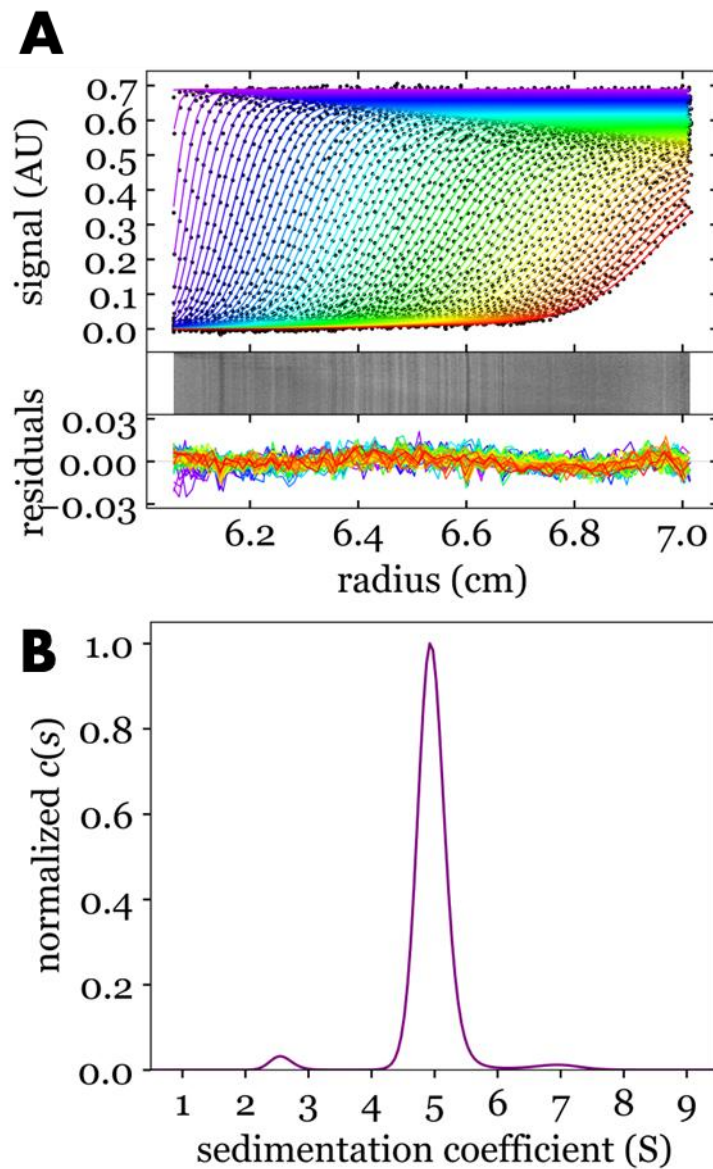


Figure 4.11 –Sedimentation Velocity of ExtA at 0.6 μM . A) Sedimentation velocity of ExtA monitored at 410 nm fitted to the Lamm equation B) $c(s)$ distribution from Sedimentation Velocity

To further investigate the proposed trimeric state, Sedimentation Equilibrium (SE) was performed to reinforce the trimer characterisation, *Figure 4.12*. SE was run with concentrations of ExtA at 0.24, 0.78 and 2.13 μM , calculated based on monomeric conformation. Sedimentation was monitored using UV-vis absorbance at 410 nm for the lower concentrations and 552 nm for the strongest concentration, based on the position of the Soret and the Q-bands. Data was analysed and fitted to a 1-component model using Sedfit and Sedphat. Using SE

to estimate the molecular mass of ExtA at 122.126, 116.552 and 110.179 kDa respectively across the three concentrations analysed. Further suggesting that ExtA is dominantly in a trimeric state whilst in solution.

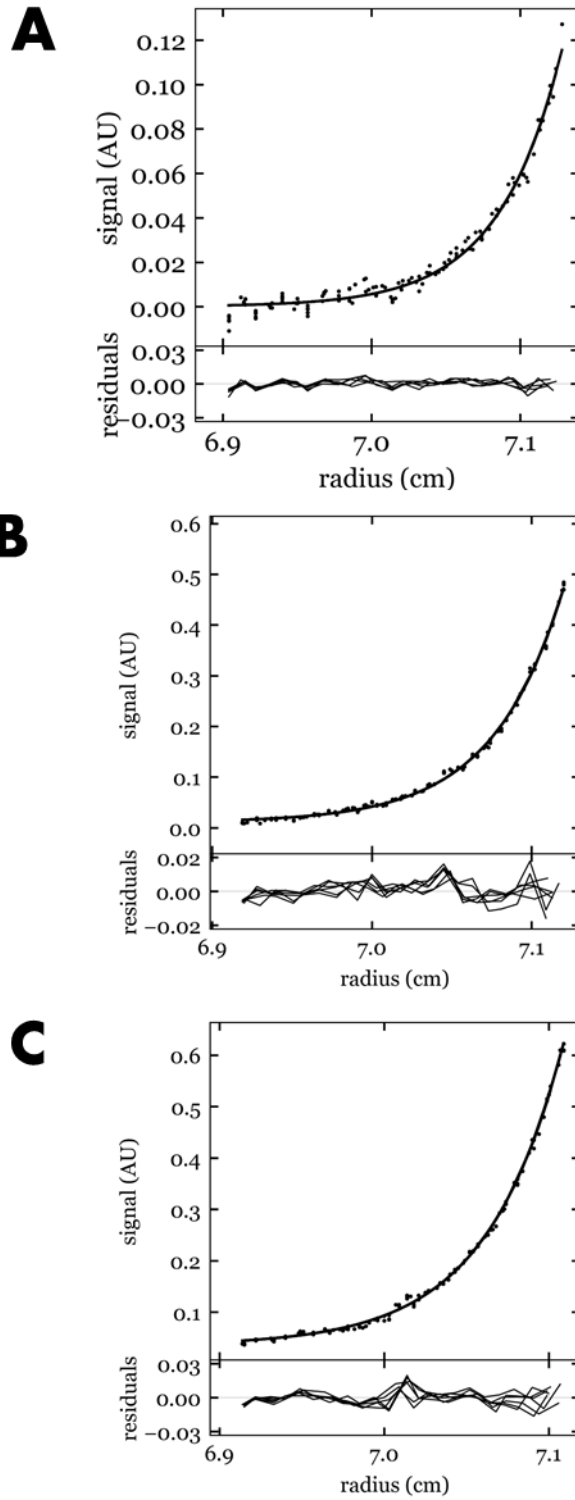


Figure 4.12 –Sedimentation equilibrium of ExtA at A) 0.24 μM , B) 0.78 μM and C) 2.13 μM

A final investigation into the trimeric state of ExtA was performed using analytical gel filtration. Generation of a molecular ruler was first done by taking proteins of known size, *Table 4.2*, and recording the point of elution from a Superose 6 10/300 GL column equilibrated with 100 mM Tris, and 50 mM NaCl at pH 8. The point at which each protein was eluted was recorded to generate a molecular ruler. As BSA was present in both monomeric and dimeric forms two values were obtained.

Table 4.2- Proteins including molecular weights of proteins used to construct molecular ruler using analytical gel filtration

Protein	Molecular Weight, Da
MtrC	75,830
L-Glutamic Dehydrogenase	310,000
ExtD	27,680
L-Lactic Dehydrogenase	70,000
BSA (Dimer)	132,906
BSA (Monomer)	66,453

A molecular weight ruler was constructed, *Figure 4.13*, revealing a linear relationship between the elution profile of the protein and the logarithmic molecular weight. The equation for this line was used to predict the elution profile of ExtA in monomeric and trimeric forms. The elution of ExtA from the column occurred at 16.74 mL and this was plotted on the graph using both the monomeric and trimeric predicted molecular weight. As seen in *Figure 4.12* plotting the elution volume against the monomeric molecular weight falls outside the constructed molecular ruler by a large amount that is outside the expected error. However, plotting the point of elution against the predicted molecular weight for the trimer aligns very closely with the molecular ruler. This therefore suggests that ExtA is in a trimeric conformation. The constructed

molecular ruler showed a linear relationship between the elution point of the protein and the logarithmic molecular weight. Using this relationship to estimate the trimeric molecular mass of ExtA showed that a protein eluted at 16.74 mL corresponds to a molecular mass of 109,911 Da, supporting the hypothesis that ExtA is a trimer in solution.

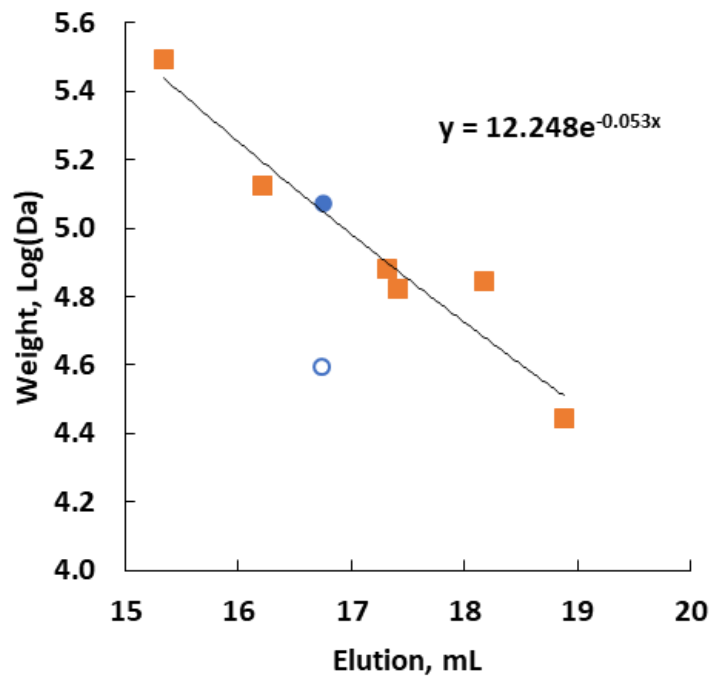


Figure 4.13- Molecular ruler constructed through Analytical Gel Filtration. Proteins were analysed using a Superose 6 10/300 GL column equilibrated with 100 mM Tris, 50 mM NaCl at pH 8. Proteins used to construct ruler are shown in orange plotting the point at which they were eluted from the column against the logarithmic molecular weight. The blue circles show the point at which ExtA was eluted and plotted against the predicted weight of the monomer (hollow circle) and trimer (filled circle).

4.2.6. In-silico modelling of ExtA

A structural model of the ExtA was made using AlphaFold 2 ¹², Figure 4.14. AlphaFold 2 is unable to model cofactors, therefore the 12 c-type hemes predicted to be present in ExtA were manually inserted by aligning a c-type heme from STC (PDB ID: 6HR0) ¹³ to the CxxCH motifs of ExtA. AlphaFold provides a per-residue confidence score, between 0 and 100 %, coined pLDDT (predicted local distance difference test). A pLDDT score is assigned to each amino acid modelled through AlphaFold and determining the average pLDDT for a model simulated can give an insight into the overall probability of the simulation's

credibility. The model of ExtA had an average pLDDT of 89.3 %. The individual pLDDT for each residue was used to colour the AlphaFold model from yellow, pLDDT of residue equal to 0, to magenta, pLDDT of residue equal to 100, as shown in *Figure 4.14*. As can be seen from the model the majority of ExtA is coloured magenta showing a high probability of the model. The lowest scored part of ExtA is present at the N-terminus in the first 42 residues. Before modelling the signal peptide had previously been identified by SignalP 5.0 ⁴ and was not included in the AlphaFold modelling. Therefore, this N-terminus 'coli region' is predicted to be part of the final ExtA protein but does not show any form of secondary structure.

Validation of the ExtA AlphaFold model can be seen with the manual insertion of all 12 c-type hemes. All hemes were able to be inserted without causing any steric hindrance with the AlphaFold model. All c-type hemes were predicted to be bis-His ligated, as shown in *Figure 4.14B*. All hemes were shown to either be aligned through canonical heme stacking, t-shaped and antiparallel, apart from Heme 8 and 9 which appear to be stacked edge-to-edge adjacent to each other. This is outside the canonical heme stacking generally observed by heme cofactors ¹⁴.

ExtA was additionally modelled with the newly available AlphaFold 3 ¹⁵. Modelling with AlphaFold 3 yielded an identical model to that of AlphaFold 2 and is therefore not shown here. The models were both structurally compared to previously published structures available in the PDB using PDBeFold. However no significant structural homologues were identified.

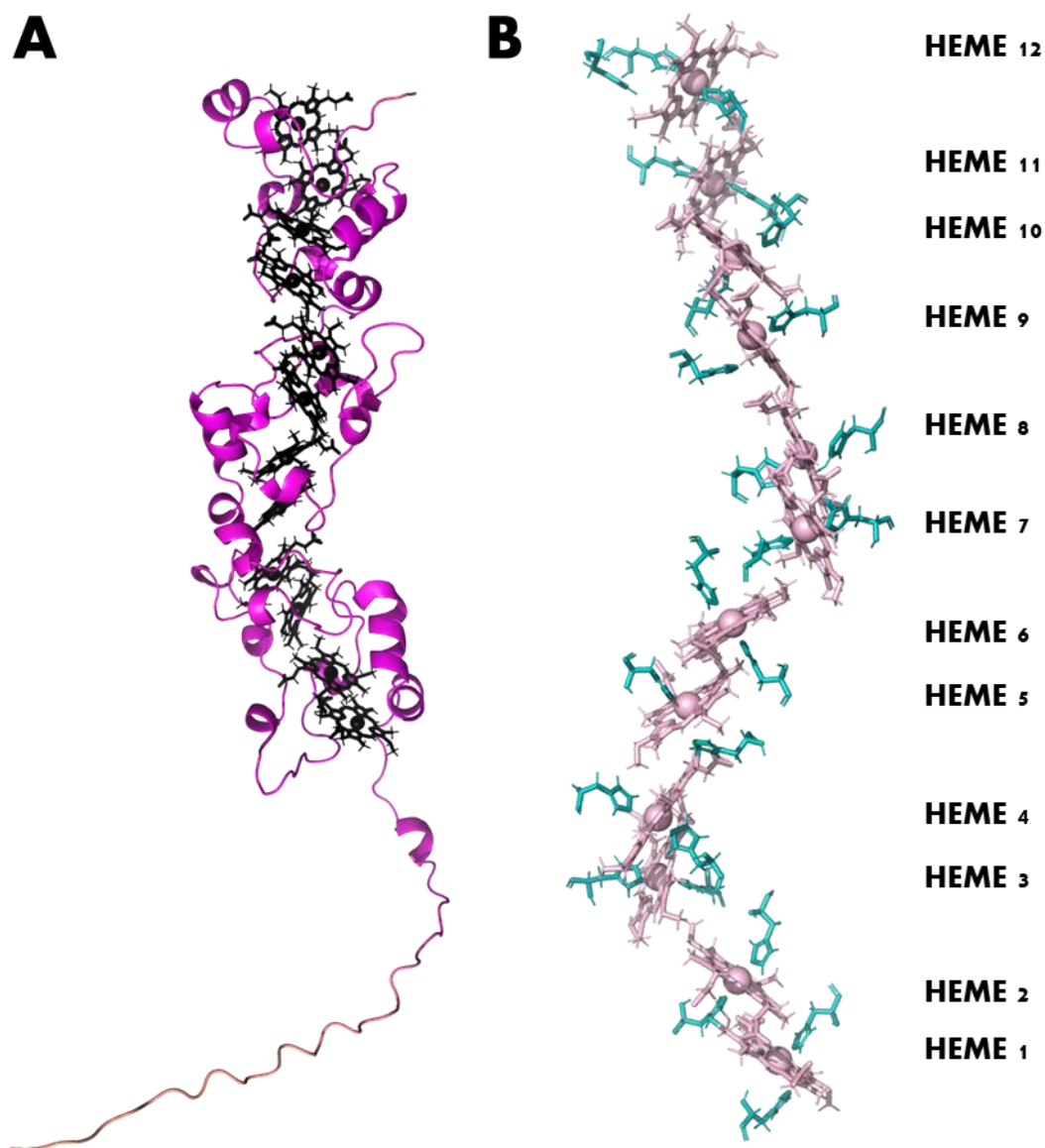


Figure 4.14- AlphaFold model of ExtA. A) Cartoon representation of ExtA. Coloured according to pLDDT value from 100 (pink) to 0 (yellow). Hemes were inserted manually after modelling and coloured black as they have no assigned pLDDT value. B) Manually inserted heme showing bis-His axial ligation. Hemes numbered through covalent attachment to CxxCH residues in ExtA amino acid sequence.

As previous results indicated that ExtA forms a homotrimer in solution AlphaFold was used to simulate a possible structure, *Figure 4.15*. Surprisingly, AlphaFold predicted ExtA to have an unconventional conformation with the N-terminus of each subunit meeting and the unstructured N-terminus 'coil region' attached to an adjacent subunit, generating a heme junction. This heme junction and

corresponding branched filaments of heme arms is, to date, a previously unreported structure seen of any known MHC. The average pLDDT of the trimeric model of ExtA is 81.92 % a decrease of 7.38 % from the monomeric simulation of ExtA. This decrease is not unexpected as AlphaFold is now modelling proteins three times larger than when modelling the monomeric conformation. An average pLDDT score of 81.92 is a strong confidence score and describes a model where the backbone of protein structure is hypothesised to be correct with side chains in approximately the correct position ¹².

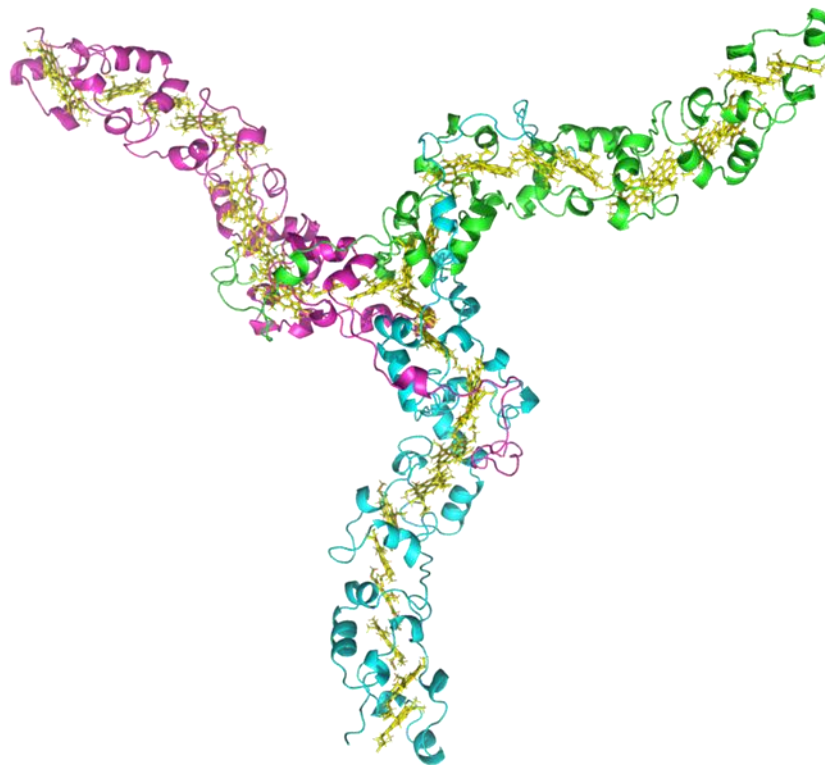


Figure 4.15- Trimeric model of ExtA generated through AlphaFold multimer

To ensure that a bias was not generated by only modelling ExtA as a trimer AlphaFold was also used to model dimeric, tetrameric states of ExtA. Both states yielded lower average pLDDT of 76.73 and 54.75 %. This is unexpected as the increasing oligomeric state of proteins modelled through AlphaFold would be predicted to lower the average pLDDT of the simulation. As both of the average pLDDT are lower than that of the trimeric conformation it can be inferred that the trimeric conformation stabilises the interaction between the monomers in a

way that the dimeric and tetrameric forms are unable. The dimeric and tetrameric models of ExtA are shown in *Figure 4.16*, models do not include hemes.

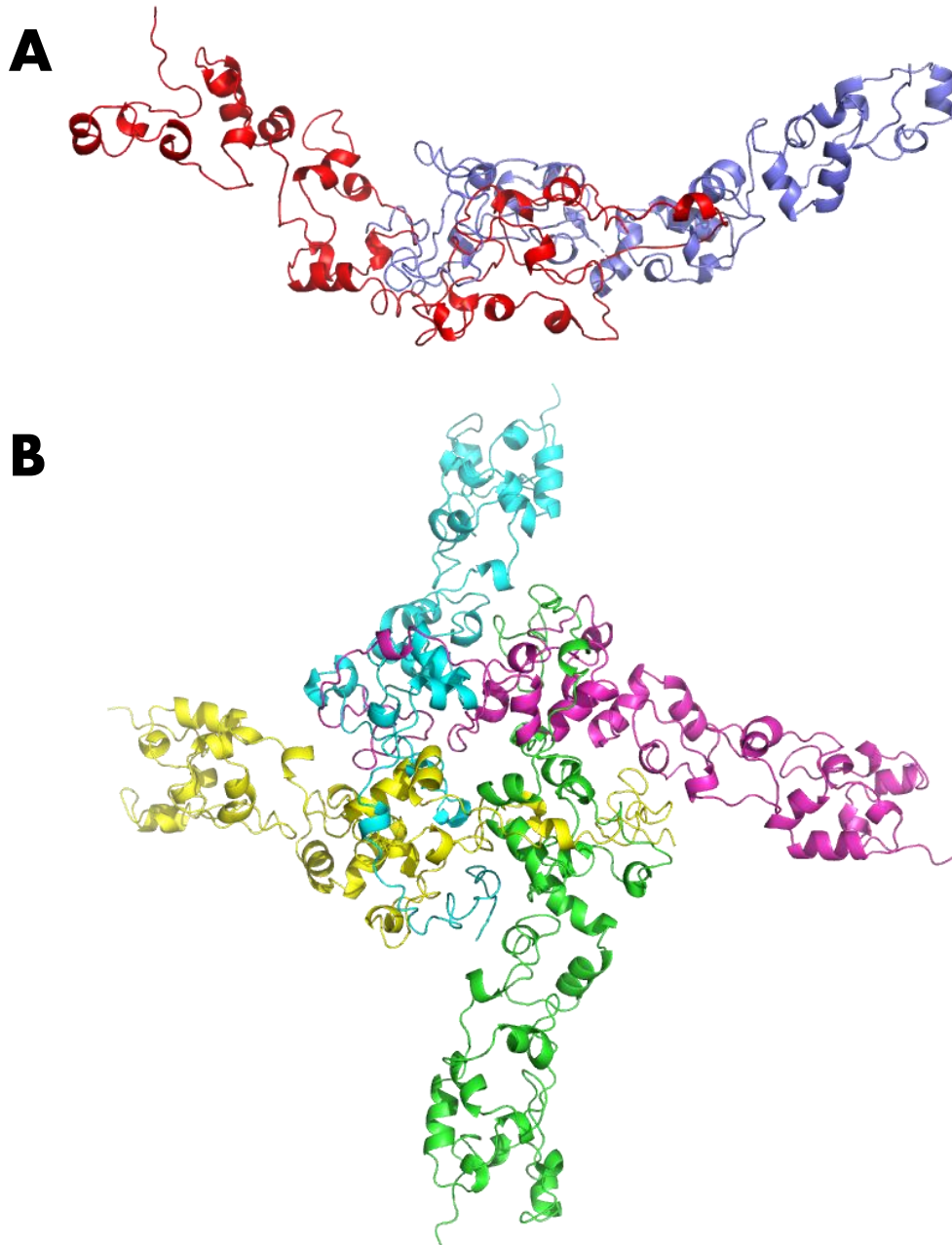


Figure 4.16- AlphaFold 2 models of A) dimeric and B) tetrameric ExtA. Heme cofactors not shown.

By comparing experimental data to estimated values predicted through SOMO¹⁰ of the AlphaFold modeling of ExtA as a monomer and a trimer a distinct conclusion can be made that the majority of the data aligns with the trimeric prediction of ExtA, *Table 4.3*. The molecular weight determined through SV, SE and analytical gel filtration all align to confirm the hypothesis that ExtA forms a homo trimer in solution. Only the LC-MS molecular weight is keeping with the monomeric molecular weight, this is likely due to the protein being denatured through this process and therefore unable to form a stable trimeric complex.

Table 4.3- Comparison of experimentally determined physical characteristics of ExtA in solution to in-silico models of monomeric and trimeric ExtA. Experimental values determined through sedimentation velocity. Values relating to monomeric and trimeric models predicted through use of SOMO

Experimental Method	Molecular Weight, Da	Sedimentation Coefficient, S_{w20}
Mass Spectroscopy	39,218	-
Sedimentation Velocity	129,500	4.96
Sedimentation Equilibrium	116,285	-
Analytical Gel Filtration	109,911	-
AlphaFold Simulation		
Monomeric	38843	2.21
Trimeric	116,530	4.67

4.2.7. N-terminus truncation of ExtA

From the AlphaFold model, it was hypothesised that trimerization of ExtA occurred at the N-terminus of ExtA. This hypothesis was tested by generating an ExtA construct that did not contain the 42 amino acids that make up the ‘coil’ region before the first heme cofactor is present. The removal of these residues was performed using Golden Gate PCR.

Golden Gate PCR primers ‘ExtA_SignalPep_For’ paired with ‘ExtA_SignalPep_Rev’ and ‘ExtA_Heme_For’ paired with ‘ExtA_Heme_Rev’ were used to amplify two fragments of the *extA* gene from *pMEGGAx_extA*, bases 1-72 and 203-903 respectively. Fragments contained both 5’ and 3’ recognition sites for the Esp3I restriction enzyme alongside complementary stick ends for

insertion into the *pMEGGAx* vector, therefore making the total length of the two fragments 99 bases and 734 bases. The amplification of these two fragments can be seen in *Figure 4.17A*. Amplified DNA was gel extracted and cleaned following the GenElute Gel Extraction Kit from Sigma. Extracted DNA fragments were combined with *pMEGGAx* in a Golden Gate reaction generating the new plasmid *pMEGGAx_extA.1*, which encodes the N-terminus truncated ExtA construct under an inducible arabinose promoter. The product of the Golden Gate reaction was run on DNA agarose gel, *Figure 4.17B* the *pMEGGAx_extA.1* vector is predicted to have a size of 4,807 base pairs, on the agarose gel the plasmid band appears at a smaller mass due to being in a supercoiled state. The plasmid was then later sequenced by Eurofins to confirm the correct insertion of *extA.1* gene.

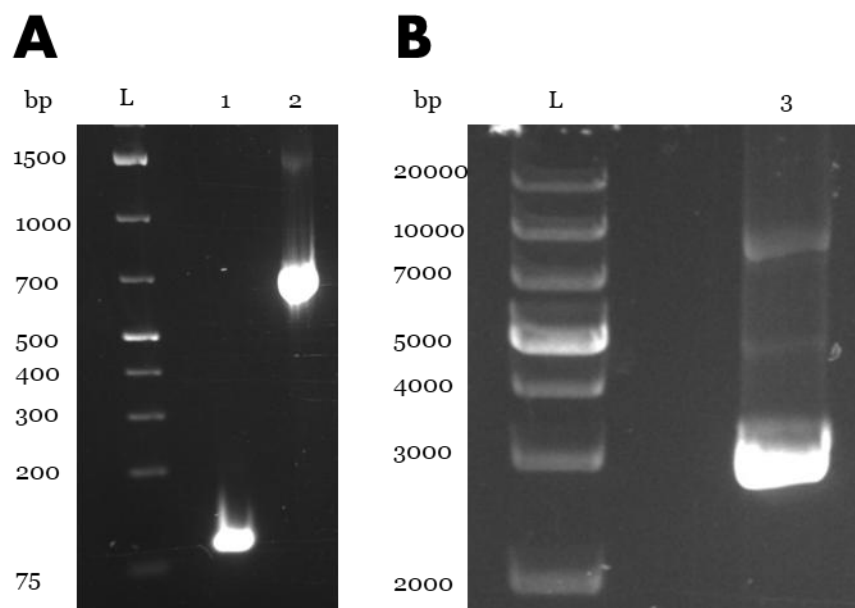


*Figure 4.17- Agarose Gel Electrophoresis of A) DNA amplification of fragments for Golden Gate reaction. Lane 1 product of primer pair 'ExtA_SignalPep_For' and 'ExtA_SignalPep_Rev' predicted to be 99 base pairs in length. Lane 2 primer pair 'ExtA_Heme_For' and 'ExtA_Heme_Rev' predicted to be 734 base pairs in length. B) Lane 3 product of Golden Gate reaction producing vector *pMEGGAx_extA.1* predicted to be 4,807 base pairs in length.*

Expression and purification of N-truncated ExtA (ExtA.1) was performed under the same conditions as full length ExtA. LS527 cells expressing ExtA.1 were lysed and ExtA.1 was extracted from cell lysate using affinity chromatography with the

STREP-tactin from Cytiva. Purified ExtA.1 was then analysed using SDS-PAGE to see if a change in protein mass could be determined from the full length ExtA, *Figure 4.18*. A change in the mass of ExtA to ExtA.1 can be observed with the full length ExtA cytochrome being just under 37 kDa and the N-truncated ExtA.1 being just above 25 kDa. The expected mass of ExtA.1 is 34,891 kDa

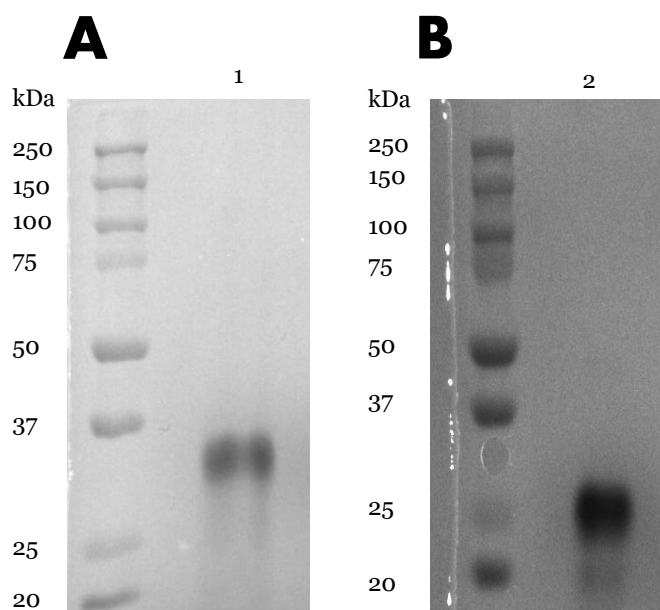


Figure 4.18- SDS Page gel of A) Full length ExtA predicted to form homo-trimer and B) N-terminus truncated ExtA. Both gels were visualised using peroxidase linked heme staining

Spectra of ExtA.1, *Figure 4.19A*, portrays vastly different spectral features than full form ExtA, being closer in formation to that of typical cytochrome spectra. The oxidised spectra show a Soret peak at 407 nm which shifts to 421 nm when the cytochrome becomes reduced. The Q-bands for ExtA.1 are comparable to the full length ExtA spectrum however a minimal blue-shift is observed with the α -band and β -band now present at 552 and 522 nm respectively. For comparison the spectra of ExtA is additional shown in *Figure 4.19B*.

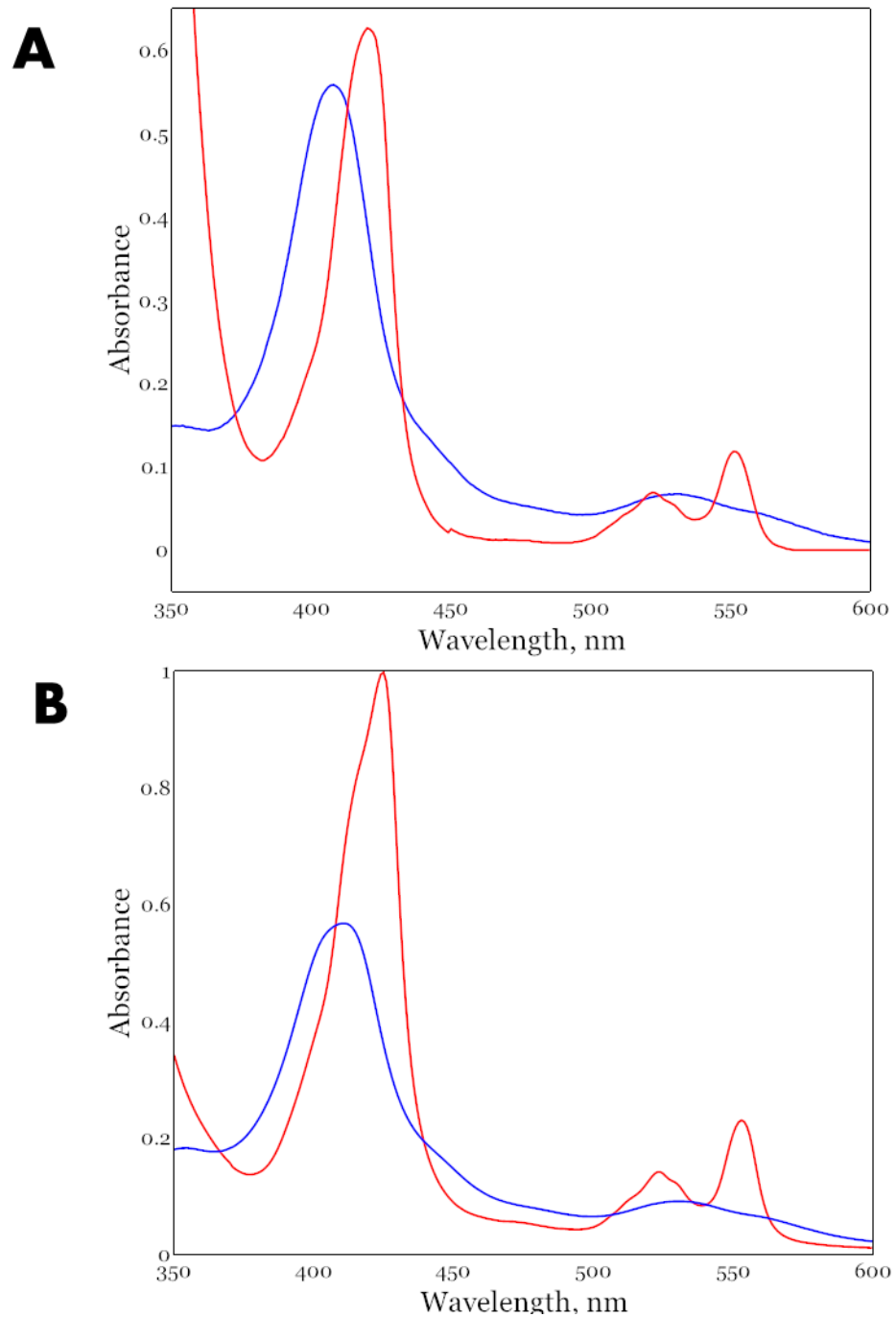


Figure 4.19- Spectra of A) ExtA.1 and B) ExtA under air oxidised (blue) and reduced with 10 μ M sodium dithionite (red)

SV was repeated using the ExtA.1 construct to determine if trimerization of the cytochrome had been prevented by removal of the unstructured N-terminus coil, Figure 4.20. A sample of ExtA.1 at 0.6 μ M in 100 mM Tris, 150 mM NaCl and 1 mM EDTA at pH 8 was analysed by ultracentrifugation with absorbance at 410 nm recorded periodically throughout the experiment. Data from the ExtA.1 SV

experiment was fitted to the Lamm equation using Sedfit and revealing a $c(s)$ distribution with a peak at 3.02 S (S_{w20}) corresponding to a molecular mass of 30.9 kDa, with the predicted mass of the ExtA.1 construct being 34.9 kDa. The results indicate that the ExtA.1 construct is no longer in a trimeric conformation, suggesting that the coil region of the N-terminus is essential for this polymerization.

Comparison to the SV data for trimeric ExtA the data for ExtA.1 demonstrates a monomeric cytochrome in solution with no evidence of a trimeric conformation. The frictional ratio associated with this mass was found to be 1.12, compared to ExtA full length which had a frictional ratio of 1.55 suggesting that removal of the N-terminus coil region causes ExtA.1 to be less elongated compared to the trimeric ExtA. Comparison of the sedimentation profile seen from ExtA.1 to the sedimentation peak correlating to the believed monomeric ExtA, from the untruncated SV experiment, reveals small changes between the two caused by the removal of the N-terminus coil. With the N-terminus coil still present monomeric ExtA has a sedimentation coefficient, converted to S_{w20} , of 2.43 S which is increased to 3.02 S in the ExtA.1 construct. A possible explanation for this is that with the N-terminus coil present the buoyancy of the cytochrome is higher and when removed the cytochrome is more easily sedimented and thus has a larger sedimentation coefficient.

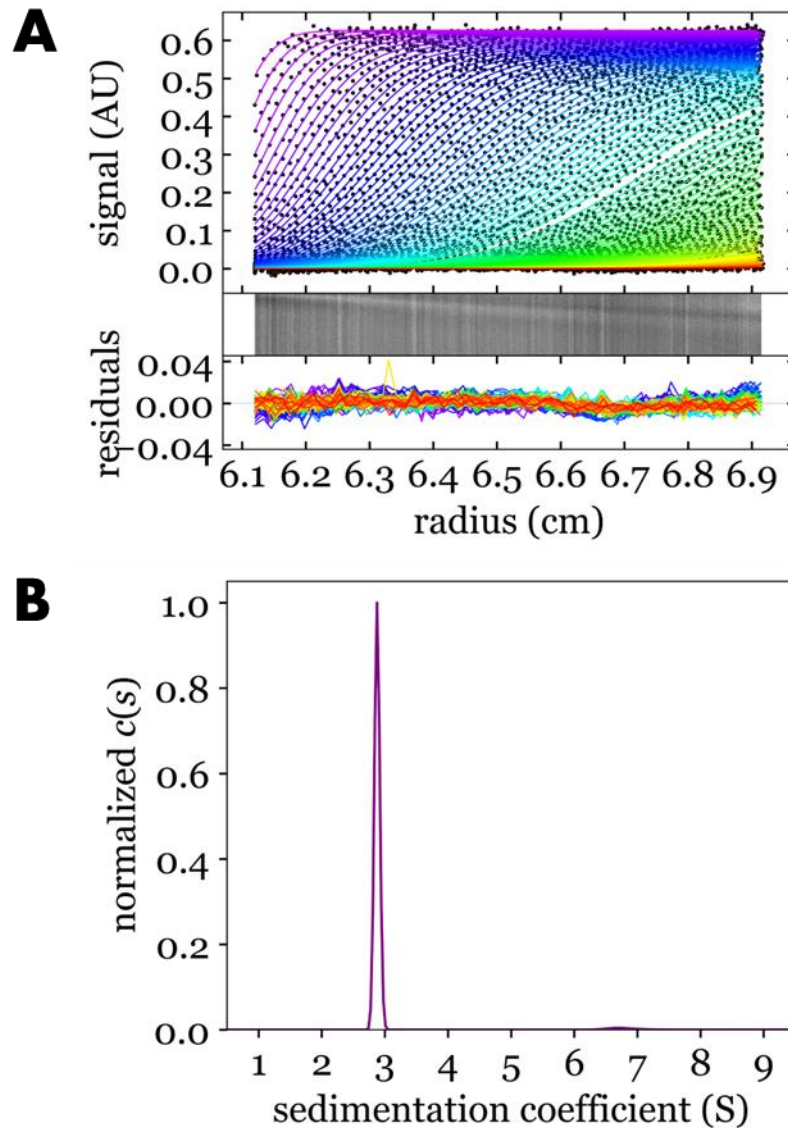


Figure 4.20 –Sedimentation Velocity of ExtA.1 at 0.6 μM . A) Sedimentation velocity data fitted to the Lamm equation B) $c(s)$ distribution from Sedimentation Velocity

4.3. Discussion

Expression and purification of ExtA from *G. sulfurreducens* was performed in this chapter. Whilst the heterologous expression of ExtA using *S. oneidensis* LS527 remained low, resulting in 2.4 ng of protein per litre of culture grown, it allowed for initial characterisation of the cytochrome. Solution based physical characterisation of ExtA revealed a trimeric conformation, with *in situ* structural modelling using AlphaFold suggesting trimerization occurring at the N-terminus of the cytochrome. As ExtA has been expressed heterologously in *Shewanella* it

is not definitive that the trimeric conformation observed will be present in native host *Geobacter*. However, it has previously been shown that expression levels of the genes encoding ExtABCD are not equal in *Geobacter sulfurreducens* PCA¹. Using mRNA to monitor expression levels of the associated genes it was seen that *extC* and *extB* are expressed at similar rates with *extD* being expressed at roughly half this level. Whilst expression levels of *extA* are approximately three times that of *extBC* expression. If ExtA is monomeric in *Geobacter* then the ratio of ExtA to ExtB would be close to 3:1 whilst if the trimeric structure observed is true to native conditions, then the relative ratio of trimeric ExtA to ExtB would be 1:1.

The trimeric structure of ExtA is unique among MHCs having, to knowledge, previously not been a known conformation of any reported MHC. The structure suggests that trimeric ExtA would have three branched chains of hemes with a heme junction located at the N-terminus of the protein. This is a novel discovery which has the potential to revolutionise many aspects of the electromicrobiology field. For example, the branched heme chains of ExtA have the potential to be used in novel biotechnology to build molecular logic gates¹⁶.

ExtA has been predicted to be localised to the outer membrane and insulated in the 'porin-like' β -barrel ExtB. Porin structures in nature commonly form homo-trimers^{17,18} whilst it has not been shown that the 'porin-like' proteins that are found in PCC also behave similarly. Currently, the only structurally determined porin-like protein related to a PCC is MtrB from *Shewanella* which was not identified as forming a homo-trimer¹⁹. Also as stated above the relative abundance of mRNA encoding ExtA is approximately three times higher than that of ExtB therefore the native abundance of ExtA to ExtB is likely 3:1. This nulls the hypothesis of the three arms of ExtA each being associated with ExtB. The role of ExtA is therefore currently undefined but with localisation of ExtA predicted to be in the periplasm it is probable that ExtA acts as a periplasmic shuttle between the inner membrane and ExtBCD.

Protein film voltammetry revealed that ExtA has a potential window of 0 to -450 mV with a midpoint potential of -215 mV. If ExtA does indeed act as a periplasmic shuttle it has an extremely low midpoint potential in comparison to other characterised periplasmic shuttles in *Geobacter*, midpoint potentials are summarised in *Table 4.4*, with the other periplasmic shuttles having a midpoint potential close to 100 mV more positive than that observed by ExtA. The genes encoding ExtABCD are more highly expressed when *Geobacter* cells are grown at lower potentials²⁰. Therefore, it is likely that electrons that reduce ExtABCD are released to the periplasm by the quinol dehydrogenase CbcBA, which has been shown to be essential for the growth of *Geobacter* below -210 mV²¹. Whilst physical characterisation of CbcBA has yet to be performed researchers will likely discover that the midpoint potential is lower than that of other known inner membrane dehydrogenases ImcH and CbcL. Therefore, it is plausible to hypothesise that known periplasmic shuttle PccA-E may not be able to interact with CbcBA or very minimally. Therefore, ExtA with a lower potential than PccA-E would be proposed to interact directly interact with CbcBA and transfer electrons across the periplasm to ExtBCD.

Table 4.4- Midpoint potential of known cytochromes shown from *Geobacter sulfurreducens* PCA hypothesised to be a quinol dehydrogenase or a periplasmic shuttle

Cytochrome	Localization in <i>Geobacter</i>	Midpoint Potential, mV vs SHE	Reference
ImcH	Inner Membrane	-200	22
CbcL	Inner Membrane	-194	23
CbcBA	Inner Membrane	Unknown	N/A
PpcA	Periplasm	-117	24
PpcB	Periplasm	-137	24
PpcC	Periplasm	-143	25
PpcD	Periplasm	-132	26
PpcE	Periplasm	-134	26
GSU1999	Periplasm	-124	25
ExtA	Periplasm	-215	This Work

Geobacter is known to grow on electrodes at low potentials however the relative ATP production associated with this potential is on the border of being sustainable to the cell without any health decrements. The whole of the ExtABCD cluster is known to be expressed highest when cells are grown at a low potential and *Geobacter* has been shown to build an intracytoplasmic membrane under the same conditions^{20,27}.

Spectroscopically ExtA and ExtA.1 displayed unique oxidised and reduced spectra. It was seen that ExtA.1 no longer exhibited the reduced split Soret, suggesting that it was the trimerization of ExtA and branching of heme chains that caused this split-Soret to appear, leading to similar conclusions from the ExtD split-Soret, see Chapter 3.5 for further discussion. Also, of note here is the presence of side-to-side heme stacking in the ExtA model, which as previously discussed may be the cause of the split Soret. However, as the ExtA model is

purely computational based and there is currently no available structure (from X-ray crystallography, Cryo-EM, etc.) it is not possible to determine if the adjacent heme stacking is seen in ExtA. However, whilst the reduced Soret no longer exhibits atypical characteristics the oxidised Soret does not conform to a standard cytochrome. Comparing the spectra of ExtA.1 to MtrC from *Shewanella baltica* the difference in features can be seen. Whilst the half-width height of the MtrC oxidised Soret is 27 nm whilst for ExtA.1 the half-width height is 38 nm. This is a 1.4 times increase in Soret width and suggests that whilst some of the atypical spectroscopy seen from the full length ExtA has been removed through the forced monomerization of the cytochrome, inherent physical characteristics still differ the cytochrome spectroscopy from normative cytochrome spectrum.

4.4. References

1. Jiménez Otero, F., Chan, C. H. & Bond, D. R. Identification of Different Putative Outer Membrane Electron Conduits Necessary for Fe(III) Citrate, Fe(III) Oxide, Mn(IV) Oxide, or Electrode Reduction by *Geobacter sulfurreducens*. *J Bacteriol* **200**, (2018).
2. Jiménez Otero, F. *et al.* Evidence of a Streamlined Extracellular Electron Transfer Pathway from Biofilm Structure, Metabolic Stratification, and Long-Range Electron Transfer Parameters. *Appl Environ Microbiol* **87**, (2021).
3. Hartshorne, R. S. *et al.* Characterization of an electron conduit between bacteria and the extracellular environment. *Proceedings of the National Academy of Sciences* **106**, (2009).
4. Almagro Armenteros, J. J. *et al.* SignalP 5.0 improves signal peptide predictions using deep neural networks. *Nat Biotechnol* **37**, 420–423 (2019).
5. Mayhew, S. G. The Redox Potential of Dithionite and SO₂ from Equilibrium Reactions with Flavodoxins, Methyl Viologen and Hydrogen plus Hydrogenase. *Eur J Biochem* **85**, 535–547 (1978).
6. Barr, I. & Guo, F. Pyridine Hemochromagen Assay for Determining the Concentration of Heme in Purified Protein Solutions. *Bio Protoc* **5**, (2015).
7. Berry, E. A. & Trumpower, B. L. Simultaneous determination of hemes a, b, and c from pyridine hemochrome spectra. *Anal Biochem* **161**, 1–15 (1987).
8. Fourmond, V. QSoas: A Versatile Software for Data Analysis. *Anal Chem* **88**, 5050–5052 (2016).
9. Butt, J. N., Jeuken, L. J. C., Zhang, H., Burton, J. A. J. & Sutton-Cook, A. L. Protein film electrochemistry. *Nature Reviews Methods Primers* **3**, 77 (2023).

10. Brookes, E. & Rocco, M. Recent advances in the UltraScan SOLUTION MOdeller (US-SOMO) hydrodynamic and small-angle scattering data analysis and simulation suite. *European Biophysics Journal* **47**, 855–864 (2018).
11. Philo, J. S. SEDNTERP: a calculation and database utility to aid interpretation of analytical ultracentrifugation and light scattering data. *European Biophysics Journal* (2023).
12. Jumper, J. *et al.* Highly accurate protein structure prediction with AlphaFold. *Nature* **596**, 583–589 (2021).
13. Fonseca, B. M. *et al.* Optimizing Electroactive Organisms: The Effect of Orthologous Proteins. *Front Energy Res* **7**, (2019).
14. Janiak, C. A critical account on π – π stacking in metal complexes with aromatic nitrogen-containing ligands. *Journal of the Chemical Society, Dalton Transactions* 3885–3896 (2000).
15. Abramson, J. *et al.* Accurate structure prediction of biomolecular interactions with AlphaFold 3. *Nature* (2024)
16. Lai, Y.-H., Sun, S.-C. & Chuang, M.-C. Biosensors with Built-In Biomolecular Logic Gates for Practical Applications. *Biosensors (Basel)* **4**, 273–300 (2014).
17. Hancock, R. E. Role of porins in outer membrane permeability. *J Bacteriol* **169**, 929–933 (1987).
18. Weiss, M. S., Wacker, T., Weckesser, J., Weite, W. & Schulz, G. E. The three-dimensional structure of porin from *Rhodobacter capsulatus* at 3 Å resolution. *FEBS Lett* **267**, 268–272 (1990).
19. Edwards, M. J., White, G. F., Butt, J. N., Richardson, D. J. & Clarke, T. A. The Crystal Structure of a Biological Insulated Transmembrane Molecular Wire. *Cell* **181**, 665-673.e10 (2020).
20. Howley, E., Krajmalnik-Brown, R. & Torres, C. I. Cytochrome gene expression shifts in *Geobacter sulfurreducens* to maximize energy conservation in response to changes in redox conditions. *Biosens Bioelectron* **237**, 115524 (2023).
21. Joshi, K., Chan, C. H. & Bond, D. R. *Geobacter sulfurreducens* inner membrane cytochrome CbcBA controls electron transfer and growth yield near the energetic limit of respiration. *Mol Microbiol* **116**, 1124–1139 (2021).
22. Pimenta, A. I. *et al.* Characterization of the inner membrane cytochrome ImcH from *Geobacter* reveals its importance for extracellular electron transfer and energy conservation. *Protein Science* **32**, (2023).
23. Antunes, J. M. A., Silva, M. A., Salgueiro, C. A. & Morgado, L. Electron Flow From the Inner Membrane Towards the Cell Exterior in *Geobacter sulfurreducens*: Biochemical Characterization of Cytochrome CbcL. *Front Microbiol* **13**, (2022).
24. Morgado, L. *et al.* Structural insights into the modulation of the redox properties of two *Geobacter sulfurreducens* homologous triheme cytochromes. *Biochimica et Biophysica Acta (BBA) - Bioenergetics* **1777**, 1157–1165 (2008).

25. Santos, T. C., Silva, M. A., Morgado, L., Dantas, J. M. & Salgueiro, C. A. Diving into the redox properties of *Geobacter sulfurreducens* cytochromes: a model for extracellular electron transfer. *Dalton Transactions* **44**, 9335–9344 (2015).
26. Morgado, L., Bruix, M., Pessanha, M., Londer, Y. Y. & Salgueiro, C. A. Thermodynamic Characterization of a Triheme Cytochrome Family from *Geobacter sulfurreducens* Reveals Mechanistic and Functional Diversity. *Biophys J* **99**, 293–301 (2010).
27. Howley, E., Mangus, A., Williams, D. & Torres, C. I. Intracytoplasmic membranes develop in *Geobacter sulfurreducens* under thermodynamically limiting conditions. *NPJ Biofilms Microbiomes* **9**, 18 (2023).

*Chapter 5: Initial Characterisation of
lipo-cytochrome ExtC as part of the
ExtABCD Porin Cytochrome Complexes
from G. sulfurreducens PCA*

5.1. Introduction

The pentaheme cytochrome ExtC is part of the ExtABCD porin cytochrome complex (PCC) and has previously been predicted to play an essential role in the transfer of electrons across the outer membrane in *Geobacter sulfurreducens* PCA¹. Single gene deletions of *extC* have been shown to result in a drastic decrease in current density produced from *G. sulfurreducens* cells grown on graphite electrodes poised at +240 mV vs SHE, with an approximate 80 % decrease in total current output compared to wildtype¹. This marks ExtC as a key component of the ExtABCD complex, however characterisation of the cytochrome has been limited with no characterisation of ExtC being shown apart from effects of gene deletions. Predicted to be a lipo-cytochrome, ExtC is hypothesised to be covalently bound to the outer membrane of the *G. Sulfurreducens* PCA, alongside ExtD, in order to reduce terminal electron acceptors. Currently, ExtABCD is the only reported PCC to contain two lipo-cytochromes that are both expected to be positioned on the outer leaflet.

The predicted porin-like protein ExtB is expected to be an integral component of the ExtABCD PCC and essential for electron transfer across the outer membrane in *G. sulfurreducens*¹. Porin-like outer membrane proteins are generally homologous to the known porin MtrB from *Shewanella oneidensis* MR-1. MtrB and close homologues have been predicted to contain a total of 28 predicted trans-outer membrane motifs². However, later the structure of MtrB revealed MtrB to be a 26 β -stranded porin³. In contrast, the porin-like protein ExtB was predicted to contain only 20 trans-outer membrane motifs². This implies that ExtB is considerably smaller than its counterparts and the pore formed by ExtB would be decreased in total volume.

In this chapter expression, purification and characterisation of the ExtC cytochrome is performed. However, the yield of ExtC remained low only allowing for basic initial characterisation of the cytochrome and interactions with ExtA/D. An *in-silico* based assessment of the ExtABCD PCC was additionally performed,

informed by previous *in-vitro* analysis from this thesis, to construct a hypothetical structural model of the complex.

5.2. Results

5.2.1. Expression and Initial Physical Characterisation of ExtC

The *extC* gene was kindly provided by Dr Marcus Edwards (Essex University, UK) in the *pMEGGAx* vector, which is arabinose inducible and provides kanamycin resistance to host bacteria. The *extC* gene from *Geobacter sulfurreducens* PCA (gene: GSU2644) was optimised for expression in *Escherichia coli* K12 with signal peptide exchanged from native sequence to signal peptide sequence corresponding to MtrB from *Shewanella oneidensis* MR-1. Additionally, the 5' end of the *extC* gene encoded a HIS tag for ease of purification.

Expression of *extC* was initially trialled in host organisms *E. coli* BL21 and *S. oneidensis* LS527 by varying arabinose induction and harvest time. However, throughout these trials, no ExtC product was visualised from whole-cell SDS-PAGE analysis. An affinity tag switch was performed removing DNA encoding a HIS tag and substituting it with the DNA encoding a STREP-II Tag (SAWSHPQFEK).

Primers were designed to amplify the *extC* gene and the plasmid backbone of *pMEGGAx* not including the genes encoding the HIS-tag. PCR amplification was performed, and the product was assessed using agarose gel electrophoresis, *Figure 5.1*. The expected amplification size was 4498 bp and DNA bands were visualised on the agarose gel between 4000 and 5000 bp, indicative of a successful amplification.

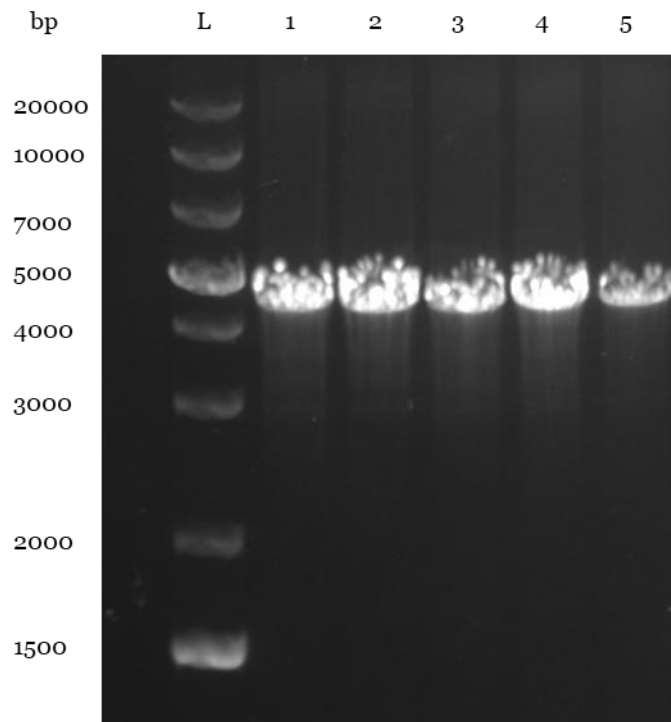


Figure 5.1- Agarose Gel Electrophoresis of product from *extC* affinity tag switch PCR. All lanes show linear PCR product with varied annealing temperatures.

The amplified DNA was then circularised to generate the vector *pMEGGAx_extC_STREP*, encoding the protein ExtC_STREP. The plasmid was sequenced by Eurofins to ensure no mutations had occurred and the *extC_STREP* gene was encoded successfully. The *pMEGGAx_extC_STREP* plasmid was electroporated into *S. oneidensis* LS527 with expression of *extC* following the same protocol as optimised *extD_HIS* expression utilising a STREP-II tag purification over a 6xHis Tag. *S. oneidensis* LS527 cells expressing ExtC were lysed by the French Press and ExtC was purified from cell lysate by affinity chromatography using the STREP-TACTIN XT 4FLOW column.

The predicted amino acid sequence from the optimised *extC* gene is shown in Figure 5.2. The signal peptide of the optimised ExtC is predicted through SignalP 5.0⁴ to be cleaved positions Ala21 and Ala22. The predicted molecular mass of ExtC_STREP was calculated from the protein backbone to be 17,190 Da. ExtC is predicted to covalently bind five c-type hemes through the CxxCH motifs

contained in the sequence. A single c-type heme has a molecular weight of 615.2 Da therefore with the insertion of all five predicted c-type hemes the total molecular mass of ExtC is predicted to be 20,270 Da.

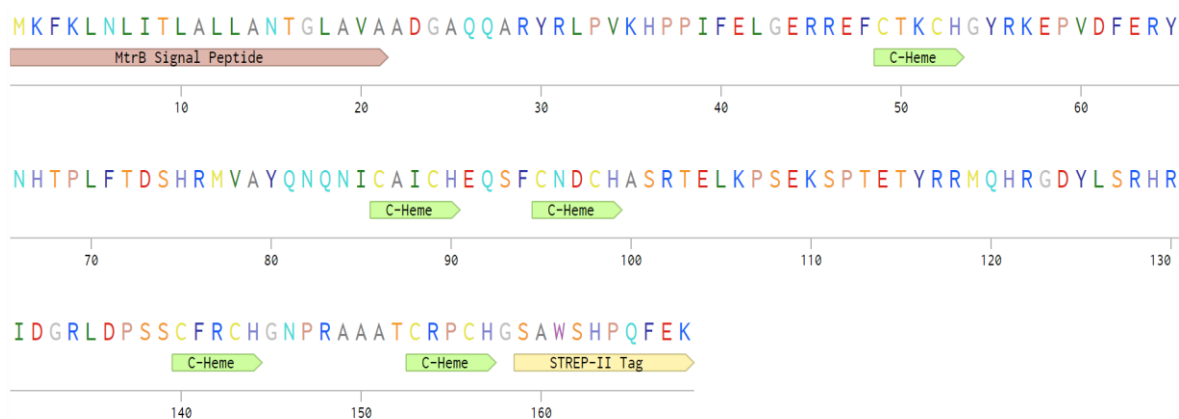


Figure 5.2 - Amino acid sequence of ExtC from optimised *extC* gene.

Purification of ExtC from *S. oneidensis* LS527 expressing cells was performed using affinity chromatography with the STREP column. Heme containing product from purification was consolidated and passed through a size exclusion column (SEC) before being analysed with SDS-PAGE. Visualization of heme-containing proteins was performed using peroxidase-linked heme-staining, Figure 5.3. A cytochrome was visualized between the molecular markers for 10 and 20 kDa, this is lower than the predicted mass of 20.2 kDa. No other cytochrome was in the SDS-PAGE and therefore is determined to be pure. AKTA product was additionally analysed using Coomassie Blue allowing for visualization of all proteins in the sample, Figure 5.2B. There are two distinct protein bands seen in the Coomassie stained gel, the ExtC band around 20 kDa and a band corresponding to a higher mass at approximately 50 kDa. Therefore, whilst the ExtC containing fraction was heme pure it still contained protein contaminants, even after size exclusion chromatography.

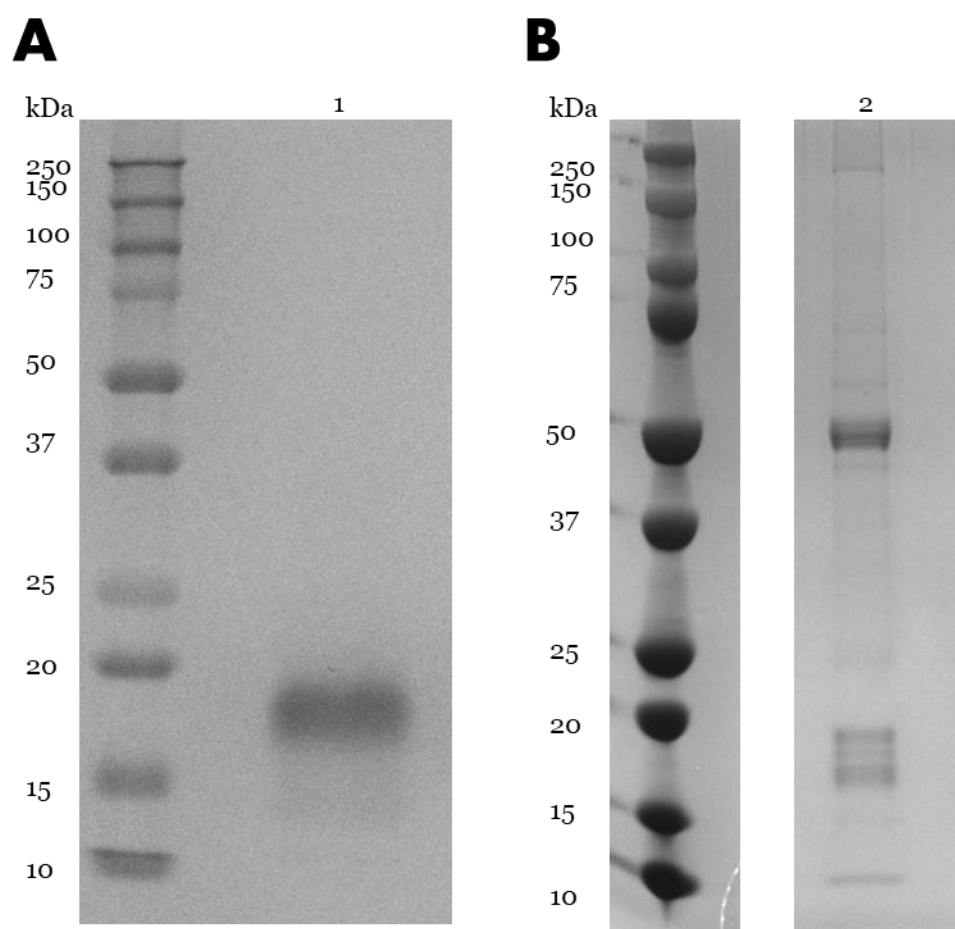


Figure 5.3- SDS-PAGE of product from STREP-II tag affinity chromatography using AKTA prime. Sample from LS527 cells expressing ExtC. A) Protein visualized with peroxidase linked heme staining. B) Protein visualized with Coomassie Blue.

The yield of ExtC purified from *S. oneidensis* LS527 cultures was extremely low and therefore in-depth characterisation of the cytochrome could not be conducted. The quantity of ExtC harvested from 1 L of *S. oneidensis* LS527 was calculated to be 0.85 ng. Additionally, ExtC was observed to be prone to degradation with protein samples being highly unstable and unsuitable for long-term storage. Therefore, techniques were utilised that rely on the strong spectral properties of the heme cofactors without the need for high concentrations of the cytochrome.

Purified ExtC was spectrally characterised using UV-visible absorbance between 350-700 nm. Spectra were taken under air oxidised and reducing the cytochrome

with an excess of sodium dithionite, *Figure 5.4*. A Soret maxima was observed at 408 nm transitioning to a Soret maxima at 420 nm when reduced with excess sodium dithionite. The appearance of α - and β - bands in the reduced ExtC spectrum was seen at 550 and 522 nm respectively. Unlike other cytochromes of the ExtABCD complex ExtC displays canonical heme spectral properties⁵ with no evidence of a split Soret present, as was previously seen with ExtA and ExtD.

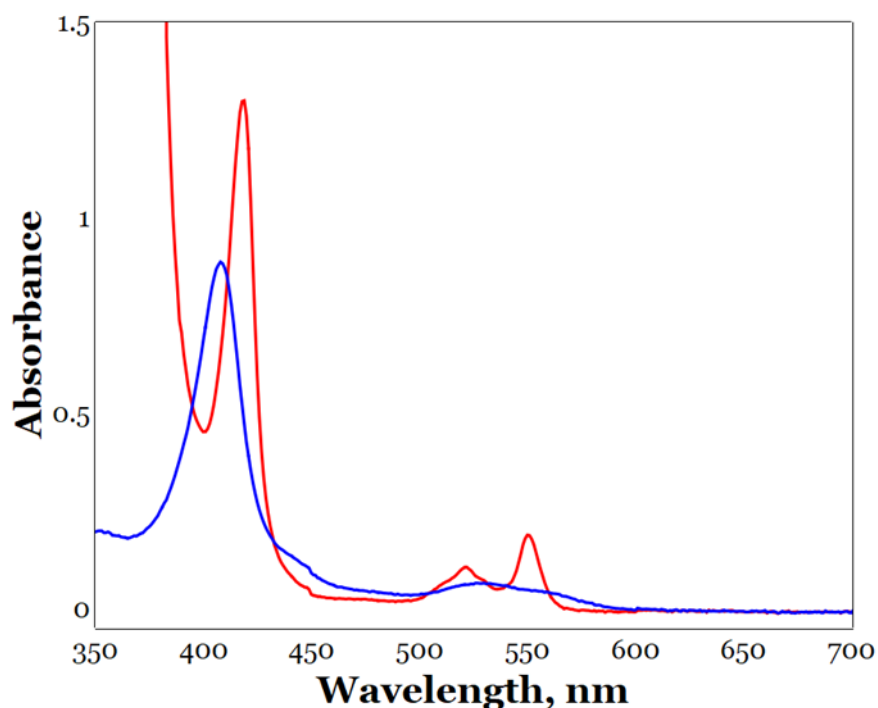


Figure 5.4- UV-visible absorbance spectra of air oxidised ExtC (blue) and sodium dithionite reduced (red)

The extinction coefficient of ExtC was determined using the pyridine hemochromagen assay⁶. Spectra of ExtC under native and denatured with pyridine conditions were recorded. Both samples were prepared from the same cytochrome stock and diluted with equal volumes of either 100 mM Tris, 150 mM NaCl and 1 mM EDTA 0.5 % glycerol or 0.1 M NaOH and 20 % (v/v) pyridine. The extinction coefficient was determined by calculating the difference spectra of reduced minus oxidised spectra from ExtC treated with pyridine. The literature value⁷ for a single bis-pyridine ligated c-type heme of $\epsilon_{550-535} = 23.97 \text{ mM}^{-1}\text{cm}^{-1}$

was used to calculate the $\epsilon_{550-535}$ of ExtC treated with pyridine, $119.85 \text{ mM}^{-1}\text{cm}^{-1}$. From this, the concentration of the ExtC samples was determined to be 942.84 nM . The extinction coefficient of ExtC at 408 nm was then calculated from the native spectra taken of ExtC, giving a value of $\epsilon_{408} = 620.40 \text{ mM}^{-1}\text{cm}^{-1}$.

The physical properties of ExtC in solution were assessed using the analytical ultracentrifuge (AUC) technique sedimentation velocity (SV) in order to determine the oligomeric state and approximate size. Sedimentation of ExtC was measured using absorbance spectroscopy measuring at 410 nm whilst centrifuging. Absorbance data was collected at timed intervals throughout the SV run with analysis performed afterwards using SEDFIT⁸ to fit the results to the Lamm equation, *Figure 5.5*. In the $c(s)$ distribution, a main peak at 2.18 S (S_{w20}) was observed. This sedimentation peak correlates to a frictional coefficient of 1.12 and has an estimated molecular mass of $19,974 \text{ Da}$. This molecular mass aligns closely with the predicted molecular mass calculated from the amino acid sequence of $20,026 \text{ Da}$. Therefore, it is concluded that the sedimentation coefficient of 2.18 S also correlated to ExtC. The presence of a larger peak at 7.26 S was also noted in the $c(s)$ distribution, however the origin of this peak is unknown, as no other cytochrome was present on SDS-PAGE gel, and likely caused by aggregation of ExtC.

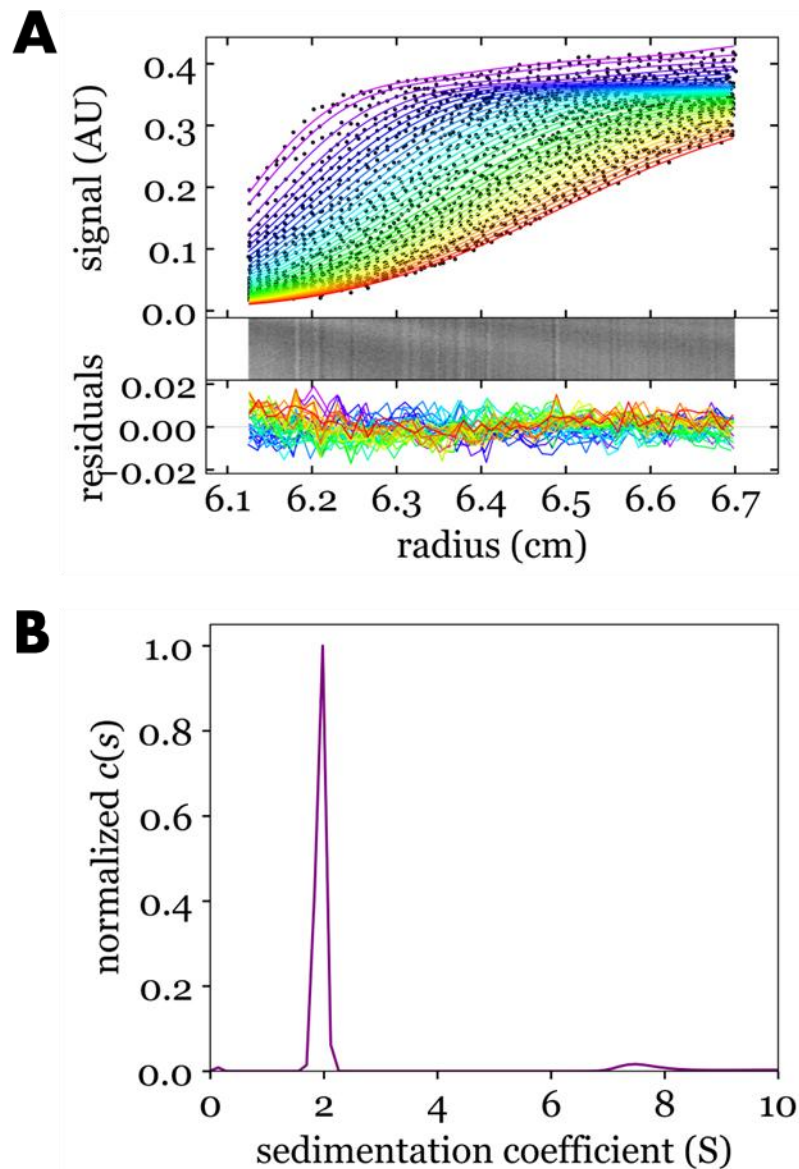


Figure 5.5- Sedimentation velocity analysis of ExtC at 1.12 μM . A) Absorbance data fitted to Lamm equation. B) $c(s)$ distribution of SV produced using SEDFIT.

AlphaFold 2⁹ was used to produce a structural model for ExtC using the native amino acid sequence, *Figure 5.6*. Before structural modelling, the signal peptide of ExtC was identified by SignalP 5.0⁴ and removed. ExtC is predicted to be a lipoprotein and analysis of the amino acid sequence reveals a lipid box of 'VVSC'. Typically, the -3 residue in a lipobox is a Leu residue but in the case of ExtC the -3 residue is instead a Val residue, this is an uncommon residue to find in this position and accounts for approximately 4 % of known lipoboxes¹⁰. Cleavage of

the signal peptide between Ser20 and Cys21 was additionally predicted by SignalP 5.0⁴. As AlphaFold 2 is not able to model cofactors, hemes were manually inserted by aligning a c-type heme from the periplasmic shuttle STC of *Shewanella algae* (PDB ID: 6HR0)¹¹ to the CxxCH motifs of ExtC. All models predicted through AlphaFold have a predicted local-distance difference test (pLDDT) which gives a confidence score for each residue between 0, low confidence, and 100, high confidence. The pLDDT score can be averaged for the entire simulation and used to describe the overall confidence of the model. For the simulated ExtC model the average pLDDT score is 81.5 %. All five hemes were manually inserted to align with the CxxCH motifs without causing overlap between the hemes and the protein backbone. All hemes inserted are suggested to be bis-His ligated with His 12, 44, 52, 98 and 106 acting as the distal axial ligand. With the emergence of AlphaFold 3¹² ExtC was modelled again, however the model closely aligned to the AlphaFold 2 model and is therefore not included. Attempts to find structural homologues to the AlphaFold models of ExtC using PDBeFold yield no significant results.

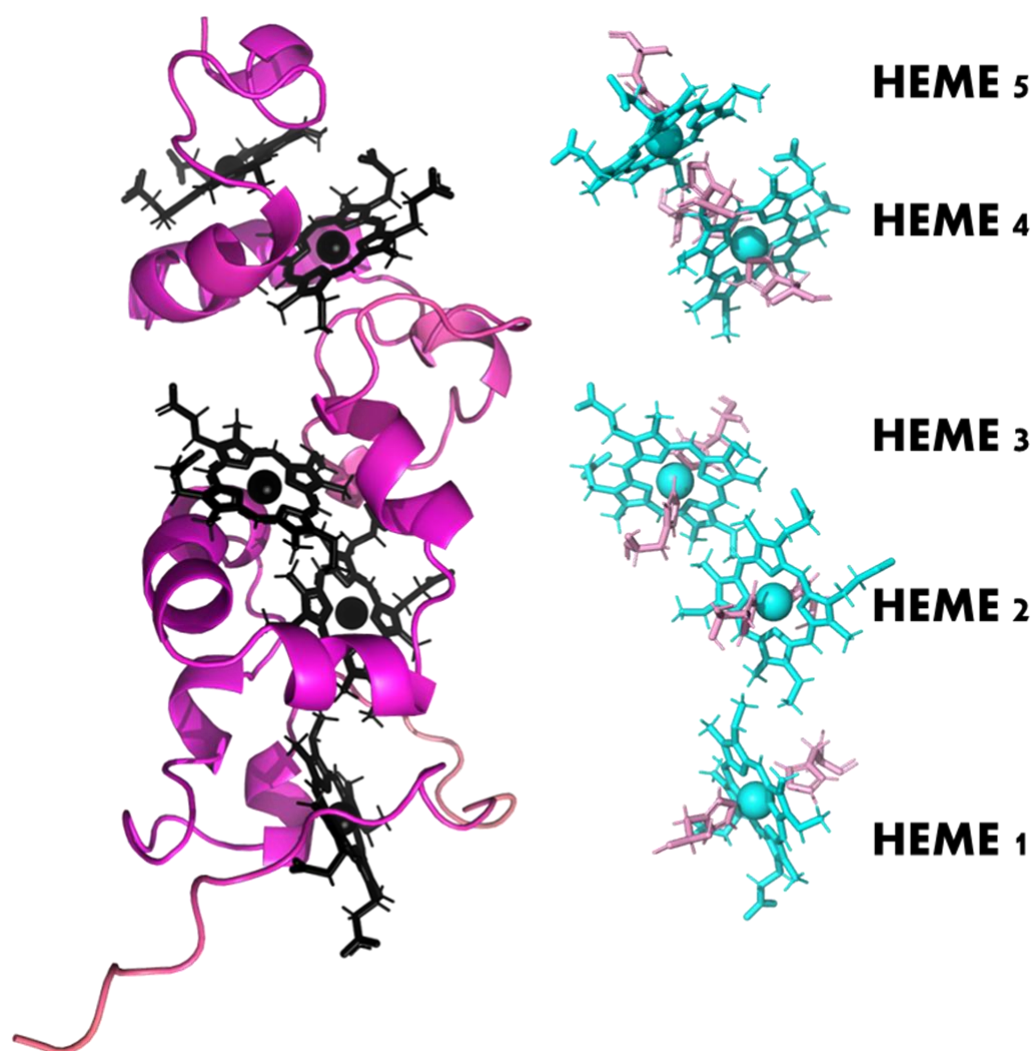


Figure 5.6- AlphaFold 2 model of ExtC. ExtC coloured by pLDDT score, spectrum purple (pLDDT=100) to yellow (pLDDT=0). Hemes of ExtC showing bis-His coordination. Hemes numbered dependent of placement of CxxCH motif in amino acid sequence.

The predicted heme stacking in ExtC has hemes in proximity, between 5.6 to 10.1 Å with the largest gap seen between Hemes 3 and 4. These hemes are still within the allowed limit for electron transfer, with the gap between Hemes 3 and 4 being at the upper limit of generally acceptable electron transfer difference between hemes. The gap between Heme 3 and 4 is however large enough to pose a potential challenge in electron transfer, therefore it would be predicted that aromatic amino acids bridge this gap however no aromatic amino acids are seen in this gap. To predict if the chain of hemes generates a linear or branched pathway for electron transport the solvent accessible surface area (SASA) of each

of the hemes was calculated using Areaimol¹³ through CCP4 suite¹⁴, and shown in *Table 5.1*. Out of the five hemes, all but Heme 2 have a SASA of over 20 %, for comparison the hemes of MtrC have a SASA ranging from 2.7-32.0 %³. As Hemes 1, 3, 4 and 5 all have equally high SASA it can be hypothesised that if ExtC is free in solution these hemes would be able to freely interact with compatible redox partners in the environment, generating multiple entry/exit pathways for electrons within ExtC.

Table 5.1- Solvent accessible surface area of hemes manually inserted into AlphaFold model of ExtC. SASA calculated using Areaimol.

Heme	Solvent Accessible Surface Area, Å ²	Percent of Solvent Accessible, %
1	235.3	28.5
2	79.5	9.6
3	190.9	23.1
4	236.1	28.6
5	229.6	27.8

Validation of the ExtC AlphaFold 2 model can be performed by comparing estimates from SOMO¹⁵ of the sedimentation and frictional coefficients with experimentally determined values from SV analysis, *Table 5.2*. There are expected to be slight differences between the two methods of determination due to the AlphaFold model not including the STREP-II which is found on the C-terminus of the heterologously purified ExtC used for SV. The predicted mass of ExtC from the optimized sequence used in *pMEGGAx_extC_STREP* is 20,026 Da which is close to the mass observed through SV however the mass predicted by the AlphaFold model is significantly lower. As the AlphaFold model is of the native protein and therefore does not factor in the presence of the STREP-II tag this difference in mass is easily justified. The sedimentation coefficients from the experimental SV analysis and predicted from the theoretical model differ by 0.26 S, this is a small difference and with the sedimentation coefficient predicted

through SOMO being the smaller of the two the inclusion of the STREP-II tag would justify this difference. Sedimentation velocity analysis showed that ExtC had a frictional coefficient of 1.12. This implies that ExtC is spherical. This contrasts with the AlphaFold 2 model which models ExtC in a pole shape. The estimated frictional ratio for the AlphaFold model is 1.30, suggesting that ExtC is more elongated. The difference between frictional ratios calculated from SV and the AlphaFold model can be attributed to the inability of AlphaFold to model

Table 5.2- Validation of AlphaFold model of ExtC to key values determined from experimental analysis.

Value	Sedimentation Velocity	AlphaFold Simulation Predictions
Molecular Weight, Da	19,974	18,963
Sedimentation Coefficient, S_{w20}	2.18	1.92
Friction Coefficient, f/f_0	1.12	1.30

5.2.2. Sedimentation Velocity Studies of ExtACD Interactions

Sedimentation velocity (SV) was utilised to investigate interactions between the cytochromes; ExtA, ExtC and ExtD; to gain further insight into how these cytochromes plausibly could interact with nature to form complexes.

SV analysis of ExtA and ExtD was initially determined using equimolar concentrations of ExtA and ExtD, with sedimentation monitored at 410 nm. Fitting experimental data to the Lamm equation revealed the presence of two cytochromes with sedimentation coefficients of 4.81 and 2.45 S_{w20} , *Figure 5.7A-B*. These values aligned closely to the previously determined sedimentation coefficients for ExtA and ExtD, 4.96 and 2.49 S (as previously discussed in Chapters 3 and 4). If ExtA and ExtD were to interact and form a complex, even a transient interaction, a third peak would be expected to be present in the $c(s)$ distribution at a larger S_{w20} value. However, only the two individual

sedimentation peaks were observed with no evidence implying an interaction between ExtAD. By overlaying the sedimentation profiles of the individual cytochromes, for description of individual SV analysis of ExtD and ExtA see Chapters 3 and 4, with the sedimentation profile for ExtAD, *Figure 5.7C*, it can be seen there is little variation between the placement of the sedimentation peaks. The slight difference seen in the sedimentation peak for ExtA between the individual and complex SV experiments is likely caused by the difference in buffer properties, with the $c(s)$ distributions not normalised to S_{w20} to remove the effects of buffer properties.

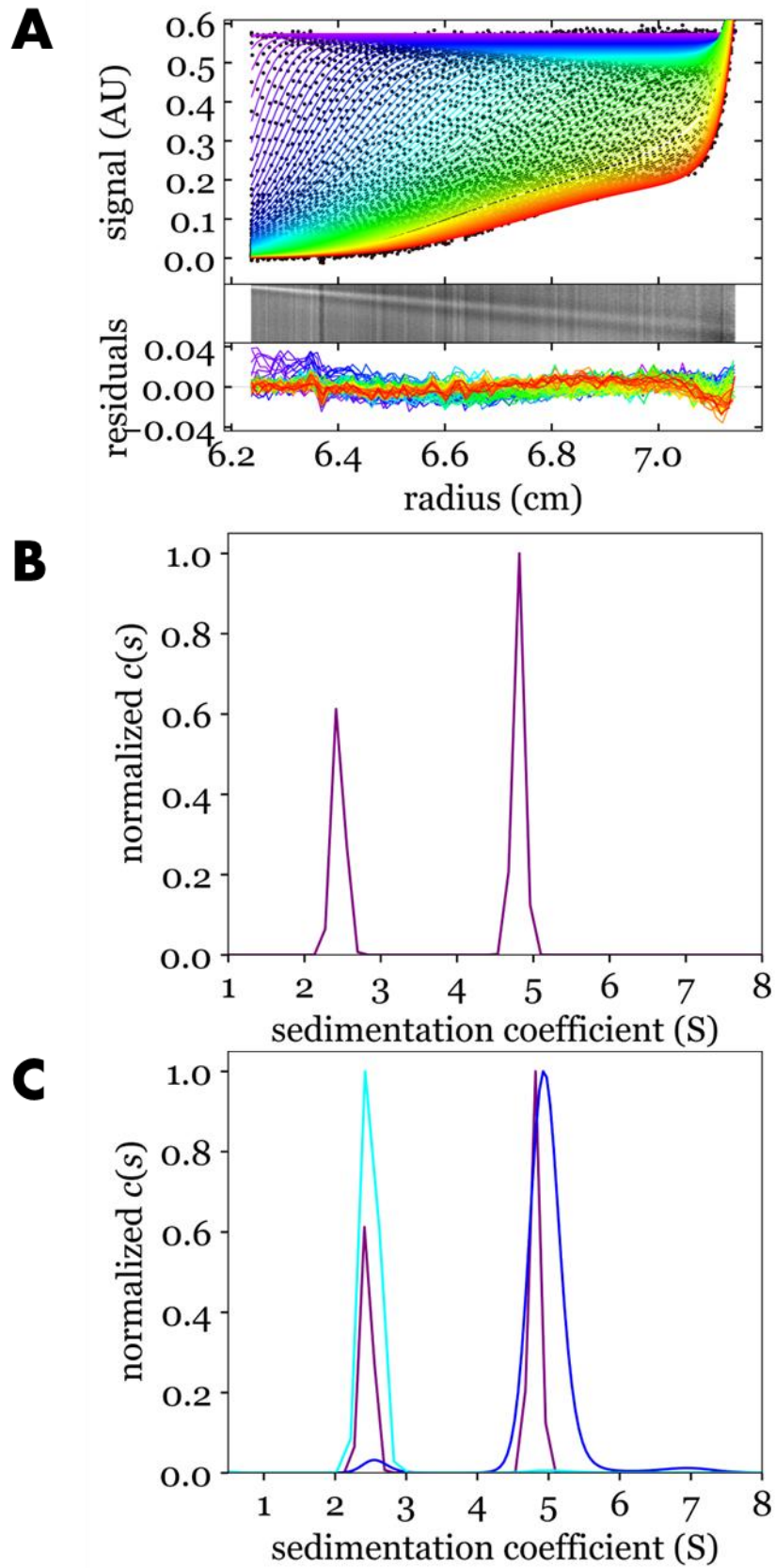


Figure 5.7- Sedimentation Velocity analysis of combined ExtA and ExtD. A) Absorbance data fitted to the Lamm equation of ExtAD. B) $c(s)$ distribution of ExtCD. C) $c(s)$ distribution of ExtCD (purple) overlaid with $c(s)$ distribution of ExtA (blue) and ExtD (cyan) from single protein SV experiments

Interactions of ExtA and ExtC were investigated similarly utilising SV, using an equal molar concentration of ExtC and ExtA. Sedimentation of the cytochromes was monitored at 410 nm with the fitting of the data to the Lamm equation performed using SEDFIT. Analysis revealed the presence of two individual peaks in the $c(s)$ distribution one at 2.19 S and 5.20 S_{w20} , *Figure 5.8A-B*. Which align closely with the previous S_{w20} sedimentation coefficients already discussed for ExtC and ExtA, 2.16 S and 4.96 S. The differing values of the sedimentation coefficients between the single and complex SV analysis can be attributed to the varying frictional coefficients between ExtC and ExtA, 1.12 and 1.55 respectively. When modelling with SEDFIT the data is fitted using an average frictional coefficient of the two cytochromes being studied^{16,17}. As the frictional coefficient is inversely proportional to the sedimentation coefficient, this will lead to a slight difference between modelling a single cytochrome and two cytochromes. When the $c(s)$ distribution of ExtA:ExtC is overlaid with that of single SV experiments of ExtA and ExtC no additional $c(s)$ peaks are observed that aren't present in the single cytochrome experiments, *Figure 5.8C*. This suggests that ExtA and ExtC do not form a complex interaction in solution.

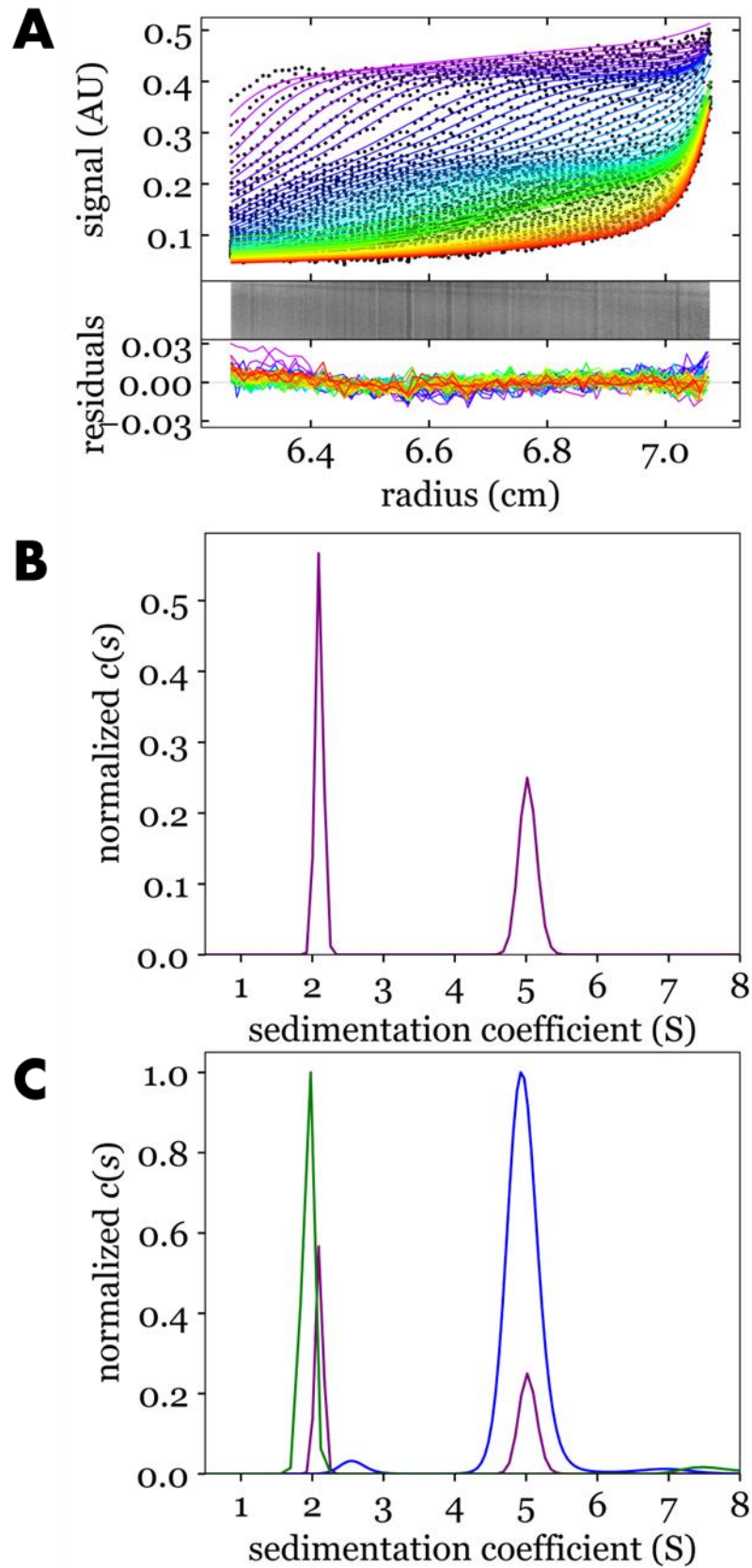


Figure 5.8- Sedimentation Velocity analysis of combined ExtA and ExtC. A) Absorbance data fitted to the Lamm equation of ExtAC. B) $c(s)$ distribution of ExtCD. C) $c(s)$ distribution of ExtAC (purple) overlaid with $c(s)$ distribution of ExtA (blue) and ExtC (green) from single protein SV experiments

Lastly, interactions between ExtC and ExtD were assessed utilising SV. As previously, equimolar concentrations of the cytochromes were used in this analysis, with sedimentation of the cytochromes monitored at 410 nm and fitting the data to the Lamm equation performed using SEDFIT. The $c(s)$ distribution was generated by fitting the sedimentation absorbance data to the Lamm equation, *Figure 5.9A-B*, and revealed a large sedimentation peak at 2.41 S_{w20} which contributed 87.3 % of the total absorbance presence. The sedimentation peak was correlated to a molecular weight of 28,657 Da. There were also two smaller peaks at 3.71 and 0.77 S_{w20} correlating to molecular masses of 54,640 Da and 5,830 Da.

The presence of individual peaks for ExtC and ExtD were not observed in the ExtCD combined SV, however overlaying the individual SV runs from ExtC and ExtD, SV of individual cytochromes discussed here and in Chapter 3 respectively, the $c(s)$ peaks overlay with the main peak of the ExtC:ExtD sedimentation profile at 2.41 S_{w20} , *Figure 5.9C*. The smallest sedimentation peak at 0.77 S_{w20} was attributed to the deterioration of the cytochromes.

The absence of the individual sedimentation peaks seen for ExtD and ExtC is likely due to SEDFIT's attempts to fit the SV data to the Lamm equation corresponding to a single species. Overlaying the single cytochrome SV analysis of ExtD and ExtC, *Figure 5.8C*, it can be seen that neither sedimentation profile directly corresponds to the one observed for the mixed population of cytochromes and that each profile lies on either side of the sedimentation peak detected from the joint ExtC and ExtD SV analysis. As the two sedimentation peaks for the individual SV analysis of ExtC and ExtD are close in size it is probable that SEDFIT has been unable to distinguish the two profiles, due to differences in frictional ratio and molecular mass of the individual cytochromes. This therefore has the potential to result in the presence of a single sedimentation peak that correlates to two individual cytochromes that is not indicative of a complex being formed.

The sedimentation peak observed at 3.71 S is a possible indication of an interaction observed between ExtC and ExtD. The predicted combined molecular mass of ExtCD is 47,706 Da. This correlates to the expected molecular mass of the 3.71 S sedimentation peak at 54,640 Da. As SV is not an accurate method for determining molecular masses the difference detected between the predicted and observed molecular masses is likely due to Sedfit being insufficient to model multiple proteins of different sizes and frictional ratios.

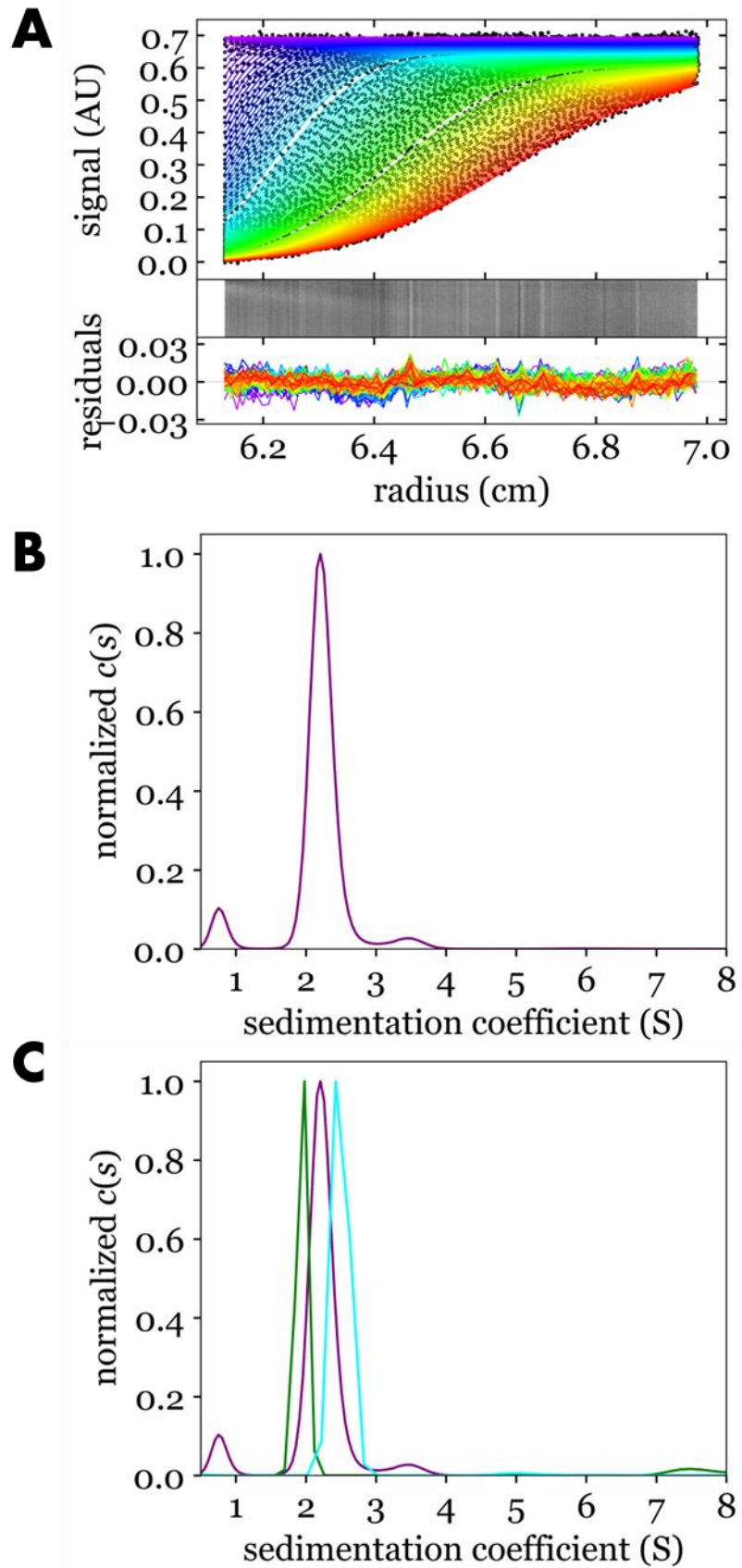


Figure 5.9- Sedimentation Velocity analysis of combined ExtC and ExtD. A) $c(s)$ distribution of ExtCD. B) Absorbance data fitted to the Lamm equation of ExtCD. C) $c(s)$ distribution of ExtCD (purple) overlaid with $c(s)$ distribution of ExtC (green) and ExtD (cyan) from single protein SV experiments

5.2.3. *in-silico* Characterisation of Porin ExtB

The final component of the ExtABCD complex that has yet to be discussed in this thesis is the β -barrel protein ExtB (gene: GSU2644). Expression and purification of ExtB were not attempted due to foreseen issues of heterologously expressing a porin outside of the *Geobacter* family. Additionally, it has been shown that expression and purification of MtrB from *Shewanella oneidensis* is not possible without joint expression of the MtrA cytochrome¹⁸. It is therefore likely that for expression and correct localisation of ExtB in the outer membrane of *S. oneidensis* LS527 the corresponding multi-heme cytochrome would also have to be jointly expressed. In place of physical characterisation in this thesis, an *in silico-based* bioinformatics approach was taken to characterise ExtB solely from its known amino acid sequence. The signal peptide of ExtB was predicted using SignalP 5.0⁴ with results suggesting cleavage of the signal peptide between residues 26 and 27, resulting in a protein of 394 amino acids in length. ExtB is predicted to be situated in the outer membrane of *G. sulfurreducens* PCA and the use of an online application for subcellular location predictor CELLO¹⁹ aligned with this prediction with the localisation of ExtB to the outer membrane.

The online application PRED-TMBB²⁰ utilises a Hidden Markov Model allowing for the prediction of transmembrane β -barrel protein was employed to predict the number of β -strands encoded by the amino acid sequence of ExtB, *Figure 5.10*. PRED-TMBB predictions suggest that ExtB contains 20 anti-parallel β -strands with 10 extracellular loops, aligning with previous genomic analysis². Comparatively, MtrB from *Shewanella baltica* OS185, whose structure has been solved by X-ray crystallography, contains a total of 26 anti-parallel β -strands³.

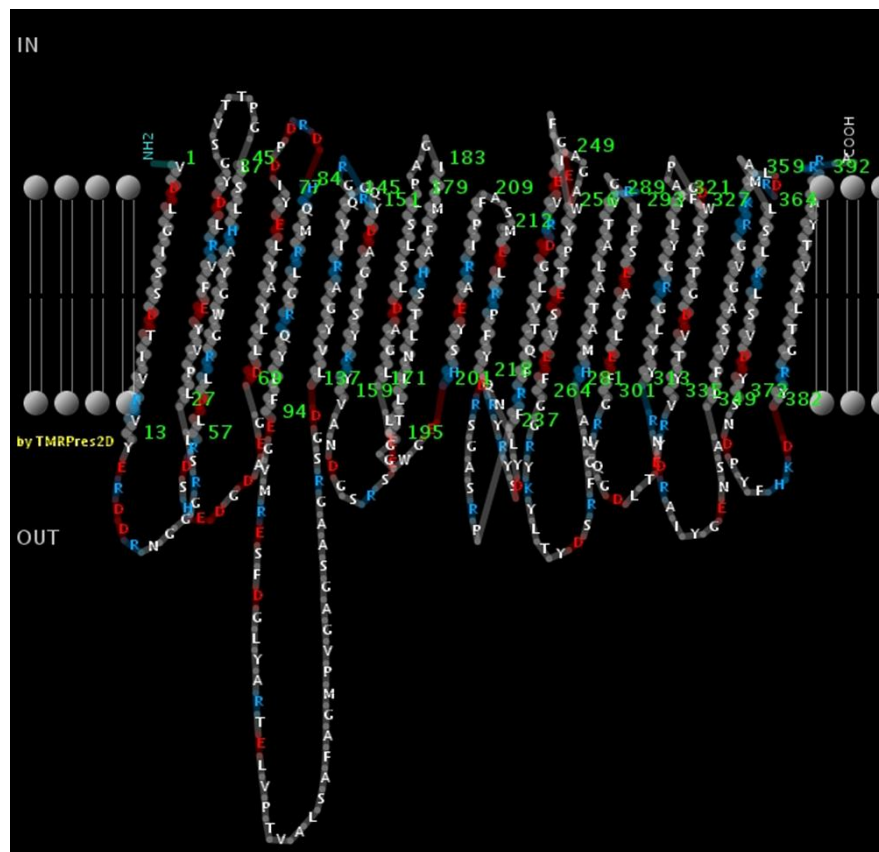


Figure 5.10- PRED-TMBB graphical output showing predicted transmembrane regions of ExtB. Where IN is the periplasmic side of the outer membrane and OUT is the extracellular space.

AlphaFold 2⁹ was utilised to model a 3D structure for ExtB, generating a model of the full protein with the predicted signal peptide removed, *Figure 5.11A*. The ExtB model predicts a β -barrel with dimensions of 40 x 40 x 40 Å (height x width x length). The average pLDDT associated with the AlphaFold model is 90.86 %. This is a high average pLDDT score which suggests AlphaFold has predicted the backbone and sidechain orientation with high accuracy to what they propose would be the native structure of ExtB⁹. With the recent advancements and introduction of AlphaFold 3, a new ExtB model was generated. However, as the output was identical to the previous AlphaFold 2 model it is not shown here.

The spatial orientation of the β -barrel ExtB in the membrane is predicted to resemble that of MtrB with the N-terminus being positioned at the inner leaflet of the outer membrane and the extracellular loops being outside the bacteria, as predicted through the PRED-TMBB. However, whilst the results from PRED-TMBB suggest that ExtB contains 20 anti-parallel β -sheets the AlphaFold model is formed of 22 anti-parallel β -sheets. The AlphaFold model was then processed through APBS²¹, *Figure 5.11B* to analyse the electrostatic potential between -10 (red) and +10 (blue) kT/e. Viewing the protein in this manner reveals that the simulated ExtB has only a slight electrostatic potential, with the top face (predicted to be extruding from the outer membrane facing the extracellular space) having a low negative charge.

From the predicted ExtABCD complex it has been hypothesised in the literature that ExtAB would form the PCC with ExtC and ExtD being extracellular cytochromes. Modelling of ExtAB in the complex was attempted with AlphaFold 2, however a PCC was not able to be formed. Due to this ExtBC and ExtBD were also modelled to see if the porin cytochrome complex could be formed. Whilst modelling of ExtBD did not yield a PCC modelling of ExtBC successfully modelled a PCC, *Figure 5.11C*. The ExtBC model had an average pLDDT score of 87.92 %.

A solvent channel was identified in the ExtBC by using the Pymol plugin CAVER 3.0²², *Figure 5.11D*. This channel is similar in appearance to the solvent tunnel identified in MtrAB, where it is suggested a possible functionality of the channel being used for proton transport³. The transfer of protons across the outer membrane has been suggested to be a rate-limiting step in the reduction of flavins by the MtrC cytochrome from *S. oneidensis* MR-1²³. The solvent channel predicted in the ExtBC complex may perform a similar role. Whilst *Geobacter* strains had previously not been observed to secrete flavins, recent research has shown the use of flavins in extracellular electron transport in some *Geobacter* strains^{24–26}.

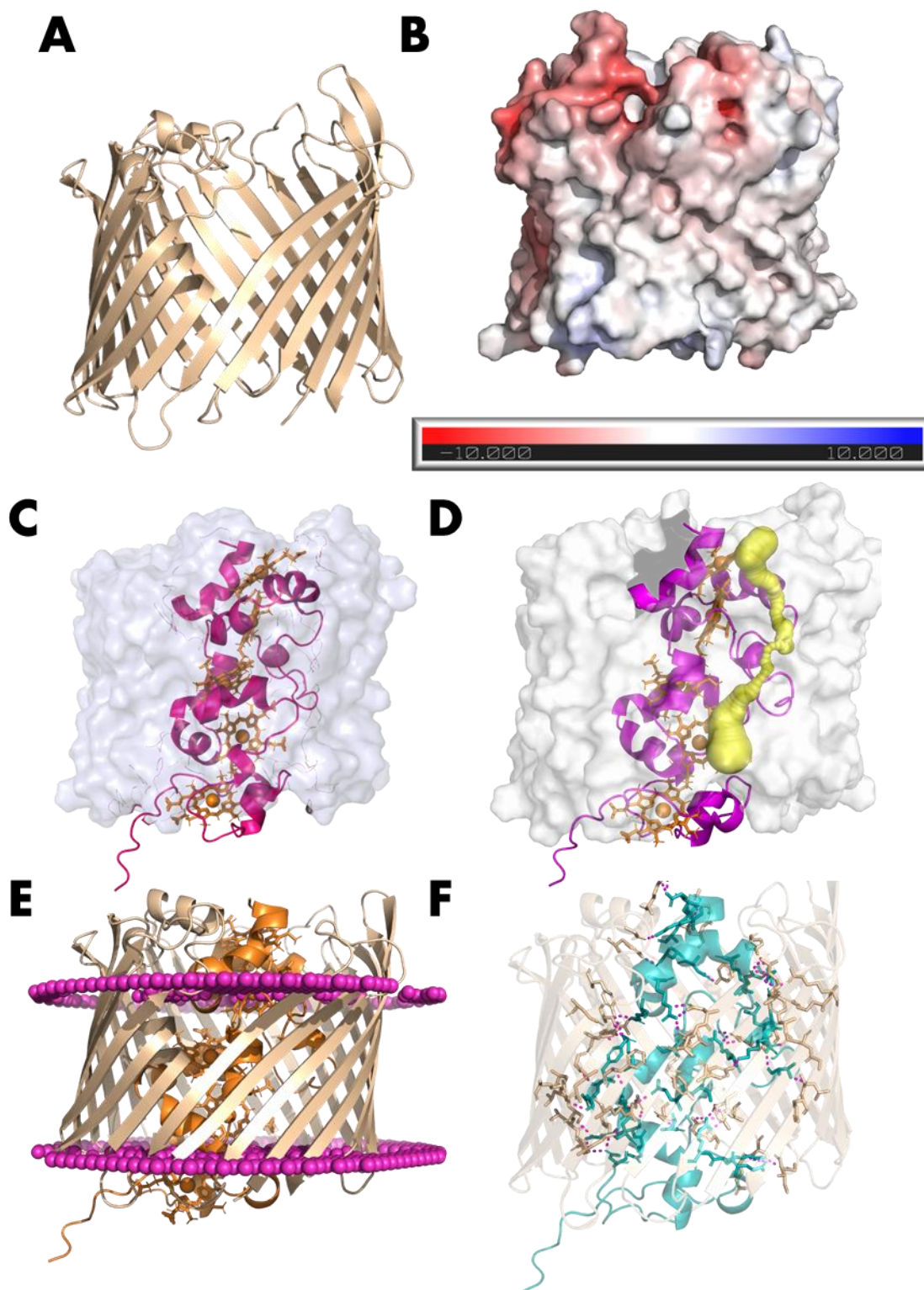


Figure 5.11- AlphaFold 2 modelling of ExtB as a monomer and in complex with ExtC. A) AlphaFold model of ExtB, coloured by pLDDT (high pink, low yellow). B) Electrostatic potential of ExtB between -10 kT/e (red) and +10 kT/e (blue), performed using APBS. C) AlphaFold multimer model of ExtB in complex with ExtB. D) Identification of tunnel (yellow spheres) present in ExtBC Tunnel calculated using CAVER. E) Simulation of Gram-negative outer membrane on AlphaFold model of ExtB. F) Hydrogen bond (purple) interactions seen between ExtB (beige) and ExtC (cyan).

The heme chain predicted from ExtBC shows shorter heme distances than the ExtC AlphaFold model. Now heme distances are observed between 3.9 to 7.3 Å with the largest distance seen between Hemes 3 and 4. Whereas in the AlphaFold 2 model of ExtC, *Figure 5.6*, the largest heme gap was 10.6 Å between Heme 3 and 4, the ExtBC AlphaFold model has considerably shortened this distance with the hemes now forming a tightly packed chain potentially allowing for rapid electron transfer. The SASA of ExtC heme cofactors was recalculated using Areaimol. Whilst in complex with ExtB the SASA of all the heme cofactors has been decreased, *Table 5.3*. The decrease in SASA for the hemes suggests that ExtC now acts as a wire with lateral movement of electrons from Heme 1 to Heme 5, or *vice versa*. To determine the hypothetical orientation of ExtBC in the outer membrane of *G. sulfurreducens* the web tool PPM 3.0²⁷, which predicts the energetically optimal spatial positions of proteins in a pre-selected membrane, was utilised. The orientation prediction is shown in *Figure 5.10E* and the prediction suggests that N and C-terminus would be positioned facing the periplasm. This would also position the N-terminus of ExtC in the periplasm, as the N-terminus contains a Cys residue predicted to be functional as a lipid anchor it would indicate that ExtC would be covalently attached to the inner leaflet, not the outer leaflet as previously hypothesised.

Table 5.3- Comparison of solvent accessible surface area of hemes from AlphaFold 2 model of ExtC and complex ExtBC.

Heme	ExtC		ExtBC	
	Solvent Accessible Surface Area, Å ²	Percent of Solvent Accessible, %	Solvent Accessible Surface Area, Å ²	Percent of Solvent Accessible, %
1	235.3	28.5	193.0	23.4
2	79.5	9.6	104.9	12.7
3	190.9	23.1	22.0	2.7
4	236.1	28.6	79.2	9.6
5	229.6	27.8	108.9	13.2

From the ExtBC AlphaFold model, potential sites for electrostatic interaction between the two proteins were identified, *Figure 5.10F*. The existence of these

interactions is important to note as they are likely required for correct formation in the outer membrane of *G. sulfurreducens* PCA and the identification of them lends approval to the ExtBC model. Polar contacts were identified in ExtBC that presented at a maximum distance of 4 Å. Multiple van der Waals interactions were shown to be potentially possible between ExtB and ExtC. These would allow for a stable interaction between the two proteins supporting the hypothesis that ExtBC form the porin:cytochrome complex.

Whilst AlphaFold 2 was unable to form a porin cytochrome complex of both ExtAB and ExtBD the newest version of AlphaFold, version 3¹², could generate PCC models for ExtAB and ExtBD, *Figure 5.12*. These however had a lower average pLDDT score, 73.42 % for ExtAB and 62.53 % for ExtBD. Whilst, these average pLDDT scores are high and suggest a potential for the PCC structure analysis of both models revealed details that would be impossible and discredited the models. In the ExtAB model, the positioning of the two subunits of ExtA not insulated by ExtB would be extended into the extracellular space. This is an improbable hypothesis as ExtA would not be able to pass through the porin in its trimeric form freely and the native signal peptide of ExtA does not encode specification for localisation to the extracellular space. The model for ExtBD contains features that discredit the probability of a truthful model. Comparing AlphaFold models of ExtD simulated as a monomer and in complex with ExtB reveals a large distortion between the two. The AlphaFold 3 model for monomeric ExtD has an average pLDDT value of 72.52 % whilst ExtD in the ExtBD simulation has an average pLDDT of 41.46 %. This low score for the ExtD modelled with ExtB simulation indicates a model that is probable to have large highly disordered regions and limited confidence in the placement of protein backbone and side chains. Modelling complexes of ExtABC and ExtBCD showed that AlphaFold 3 preferentially models ExtBC as the PCC.

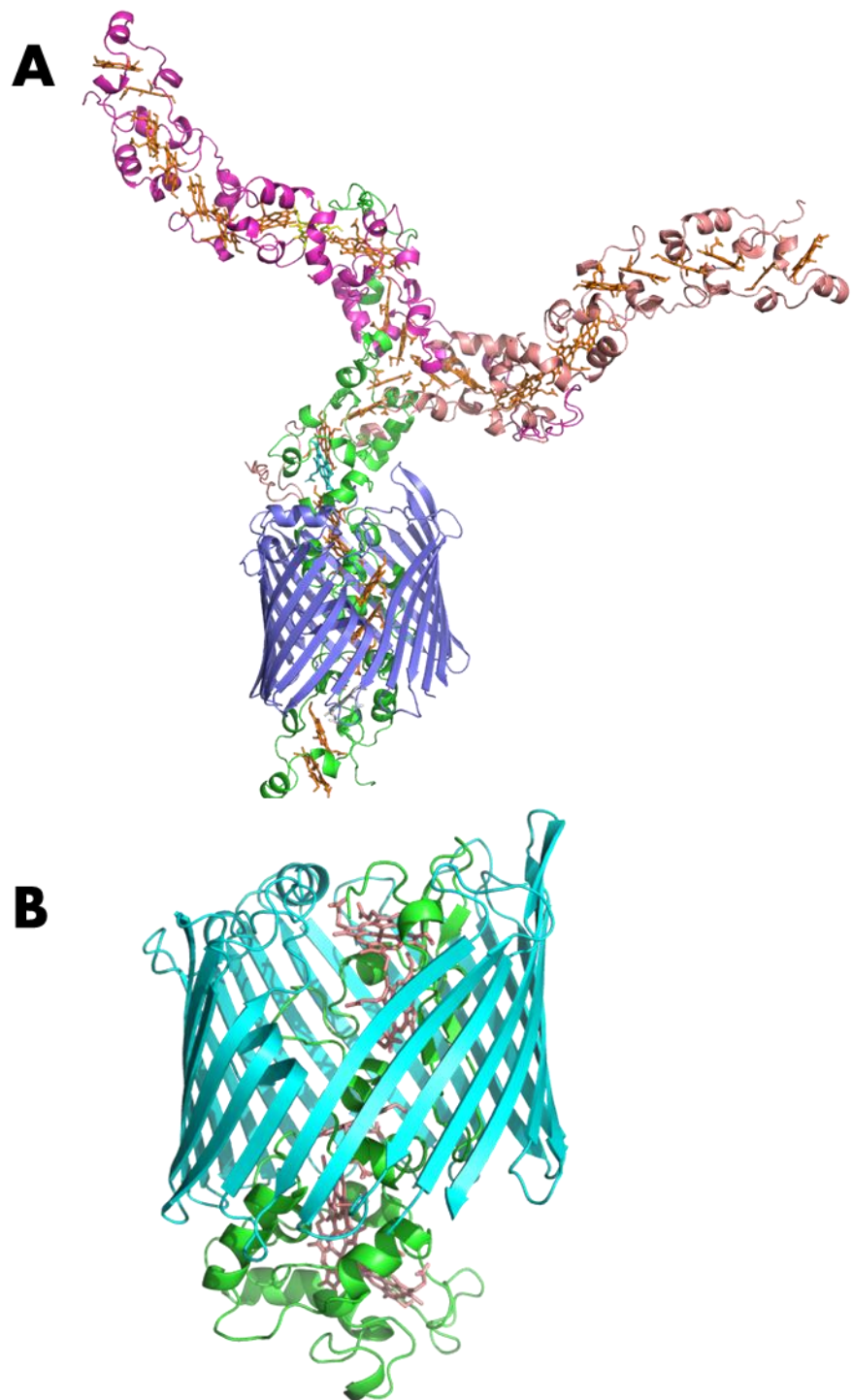


Figure 5.12- AlphaFold 3 models of A) ExtAB and B) ExtBD.

Utilising AlphaFold 2 and 3 to generate a whole structural model of the ExtABCD complex was unfortunately unsuccessful. Whilst both versions of AlphaFold are capable of forming a complex between ExtBC localisation of ExtA was shown to

be inconsistent between models, with no preference given to localisation of ExtA on what would be the periplasm or extracellular space. ExtD was simulated by AlphaFold to be oriented facing the extracellular space with Heme 1 of ExtD in proximity, 7.7 Å between porphyrin rings, to Heme 5 of ExtC. In contrast placement of ExtA differed between simulations with placement of ExtA seen in the extracellular and periplasmic space alongside being modelled parallel to ExtBC. This is a flaw with AlphaFold as it currently does not account the presence of membranes. Therefore, to construct a structural model of ExtABCD individual AlphaFold models were combined under the hypothesis that ExtA would be localised to the periplasm with the most probable interaction between ExtC and ExtA occurring at the N-terminus of ExtA were the tri-heme junction is predicted, *Figure 5.13*. It is currently unknown if ExtA would remain stationary at the base of the ExtBCD complex or move throughout the periplasmic space. As SV analysis of interactions between the ExtABCD cytochromes additionally did not reveal an interaction between ExtA and partner cytochromes there is a potential for ExtA to be dynamic in the periplasmic space. Under the assumption that ExtA is not closely associated with the ExtBCD complex, a molecular wire spanning from Heme 1 of ExtC to Heme 6 of ExtD would be generated spanning 79.3 Å in length. Comparatively, the MtrCAB complex has a molecular nanowire spanning 159.8 Å³.

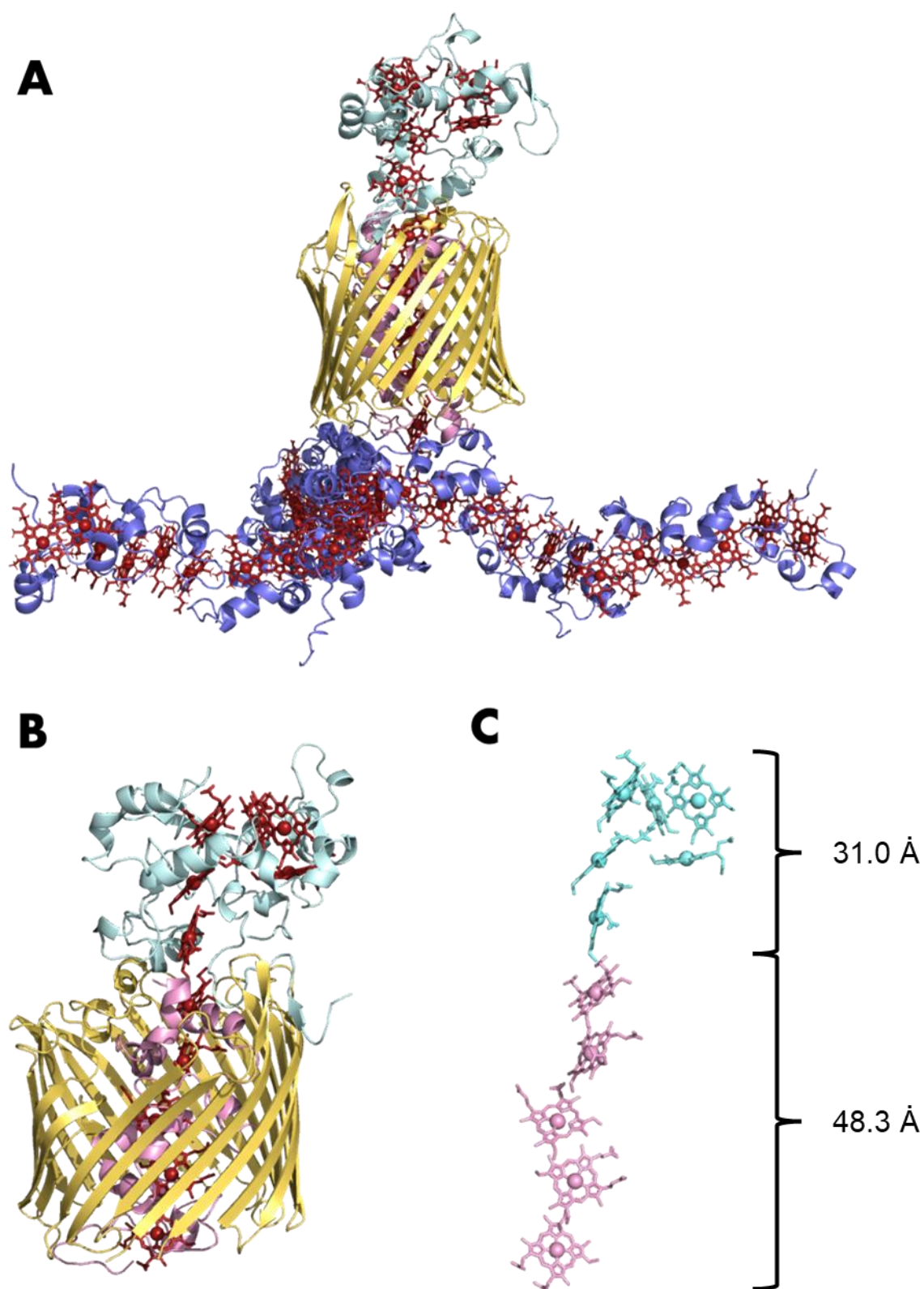


Figure 5.13- AlphaFold 3 models of the ExtABCD complex. A) Simulation of ExtABCD, produced by modelling trimeric ExtA and ExtBCD separately. B) Simulation of ExtBCD C) Heme nanowire formed from ExtBCD AlphaFold 3 model.

5.3. Discussion

Work started in this chapter has shown that heterologous expression of *extC* in *S. oneidensis* LS527 is achievable. However, the yield of ExtC from *S. oneidensis* cells remains low, with only 0.85 ng of protein harvested per litre of *S. oneidensis* LS527 grown, and therefore protein characterisation was limited. UV-visible absorbance spectroscopy revealed that ExtC showed canonical heme spectral properties⁵. This is in contrast to ExtA and ExtD which were both characterised with a split Soret. Analysis through sedimentation velocity showed that ExtC is monomeric in solution with a S_{w20} value of 2.18 S.

Sedimentation velocity analysis investigating the interaction of cytochromes present in ExtABCD suggests that whilst ExtC and ExtD have some form of stable interaction occurring neither of those two cytochromes were observed to interact with ExtA. This is an interesting observation and leads to the hypothesis that ExtA may only very transiently interact with the ExtBCD complex. The lack of observable interaction between ExtA and ExtCD could be explained by the AlphaFold prediction of ExtBC forming the porin:cytochrome interface and therefore ExtA would not be predicted to interact with ExtD. The absence of an interaction between ExtA and ExtC could potentially suggest that if ExtA behaves as a periplasmic shuttle it does not have a strong interaction with ExtC potentially being non-specific to the ExtBCD complex and able to reduce multiple PCCs. Alternatively, ExtA may be specific to the ExtBCD complex but only form a stable interaction with the porin ExtB.

AlphaFold models simulating potential porin:cytochrome interactions suggest the presence of ExtBC as a complex. This would differ from previous hypotheses in the literature that ExtAB would form the porin:cytochrome interface^{1,28}. Interestingly both AlphaFold 2 and 3 position ExtC in the porin with the N-terminus exposed to the inner leaflet of the outer membrane. ExtC contains a cysteine predicted to act as a lipid anchor and a functional lipid box at the signal peptide's 3' prime end. Therefore, ExtC is likely to be covalently bound to the outer membrane of *G. sulfurreducens*. This would position the Cys of ExtC in the

inner leaflet of the OM. Whilst it is common for proteins to be covalently attached to the inner leaflet there is currently no known multiheme cytochrome to be bound this was with lipo-multiheme cytochromes positioned in the outer leaflet of the outer membrane or the inner membrane. The ExtEFG predicted PCC from *G. sulfurreducens* also contains two putative lipocytochromes, ExtF and ExtG. Currently, it is unknown which cytochrome will be insulated by ExtE in both cases the cytochrome is liable to be covalently bound to the outer membrane similar to the proposed ExtBC lipid attachment.

The potential functionality of ExtA as a periplasmic shuttle is an intriguing hypothesis. It is currently unknown if ExtA would be fixed to the base of the ExtBCD complex through electrostatic interactions with ExtB or if ExtA could move freely across the periplasm. Due to the size of trimeric ExtA, it is also potential that ExtA would be able to extend the full width of the periplasm forming an 'electron bridge' between inner membrane quinol dehydrogenases and the ExtBCD complex. However, the periplasm gap in *G. sulfurreducens* has been quoted to be 400 Å between the inner and outer membrane²⁹ and based on the AlphaFold model of trimeric ExtA the full extension possible is approximately 210 Å. This therefore would not allow for an 'electron bridge' to be directly formed from the inner membrane to the outer membrane. However, as seen through the SV analysis ExtA is predicted to also form a hexamer potentially allowing for the 'electron bridge' to be formed.

Localisation of lipoproteins to the inner or outer membrane involves the employment of many proteins which have been seen to be highly conserved in Gram-negative bacteria^{30,31}. Firstly, proteins containing a single peptide are translocated across the inner membrane to the periplasm through either the SEC or TAT translocon. If a lipoprotein is present, it will be recognised by the Lgt protein and the sulphide group of the +1 Cys residue will be bound to diacylglycerol at which point the signal peptide can be cleaved by LspA³². Covalent attachment of the lipoprotein occurs when the Lnt protein causes the Cys residue to become N-acylated generating mature triacylated lipoprotein³³.

Lipoproteins are now incorporated into the inner membrane and will either remain or be translocated to the outer membrane through the Lol pathway. The majority of lipoproteins will be translocated to the outer membrane unless they contain a Lol inhibitor signal which is hypothesised to be the appearance of an Asp residue at the +2 position³⁴. Lipoproteins that are translocated to the outer membrane through the Lol pathway will be inserted into the inner leaflet. Lipoproteins are present on the outer leaflet of Gram-negative bacteria, however the mechanism for translocation to the outer membrane is still unknown. By reviewing sequences with known placement in the outer membrane, *Figure 5.14*, it can be suggested that the sequence of amino acids downstream of the lipid anchor factor into the placement of lipoproteins in the inner or outer leaflet. It is seen that in the majority of lipoproteins known to be localised to the outer leaflet adjacent downstream to the lipid anchor is the presence of Gly and Ser residues, which is not present in proteins known to be orientated to the inner leaflet.

ExtC:	LALVVS	<u>CA</u> QQARY	Inner	Leaflet
LolB:	VALAAG	<u>CAT</u> VPPQ	Inner	Leaflet
ExtF:	ALTLTA	<u>C</u> THMLSK	Inner	Leaflet
ExtD:	TLTLAG	<u>C</u> GGGSNA	Outer	Leaflet
OmcB:	AAALAG	<u>C</u> GSENKE	Outer	Leaflet
ExtG:	GLALWG	<u>C</u> SSGSGD	Outer	Leaflet
MtrC:	TMALTG	<u>C</u> GGSDGN	Outer	Leaflet

Figure 5.14- Amino acid sequence of known lipoproteins and their positioning in the outer membrane

Previous, genomic analysis studies³⁵ have shown that homologues of the *extA* gene in *Geobacter* species are not always located in the *extBCD* gene cluster and instead located elsewhere in the host genome. Additionally, single gene

knockouts of the *extABCD* genes in *Geobacter sulfurreducens* PCA were assessed against their ability to reduce electrodes poised at +240 mV vs SHE. Deletion of the *extA* gene showed only a small decrease in current output compared to wildtype strains. Single deletion of remaining *extBCD* genes showed a drastic decrease in current output compared to wildtype¹. This is suggestive of ExtA not being an integral part of the ExtABCD PCC and either ExtC or ExtD forming the PCC with ExtB. This is in line with complex modelling using AlphaFold it is ExtBC that forms the PCC.

The new structural model of ExtBCD, *Figure 5.12*, is similar in structure to the only experimentally determined structure of PCC, MtrCAB from *Shewanella baltica*³. With the overall presence of MHC being insulated in a porin-like protein and an extracellular lipid-anchored OMC. However, one key difference between the two PCCs is the size of the cytochromes employed. MtrC is the extracellular component of the MtrCAB complex and protrudes 99 Å from the bacterial surface. Comparatively, ExtD is now hypothesised to be the sole extracellular cytochrome of the ExtBCD complex and is considerably shorter in size only protruding 32 Å from the cell surface. Additionally, MtrA contains 10 hemes and crystal structures have shown that there is an overhang on both the periplasmic and extracellular side of the outer membrane. In contrast, ExtC contains 5 heme and when modelled through AlphaFold with ExtB there is no overhang of hemes on either side. This is unusual for a PCC, with MtoAB, PioAB and MtrAB all predicted to have overhanging hemes. However, the fusion porin-cytochrome Cyc2 from *Sideroxydans lithotrophicus* ES-1 contains only one heme located towards the periplasmic space and is predicted to be functional at oxidising iron located in the extracellular space³⁶.

5.4. References

1. Jiménez Otero, F. *et al.* Evidence of a Streamlined Extracellular Electron Transfer Pathway from Biofilm Structure, Metabolic Stratification, and Long-Range Electron Transfer Parameters. *Appl Environ Microbiol* **87**, (2021).

2. Shi, L., Fredrickson, J. K. & Zachara, J. M. Genomic analyses of bacterial porin-cytochrome gene clusters. *Front Microbiol* **5**, (2014).
3. Edwards, M. J., White, G. F., Butt, J. N., Richardson, D. J. & Clarke, T. A. The Crystal Structure of a Biological Insulated Transmembrane Molecular Wire. *Cell* **181**, 665-673.e10 (2020).
4. Almagro Armenteros, J. J. *et al.* SignalP 5.0 improves signal peptide predictions using deep neural networks. *Nat Biotechnol* **37**, 420–423 (2019).
5. Moore, G. R. & Pettigrew, G. W. *Cytochromes c: Evolutionary, Structural and Physicochemical Aspects*. (Springer Berlin Heidelberg, Berlin, Heidelberg, 1990).
6. Barr, I. & Guo, F. Pyridine Hemochromagen Assay for Determining the Concentration of Heme in Purified Protein Solutions. *Bio Protoc* **5**, (2015).
7. Berry, E. A. & Trumpower, B. L. Simultaneous determination of hemes a, b, and c from pyridine hemochrome spectra. *Anal Biochem* **161**, 1–15 (1987).
8. Schuck, P. Size-Distribution Analysis of Macromolecules by Sedimentation Velocity Ultracentrifugation and Lamm Equation Modeling. *Biophys J* **78**, 1606–1619 (2000).
9. Jumper, J. *et al.* Highly accurate protein structure prediction with AlphaFold. *Nature* **596**, 583–589 (2021).
10. Braun, V. & Wu, H. C. Lipoproteins, structure, function, biosynthesis and model for protein export. in 319–341 (1994).
11. Fonseca, B. M. *et al.* Optimizing Electroactive Organisms: The Effect of Orthologous Proteins. *Front Energy Res* **7**, (2019).
12. Abramson, J. *et al.* Accurate structure prediction of biomolecular interactions with AlphaFold 3. *Nature* (2024)
13. Lee, B. & Richards, F. M. The interpretation of protein structures: Estimation of static accessibility. *J Mol Biol* **55**, 379-IN4 (1971).
14. Agirre, J. *et al.* The CCP4 suite: integrative software for macromolecular crystallography. *Acta Crystallogr D Struct Biol* **79**, 449–461 (2023).
15. Brookes, E. & Rocco, M. Recent advances in the UltraScan SOLUTION MOdeller (US-SOMO) hydrodynamic and small-angle scattering data analysis and simulation suite. *European Biophysics Journal* **47**, 855–864 (2018).
16. Cole, J. L., Lary, J. W., P. Moody, T. & Laue, T. M. Analytical Ultracentrifugation: Sedimentation Velocity and Sedimentation Equilibrium. in 143–179 (2008).
17. Dam, J. & Schuck, P. Calculating Sedimentation Coefficient Distributions by Direct Modeling of Sedimentation Velocity Concentration Profiles. in 185–212 (2004).
18. Schicklberger, M., Bücking, C., Schuetz, B., Heide, H. & Gescher, J. Involvement of the *Shewanella oneidensis* Decaheme Cytochrome MtrA in the Periplasmic Stability of the β -Barrel Protein MtrB. *Appl Environ Microbiol* **77**, 1520–1523 (2011).

19. Yu, C., Lin, C. & Hwang, J. Predicting subcellular localization of proteins for Gram-negative bacteria by support vector machines based on n -peptide compositions. *Protein Science* **13**, 1402–1406 (2004).
20. Bagos, P. G., Liakopoulos, T. D., Spyropoulos, I. C. & Hamodrakas, S. J. PRED-TMBB: a web server for predicting the topology of β -barrel outer membrane proteins. *Nucleic Acids Res* **32**, W400–W404 (2004).
21. Jurrus, E. *et al.* Improvements to the APBS biomolecular solvation software suite. *Protein Science* **27**, 112–128 (2018).
22. Chovancova, E. *et al.* CAVER 3.0: A Tool for the Analysis of Transport Pathways in Dynamic Protein Structures. *PLoS Comput Biol* **8**, e1002708 (2012).
23. Okamoto, A., Tokunou, Y., Kalathil, S. & Hashimoto, K. Proton Transport in the Outer-Membrane Flavocytochrome Complex Limits the Rate of Extracellular Electron Transport. *Angewandte Chemie International Edition* **56**, 9082–9086 (2017).
24. Thirumurthy, M. A. & Jones, A. K. *Geobacter* cytochrome OmcZs binds riboflavin: implications for extracellular electron transfer. *Nanotechnology* **31**, 124001 (2020).
25. Michelson, K., Sanford, R. A., Valocchi, A. J. & Werth, C. J. Nanowires of *Geobacter sulfurreducens* Require Redox Cofactors to Reduce Metals in Pore Spaces Too Small for Cell Passage. *Environ Sci Technol* **51**, 11660–11668 (2017).
26. Okamoto, A. *et al.* Uptake of self-secreted flavins as bound cofactors for extracellular electron transfer in *Geobacter* species. *Energy Environ. Sci.* **7**, 1357–1361 (2014).
27. Lomize, A. L., Todd, S. C. & Pogozeva, I. D. Spatial arrangement of proteins in planar and curved membranes by PPM 3.0. *Protein Science* **31**, 209–220 (2022).
28. Clarke, T. A. Plugging into bacterial nanowires: a comparison of model electrogenic organisms. *Curr Opin Microbiol* **66**, 56–62 (2022).
29. Howley, E., Mangus, A., Williams, D. & Torres, C. I. Intracytoplasmic membranes develop in *Geobacter sulfurreducens* under thermodynamically limiting conditions. *NPJ Biofilms Microbiomes* **9**, 18 (2023).
30. Konovalova, A. & Silhavy, T. J. Outer membrane lipoprotein biogenesis: Lol is not the end. *Philosophical Transactions of the Royal Society B: Biological Sciences* **370**, 20150030 (2015).
31. Okuda, S. & Tokuda, H. Lipoprotein Sorting in Bacteria. *Annu Rev Microbiol* **65**, 239–259 (2011).
32. Sankaran, K. & Wu, H. C. Lipid modification of bacterial prolipoprotein. Transfer of diacylglycerol moiety from phosphatidylglycerol. *Journal of Biological Chemistry* **269**, 19701–19706 (1994).
33. Gupta, S. D. & Wu, H. C. Identification and subcellular localization of apolipoprotein N-acyltransferase in *Escherichia coli*. *FEMS Microbiol Lett* **78**, 37–42 (1991).
34. Yamaguchi, K., Yu, F. & Inouye, M. A single amino acid determinant of the membrane localization of lipoproteins in *E. coli*. *Cell* **53**, 423–432 (1988).

35. Jiménez Otero, F., Chan, C. H. & Bond, D. R. Identification of Different Putative Outer Membrane Electron Conduits Necessary for Fe(III) Citrate, Fe(III) Oxide, Mn(IV) Oxide, or Electrode Reduction by *Geobacter sulfurreducens*. *J Bacteriol* **200**, (2018).
36. Jiang, V., Khare, S. D. & Banta, S. Computational structure prediction provides a plausible mechanism for electron transfer by the outer membrane protein Cyc2 from *Acidithiobacillus ferrooxidans*. *Protein Science* (2021)

Chapter 6: General Discussion

6.1. Thesis Summary

In Chapter 3 heterologous expression and protein characterisation of the hexaheme cytochrome ExtD from *Geobacter sulfurreducens* PCA was performed. Expression of *extD* in both heterologous hosts *Escherichia coli* BL21 and *Shewanella oneidensis* LS527 was trialled utilising both HIS-tag and STREP-II tag purification. Expression of *extD_HIS* in *S. oneidensis* LS527 was seen to yield the highest abundance of cytochrome, however concentration of ExtD remained low after purification so did not allow for full characterisation of cytochrome. Initial characterisation of ExtD through the use of sedimentation velocity confirmed ExtD to be monodispersed in solution. The spectra of ExtD revealed unique spectral features that were unexpected of multiheme cytochromes, with a broad oxidised Soret and a reduced split Soret. The presence of the reduced split Soret has been observed in research less than five times and the cause remains unknown¹⁻⁴. The hypothesis proposed in this thesis for the cause of the split Soret is that the six hemes of ExtD are arranged in two distinct heme chains that do not share a π orbital electron density. This aligns with the current theory of multiheme cytochromes sharing electron density through π orbitals causing an identical splitting of all π to π^* transitions⁵. This could potentially be caused by the diversion of the canonical t-shaped or stacked heme packing instead of hemes being adjacent to one another, as suggested by the hypothetical AlphaFold model.

In Chapter 4 characterisation of the dodecaheme cytochrome ExtA from *G. sulfurreducens* PCA was performed. Similar to spectra of ExtD, ExtA was also shown to have a noncanonical cytochrome spectrum also showing a reduced split Soret. Through the use of analytical ultracentrifugation techniques and size exclusion chromatography, ExtA was observed to be predominately in a trimeric conformation. Previously research had hypothesised that ExtA was to be insulated by the predicted porin-like protein ExtB in the outer membrane^{6,7}, but the discovery of a trimeric ExtA makes this hypothesis unlikely. Here it is proposed that ExtA functions as a periplasmic shuttle bridging electron transfer between the quinol dehydrogenases of the inner membrane to the porin

cytochrome clusters of the outer membrane. ExtA is hypothesised to be trimerized by the conjunction of the N-termini forming a unique 'heme-junction'. Whilst this structural conformation has not been proven, truncation of the N-terminus through molecular biology showed that ExtA was no longer able to form a trimer and therefore suggests the proposed hypothesis of trimerization of ExtA at the N-terminus. The truncation of ExtA also shifted the spectral features with ExtA.1 no longer forming a split Soret. This could be an implication that the proposed 'heme junction' is the cause of the split Soret in ExtA due to its unusual heme stacking potentially leading to hemes unable to share π orbital electron density.

In Chapter 5 purification of ExtC from *S. oneidensis* LS527 and initial protein characterisation was attempted. However, due to insufficient yields of protein it was not possible to do extensive characterisation of this cytochrome. From initial findings, ExtC appears to display typical cytochrome characteristics unlike the other cytochromes of the ExtABCD complex. Sedimentation velocity additionally confirmed ExtC to be monomeric in solution. Interactions between the cytochromes of the ExtABCD PCC were also investigated using sedimentation velocity. No interaction was observed between ExtA and ExtC or ExtD however a potential interaction between ExtC and ExtD was observed. An *in-silico* investigation into ExtB suggests that it does indeed form the porin component of the ExtABCD PCC. AlphaFold modelling shows the ExtB porin to be comprised of 20 anti-parallel β -sheets. This is considerably smaller than MtrB of the MtrCAB PCC from *S. baltica* which contains 26 anti-parallel β -sheets ⁸, suggesting that smaller porin-like proteins may be employed by *G. sulfurreducens* PCA.

Consolidating results generated from the entirety of this thesis a new model for ExtABCD was proposed, *Figure 6.1*. Previous models have suggested that ExtAB form the porin-cytochrome interface ⁷, however this work now suggests that it is ExtBC that forms this interface, the new role for ExtA as a periplasmic shuttle is now proposed. Whilst SV experiments show that ExtC and ExtA do not form a stable complex it is possible that ExtA and ExtB are able to interact and this would

cause ExtA to be permanently positioned at the inner leaflet of the outer membrane, this has however not been proven and further investigations into how, if at all, ExtA interacts with ExtBCD should be conducted. The possibility of ExtA as a periplasmic shuttle also leads to the question of if the cytochrome is cable of bridging the periplasmic gap allowing for a fast throughput of electrons directly from quinol dehydrogenases in the inner membrane to outer membrane PCCs. Whilst this is a nice hypothesis the potential for this is limited, recent studies have shown that the periplasmic space of *Geobacter* is approximately 40 nm⁹ in width whilst the maximum possible length of ExtA fully extended would only be approximately 17 nm, making this possibility unlikely.

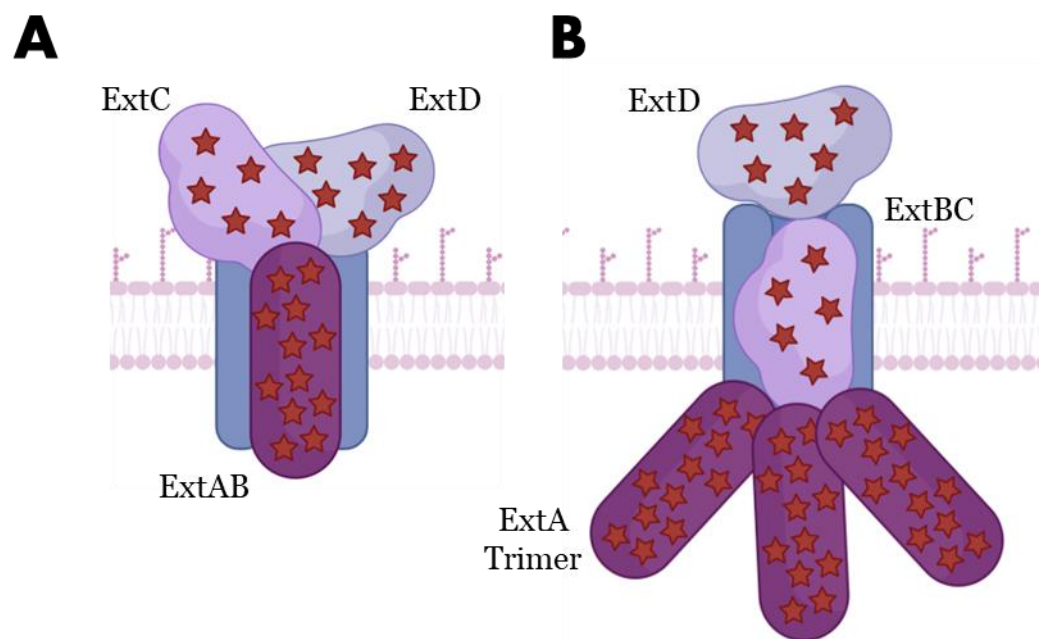


Figure 6.1- Cartoon of previous and newly hypothesised schematic of ExtABCD localisation in the outer membrane. A) Previous hypothesised schematic of ExtABCD localisation, with ExtAB forming the porin cytochrome complex and ExtC and ExtD positioned as extracellular lipo-cytochromes. B) Newly hypothesised schematic for ExtABCD localisation based on work from this thesis. ExtA being a homotrimer acting as a periplasmic electron shuttle, ExtBC forming the porin cytochrome complex and ExtD being the sole extracellular lipo-cytochrome.

The new hypothetic model for ExtD localises the cytochrome on the outer leaflet of *G. sulfurreducens* making it the sole outer membrane cytochrome (OMC) of the ExtABCD PCC. Compared to other OMCs believed to function in similar roles,

ExtD is considerably smaller. Comparison of structurally solved OMCs MtrC from *S. baltica*⁸ and OcwA from *Thermincola potens* JR¹⁰ highlight the difference in size between ExtD and other OMCs, *Figure 6.2*. ExtD is predicted to contain six c-type hemes compared to MtrC with 10 hemes and OcwA with 9 hemes. The total predicted height of ExtD is 47 Å, approximately half the height of MtrC and OcwA. The size of ExtD is expected to limit the ability of ExtD to interact with terminal electron acceptors, with a large proportion of the cytochrome predicted to be obscured by polysaccharides present on the outer leaflet.

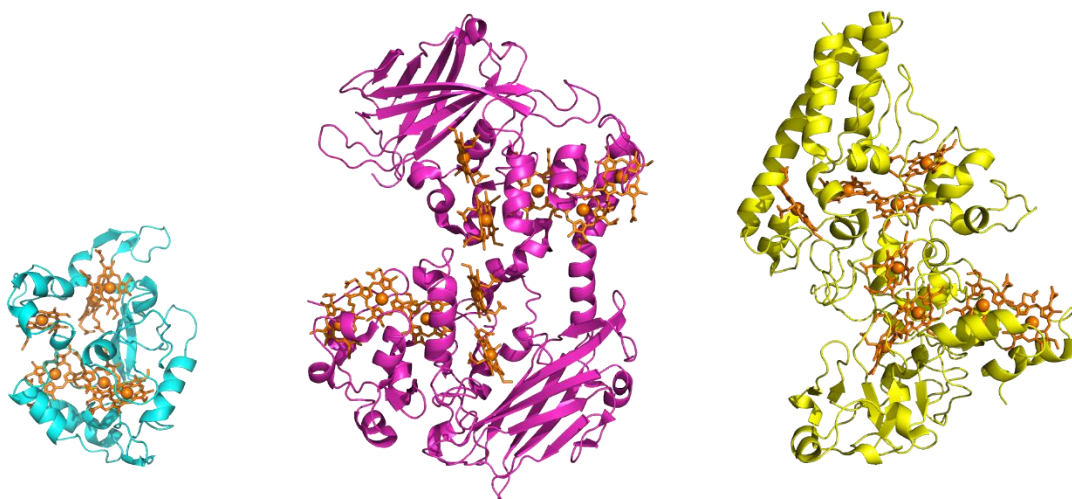


Figure 6.2- Structures of outer membrane cytochromes. A) AlphaFold 3 model of ExtD from Geobacter sulfurreducens. B) Crystal structure of MtrC from Shewanella baltica (PDB: 6QYC). Crystal structure of OcwA from Thermincola potens JR (PDB: 6I5B)

6.2. Models of Geobacter Porin Cytochrome Complexes

In this thesis the characterisation of ExtABCD revealed potential divergences from the model for PCCs. *Geobacter* contains at least five PCCs⁶ with no structural characterisation as of yet performed on any of the complexes. Here AlphaFold is used to investigate possible conformations of *Geobacter's* PCCs.

AlphaFold 3¹¹ models were generated for the remaining PCCs of *G. sulfurreducens* PCA: Gpc1, Gpc2, ExtEFG and ExtHIJKL. Before being modelled by

AlphaFold all protein sequences were entered into SignalP 5.0 ¹² and the predicted signal peptide was removed from the sequence.

6.2.1. AlphaFold modelling of predicted PCCs Gcp1 and Gcp2

Gpc1 and Gp2 (OmaB-OmbB-OmcB and OmaC-OmbC-OmcC) are predicted PCCs from *G. sulfurreducens* PCA. The two clusters are predicted to be homologous and the result of gene duplication and are therefore often paired together. Using AlphaFold 3 models of the Gcp1 and Gcp2 complex and component proteins were generated, *Figure 6.3*. Models of the predicted outer membrane components OmcB and OmcC, *Figure 6.3A-B*, both have a high average pLDDT score, 90.7 and 89.5 % respectively. The heme coordination predicted the presence of 11 bis-His coordinated hemes and in both cases, Heme 5 had a penta-coordination. The AlphaFold models of predicted porin-like components OmbB and OmbC, *Figure 6.3C-D*, both had an average pLDDT score of 95.2 %. AlphaFold predicted that both porin-like proteins would be formed of 22 anti-parallel β -sheets. The predicted multiheme cytochromes OmaB and OmaC were modelled through AlphaFold, *Figure 6.3E-F*, and had an average pLDDT score of 73.1 and 75.0 % respectively. The heme coordination predicted for OmaB and OmaC showed that all hemes were bis-His coordinated. A full complex model of Gcp1 is shown in *Figure 6.3G*, Gcp2 is not shown as homologous to Gcp1, predicted that OmaB and OmbB would form the porin-cytochrome complex with OmcB being positioned extracellularly.

Structurally this is similar to the previously characterised MtrCAB from *S. baltica*. A key difference of note is the overhang of three hemes from OmaB into the extracellular space. In MtrAB there is an overhang of three hemes from MtrA, however extended towards the periplasm ⁸. Additionally, the porin OmbB is predicted to be considerably smaller than MtrB, with OmbB only insulating five hemes of OmaB compared to the seven hemes of MtrA insulated by MtrB.

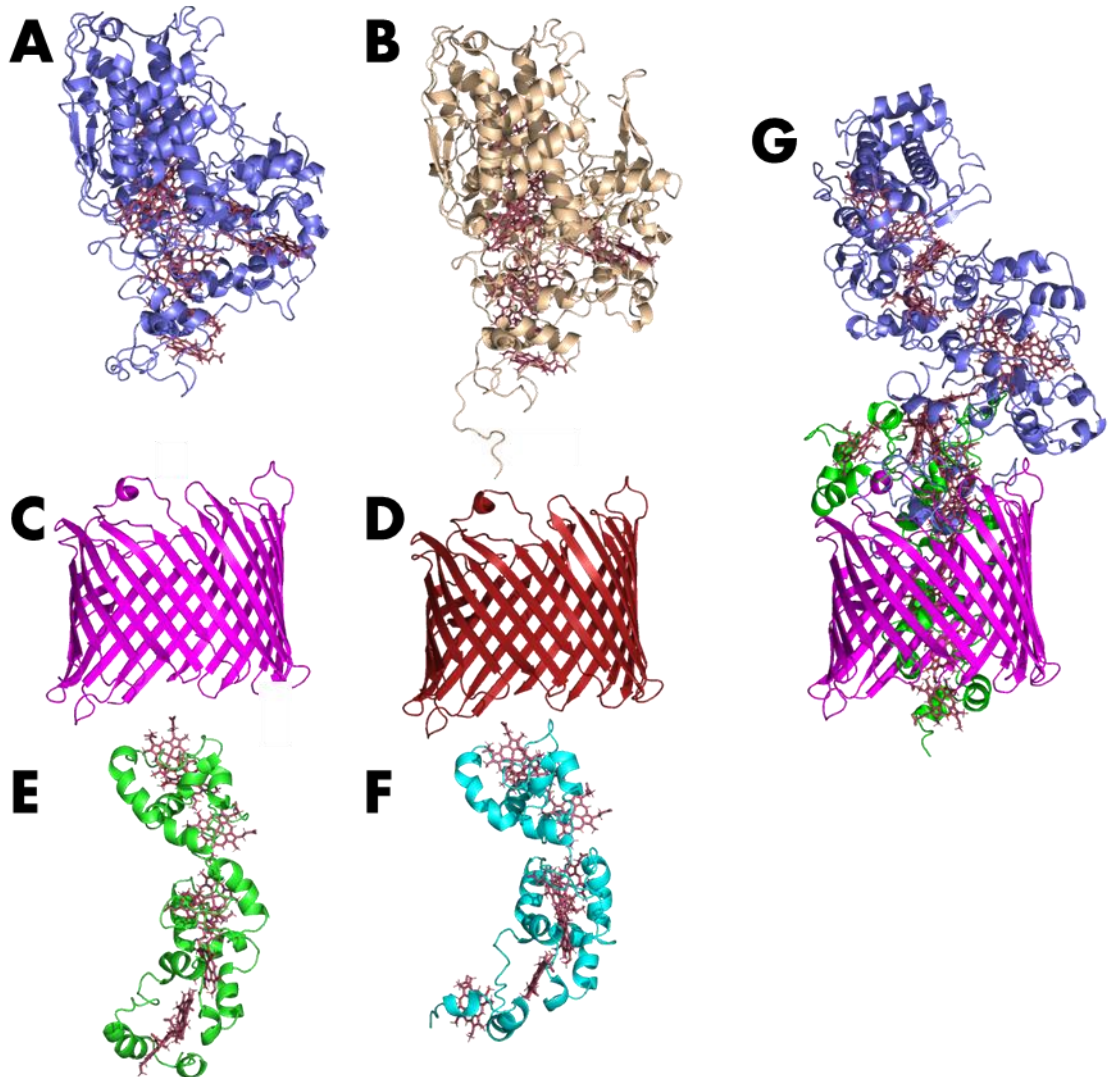


Figure 6.3- AlphaFold models of Gcp1 and Gcp2 components, A) OmaB B) OmaC C) OmbB D) OmbC E) OmcB F) OmcC G) Gpc1 complex.

6.2.2. AlphaFold modelling of predicted PCC ExtEFG

ExtEFG is a predicted PCC from *G. sulfurreducens* PCA hypothesised to be comprised of ExtE a porin-like protein, ExtF a pentaheme lipo-cytochrome and ExtG a 20-heme lipo-cytochrome⁶. Modelling of ExtE by AlphaFold 3 simulated a porin-like structure with 22 transmembrane regions with an average pLDDT of 90.08 %, Figure 6.4A. Using APBS¹³ to visualize the electrostatic potential of the

ExtE model between -10 (Red) and 10 (Blue) kT/e, shown in *Figure 6.4B*. Visualization of the protein in this way reveals a strong negatively charged band along the top, facing the outer leaflet, similar to the electrostatic potential seen in MtrB from *S. baltica*⁸, and is predicted to act as a docking station for extracellular complex components.

The lipo-cytochrome ExtF has a total of five CxxCH motifs within its sequence and is therefore predicted to be capable of covalently binding five c-type cytochromes. Structural modelling using AlphaFold generated a representation of ExtF, *Figure 6.4C*, with all five CxxCH motifs aligned in such a way so that manual insertion of c-type hemes was plausible with the His residue of each motif being in position to act as the proximal axial ligand. All six hemes of ExtF were predicted to be hexa-coordinated with His acting as the distal ligand. The model predicted by AlphaFold had an average pLDDT score of 79.35 %.

The lipo-cytochrome ExtG has a total of 20 predicted c-type heme binding sites, with atypical c-type heme binding motifs seen at Hemes 2 and 8 with predicted Cx₉CH motif, Hemes 6 and 10 with predicted Cx₅CH, Heme 15 with predicted Cx₁₅CH motif and Hemes 17 and 20 with predicted Cx₃CH motif. Modelling of ExtG by AlphaFold 2, *Figure 6.4D*, yielded a simulated structure where it was possible to insert all 20 hemes into the Cx_nCH pockets so that the Cys lined up with the vinyl groups of the hemes and the His residue would theoretically be able to act as the proximal ligand. In this model all hemes except for Hemes 9, 10, 12, 14 and 20 are modelled to be bis-His ligated, instead showing predicted penta-coordination. However, with these hemes there is a high degree of unlikelihood that the simulated structure is correct as the hemes are clashed with each other and nearby residues. The average pLDDT score given by AlphaFold for the model ExtG is 65.87 % with the lowest scores seen in the immediate areas around hemes 9, 10, 12, 14 and 20. This is suggestive that these areas are the least likely to be modelled correctly. As well as indicating low probability of successful modelling a low average pLDDT has also been suggested by some researchers to suggest area of the protein that are dynamic¹⁴. The

amino acid backbone between hemes 10 and 11 is extremely unstructured and is also the site of the lowest confidence score possibly suggesting a large amount of flexibility to be observed in this area, potentially allowing for hemes 12 to 20 to act as an independent arm searching for potential terminal electron acceptors.

Previous hypotheses had predicted that ExtEG would form the porin-cytochrome complex, however AlphaFold 3 was unable to model this interaction. Therefore, the possibility that ExtF would perform this function was investigated with AlphaFold successfully generating an ExtEF complex, *Figure 6.4E*. The complex had an average pLDDT score of 91.47 % an improved score from the monomeric predictions. This is suggestive of a strong interaction between the two proteins. If this predicted complex is correct ExtEF would be the second PCC in *G. sulfurreducens* to utilise a lipo-cytochrome in the porin-cytochrome complex, after ExtBC. In both cases ExtC and ExtF have been predicted through the AlphaFold models to be covalently attached to the inner leaflet.

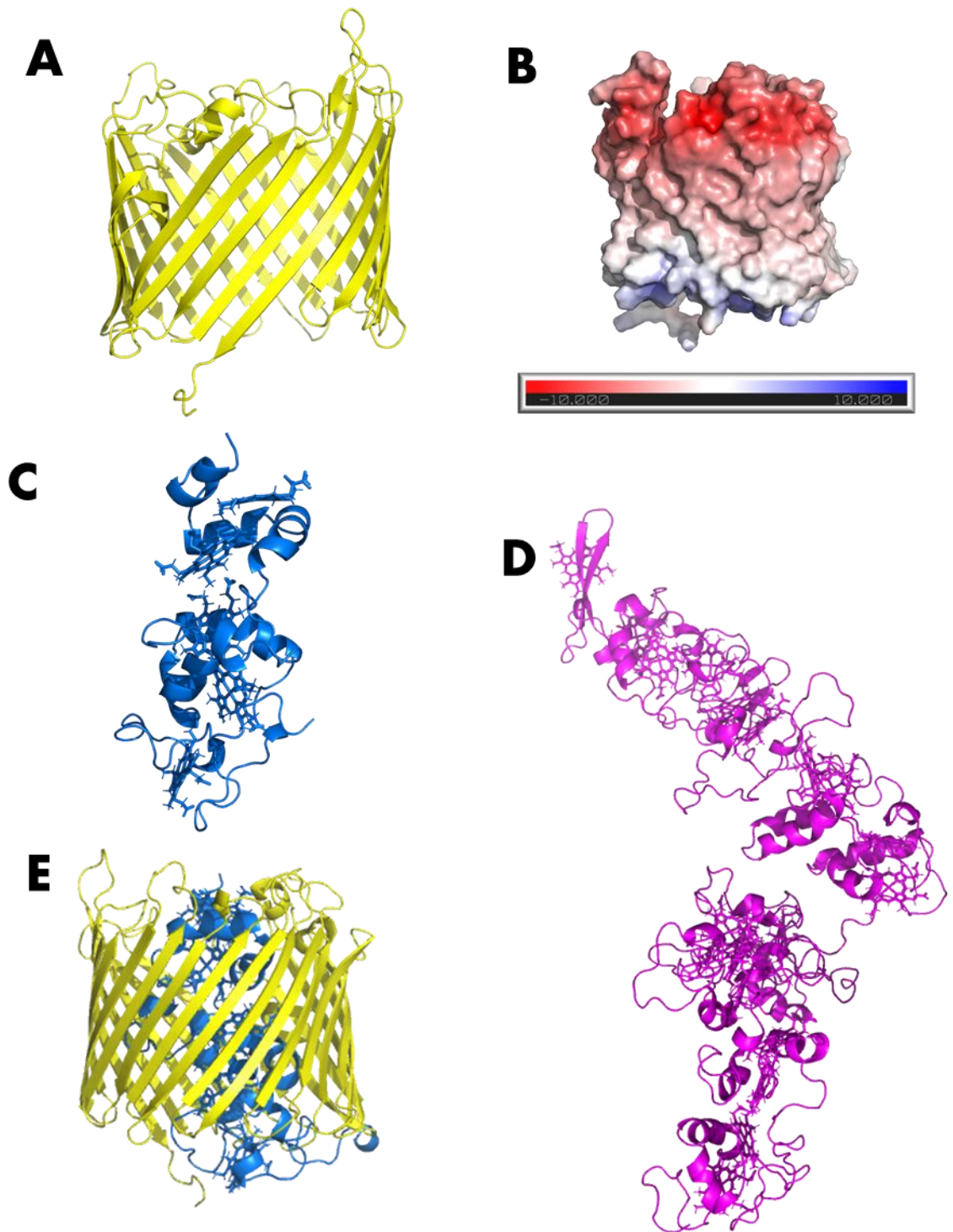


Figure 6.4- AlphaFold models of the ExtEFG complex from *Geobacter sulfurreducens* PCA. A) ExtE a porin-like protein, B) Electrostatic potential of ExtE between -10 (red) and +10 (blue) kT/e, produced using APBS D) ExtF a pentaheme lipo-cytochrome, D) ExtG a icosaheme cytochrome, E) the porin cytochrome complex formed by ExtEF

6.2.3. AlphaFold modelling of predicted PCC ExtHIJKL

The final predicted PCC from *G. sulfurreducens* PCA's genome is the ExtHIJKL complex. Unlike other PCCs discussed here ExtHIJKL contains additional proteins that are not proposed to be cytochromes or porins as well as containing small proteins of hitherto unknown functionality.

The first component of the ExtHIJKL complex is ExtH predicted to be a lipoprotein covalently bound to the outer leaflet of the outer membrane. ExtH is not predicted to be a cytochrome and instead predicted to be of a protein of the rhodanese-family. Rhodanese proteins are capable of detoxifying cyanide by chemical conversion to thiocyanate, with related proteins also been shown to function in the biosynthesis of molybdenum cofactors¹⁵ and selenite reduction¹⁶. ExtH is predicted to be in the subclass of rhodanese proteins functioning as a selenite reductase¹⁷. Using AlphaFold a simulated structure was generated, *Figure 6.5A*, the average pLDDT associated with this model was 90.21 %.

The predicted porin-like component of the ExtHIJKL PCC is ExtI. Structural modelling using AlphaFold reveals a porin-like structure containing 16 transmembrane β -sheets, *Figure 6.5B*. The ExtI model has an average pLDDT of 96.40 % making it the highest scored protein discussed here and above the AlphaFold threshold of 95 % which suggests a model will be near identical to experimental methods of structure determination. As experimental studies investigating the structure of ExtI have yet to be accomplished this claim cannot be confirmed. Using APBS to visualize the electrostatic potential of the ExtI model, *Figure 6.4B*, it is seen that the majority of ExtI has a weak electronegative potential across the whole of the protein with strong band of electronegativity across the top, facing the extracellular space, as seen with other porin-like proteins discussed previously in this chapter.

The small periplasmic protein ExtJ is the next component of the ExtHIJKL PCC. ExtJ is predicted to be localised to the periplasmic space however its functionality is currently unknown. ExtJ is predicted to be formed of 104 amino acid and with

removal of the signal peptide predicted to occur between Ala23 and Ala24 producing a functional ExtJ with a length of 81 amino, producing the smallest protein of all those discussed from all of *Geobacter's* PCCs. Using AlphaFold to model the protein revealed a protein formed of five β -sheets and one α -helix, *Figure 6.5C*. The average pLDDT score associated with this model is 90.57 %.

The only predicted cytochrome component of the ExtHIJKL complex is the pentaheme ExtK. Originally predicted to be 324 amino acids in length it has been hypothesised that the predicted STOP codon of the *extK* gene actually encodes a selenocysteine and the previously predicted ExtL protein is also included in the final protein^{17,18}. This claim is supported by analysis of ExtL with SignalP 5.0 unable to predict a signal peptide associated with the predicted amino acid sequence of ExtL. As ExtL is also predicted to part of the ExtHIJKL complex it would be suspected that localisation to the periplasm would be essential and without a signal peptide this would be unlikely. Modelling of ExtK by AlphaFold reveals a structure that has an average pLDDT of 95.82 % whilst AlphaFold modeling of ExtL has an average pLDDT of 80.54 %, *Figure 6.5D-F*. Modelling of selenocysteine ExtKL was also performed however as AlphaFold is currently not able to model amino acids outside of the standard 20 therefore a Cys residue was used, produces a model with an average pLDDT of 94.67 %. By only calculating the average pLDDT for the ExtL portion of the ExtKL model an increase in the average pLDDT raising to 92.64 %. The structure of ExtL also changes between being modelled individually and as a selenocysteine protein with the addition of more structured regions. This would suggest a positive interaction between the two proteins when modelled as a selenocysteine. As ExtK is expected to be insulated by the porin, ExtI, it is unusual to see AlphaFold model the cytochrome as a globular protein rather than a oblong structure. The widest part of the ExtKL structure was calculated to be 54 Å whilst the internal diameter of ExtB was calculated to be 33 Å suggesting they do not form a complex with homology to MtrAB from *Shewanella*.

AlphaFold was unable to model a complex structure for ExtHIJKL and was additionally unable to model any interaction between ExtI and another protein from this complex. For each individual protein modelled AlphaFold shows a high confidence, average pLDDT scores above 90 %, it is surprising to see that AlphaFold is unable to predict any complex interactions. This could suggest that the proteins functionality is that not of a conventional PCC but of a selenite uptake system, as has been suggested by some researchers ^{17,18}.

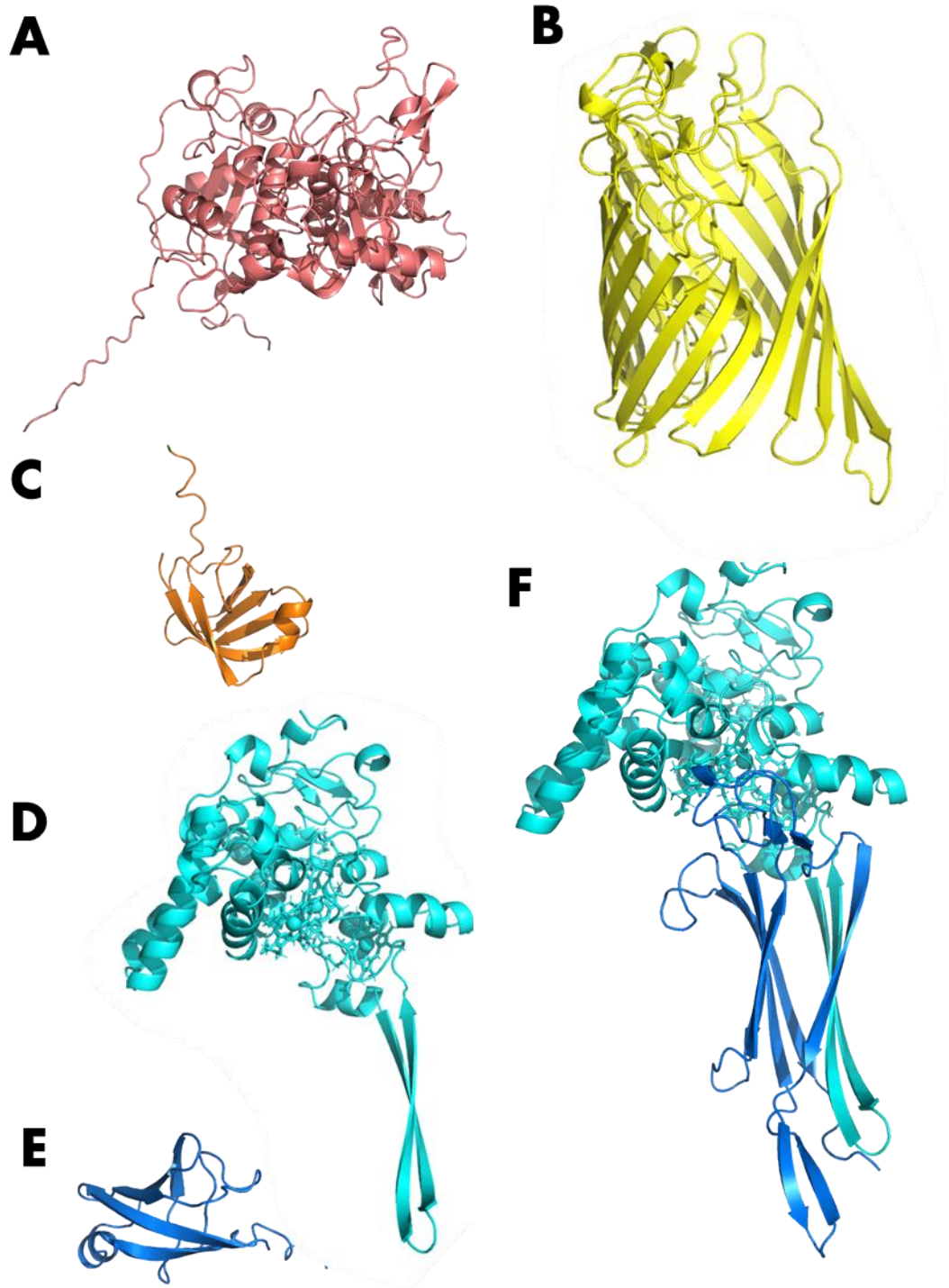


Figure 6.5- AlphaFold models of the ExtHIJKL complex. A) ExtH a rhodanese like protein, B) ExtI a porin like protein, C) ExtJ a small protein of unknown function, D) ExtK pentaheme c-type cytochrome, E) ExtL a small protein of unknown function and F) potential selenocysteine protein ExtKL

Using AlphaFold to model all the known predicted PCCs from *Geobacter sulfurreducens* PCA revealed interesting findings that question the known criterion of PCCs. In the cases of ExtBC and ExtEF both of the cytochromes are predicted to also contain lipid anchors. This is novel to *Geobacter* with other researched PCCs from varying bacteria not predicted to contain a lipid anchored porin-cytochrome complex. Additionally, both ExtC and ExtF are predicted to be penta-hemes whilst other cytochromes that are predicted to form a similar function generally have 10 or more hemes, eg. MtrA from *Shewanella oneidensis*, MtoA from *Sideroxydans lithotrophicus* and PioA from *Rhodopseudomonas palustris*^{8,19,20}. In both ExtBC and ExtEF the five heme wire is capable of spanning the entire height of the porin potentially allowing for electron transport from one side to the other. This is dissimilar to the structure of MtrAB⁸, where the hemes of MtrA overhang on either side of MtrB. This could suggest that the hemes of ExtC and ExtF will be comparably less solvent accessible than those of larger MHCs predicted to perform a similar function.

6.3. Future Perspectives

Characterisation of ExtD and ExtA have revealed that both cytochromes contain a split Soret within their UV-Vis spectra. This atypical feature of a cytochrome spectrum was not fully answered here but the hypothesis has been proposed that the source of this feature is due to non-canonical heme stacking that separates the heme chains in two separate groups. Future work should attempt to resolve this hypothesis. If the purification of ExtA and ExtD was able to be increased the possibility of resolving their structure becomes available, through the use of X-ray crystallography. This would allow for accurate determination of the heme stacking within ExtA and ExtD without having to rely on AlphaFold or similar *in-silico* structural modelling.

Here expression of the cytochromes from the ExtABCD porin cytochrome complex was done separately and without the inclusion of ExtB. Future work should aim to rectify this by also expressing the *extB* gene. However, this work

would be challenging as the insertion of a porin into a heterologous host has been shown previously to have limited success. Therefore, it is probable that purification of the ExtABCD complex as a whole would have to be done in *G. sulfurreducens* PCA. This would involve generating a new method for using *G. sulfurreducens* as a model organism for protein purification. This approach has not been trialled due to the slow growth time of *G. sulfurreducens* limiting the amount of biomass that can be obtained. However, if expression systems in *G. sulfurreducens* PCA could be implemented it would allow for homologous expression and purification of the ExtABCD complex.

If the ExtABCD complex was to be purified as a whole complex, research should look at determining the structure through utilising cryo-EM. This would allow for either an acceptance or rejection of the hypothesis proposed here for the arrangement of these proteins in the outer membrane. If it is shown that ExtA does function as a periplasmic shuttle what is the interaction with the rest of the complex. Specifically, it would be interesting to determine if the interaction between ExtA and ExtC occurred at the N- or C-terminus of ExtA. This is an important factor to consider as if ExtA is fully reduced then all 36 electrons could potentially be channelled through one ExtBCD if the interaction is at the N-terminus of ExtA. Alternatively, if the C-terminus of ExtA shows a preferential interaction with ExtBCD then there are three potential entry/exit points for electrons from the cytochrome. This could potentially allow three ExtBCD complexes to be reduced at one time tripling the electron flux to extracellular terminal electron acceptors.

6.4. References

1. Pereira, M. M., Carita, J. N. & Teixeira, M. Membrane-Bound Electron Transfer Chain of the *Thermohalophilic* Bacterium *Rhodothermus marinus*: A Novel Multihemic Cytochrome bc, a New Complex III. *Biochemistry* **38**, 1268–1275 (1999).
2. Arciero, D. M., Balny, C. & Hooper, A. B. Spectroscopic and rapid kinetic studies of reduction of cytochrome c554 by hydroxylamine oxidoreductase from *Nitrosomonas europaea*. *Biochemistry* **30**, 11466–11472 (1991).

3. Abreu, I. A. *et al.* A novel iron centre in the split-Soret cytochrome c from *Desulfovibrio desulfuricans* ATCC 27774. *JBIC Journal of Biological Inorganic Chemistry* **8**, 360–370 (2003).
4. Mendez, D. L. *et al.* Engineered holocytochrome c synthases that biosynthesize new cytochromes c. *Proceedings of the National Academy of Sciences* **114**, 2235–2240 (2017).
5. van Wonderen, J. H. *et al.* Do multiheme cytochromes containing close-packed heme groups have a band structure formed from the heme π and π^* orbitals? *Curr Opin Electrochem* **47**, 101556 (2024).
6. Jiménez Otero, F., Chan, C. H. & Bond, D. R. Identification of Different Putative Outer Membrane Electron Conduits Necessary for Fe(III) Citrate, Fe(III) Oxide, Mn(IV) Oxide, or Electrode Reduction by *Geobacter sulfurreducens*. *J Bacteriol* **200**, (2018).
7. Jiménez Otero, F. *et al.* Evidence of a Streamlined Extracellular Electron Transfer Pathway from Biofilm Structure, Metabolic Stratification, and Long-Range Electron Transfer Parameters. *Appl Environ Microbiol* **87**, (2021).
8. Edwards, M. J., White, G. F., Butt, J. N., Richardson, D. J. & Clarke, T. A. The Crystal Structure of a Biological Insulated Transmembrane Molecular Wire. *Cell* **181**, 665–673.e10 (2020).
9. Howley, E., Mangus, A., Williams, D. & Torres, C. I. Intracytoplasmic membranes develop in *Geobacter sulfurreducens* under thermodynamically limiting conditions. *NPJ Biofilms Microbiomes* **9**, 18 (2023).
10. Costa, N. L. *et al.* How Thermophilic Gram-Positive Organisms Perform Extracellular Electron Transfer: Characterization of the Cell Surface Terminal Reductase OcwA. *mBio* **10**, (2019).
11. Abramson, J. *et al.* Accurate structure prediction of biomolecular interactions with AlphaFold 3. *Nature* (2024)
12. Almagro Armenteros, J. J. *et al.* SignalP 5.0 improves signal peptide predictions using deep neural networks. *Nat Biotechnol* **37**, 420–423 (2019).
13. Jurrus, E. *et al.* Improvements to the APBS biomolecular solvation software suite. *Protein Science* **27**, 112–128 (2018).
14. Ma, P., Li, D. & Brüschweiler, R. Predicting protein flexibility with AlphaFold. *Proteins: Structure, Function, and Bioinformatics* **91**, 847–855 (2023).
15. Matthies, A., Rajagopalan, K. V., Mendel, R. R. & Leimkühler, S. Evidence for the physiological role of a rhodanese-like protein for the biosynthesis of the molybdenum cofactor in humans. *Proceedings of the National Academy of Sciences* **101**, 5946–5951 (2004).
16. Wells, M. *et al.* Respiratory Selenite Reductase from *Bacillus selenitireducens* Strain MLS10. *J Bacteriol* **201**, (2019).
17. Jahan, Mst. I. *et al.* Selenite uptake by outer membrane porin ExtI and its involvement in the subcellular localization of rhodanese-like lipoprotein ExtH in *Geobacter sulfurreducens*. *Biochem Biophys Res Commun* **516**, 474–479 (2019).

18. Jahan, Mst. I., Tobe, R. & Mihara, H. Characterization of a Novel Porin-Like Protein, ExtI, from *Geobacter sulfurreducens* and Its Implication in the Reduction of Selenite and Tellurite. *Int J Mol Sci* **19**, 809 (2018).
19. Liu, J. *et al.* Identification and Characterization of MtoA: A Decaheme c-Type Cytochrome of the Neutrophilic Fe(II)-Oxidizing Bacterium *Sideroxydans lithotrophicus* ES-1. *Front Microbiol* **3**, (2012).
20. Li, D.-B. *et al.* His/Met heme ligation in the PioA outer membrane cytochrome enabling light-driven extracellular electron transfer by *Rhodospseudomonas palustris* TIE-1. *Nanotechnology* **31**, 354002 (2020).

Appendix

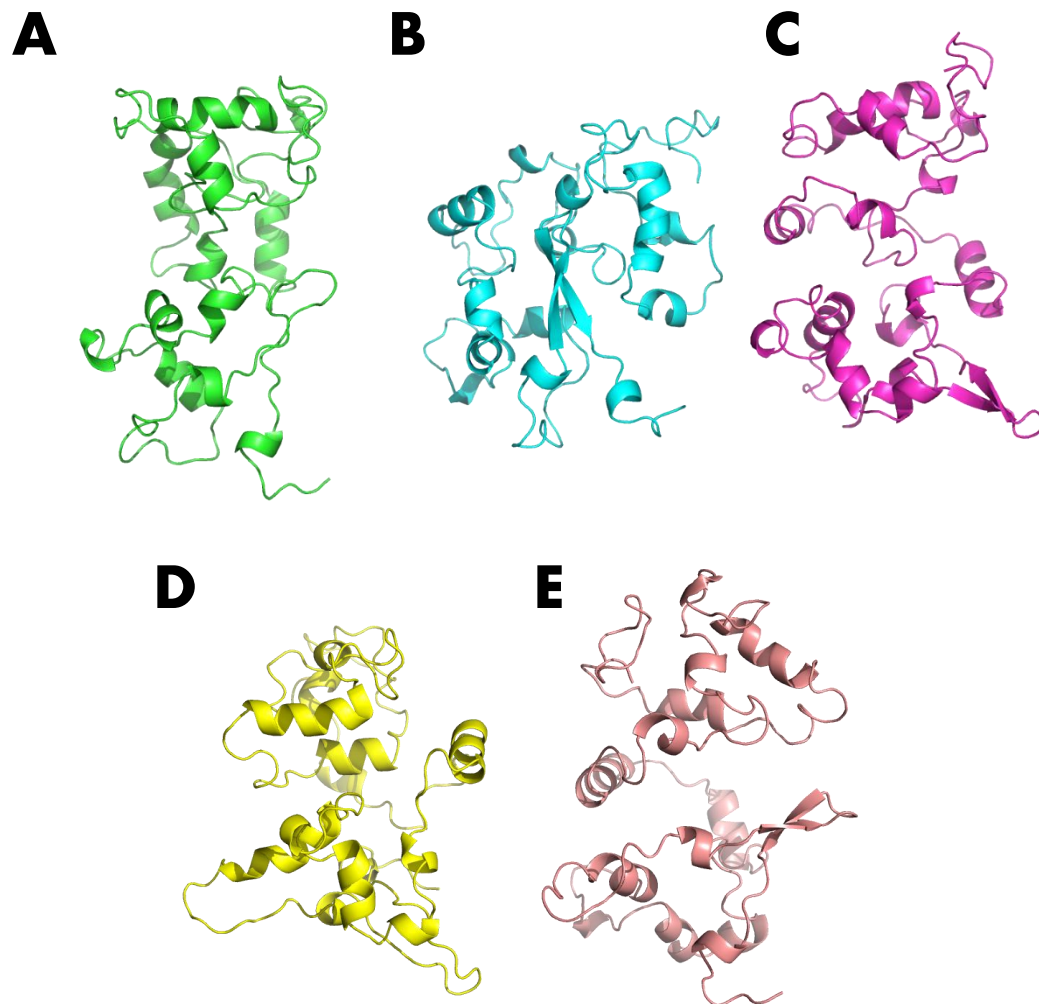


Figure A.1- Ranked AlphaFold 2 outputs of ExtD. A) Ranked_0 output with an average pLDDT of 53.96 %. B) Ranked_1 output with an average pLDDT of 48.02 %. C) Ranked_2 output with an average pLDDT of 47.90 %. D) Ranked_3 output with an average pLDDT of 46.94 %. E) Ranked_4 output with an average pLDDT of 45.32 %.

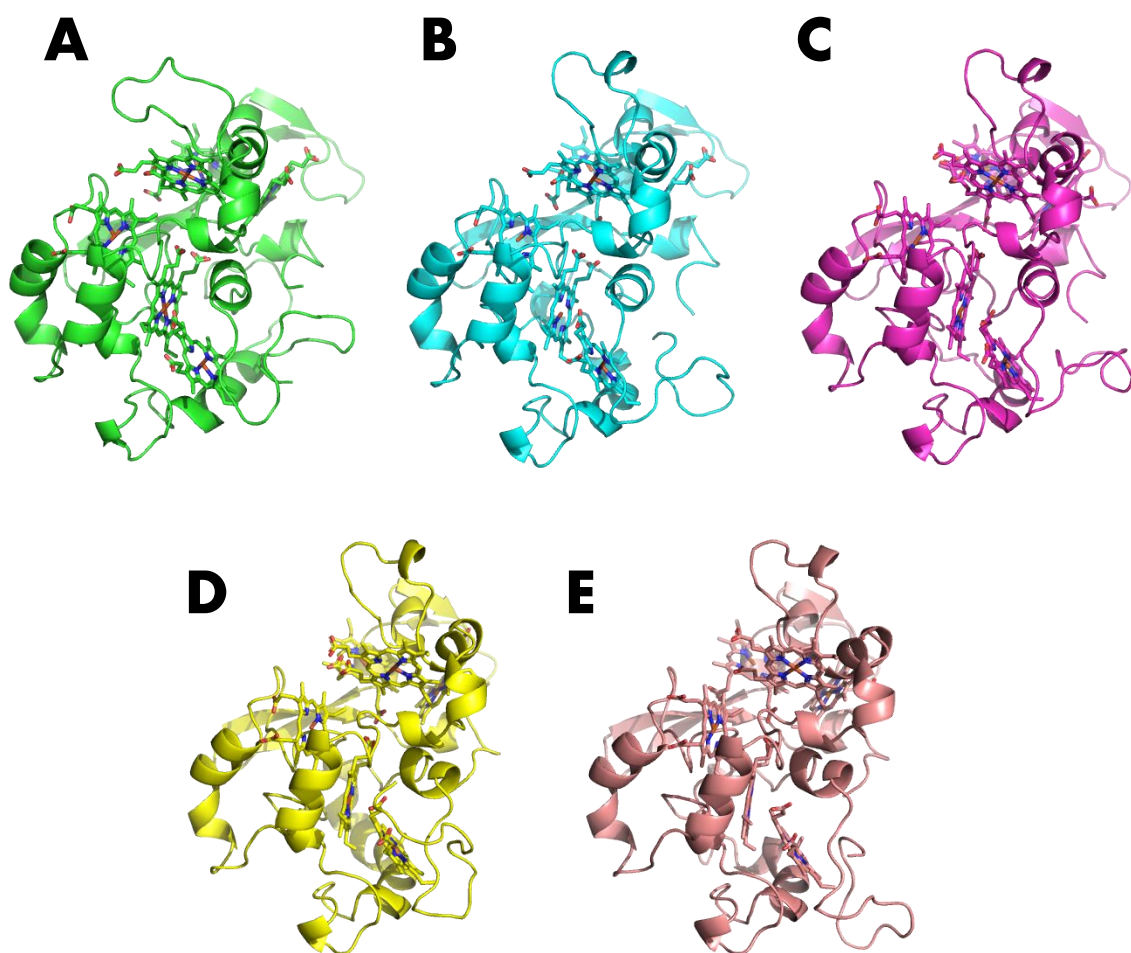


Figure A.2- Ranked AlphaFold 3 outputs of ExtD. A) Ranked_0 output with an average pLDDT of 73.00 %. B) Ranked_1 output with an average pLDDT of 72.51 %. C) Ranked_2 output with an average pLDDT of 72.49 %. D) Ranked_3 output with an average pLDDT of 72.08 %. E) Ranked_4 output with an average pLDDT of 72.36 %.

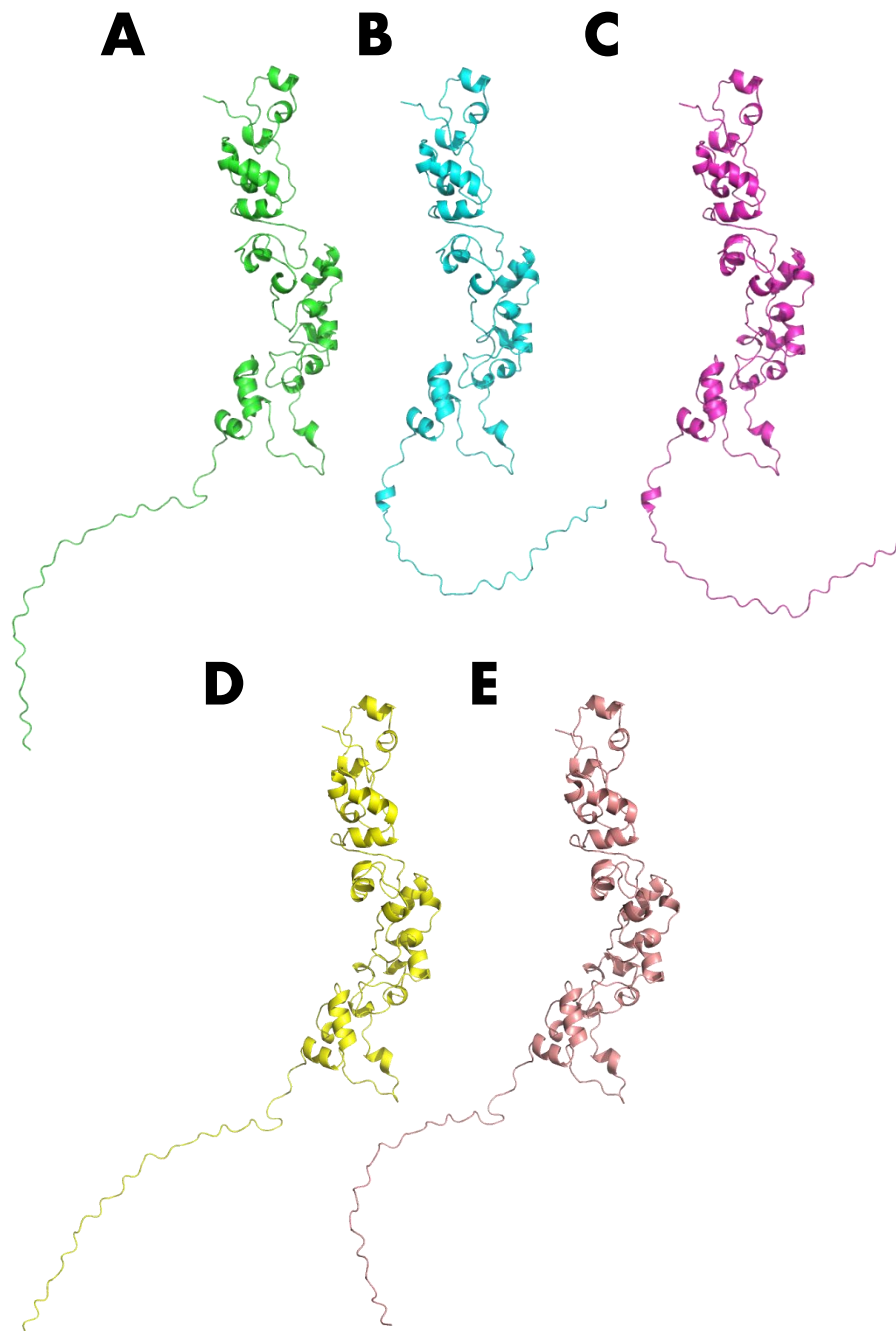


Figure A.3- Ranked AlphaFold 2 outputs of ExtA. A) Ranked_0 output with an average pLDDT of 86.66 %. B) Ranked_1 output with an average pLDDT of 89.88 %. C) Ranked_2 output with an average pLDDT of 90.18 %. D) Ranked_3 output with an average pLDDT of 88.85 %. E) Ranked_4 output with an average pLDDT of 79.97 %.

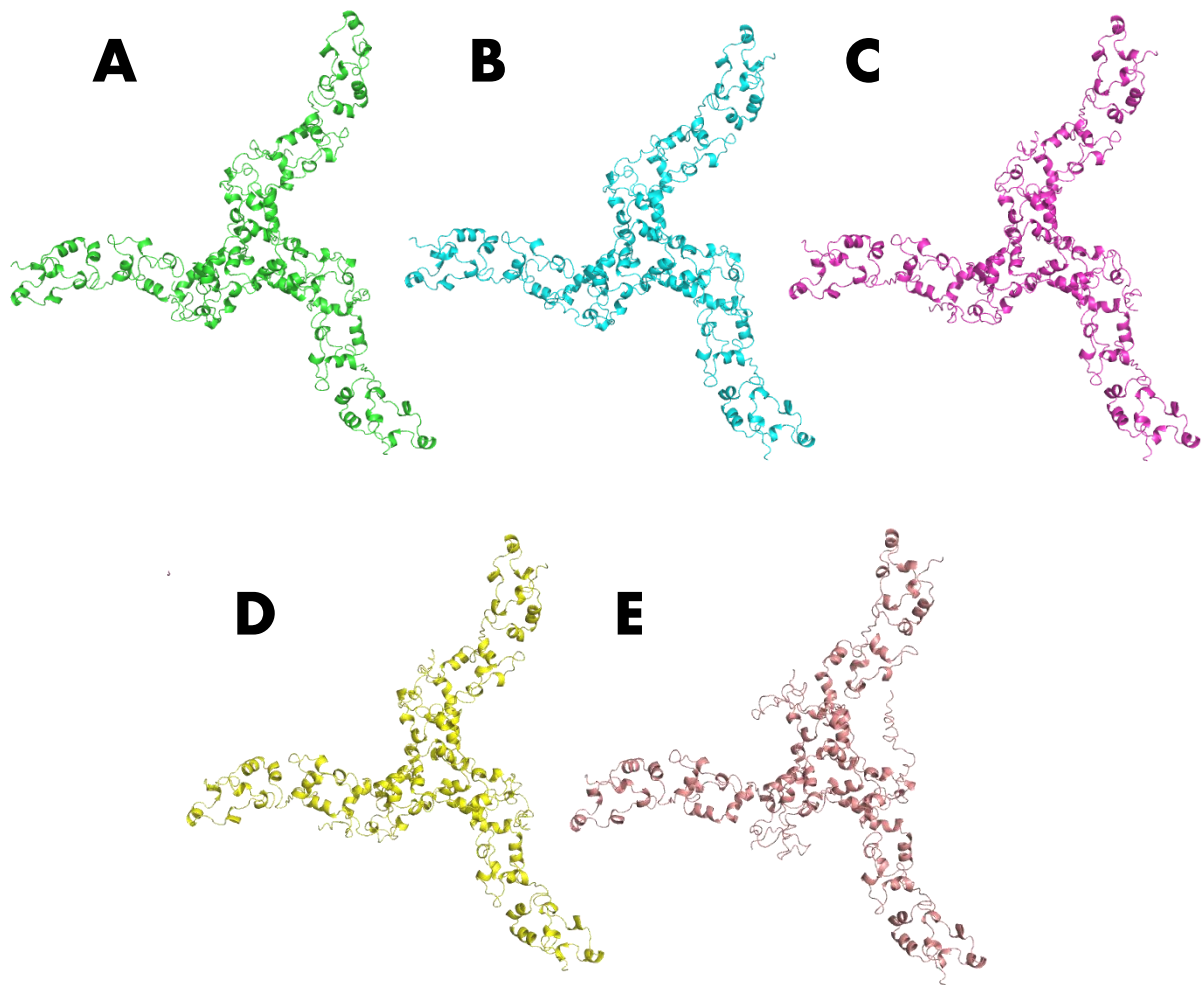


Figure A.4- Ranked AlphaFold 2 outputs of trimeric ExtA. A) Ranked_0 output with an average pLDDT of 81.92 %. B) Ranked_1 output with an average pLDDT of 75.14 %. C) Ranked_2 output with an average pLDDT of 83.04 %. D) Ranked_3 output with an average pLDDT of 83.74 %. E) Ranked_4 output with an average pLDDT of 79.97 %.

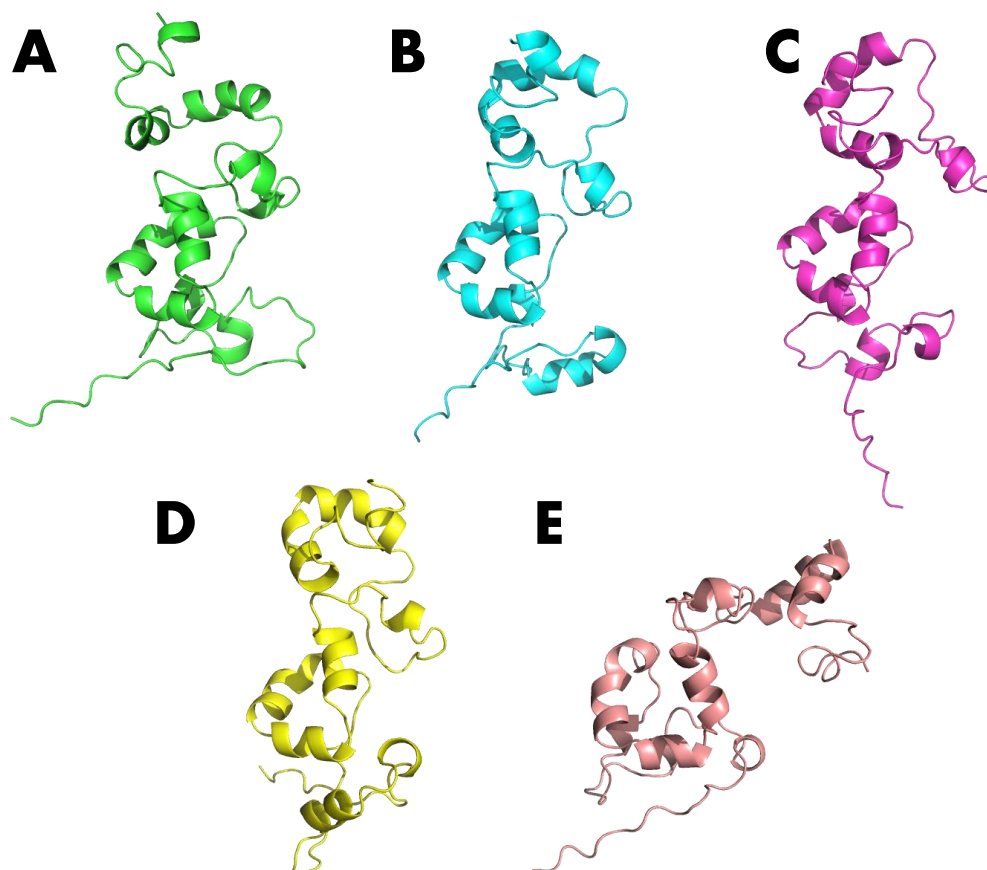


Figure A.5- Ranked AlphaFold 2 outputs of trimeric ExtC. A) Ranked_0 output with an average pLDDT of 81.53 %. B) Ranked_1 output with an average pLDDT of 80.46 %. C) Ranked_2 output with an average pLDDT of 79.60 %. D) Ranked_3 output with an average pLDDT of 70.67 %. E) Ranked_4 output with an average pLDDT of 69.24 %.

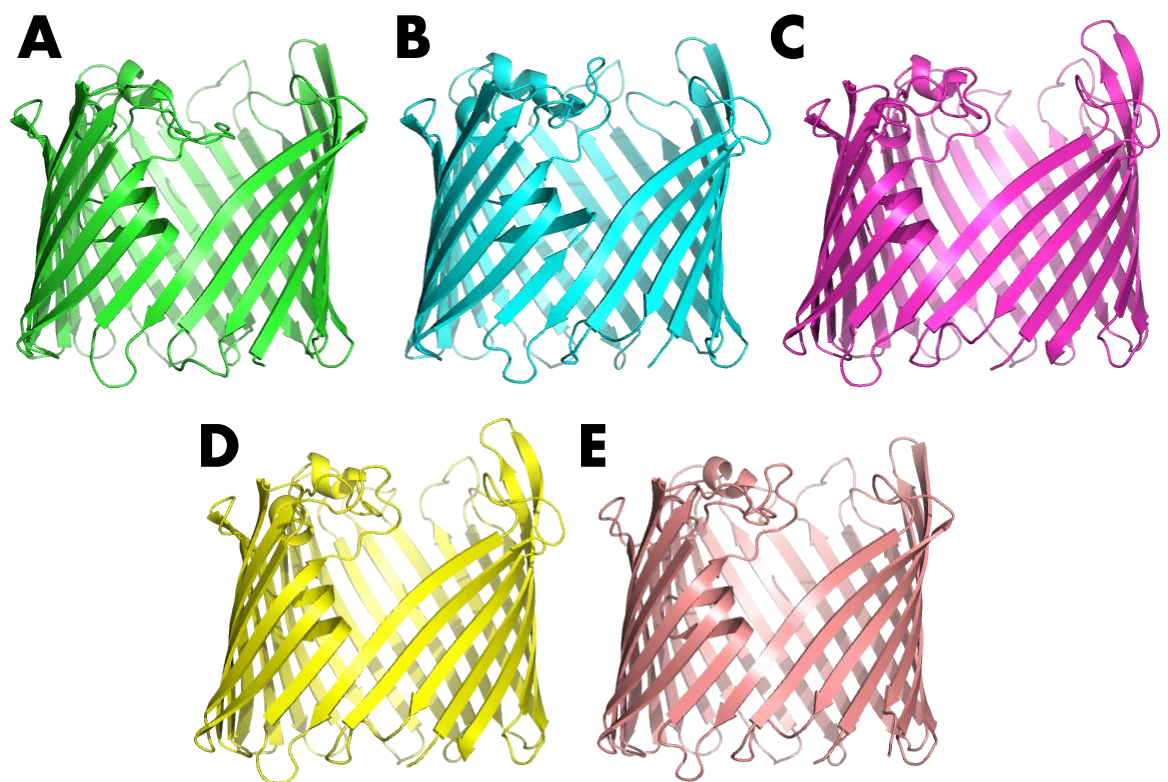


Figure A.6- Ranked AlphaFold 2 outputs of ExtB. A) Ranked_0 output with an average pLDDT of 90.88 %. B) Ranked_1 output with an average pLDDT of 88.90 %. C) Ranked_2 output with an average pLDDT of 85.23 %. D) Ranked_3 output with an average pLDDT of 89.13 %. E) Ranked_4 output with an average pLDDT of 87.50 %.

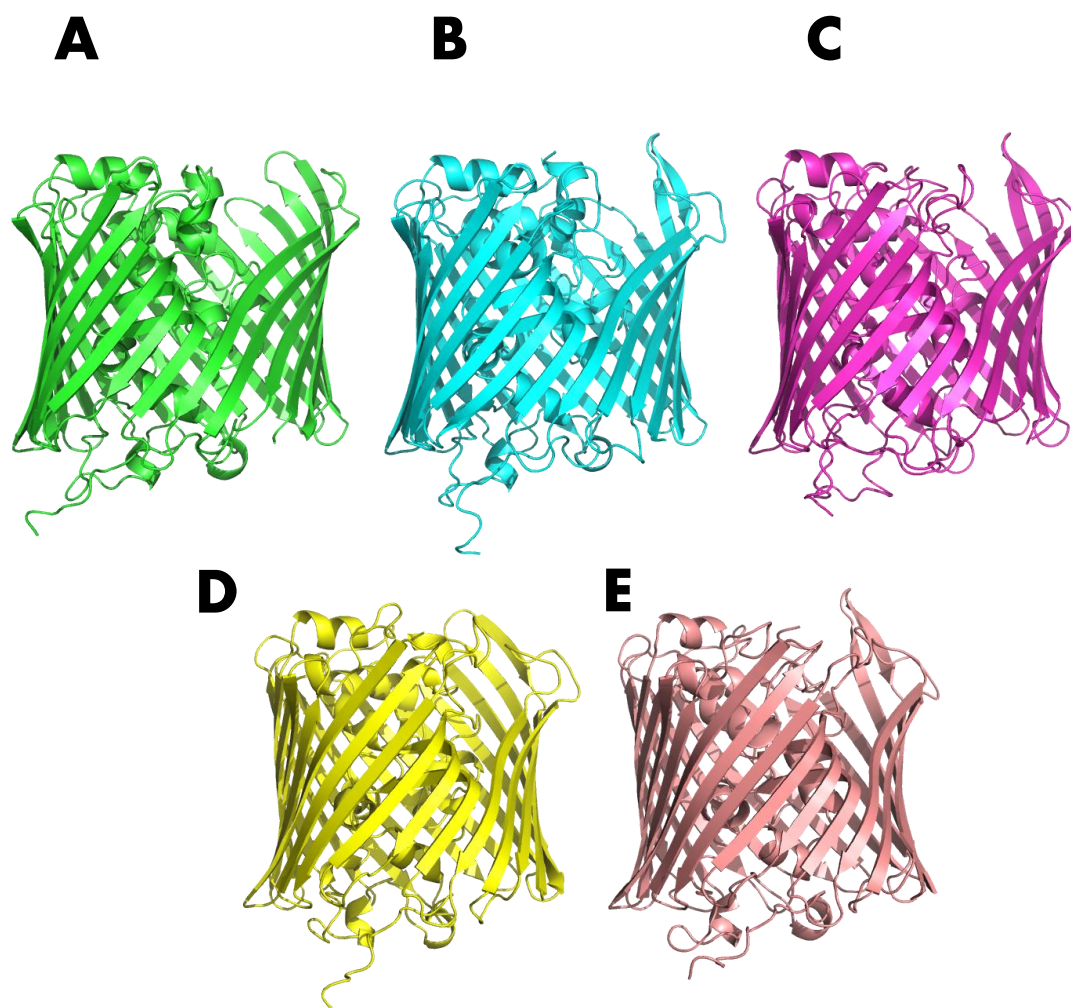


Figure A.7- Ranked AlphaFold 2 outputs of ExtBC. A) Ranked_0 output with an average pLDDT of 86.20 %. B) Ranked_1 output with an average pLDDT of 88.90 %. C) Ranked_2 output with an average pLDDT of 85.23 %. D) Ranked_3 output with an average pLDDT of 89.13 %. E) Ranked_4 output with an average pLDDT of 87.50 %.